QUANTUM PRECISION MEASUREMENT AND COLD ATOM PHYSICS

EDITED BY: Jingbiao Chen, Xuzong Chen, Fang Fang, Hong Guo,
Zhiwen Liu, Yanhui Wang and Xiaoji Zhou
PUBLISHED IN: Frontiers in Physics

frontiers Research Topics

ISSN 1664-8714
ISBN 978-2-83250-229-7
DOI 10.3389/978-2-83250-229-7

About Frontiers

Frontiers is more than just an open-access publisher of scholarly articles: it is a pioneering approach to the world of academia, radically improving the way scholarly research is managed. The grand vision of Frontiers is a world where all people have an equal opportunity to seek, share and generate knowledge. Frontiers provides immediate and permanent online open access to all its publications, but this alone is not enough to realize our grand goals.

Frontiers Journal Series

The Frontiers Journal Series is a multi-tier and interdisciplinary set of open-access, online journals, promising a paradigm shift from the current review, selection and dissemination processes in academic publishing. All Frontiers journals are driven by researchers for researchers; therefore, they constitute a service to the scholarly community. At the same time, the Frontiers Journal Series operates on a revolutionary invention, the tiered publishing system, initially addressing specific communities of scholars, and gradually climbing up to broader public understanding, thus serving the interests of the lay society, too.

Dedication to Quality

Each Frontiers article is a landmark of the highest quality, thanks to genuinely collaborative interactions between authors and review editors, who include some of the world's best academicians. Research must be certified by peers before entering a stream of knowledge that may eventually reach the public - and shape society; therefore, Frontiers only applies the most rigorous and unbiased reviews.
Frontiers revolutionizes research publishing by freely delivering the most outstanding research, evaluated with no bias from both the academic and social point of view. By applying the most advanced information technologies, Frontiers is catapulting scholarly publishing into a new generation.

What are Frontiers Research Topics?

Frontiers Research Topics are very popular trademarks of the Frontiers Journals Series: they are collections of at least ten articles, all centered on a particular subject. With their unique mix of varied contributions from Original Research to Review Articles, Frontiers Research Topics unify the most influential researchers, the latest key findings and historical advances in a hot research area! Find out more on how to host your own Frontiers Research Topic or contribute to one as an author by contacting the Frontiers Editorial Office: frontiersin.org/about/contact

QUANTUM PRECISION MEASUREMENT AND COLD ATOM PHYSICS

Topic Editors:
Jingbiao Chen, Peking University, China
Xuzong Chen, Peking University, China
Fang Fang, National Institute of Metrology, China
Hong Guo, Peking University, China
Zhiwen Liu, The Pennsylvania State University (PSU), United States
Yanhui Wang, Peking University, China
Xiaoji Zhou, Peking University, China

Citation: Chen, J., Chen, X., Fang, F., Guo, H., Liu, Z., Wang, Y., Zhou,X., eds. (2022). Quantum Precision Measurement and Cold Atom Physics. Lausanne: Frontiers Media SA. doi: 10.3389/978-2-83250-229-7

Table of Contents

frontiers | Frontiers in Physics

TYPE Editorial
PUBLISHED 15 September 2022
DOI 10.3389/fphy.2022.1035435

EDITED AND REVIEWED BY
Michael Charlton,
Swansea University, United Kingdom

*CORRESPONDENCE
Jingbiao Chen,
jbchen@pku.edu.cn

SPECIALTY SECTION
This article was submitted to Atomic and Molecular Physics,
a section of the journal
Frontiers in Physics

RECEIVED 02 September 2022
ACCEPTED 08 September 2022
PUBLISHED 15 September 2022

CITATION
Chen X, Zhou X, Ye A, Wang Y and Chen J (2022), Editorial: Quantum precision measurement and cold atom physics.
Front. Phys. 10:1035435.
doi: 10.3389/fphy.2022.1035435

Editorial: Quantum precision measurement and cold atom physics

Xuzong Chen[1], Xiaoji Zhou[1], Anpei Ye[2], Yanhui Wang[1] and Jingbiao Chen[1]*

[1]State Key Laboratory of Advanced Optical Communication, System and Network, School of Electronics, Peking University, Beijing, China, [2]Key Laboratory for the Physics and Chemistry of Nanodevices, School of Electronics, Peking University, Beijing, China

KEYWORDS

atomic clock, laser cooling, bose einstein condensate, optical clock, cold atom physics, optical tweezers

Editorial on the Research Topic
Quantum precision measurement and cold atom physics

Ever since the invention of the cesium beam atomic clock in 1955, quantum frequency standards have seen considerable development over the decades, as a representative of quantum precision measurement. The progress in frequency measurements achieved in the past allows one to perform measurements of other physical and technical quantities with unprecedented precision, whenever they could be traced back to frequency measurements. Using atomic transitions as frequency references, quantum frequency standards are far less susceptible to external perturbations, and the quantum identity principle of microscopic particles allows easy replication of quantum frequency standards with the same frequency at any time and place. With laser cooling and trapping, cold atomic ensembles eliminate Doppler shift broadening and have become the go-to quantum reference when precision is required.

The advancement of laser cooling and cold atom physics, in addition to novel physical matter states such as Bose-Einstein Condensation, gives rise to new experimental techniques in quantum precision measurement, especially quantum frequency standards, such as cesium fountain clocks dictating the SI second, as well as optical lattice clocks and single-ion optical clocks pushing the *Frontier of Quantum Metrology*. Other areas of quantum metrology, such as gravitometers and magnetometers, also benefit greatly from cold atoms. Challenges still remain, as researchers strive to push forward the limit in quantum precision measurement and search for novel physical phenomena in cold atomic systems.

In this regard, we organized the Research Topic "*Quantum Precision Measurement and Cold Atom Physics*" in Frontiers in Physics.

As a tribute to his 90th birthday on September 20, we dedicate this Research Topic to the venerable Prof. Yiqiu Wang, a pioneering figure in China's development of quantum precision measurement and cold atom physics. Chen et al. chronicled the scientific career and contributions of Prof. Wang in a Review article, including his early research on nuclear magnetic resonance, his later works on microwave atomic clocks, laser cooling, and Bose-Einstein Condensate, as well as his foray into the fields of optical tweezers and optical atomic clocks. Currently, including the aforementioned Review, fifteen contributed articles have been collected on this topic.

The first part of contributions has been made on recent advancements in the field of quantum precision measurement. Utilizing diffuse laser cooling, Meng et al. realized a compact cold atomic clock suitable for satellite-borne operation, with applications in satellite navigation. While cesium fountain clocks have long been used for defining the SI second, rubidium fountain clocks also show great potential for robustness and excellent long-term stability for timekeeping, as demonstrated by Chen et al at the National Institute of Metrology in China. Meanwhile, Wang et al.'s work produced an optical system for a microwave atomic clock based on optical-lattice trapped atoms, with the potential for performance beyond the atomic fountain. Ever seeking innovation, researchers have made various improvements to the cesium beam atomic clock. Chen et al.'s mini-review discusses the optically detected magnetic-state-selected cesium beam clock, which combines the advantages of the magnetic state selecting scheme and fluorescence detecting method. He et al.'s review article records their effort in improving the short- and long-term stability of high-performance portable optically pumped cesium beam atomic clock. Chen et al. designed an optically pumped cesium beam tube with a hexapole magnetic system, achieving a longer lifetime and better signal-to-noise ratio. Chen et al. also analyze the characteristics of a compact magnetic state-selection cesium atomic clock called LIP Cs-3000 in their article. Moving on to hydrogen masers, we have Que et al. designing a vacuum system for an active hydrogen maser in space, and Dai et al. reviewing the development of the hydrogen maser, as well as its space applications. In the field of optical frequency standards, Wang et al. recount how they were able to trace the optical frequency to the SI second, applying the frequency comparison link from UTC(NIM) to International Atomic Time. Shi et al.'s research on active-optical-clock lasing on the Cs 7S 1/2-6P3/2 transition under a weak magnetic field shed new light on the active optical clock concept.

The second part of the contributions focuses on works on laser cooling and various aspects of cold atom physics. Li et al. demonstrate a deep cooling scheme of quantum degenerate gas for the Chinese Space Station and verified the scheme with a ground experiment. The manipulation of ultracold atoms of high orbitals in optical lattices under nonadiabatic holonomic quantum control is also discussed in Jin et al.'s Review. Tong et al.'s article recounts their effort in detecting the pH-dependent liquid-liquid phase separation of single levitated aerosol microdroplets using a laser tweezers Raman spectroscopy system.

We conclude our Editorial with our most sincere thanks to all the authors of the articles published on this Research Topic for their valuable contributions, and the Frontiers in Physics team for their assistance with publishing.

Author contributions

All authors listed have made a substantial, direct, and intellectual contribution to the work and approved it for publication.

Conflict of interest

The authors declare that the research was conducted in the absence of any commercial or financial relationships that could be construed as a potential conflict of interest.

Publisher's note

frontiers | Frontiers in Physics

TYPE Original Research
PUBLISHED 17 August 2022
DOI 10.3389/fphy.2022.970705

OPEN ACCESS

EDITED BY
Jingbiao Chen,
Peking University, China

REVIEWED BY
Yang Shiyu,
Lanzhou institute of physics, China
Xiumei Wang,
PKU-HKUST Shenzhen-Hongkong Institution, China

*CORRESPONDENCE
Jiayu Dai,
daijy@shao.ac.cn
Xueling Hou,
flybird1656@163.com

SPECIALTY SECTION
This article was submitted to Atomic and Molecular Physics,
a section of the journal
Frontiers in Physics

RECEIVED 16 June 2022
ACCEPTED 22 July 2022
PUBLISHED 17 August 2022

CITATION
Que H, Xu W, Li Q, Xiang J, Lu T, Liu T, Cai Y, Dai J and Hou X (2022), Design of a vacuum system for space active hydrogen maser.
Front. Phys. 10:970705.
doi: 10.3389/fphy.2022.970705

Design of a vacuum system for space active hydrogen maser

Haohui Que[1,2], Wujiabei Xu[1,2], Qi Li[1,2], Jie Xiang[3], Tao Lu[3], Tiexin Liu[2], Yong Cai[2], Jiayu Dai[2]* and Xueling Hou[1]*

[1]School of Materials Science and Engineering, Shanghai University, Shanghai, China, [2]Laboratory of Time and Frequency Technology Research, Shanghai Astronomical Observatory, Chinese Academy of Sciences, Shanghai, China, [3]Shanghai Kingv Material Technology Co., Ltd, Shanghai, China

With the high precision and stability of its frequency signal outputs, active hydrogen maser plays an important role in such fields as timing, satellite navigation, and communication. However, it needs to be lighter so as to be applied in space. We made a research, based on the calculation of the hydrogen flow and the adsorption efficiency of the adsorption unit, on the parameters of the vacuum system and the structural requirements, and designed a combined vacuum pump for the Space Active Hydrogen Maser (SAHM). This vacuum pump consists of a getter pump and a small ion pump, the total mass of which is about 5 kg. The pumping speed will be about 474 L/s by computation, when an amount, 2.5 MPa L, of hydrogen has been adsorbed by getters. Theoretically, the total source hydrogen inflow in lifetime is not higher than 20% of the total capacity getter pump, thus the design should amply meet the requirements of the SAHM vacuum system, and is of great significance for future SAHM applications.

KEYWORDS
hydrogen maser, space, active, vacuum system, getter pump, design

1 Introduction

The hydrogen maser, which uses the hyperfine energy level transition signal of the hydrogen atoms for precise timing, has excellent measurement accuracy and stability. It has developed rapidly since the advent of the first hydrogen maser in 1960 [1]. Many companies and organizations, such as Chinese Shanghai Observatory, Beijing Institute of Radio Metrology and Measurement, American Symmetricomg Company, Switzerland Spectratime, T4Science Company, Russia KVARZ, Vremya-CH Company and the Russian-British joint venture Quartzlock Company, have offered various kinds of high-performance hydrogen maser products which were widely applied in timing, navigation, communications, space exploration and other fields [2–5].

With the continuous development of space science experimental projects, new requirements are put forward for hydrogen masers applied in space. It not only needs better frequency stability and reliability, but also needs to meet the requirements of space applications such as light weight, small size and low power consumption. The performance of the active hydrogen maser is better than that of the passive hydrogen

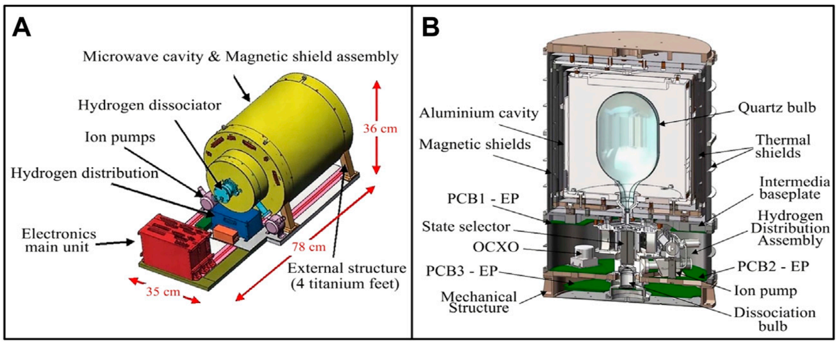

FIGURE 1
35 kg space active hydrogen maser **(A)**; 40 kg space active hydrogen maser **(B)**.

maser, thus the before is a better choice for the frequency standard in space. However, it is currently too bulky to be applied in space.

At present, the countries that carry out the research and development of space active hydrogen masers mainly include Europe [5–8], Russia [9–11], and China [12–14]. The Neuchatel Observatory in Switzerland used a high-Q sapphire microwave resonator to replace the traditional resonator in space active hydrogen maser, which greatly reduced the mass of the entire system to about 35 kg (Figure 1A), and the frequency stability could reach 1.5×10^{-13}/s and $1.5 \times 10^{-15}/10^5$ s [6, 7]. SpectraTime (SpT) developed a 40 kg lightweight active Space Hydrogen Maser (Figure 1B) for the European Space Atomic Clock Ensemble in Space (ACES) mission which would be flown on the International Space Station (ISS) in 2013 [5]. The Russian Vremya-CH company uses a glass-ceramic resonator to reduce the total mass of the active hydrogen maser to 60 kg. It could achieve a long-term stability 2×10^{-14}/day, and was launched in 2011 [10, 11]. Beijing Institute of Radio Metrology and Measurement has also developed a space active hydrogen maser with a mass of about 45 kg, its stability could reach 2.3×10^{-15}/day and might be launched with satellites in 2022. Meanwhile, it is still continuing to optimize its performance, and it will be applied in Chinese space station projects in the future [13].

The space hydrogen maser has high requirements on vacuum system, generally about 10^{-5} Pa [15]. The poor vacuum environment will lead to broadening of transition spectral lines and weakening of signals, which will significantly affect the overall performance. Therefore, a vacuum system that can maintain working conditions for a long time is particularly important. As a comparison, the ground active hydrogen maser uses a sputtering ion pump, equipped with two large magnets of about 50 kg, to maintain the vacuum state of the system. This type of vacuum pump has good stability, high reliability and long service life, whereas it is so bulky that cannot be used in SAHM.

The spaceborne passive hydrogen maser adopts a scheme of combined pump system to meet the vacuum requirements of space applications [16]. The combined pump consists of a getter pump and a small ion pump, in which the getter pump mainly absorbs reactive gases (mainly hydrogen), and the ion pump absorbs the inert gas in the system. This type of combined pump system turned out to have the high stability and reliability, the large capacity and particularly the small volume and light mass while, which is very consistent with the development trend of the hydrogen maser. Compared with the passive hydrogen maser, the active ones have better stability and accuracy. However, the active hydrogen maser also has larger hydrogen load flow rate, for which the vacuum system needs to be redesigned to meet the needs of the space active hydrogen maser.

Space active hydrogen masers are mainly used for space station punctuality, space high-precision scientific experiments and large scientific installations such as space telescopes and space VLBI (Very Long Baseline Interferometry) projects. Active hydrogen maser has not yet had space applications in China. The Shanghai Astronomical Observatory Space VLBI Project requires higher time-frequency accuracy and stability, which promotes the space application process of active hydrogen masers.

This work aims to design a lightweight vacuum combined pump for space application of active hydrogen masers. The combined pump combines a zirconium iron vanadium alloy getter pump and a small ion pump, with a total mass of about 5 kg, which is 90% lighter than that of the ground active hydrogen masers. In terms of performance, the theoretical pumping rate and total pumping volume of the design's 10-year service period (according to the requirements of the national research task) far exceeded the expectations, which reflect the excellent gas adsorption and vacuum retention capabilities. This design amply satisfies the vacuum degree and life requirements of

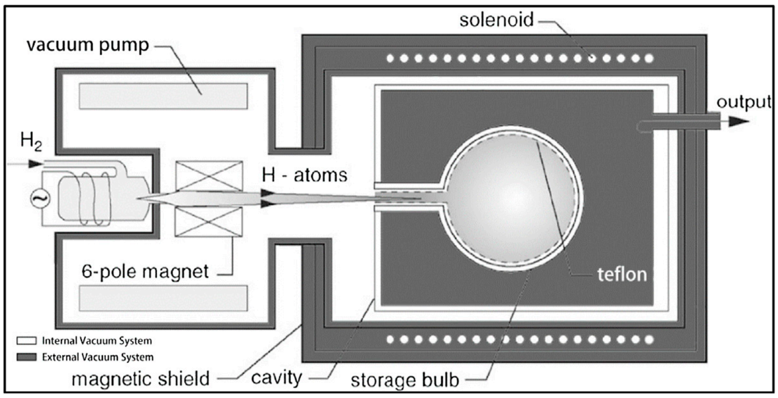

FIGURE 2
Basic structure of the physical part of the hydrogen maser.

the vacuum system, and provides significant reference for the active hydrogen maser application in space.

2 Theory and method

2.1 Vacuum system of hydrogen maser

Figure 2 shows the basic physical structure of the hydrogen maser. After purification, ionization, and state selection, the hydrogen gas enters the storage bubble, where the energy level transition occurs and a microwave signal of a specific frequency is generated. Finally, it will be collected by the vacuum pump. The storage time of hydrogen atoms in the atomic storage bubble is about 1 s. In order to avoid collisions between high-energy hydrogen atoms ($F = 1$, $m_F = 0$) and other atoms, which will cause collision broadening and lead to a decrease in the signal-to-noise ratio of hydrogen atom transition signals, this process generally needs to be carried out in a high vacuum environment.

In a high vacuum environment, the particle density in the atomic storage bubble is at a low level, which increases the average free path of high-energy hydrogen atoms, and reduces the collision probability between hydrogen atoms or with other particles, thereby prolonging their interaction time. At present, the space hydrogen maser mainly adopts a double vacuum system [17]. The background vacuum degree of the internal vacuum system during operation is about 10^{-5} Pa. The stable system vacuum degree is one of the important influence factors affecting the long-term stability of the hydrogen maser. The vacuum pump system turns out to be the most critical part that affects the vacuum degree of hydrogen masers.

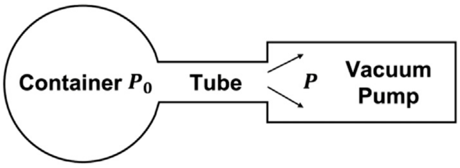

FIGURE 3
Brief schematic diagram of vacuum system.

2.2 Basic parameters of hydrogen maser vacuum system

2.2.1 Gas flow Q_G

The temperature is almost constant in the vacuum system of hydrogen maser. According to The Boyle's law, the product of the gas volume V and the pressure P is constant if only the pressure changes. Therefore, in a vacuum system, the product $P \times V$ is generally used to represent the amount of gas, we can obtain the expression of flow after differentiating time:

$$Q_G = V\frac{d_p}{d_t} + P\frac{d_V}{d_t} \tag{1}$$

The pressure everywhere remains generally constant when the system is stable, and the pressure changes little in a short time interval. At this time, Formula 1 can be written as:

$$Q_G = P\frac{d_V}{d_t} \tag{2}$$

This is the constant pressure expression of flow, unit for Pa·m^3·s^{-1} or Pa·m^3·s^{-1}.

2.2.2 Pumping rate S_p and effective pumping rate S_0

Figure 3 is a brief schematic diagram of the vacuum system. When the vacuum pump starts pumping, the pressure P at the inlet of the vacuum pump is less than the pressure P_0 in the container, thus the gas flows to the vacuum pump and is collected or discharged out of there. The pumping speed S_p of a vacuum pump is the ratio of the gas flow $\boldsymbol{Q_G}$ to the pressure P at the pump port:

$$\boldsymbol{S_p = \frac{Q_G}{P}} \tag{3}$$

The unit is $m^3 \cdot s^{-1}$ or $L \cdot s^{-1}$. Compared with Formula 2, when the pressure P is constant, S_p is approximately equal to $\frac{d_V}{d_t}$.

Due to the pressure difference between the pumped container and the vacuum pump, there is also a difference between the pumping rate of the vacuum pump and the pumping rate of the gas in the container. To distinguish between them, the pumping speed of the gas in the container is usually called the effective pumping speed, represented by S_0, it can be obtained by dividing the gas flow Q_G by the pressure P_0 in the container:

$$\boldsymbol{S_0 = \frac{Q_G}{P_0}} \tag{4}$$

2.2.3 Flow conductance U of connecting tube

Hydrogen pressure and flow rate are both small while in the high vacuum state of the hydrogen maser, which make the probability of collision between molecules is much less than with the tube wall. After each collision, molecules will move forward or backward in different directions. Therefore, the flow of hydrogen in the connecting tube is molecular flow.

The calculation of flow conductance is closely related to the shape of the tube. The structure of hydrogen maser is very compact, and short tubes (tube length L/diameter $d < 20$) are usually used in vacuum systems. The flow conductance calculation formula of air in molecular flow state in a short tube at 20°C can be expressed as follows:

$$\boldsymbol{U_{f.20^\circ C} = \alpha \cdot 116A_0} \tag{5}$$

Where the α is the Clausing coefficient, which is related to the value of L/d; A_0 is the cross-sectional area of the tube. Under the same conditions, the conductance of hydrogen and air has the following relationship:

$$\boldsymbol{U_{H_2} = 3.78\, U_{Air}} \tag{6}$$

The conversion formula for flow conductance at different temperatures is:

$$\boldsymbol{U_T = U_{20^\circ C}\sqrt{\frac{T}{293.15}}} \tag{7}$$

Based on Formulas 5ormulas –Formulas 7, we can obtain the relationship between the flow conductance of hydrogen in the short tube and the temperature:

$$\boldsymbol{U_{H_2} = 438.48 \cdot A_0 \cdot \alpha \cdot \sqrt{\frac{T}{293.15}}} \tag{8}$$

2.2.4 Basic equation of vacuum system

When the gas flows in the tube, the pressure decreases gradually along the direction of the gas flow, so there is a dynamic pressure difference $(P_1 - P_2)$, P_1, and P_2 respectively represents the upstream and downstream gas pressure in the tube. The pressure difference is proportional to the gas flow, the formula is as follows:

$$\boldsymbol{Q_G = U(P_1 - P_2)} \tag{9}$$

In the vacuum system, assuming that there is no air leakage or air source and the air flow is in a stable state, according to the law of conservation of mass, the flow $P \cdot S_P$ at the right end of the conduit (vacuum pump inlet), the flow $P_0 \cdot S_0$ at the left end of the conduit (container outlet) and the flow $U(P_1 - P_2)$ at any section in the conduit are equal, that is:

$$\boldsymbol{U(P_1 - P_2) = U(P_0 - P)} \tag{10}$$

$$\boldsymbol{P_0 S_0 = U(P_0 - P) = PS_P} \tag{11}$$

After the convention of Formula 11, the following equation can be obtained:

$$\boldsymbol{\frac{1}{S_0} - \frac{1}{S_P} = \frac{1}{U}} \tag{12}$$

Formula 12 is the basic equation of the vacuum system when the air flow reaches a stable state. It relates the flow conductance U of connecting tube, the pumping rate $\boldsymbol{S_p}$ and the effective pumping rate $\boldsymbol{S_0}$, and plays an important role in the design of the vacuum system.

2.2.5 Effective suction area F

As the absorption of hydrogen content in the getter increases, hydrogen atoms at the surface will spread inward at a slower rate, which results in a reduced inspiratory rate. In order to ensure that the suction rate can maintain a good vacuum state of the system after absorbing a certain amount of gas during the required working life, it is necessary to ensure a certain effective suction area. The calculation formula of the effective suction area is as follows:

$$\boldsymbol{F = \frac{Q_i}{m_i q_i K_i}} \tag{13}$$

Where the Q_i is the required one-time inspiratory volume; m_i is the mass of getter per unit area; q_i is the suction amount of getter when the pump pumping speed tends to be stable; K_i is a

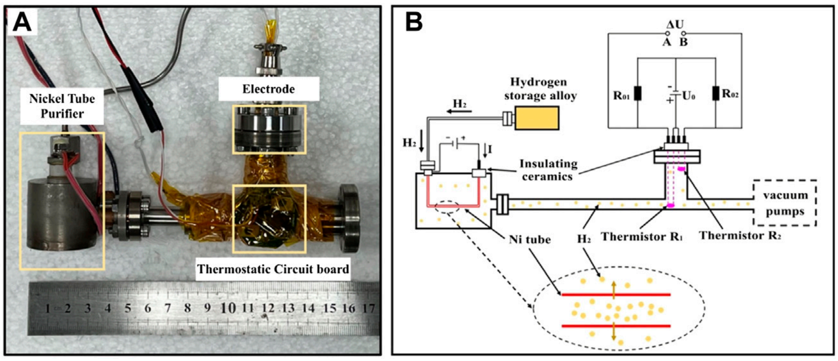

FIGURE 4
Hydrogen flow measurement experimental device **(A)**; hydrogen flow measurement experimental principle diagram **(B)**.

constant, when only one side is working, the value is 0.9, and when both sides are working, the value is 0.55.

2.2.6 Hydrogen evolution flow q of nickel purifier

The hydrogen evolution flow rate in hydrogen maser is mainly determined by the nickel tube purifier. We designed a measuring device for hydrogen permeability under different operating currents of nickel tube purifier. As shown in Figure 4A, it is mainly composed of nickel tube purifier, electrode flange, thermostatic circuit board and measuring tube. The right side of the measuring tube is connected with a vacuum pump to maintain the vacuum environment of measuring. The measuring principle is described as follows.

Under certain conditions, the heat conduction capacity of gas molecules is related to the number of gas molecules per unit volume. According to this principle, hydrogen is released from the hydrogen storage alloy bottle into the nickel tube; when the nickel tube is connected to the direct current, the joule temperature rises, and hydrogen diffuses outward into the measuring tube, where the heat exchange with the thermistor and changes the thermistor temperature. The temperature of thermistor corresponds to the resistance value, thus the voltage difference ΔU between A and B in the bridge also changes accordingly. Therefore, ΔU can be used to reflect the change in hydrogen flow rate.

In Figure 4B, R_{01} and R_{02} are standard resistors with resistance values of $100\,\text{k}\Omega$. R_1 and R_2 are the same thermistors. The resistance value is $100\,\text{k}\Omega$ at 25°C, B value is 3950 K. Hydrogen will take away part of the heat from thermistor R_1 while exchanging heat with it in the measuring tube. The heat loss per unit time can be obtained by the following formula:

$$\Delta P_{Loss} = C_P \cdot (T_0 - T_H) \cdot q \tag{14}$$

Where the C_P is the hydrogen constant pressure specific heat capacity, the T_0 is the initial temperature of the deprecated thermistor R_1 without hydrogen gas flow, the T_H is the temperature of hydrogen; and q is the hydrogen flow. Meanwhile, the heat generated by the thermistor R_1 due to the inflow current in unit time is:

$$\begin{aligned}\Delta P_e &= \left(\frac{U_0}{R_{02}+R_2}\right)^2 \cdot R_2 - \left(\frac{U_0}{R_{01}+R_1}\right)^2 \cdot R_1 \\ &= \frac{\Delta U^2 (R_{01}R_{02} - R_1R_2)}{R_{01}R_{02}(R_2 - R_1)}\end{aligned} \tag{15}$$

Where the U_0 is the voltage of the direct current supply. It was done experimentally to determine the optimal value as 1.2 V (for details, see Section 1.1 of the Supplementary Materials). According to the law of energy conservation, the heat loss ΔP_{Loss} between thermistor R_1 and hydrogen is equal to the heat ΔP_e generated by thermistor R_1. Thus, the calculation formula of hydrogen penetration q can be written as follows:

$$q = \frac{\Delta U^2 (R_{01}R_{02} - R_1R_2)}{R_{01}R_{02}(R_2 - R_1)C_p \cdot (T_0 - T_H)} \tag{16}$$

3 Design and discussion

3.1 Requirements of vacuum system design

In the vacuum system of hydrogen maser, the nickel tube purifier continuously permeates hydrogen into the system, and the vacuum state of the container needs to be maintained by the vacuum pump, which belongs to the dynamic vacuum system. In normal operation, the vacuum degree of the system should be kept at about 10^{-5} Pa, and the working life should be more than 10 years. Based on these two requirements, we calculate the required performance parameters of the vacuum pump design in the vacuum system.

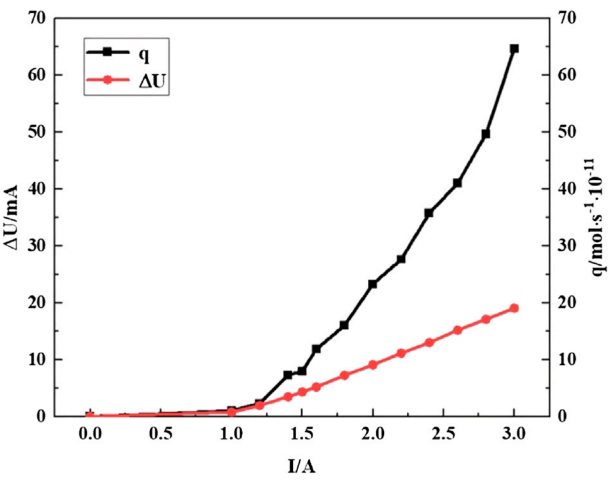

FIGURE 5
Relation curve of operating current of nickel tube and ΔU and flow of hydrogen.

3.1.1 Calculation of gas flow Q_G

In a vacuum system, the suction capacity and suction rate are the two most important parameters. In order to calculate the specific values of these two parameters, the total gas flow Q_G in the system needs to be calculated first. In general, Q_G consists of the following parts [17]:

$$\mathbf{Q_G = Q_l + Q_d + Q_p + Q_b + Q_r} \tag{17}$$

Where, Q_l is the hydrogen permeation amount in the vacuum system; Q_d is the amount of adsorbed gas desorption on the surface of the internal vacuum system; Q_p is the amount of gas discharged by diffusion or infiltration of the internal material in vacuum system; Q_b is the reflux volume of vacuum pump; Q_r is the air emission of the structural components assembled in the inner vacuum system. In the vacuum system of the hydrogen maser, the gas mainly comes from the hydrogen, which is permeated through the nickel tube during the operation, the other items are relatively little that can be ignored, thus $Q \cong Q_l$.

According to the hydrogen evolution rate experiment of the nickel purifier under different current (in Section 2.2.6), the result (shown in Figure 5) shows that the hydrogen permeability increases with the increase of the working current of the nickel tube purifier. When $I = 1.0$–3.0 A, the flow increases greatly, until when $I = 3.0$ A, $q = 1.58 \times 10^{-8}$ L s^{-1}. Considering the hydrogen maser signal and the impairment to the vacuum pump, the current of the nickel tube purifier is generally set to 3.0 A to get an optimal value of hydrogen flow (for details, see Section 1.2 of the Supplementary Materials).

Based on the hydrogen permeation amount q under this current flow, we can get the total hydrogen flow of the vacuum system $Q_G = 1.60 \times 10^{-3}$ Pa·L·s^{-1} from Formula 2 and the ideal gas equation. The total suction amount Q_A can be obtained by multiplying Q_G with working life. For 10 years, the total inspiration Q_A is about 0.5 MPa L.

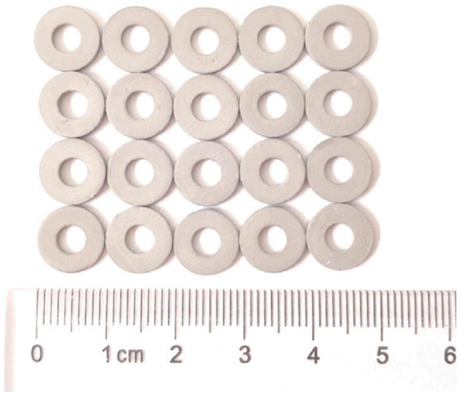

FIGURE 6
Getter tablets of vacuum pump.

3.1.2 Calculation of conduit conductivity U_{H_2}

In the vacuum system, it is a cylindrical stainless-steel tube between the pumped container and the vacuum pump, which is 70 mm in length and 60 mm in diameter. The cross-sectional area $A_0 = 2{,}827.43$ mm^2, $L/d = 1.167$, according to the table, Clausing coefficient a is 0.488. According to Formula 8, the flow conductance of hydrogen in the tube at 20°C can be calculated: $U_{H_2} = 6050$ L s^{-1}.

3.1.3 Calculation of pumping rate S_0 and effective pumping rate S_p

According to the requirement of hydrogen maser vacuum system, the gas pressure in the pumped container $P_0 = 1 \times 10^{-5}$ Pa, gas flow $Q_G = 1.60 \times 10^{-3}$ Pa L s^{-1} and the effective pumping velocity $S_0 = 160$ L s^{-1} can be calculated by Formula 4.

According to effective pumping rate $S_0 = 160$ L s^{-1} and flow conductance $U_{H_2} = 6050$ L s^{-1}, The pump speed $S_p = 164$ L S^{-1} can be calculated from the basic equation of vacuum system (Section 2.2.4).

Due to the short and large diameter of the tube, the change of gas pressure at both ends is very small, thus the calculated values of S_0 and S_p are almost equal, which to some extent reduces the requirement of vacuum pump on pumping speed.

3.1.4 Calculation of effective suction area F

In this work, Zr-V-Fe alloy getter tablets (as shown in Figure 6) is used as the basic material of the getter pump. At the beginning of the operation, there is little internal hydrogen content and the getter tablet has a high pumping rate of hydrogen. With the increase of suction volume, the pumping rate decreases gradually. Under 20° Cand 10^{-5} Pa vacuum, the initial inspiration rate of the carrier is over 2,500 cm^3·s^{-1}·g^{-1};

when the inspiratory capacity reaches 5,000 $Pa \cdot L \cdot g^{-1}$, the inspiration rate tends to stabilize at about 900 $cm^3 \cdot s^{-1} \cdot g^{-1}$.

The inner diameter of the single getter tablet is 4.0 mm, the outer diameter is 10.0 mm, the thickness is 1.3 mm, and the mass is 273.8 mg. The calculated effective suction surface area (the upper, lower and outer wall surfaces) of the single tablet is 172.9 mm^2. Therefore, the mass of getter per unit area m_i = 1.59 mg/mm^2.

According to the one-time inspiratory volume requirement, $Q_i = Q_A = 0.5$ MPa L, the suction capacity as the suction rate tends to be stable is taken as the value of $q_i = 5{,}000$ $Pa \cdot L \cdot g^{-1}$, $K_i = 0.55$ for double-sided suction, thus we obtained the suction surface area $F = 1.16 \times 10^5$ mm^2 for 10 years from Formula 13.

3.2 Design of getter pump

In the design of getter pump, the main considerations are the suction amount and suction speed. The suction amount is to ensure that the working life of the getter can meet the required number of years after one activation, and the suction rate is to ensure that the getter can maintain the vacuum state requirements until the whole service life. Generally, the more the amount of getter in the pump, the larger the maximum suction amount and suction rate will be. However, its mass and volume are limited for the space hydrogen maser, thus it is necessary to combine the actual situation to calculate the proper amount of getter and get the corresponding getter pump structure design.

3.2.1 Performance design of getter pump

According to the previous calculation, the total inspiratory Q_A of service hydrogen maser is 0.5 MPa L for 10 years. In order to prevent the getter material from embrittle, it is necessary to retain a certain amount of allowance for use [18]. Meanwhile, for maintaining the required vacuum state, the vacuum pumping rate should be faster than 164 L/s, and the effective area of the getter should be larger than 1.16×10^5 mm^2.

Considering the balance of cost, performance, weight and allowance reserve, we design a vacuum system for space active hydrogen maser based on the above research and calculations. The pump contains 527 g getter materials with a total number of 1925 getters. The single effective suction surface area is 172.9 mm^2 and the total effective suction area of about 3.3×10^5 mm^2.

The inspiratory capacity of single tablet is not less than 5,000 $Pa \cdot L \cdot g^{-1}$, thus the capacity of the total getter pump is not less than 2.5 $MPa \cdot L$, meanwhile, the suction rate is about 474 L/s, and the theoretical gas consumption is less than 20% of the full capacity, which fully meets the above performance requirements and can meet the engineering application needs of space active hydrogen maser for more than 10 years.

3.2.2 Structural design of getter pump

Based on the performance requirements and our previous work [19], the getter pump structure designed as follows.

The overall structure of the getter pump is shown in Figure 7A, which is mainly composed of a shell, getter tablet and its bracket, and heating devices. The shape of the pump and its overall size is determined by the internal requirements of the active hydrogen maser. The outer diameter is 196.0 mm, the inner diameter is 90.0 mm, and the height is 40.0 mm. The shell of the pump is composed of a Ti metal plate, which is 1.5 mm in thick, to reduce the influence of magnetic field on the performance of the hydrogen maser.

Figure 7B is the schematic diagram of the internal getter structure. There are altogether 175 getter units assembled in six layers, with 25 in the innermost layer and 30 in the outer five layers.

Figure 8A shows the structure of getter unit, which is mainly composed of base, getter tablets, Ti gasket, fixed nut, heating wire, and Ti support. Each getter unit contains 11 getter tablets, as described above, its inner diameter is 4.0 mm, outer diameter is 10.0 mm, thickness is 1.3 mm, and single mass is 273.8 mg (Figure 8B).

Each getter is separated by Ti metal gasket to increase the suction area; The bracket is a hollow structure, with an inner diameter of 3.0 mm, an outer diameter of 3.5 mm and a length of 35.0 mm (Figure 8C). Nickel-chromium alloy hot wire is installed inside the bracket to facilitate the activation of getter.

After the getter is exposed to the atmosphere or used for a long time, a passivation layer will be formed on its surface, which will reduce the rate of hydrogen absorption. Therefore, the getter pump needs to be equipped with a heating device for high temperature treatment to remove the passivation layer and obtain the fresh active surface, this process is called the getter pump activation.

The heating device uses nickel-chromium alloy heating wire with diameter of 1.0 mm and resistivity of 0.832 $\mu\Omega$ m. It has strong corrosion resistance, non-magnetic, and the operating temperature can up to 1,200°C. In the getter pump, the heating wires inside each getter unit are connected in series with a total length of 4.5 m and a resistance of 4.7 Ω. One end is connected with the pump shell as a negative pole, and the other end is connected with the ceramic electrode insulated with the pump shell as a positive pole. The total mass of the getter pump is approximately 4.5 kg, containing 527 g getter materials.

3.3 Lectotype of small ion pump

In the combined pump of small ion pump and getter pump, hydrogen absorption is mainly accomplished by the getter pump, and the small ion pump plays the role of eliminating trace impurities. The trace impurity gas in the vacuum system

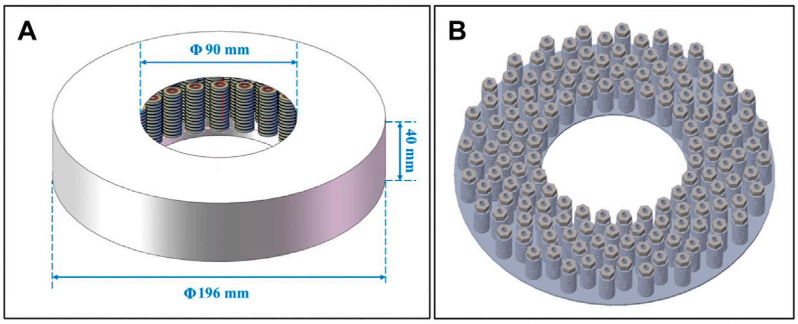

FIGURE 7
(A) External structure size of getter pump; **(B)** Schematic diagram of internal structure.

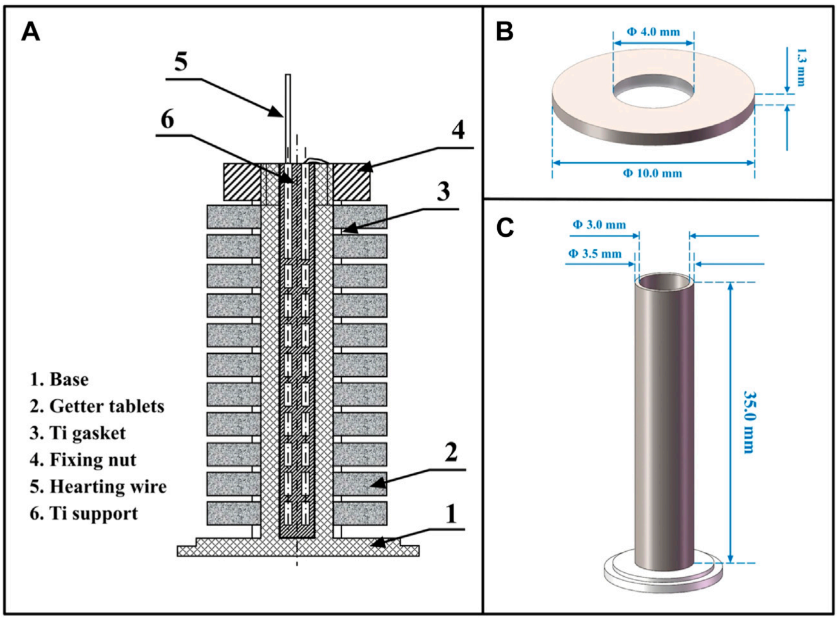

FIGURE 8
(A) Structure of getter unit; **(B)** Structural size of getter tablet; **(C)** Ti support structure size.

mainly comes from the gas leakage of the wall material, which is mainly determined by the outgassing rate of the wall material. As the outgassing rate decreases slowly with time during the service life, the maximum outgassing rate at the beginning is used for calculation to maximize the reliability requirements.

According to the existing data of the outgassing rate of the space-borne passive hydrogen maser [20], considering a larger hydrogen flow that the active hydrogen maser has than passive ones, we selected the Agilent 5 L/s small ion pump as the composite pump in this work. The pumping rate has a large surplus, which can be further optimized according to the requirements of practical application. Additionally, remote vacuum level monitoring can be achieved with ion pump current readings. The weight of this small ion pump is about 0.5 kg and the service life exceeds 10 h under above operating conditions [21], which fully meet the 10-year engineering application requirements.

4 Conclusion

The active hydrogen maser with excellent timing accuracy and wide amplitude stability plays an important role in the fields of timing and navigation. In order to meet the lighter requirements of the Shanghai Astronomical Observatory for SAHM in the space VLBI project, we designed a combined vacuum pump composed of a getter pump and an ion pump. The getter pump plays the main role of hydrogen adsorption. It is in the shape of a ring, with an outer diameter of 196 mm, an inner diameter of 91 mm, and a height of 40 mm. Among it there are 1,925 getter tablets, the mass of which is 527 g and the getter pump is about 4.5 kg. Agilent Diode small ion pump is adopted as the combined ion pump to deal with trace amounts of inert gas impurities. The total mass of the composite pump is about 5 kg. Under conditions with a background vacuum of 10^{-5} Pa for the active hydrogen maser, the effective suction area of this pump is about 3.3×10^5 mm^2, which is higher than the required value (1.16×10^5 mm^2). When the suction volume of the getter pump reaches 2.5 MPa·L, the pumping speed of is about 474 L/s, those are much higher than the total hydrogen flow rate (0.5 MPa·L) of the hydrogen maser life requirements for 10 years and the pumping speed requirements (more than 164 L/s), This design amply satisfies the vacuum degree and life requirements of the vacuum system, and provides significant reference for the active hydrogen maser application in space.

In order to avoid embrittlement of the aspirant material, it should be retained a certain suction margin during the 10-year operating time. Generally, there is only 10%–25% of the full capacity is used. The aspirator tablets selected in this design have not appeared embrittlement after a long period of hydrogen absorption in the engineering test, thus we set the 10-year theoretical suction capacity is at about 20% of the full capacity. The suction pump design still retains a large free space to balance the performance and mass of the vacuum system, and to ensure the adequate flow of gas in the suction pump and improve the effective contact area. If higher reliability requirements need to be met in future work, the use of aspirated tablets can be appropriately increased to increase capacity redundancy. Meanwhile, since there is no securable working data of the active hydrogen maser or other relevant data, we selected a large redundancy suction speed to make the lectotype of small ion pump, and remain a large space for lighter design, it can be further optimized after future data support. Otherwise, for verifying the adaptability and reliability of the designed combined pump in the extreme space environment, it should also be simulated in the space environment experiments, potential problems should be actively optimized to ensure the realization of all relevant functions expected.

Data availability statement

The original contributions presented in the study are included in the article/Supplementary Material, further inquiries can be directed to the corresponding authors.

Author contributions

HQ contributed majorly to this work. All authors participated in the writing of the manuscript.

Funding

This work was supported by the Joint Research Fund in Astronomy (No. U1531120) under cooperative agreement between the National Natural Science Foundation of China (NSFC) and Chinese Academy of Sciences (CAS).

Acknowledgments

We'd like to extend our sincerest acknowledgement to Professor Yiqiu Wang, who contribute to the research and improvement of the hydrogen masers in Shanghai Astronomical Observatory. Professor Wang is very kind to students, he is always patient to listen, and to help us to understand the physical principles of hydrogen maser, which is completely a complexity and not easy to us. Knowledge of the physical principle is vital to the research and design of Space Active Hydrogen Maser. The work on vacuum system for the SAHM, on the basis of the understanding of the hydrogen flux requirements, is made to ensure a stable on-board working performance, and is contributed by a series of lecturing given by Professor Wang.

Conflict of interest

Authors JX and TL were employed by Shanghai Kingv Material Technology Co., Ltd.

The remaining authors declare that the research was conducted in the absence of any commercial or financial relationships that could be construed as a potential conflict of interest.

Publisher's note

Supplementary material

The Supplementary Material for this article can be found online at: https://www.frontiersin.org/articles/10.3389/fphy.2022.970705/full#supplementary-material

References

1. Goldenberg HM, Kleppner D, Ramsey NF. Atomic hydrogen maser. *Phys Rev Lett* (1960) 5(8):361–2. doi:10.1103/physrevlett.5.361

2. Belyaev AA, Demidov NA, Medvedev SY, Pavlenko YK, Sakharov BA, Vorontsov VG. Russian hydrogen masers for ground and space applications. In: Paper presented at: URSI AP-RASC 2019. 2019 URSI Asia-Pacific Radio Science Conference; 2019 Mar 9-15; New Delhi, India (2019).

3. Li J, Zhang J, Bu Y, Cao C, Wang W, Zheng H. Space passive hydrogen maser a passive hydrogen maser for space applications. In: Paper presented at: IFCS 2016. 2016 IEEE International Frequency Control Symposium; 2016 May 9-12; New Orleans, LA (2016).

4. Shuai T, Xie Y. Navigation satellite on-board hydrogen atomic Clock. *Ke Xue* (2016) 68(54):11–5. 64. Chinese.

5. Goujon D, Rochat P, Mosset P, Boving D, Perri A, Rochat J, et al. Development of the space active hydrogen maser for the ACES mission. In: Paper presented at: EFTF 2010. 24th European Frequency and Time Forum; 2010 April 13-16; Noordwijk, Netherlands (2010).

6. Jornod A, Goujon D, Gritti D, Bernier LG. The 35 kg space active hydrogen maser (SHM-35) for ACES. In: Paper presented at: IEEE International Frequency Control Symposium and PDA Exhibition Jointly with the 17th European Frequency and Time Forum; 2003 May 4-8; Tampa, FL (2003).

7. Thieme B, Zoschg D, Baister G. Space worthy electronics package for the 35kg space active hydrogen maser on ACES. In: Paper presented at: EFTF 2004. 2004 18th European Frequency and Time Forum; 2004 Apr 5-7; Guildford, UK (2004).

8. Hess MP, Niedermaier T, Gollinger K, Helm A, Kehrer J, Ettori M, et al. Aces - getting ready. In: Paper presented at: IAC 2018. 69th International Astronautical Congress; 2018 Oct 1-5; Bremen, Germany (2018).

9. Demidov NA, Belyaev AA, Polyakov VA, Timofeev YV. Onboard hydrogen frequency standard for the millimetron space observatory. *Meas Tech* (2018) 61(8): 791–6. doi:10.1007/s11018-018-1503-5

10. Belyaev A, Biriukov A, Demidov N, Likhacheva L, Medvedev S, Myasnikov A, et al. Russian hydrogen masers for space applications. In: Paper presented at: Proceedings of the 45th Annual Precise Time and Time Interval Systems and Applications Meeting; 2013 Dec 2-5; Bellevue, Washington (2013).

11. Vremya-CH JSC. *Products VCH-1010 [internet]*. Nizhny Novgorod, Russia: Vremya-CH Company (2022). Available from: https://www.vremya-ch.com/english/product/index6e49.html (Accessed May 30, 2022).

12. Zhou T, Huang J, Wu Q, Gao L. Progress of the on-board sapphire active hydrogen maser for the aces space mission of CNSA. In: Paper Presented at: IAC 2014. 65th International Astronautical Congress; 2014 Sept 29-Oct 3; Toronto, Canada (2014).

13. Wu W. Chinese independent development of active hydrogen atomic clocks will appear on the space station. *Jun Min Liang Yong Ji Shu Yu Chan Pin* (2017) 23: 33. Chinese.

14. Wang W, Dew ITZ, Cabeza R. Age-related differences in medial temporal lobe involvement during conceptual fluency. *Brain Res* (2015) 2(6):48–58. Chinese. doi:10.1016/j.brainres.2014.09.061

15. Kleppner D, Berg HC, Crampton SB, Ramsey NF, Vessot RFC, Peters HE, et al. Hydrogen-Maser principles and techniques. *Phys Rev* (1965) 138(4A): A972–83. doi:10.1103/physrev.138.a972

16. Yang H, Dai J, Lin C. Application study of passive hydrogen maser aspirant pump. *Zhen Kong Ke Xue Yu Ji Shu Xue Bao* (2012) 32(4):337–40. Chinese.

17. Wang W, Zhang Y, Yang H, Zhang W. Dual vacuum active hydrogen pulse vacuum system design. *Zhen Kong Ke Xue Yu Ji Shu Xue Bao* (2012) 32(3):252–5. Chinese.

18. Zivanov S, Schweda H, Goujon D, Gritti D, Perruchoud G. Physics package of the 35kg space active hydrogen maser for the ACES space mission of ESA. In: Paper presented at: IEEE 2007. International Frequency Control Symposium Joint with the 21st European Frequency and Time Forum; 2007 May 29-Jun 1; Geneva, Switzerland (2007).

19. Xiang J. *inventors; Shanghai Kingv Material Technology Co., Ltd, assignee. [A miniature getter pump]. Chinese patent application CN202123248351.9*. Shanghai, Chinese: Shanghai Kingv Material Technology (2021).

20. Yang H. From analyzing ion pumps to improving the life of SOHM-4 hydrogen maser. *Ann Shanghai Astronomical Observatory* (2013) 0:64–71. Chinese.

21. Agilent Inc. *Agilent ion pumps [Internet]*. Santa Clara, CA: Agilent Inc (2022). Available from: https://www.agilent.com.cn/cs/library/catalogs/public/Agilent_Catalog_Ion_Pumps.pdf (Accessed May 30, 2022).

Frontiers | Frontiers in Physics

TYPE Mini Review
PUBLISHED 15 August 2022
DOI 10.3389/fphy.2022.963870

An overview of the optically detected magnetic-state-selected cesium beam clock

Sifei Chen[1], Chang Liu[2], Lifeng Fan[1], Chen Liu[1], Yuanhao Li[1], Shaohang Xu[1], Chaojie Li[1] and Yanhui Wang[1]*

[1]Institute of Quantum Electronics, School of Electronics, Peking University, Beijing, China, [2]Chengdu Synchronization Technology Ltd., Chengdu, China

EDITED BY
Nigel John Mason,
University of Kent, United Kingdom

REVIEWED BY
Ma Hongyang,
Qingdao University of Technology,
China

*CORRESPONDENCE
Yanhui Wang,
wangyanhui@pku.edu.cn

SPECIALTY SECTION
This article was submitted to Atomic and Molecular Physics,
a section of the journal
Frontiers in Physics

RECEIVED 08 June 2022
ACCEPTED 19 July 2022
PUBLISHED 15 August 2022

CITATION
Chen S, Liu C, Fan L, Liu C, Li Y, Xu S, Li C and Wang Y (2022), An overview of the optically detected magnetic-state-selected cesium beam clock.
Front. Phys. 10:963870.
doi: 10.3389/fphy.2022.963870

Among all kinds of compact cesium beam clocks, the optically detected magnetic-state-selected cesium beam clock (OMCC) combines the advantages of the magnetic state selecting scheme and fluorescence detecting method. This paper presents an overview of the OMCC. Technical issues, noise sources, frequency shifts and improvements of OMCC are reviewed. Finally, the frequency stability of five OMCC is given, which is better than the stability of the high-performance version of Microsemi 5071A.

KEYWORDS

compact atomic clocks, cesium beam, fluorescence, magnetic state selection, frequency stability

1 Introduction

Nowadays, quantum physics has a wide range of applications, such as quantum sensors, quantum computation and quantum cryptography [1–5]. Among these applications, the atomic clock is one of the most developed precision instruments with a history of nearly 70 years [6–8]. Various atomic clocks with corresponding applications have emerged. For instance, chip-scale atomic clocks based on the coherent population trapping effect are used in communication and navigation systems [9–11], and room-sized optical lattice clocks can be used to explore the gravitational redshift effect and dark matter [12, 13]. The value of atomic clocks has already penetrated all aspects of human life. Among all kinds of atomic clocks, compact cesium beam clock plays an important role in time-keeping, telecommunication systems and navigation systems for its structural simplicity, promising long-term stability and accuracy [14].

According to the different working principles, cesium beam clocks can be divided into three categories including the magnetic state selecting cesium beam clock, the optically pumped cesium beam clock and the optically detected magnetic-state-selected cesium beam clock (OMCC). Based on the Stern-Garlach experiment, traditional cesium beam clocks use inhomogeneous magnetic fields to deflect the atomic beam, thereby realizing state preparation and state detection [15]. The second magnet, combined with the hot-wire, the mass spectrometer and the electron multiplier, is used to convert the atomic state information into electric signal. The state-selecting magnet is velocity-selective. Therefore, atoms usually have a narrower velocity distribution, resulting in a narrower Ramsey linewidth [16, 17]. In addition, the system is simpler compared to the other two schemes, which makes it less sensitive to the environment condition. However, careful design of the beam optics is required, including the magnetic field intensity, the position of the cesium oven, etc. The short-term stability is often limited by the atomic shot noise due to the low density of the atomic beam [6]. Besides, technical issues are often the limiting factor for the lifetime of the electron multiplier. At present, the most widely used commercial cesium beam clock, Microsemi 5071A, is based on this scheme and has negligible frequency variation with environmental changes [18]. The fractional frequency stability of the high-performance version reaches $8.5 \times 10^{-12}\tau^{-1/2}$. Another product Cs3000C developed by Lanzhou Institute of Physics has the same stability level with 5071A [19].

Around 1980, the optical pumping technique was developed and applied to cesium beam clocks combined with the laser induced fluorescence method [20–22]. Compared with the magnetically-selected cesium atomic clock, the optically pumped cesium clock greatly improves the atom utilization efficiency and achieves a high signal-to-noise ratio. The beam optics system is simple, but the pumping light and detecting light inevitably introduce light shift into the system, which deteriorate the long-term stability. Typical compact optically pumped cesium clocks include OSA-3350 by Oscilloquartz, TA1000 by Chengdu Space on Electronics [23], and optical pumped clocks developed by Peking University [24, 25].

To combine both the advantages of the two schemes and avoid the technical issues concerning the lifetime of the electron multiplier, we proposed the magnetic-state-selecting and optical detecting scheme in 2009. After preliminary design and preparation, the first prototype was built in 2015 [26]. The short-term stability was $1.0 \times 10^{-11}\tau^{-1/2}$, which is comparable to the standard version of 5071A. To improve the long-term stability, the microwave power and C-field were stabilized, and the 5-days stability reached 2.7×10^{-14} [27]. Having optimized the stabilization scheme, the design of the cesium beam tube and the laser stabilization method, we improved the frequency stability to $4.1 \times 10^{-12}\tau^{-1/2}$, which is better than the high-performance version of 5071A [28].

This paper is an overview of the cesium beam clocks based on the magnetic-state-selecting and optical detecting scheme. In Section 2 we introduce the structure and working principle of OMCC. Section 3 focuses on its short-term and long-term stability. Optimizations concerning both the short-term and long-term stability are also summarized.

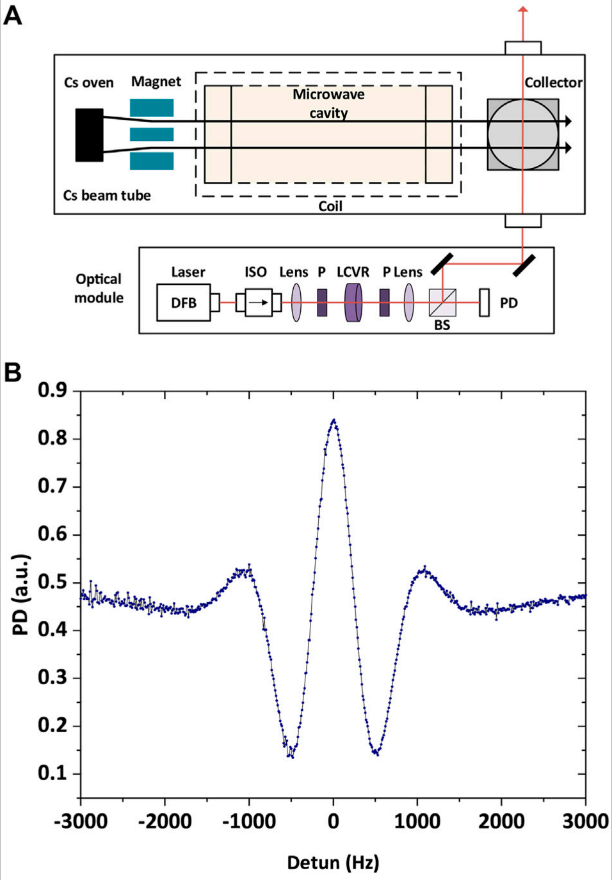

FIGURE 1
(A) Configuration of OMCC. ISO, Isolator; P, Polarizer; Lens, Convex lens; BS, Beam Splitter; PD, Photodiode; LCVR, Liquid crystal variable retarder. **(B)** Ramsey fringe.

2 Principles

The schematic of OMCC is depicted in Figure 1A. As introduced previously, OMCC is a compact cesium beam atomic clock based on the magnetic-state-selecting and optical-detecting scheme. Great care has been taken in the design of the cesium beam tube, the optical setup and the servo electronics for promising frequency stability. Here we briefly describe the outline of the system.

2.1 Cesium beam tube

The cesium beam tube adopts the double-beam structure. Compared with the single beam structure, its advantage is that it has a larger beam intensity at the same oven temperature. The cesium atoms are heated and ejected through a folded collimator [29]. We use a magnet based on the two-wire configuration to select the state of atoms in each beam [17]. Atoms in state $|F = 3\rangle$

are selected. The maximum gradient in the state selection direction is about −0.48 T/mm.

The cesium atoms in state $|F = 3\rangle$ enter the U-shaped microwave cavity and interact with the microwave field. The resonant frequency of the cavity is designed to be 9.192 GHz. The length of the single-action region is 1 cm. The distance between the two arms is 16 cm. Oxygen-free copper with high conductivity is used as the material to minimize the influence of the cavity phase difference. After tuning, the loaded quality factor of the microwave cavity is about 300–400. A static magnetic field is induced by the coils around the cavity to distinguish the transition state $|F = 3,\ m_F = 0\rangle - |F = 4,\ m_F = 0\rangle$ from others to avoid the first-order Zeeman shift. The orientation of the so-called C-field is the same as the state-selecting magnetic field for the same quantization axis for atoms to avoid Majorana transition. Three layers of magnetic shielding are applied to reduces the effect of ambient magnetic fields.

In order to improve the detection signal-to-noise ratio, a laser resonant with the cyclic transition line of the cesium D_2 line, $|F = 4 - F' = 5\rangle$, is used to realize the fluorescence detection of the $|F = 4\rangle$ atoms. Each atom in the light field can emit an average of 200–300 fluorescent photons, which is superior to other transition lines. Two spherical mirrors with different focal length are used as a fluorescence collector to converge the fluorescence onto the photodiode. The overall collection efficiency is estimated to be about 30%. Figure 1B shows the typical Ramsey fringe of OMCC. Due to the velocity-selective effect of the state-selecting magnet, the most probable velocity of the atomic beam is slower, which results in the linewidth of the OMCC being 1.5 to 2 times narrower than that of optical pumped compact cesium clocks [28].

2.2 Optical setup

The detecting light is generated by a distributed-feedback (DFB) laser (Eagleyard EYP-DFB-0852). The typical linewidth is 2 MHz which is narrower than the natural linewidth of the transition line. The optical isolator is magnetically shielded to reduce the magnetic flux leakage to the cesium beam tube. For the OMCC to operate continuously and stably, the laser frequency needs to be stabilized. Previously, the laser frequency was stabilized to the saturated absorption spectroscopy. There are some disadvantages practically. First, due to the multi-peak nature of the saturated absorption spectrum, the laser frequency is likely to be mis-locked to other peaks. The amplitude of the cyclic transition line is small compare to crossover lines in saturated absorption spectroscopy. Second, the saturated absorption spectrum is based on the atomic vapor cell, which is greatly affected by the motion of atoms, that is, by the ambient temperature. Under the saturable absorption spectrum frequency stabilization scheme of optically pumped cesium atomic clocks in literature, the laser frequency stability begins to deteriorate when the average time exceeds 100 s [30]. In addition, the saturated absorption spectrum system induces the structural complexity of the optical system, which is unfavorable to the long-term stability of OMCC.

Instead, we adopt the fluorescent spectroscopy to stabilize the laser frequency. Laser frequency is kept resonant with the atomic beam, and the mis-locking problem is avoided. The laser current is modulated, and the fluorescent signal is demodulated with the same sinusoidal wave in phase to generate the error signal. The error signal is processed by the PID module and fed back to the laser current. The loop bandwidth is about 200 Hz.

Practically, we found that there is a long-term drift in the laser power. The Allan deviation of the laser power is 4.5×10^{-3} at 10^5 s. After thorough investigation, we found that the drift results from the temperature drift of resistors in the circuit. A liquid crystal variable retarder (LCVR, Thorlabs, LCC-1111B) is used to tune the polarization of the light and stabilize the laser power. With this method, the laser power stability is increased to 3×10^{-6} at 10^5 s [31].

2.3 Servo

In order to improve the continuous running time and long-term frequency stability of OMCC, a digital servo system based on Field Programmable Gate Array (FPGA) is implemented [32]. The microwave frequency is modulated with a square wave at 10^2 Hz for the maximum error signal slope.

Conventionally, the power of the microwave field is stabilized to the response of microwave transition line to the microwave amplitude. The FPGA outputs a square wave voltage through the DAC to the voltage-controlled attenuator, forming a slow square wave modulation on the microwave power. The error signal is generated by demodulating the fluorescent signal. However, according to Ref. [17], the amplitude of the microwave field for which the error signal reaches the maximum value is not identical to that which maximize the transition probability. Thus, we demodulate the microwave frequency error signal instead to stabilize the power of the microwave field [28]. The method also minimizes the cavity pulling shift.

The strength of the C-field is stabilized *via* the adjacent transition $|F = 3, m_F = 1\rangle$ to $|F = 4,\ m_F = 1\rangle$ for its resonant frequency is proportional to the C-field. The FPGA changes the frequency to the neighboring transition every 100 s. The error signal is then used to lock the C-field.

3 Frequency stability

The frequency stability of an OMCC is affected by both the noise sources and frequency shift. Here we only introduce a few factors that have the greatest impact on the frequency stability, including atomic shot noise and laser frequency noise affecting the short-term stability, and the light shift which limiting the long-term stability.

3.1 Noise sources

The short-term frequency stability of passive cesium atomic clocks mainly depends on the Ramsey spectral line signal-to-noise ratio (SNR) and spectral linewidth. The linewidth is determined by the beam optics design, as discussed in Section 2.1. SNR refers to the ratio of the amplitude of the Ramsey fringe and the amplitude of the noise at the modulation frequency. Noise sources are considered uncorrelated, thus the corresponding power spectrum density (PSD) can be summed directly. Reference [28] shows the detailed analysis over the SNR of the OMCC.

The main noise sources of an OMCC including the atomic shot noise, laser frequency noise, photon shot noise, detecting noise, and noise in the electronics. Firstly, the atomic shot noise comes from the particle nature of the atomic beam. Atoms reach the detection zone randomly, which arousing the shot noise in the fluorescence signal [33]. The SNR corresponding to the atomic shot noise is proportional to $I_e/(I_r+\frac{1}{2}I_e)^{1/2}$, where I_e is the amplitude of the microwave spectrum, and I_r is the fluorescent signal contributed by unwanted atoms in the detected beam because of the unideal state selection [28]. The SNR corresponding to the shot noise is proportional to the square root of the atomic flux when the ratio I_r/I_e is a constant. Therefore, to increase the SNR, one possible way is to raise the oven temperature for the higher atomic flux. Since the beam optics is determined by the state-selecting magnet and mechanical structure, the velocity distribution and state selecting efficiency are not affected when raising the temperature.

Another noise source is the laser frequency noise. The fluctuation of the laser frequency results in the fluctuation of the detection signal. The PSD of the detection signal corresponding to the laser frequency noise is given in Ref. [34]. The SNR, correspondingly, is proportional to $I_e/(I_r+\frac{1}{2}I_e)$. The coefficient shows that laser frequency noise is not relevant with the total beam flux, but only relevant with the state selecting efficiency. Thus, simply raise the oven temperature does not influence the SNR corresponding to the laser frequency noise. This part of SNR is the upper limit for the SNR of a cesium beam tube. One possible solution is to use the laser with narrower linewidth. Another method is to appropriately increase the laser power to produce saturation broadening of the fluorescence spectrum.

There are other noise sources in an OMCC. The photon shot noise originates from the randomness of atomic radiation. The detecting noise comes from the imperfection of the collecting efficiency of the fluorescence collector. There are also noise sources in the circuit, including the dark current of the photodiode, the thermal noise of resistors, etc. The PSD corresponding to these noise sources is often negligible to that of the atomic shot noise and laser frequency noise [28].

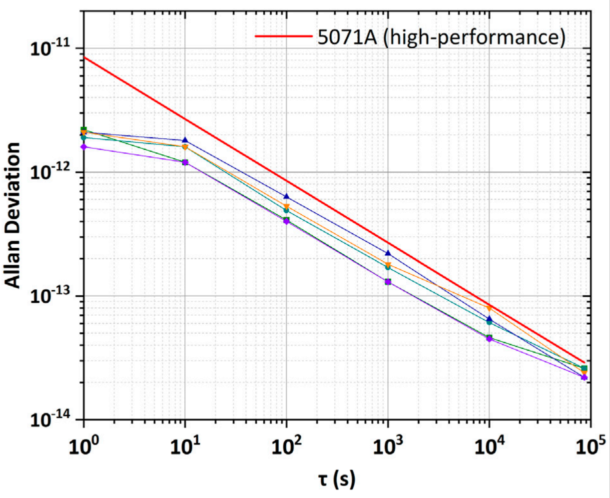

FIGURE 2
Frequency stability test result of five OMCC in comparison with the high-performance version of 5071A.

3.2 Long-term stability

The long-term stability of the OMCC is affected by several frequency shifts. The largest one is the quadratic Zeeman shift. The energy shift of cesium atoms interacting with static magnetic field can be calculated with Breit-Rabi formula. For the clock transition states $|F=3, m_F=0\rangle - |F=4, m_F=0\rangle$, the transition frequency can be written as

$$\nu = \nu_0 + 427.44 H_0^2$$

where ν_0 is the unperturbed hyperfine transition frequency of 9192631770 Hz, and the unit of the strength of the magnetic field H_0 is Oersted. The frequency difference between 0–0 line and 1–1 line ($|F=3, m_F=1\rangle - |F=4, m_F=1\rangle$) is used to stabilize the C-field current, therefore reducing the long-term frequency fluctuation due to the drift of the ambient magnetic field.

One another frequency shift is the light shift. In OMCC, both the stray light and fluorescence inevitably diffuse into the microwave cavity and shift the central frequency. The light shift changes with the deformation of the optical path and the drift of the laser power. To reduce the light shift coefficient, we apply the laser power stabilization loop, as discussed in Section 2.3. The optical module is designed to be as compact as possible to reduce the long-term deformation effect. Moreover, we find that it is possible to introduce a detuned laser into the detection light [35, 36]. With properly chosen frequency and intensity, the method can sufficiently suppress the light shift coefficient by more than an order of magnitude.

3.3 Result

The frequency stability test result of five OMCC at National Institute of Metrology in China is plotted in Figure 2. The frequency reference is an active hydrogen maser and the measure time is over 15 days. With carefully designed loop gain, the short-term stability at $\tau < 10$ s is determined by the stability of the crystal oscillator. From 10 to 10^5 s, the slope of the Allan deviation curve is −1/2, indicating that the dominating noise is white frequency noise. The result shows promising frequency stability and good consistency of OMCC.

4 Conclusion

In this paper, we review the basic principles of optically detected magnetic-state-selected cesium atomic clocks and some improvements we have made. In comparison with the traditional magnetic state selecting atomic clock and optical pumped atomic clock, OMCC has unique advantages in systematic simplicity and frequency stability. After 13 years of development, we can now achieve the better frequency stability than the high-performance version of 5071A, which proves that the scheme is quite promising. For better performance, we are now focusing on cesium beam tube design, accuracy evaluation and improvements on the environmental adaptability.

Author contributions

CaL, YW contributed to the conception of the reviewed scheme. CaL, LF, CeL, and CLi contributed to experimental setup. SC contributed to data analysis and data visualization. SC wrote the manuscript. YL and SX contributed to manuscript preparation.

Funding

This work was supported by the Joint Fund of the Ministry of Education of China (Grant No. 8091B042103).

Conflict of interest

Author CaL is employed by Chengdu Synchronization technology Ltd.

The remaining authors declare that the research was conducted in the absence of any commercial or financial relationships that could be construed as a potential conflict of interest.

Publisher's note

References

1. Degen CL, Reinhard F, Cappellaro P. Quantum sensing. *Rev Mod Phys* (2017) 89(3):035002. doi:10.1103/RevModPhys.89.035002

2. Kitching J, Knappe S, Donley EA. Atomic sensors - a review. *IEEE Sens J* (2011) 11(9):1749–58. doi:10.1109/Jsen.2011.2157679

3. Montanaro A. Quantum algorithms: An overview. *Npj Quan Inf* (2016) 2: 15023. doi:10.1038/npjqi.2015.23

4. Ma HY, He ZX, Xu PG, Dong YM, Fan XK. A quantum richardson-lucy image restoration algorithm based on controlled rotation operation and Hamiltonian evolution. *Quan Inf Process* (2020) 19(8):237. doi:10.1007/s11128-020-02723-4

5. Lo HK, Curty M, Tamaki K. Secure quantum key distribution. *Nat Photon* (2014) 8(8):595–604. doi:10.1038/Nphoton.2014.149

6. Cutler LS. Fifty years of commercial caesium clocks. *Metrologia* (2005) 42(3): S90–S9. doi:10.1088/0026-1394/42/3/s10

7. Essen L, Parry JVL. Caesium resonator. *Nature* (1955) 176(4476):281–2. doi:10.1098/rsta.1957.0010

8. Vanier J, Audoin C. The classical caesium beam frequency standard: Fifty years later. *Metrologia* (2005) 42(3):S31–S42. doi:10.1088/0026-1394/42/3/s05

9. Freeman SE, Emokpae LE, Edelmann GF. High-frequency, highly directional short-range underwater acoustic communications. In: Oceans 2015 - MTS/IEEE Washington; 19-22 October 2015; Washington, DC, USA. IEEE (2015). p. 1–4.

10. Rybak MM, Axelrad P, Seubert J, Ely T. Chip scale atomic clock-driven one-way radiometric tracking for low-earth-orbit cubesat navigation. *J Spacecr Rockets* (2021) 58(1):200–9. doi:10.2514/1.A34684

11. Zhan LW, Liu Y, Yao WX, Zhao JC, Liu YL. Utilization of chip-scale atomic clock for synchrophasor measurements. *IEEE Trans Power Deliv* (2016) 31(5): 2299–300. doi:10.1109/Tpwrd.2016.2521318

12. Bothwell T, Kennedy CJ, Aeppli A, Kedar D, Robinson JM, Oelker E, et al. Resolving the gravitational redshift across a millimetre-scale atomic sample. *Nature* (2022) 602(7897):420–4. doi:10.1038/s41586-021-04349-7

13. Kennedy CJ, Oelker E, Robinson JM, Bothwell T, Kedar D, Milner WR, et al. Precision metrology meets cosmology: Improved constraints on ultralight dark matter from atom-cavity frequency comparisons. *Phys Rev Lett* (2020) 125(20): 201302. doi:10.1103/PhysRevLett.125.201302

14. Jaduszliwer B, Camparo J. Past, present and future of atomic clocks for GNSS. *Gps Solut* (2021) 25(1):27. doi:10.1007/s10291-020-01059-x

15. Marlow BLS, Scherer DR. A review of commercial and emerging atomic frequency standards. *IEEE Trans Ultrason Ferroelectr Freq Control* (2021) 68(6): 2007–22. doi:10.1109/TUFFC.2021.3049713

16. Becker G. Recent progress in primary Cs beam frequency standards at the PTB. *IEEE Trans Instrum Meas* (1976) 25(4):458–65. doi:10.1109/Tim.1976.6312264

17. Vanier J, Audoin C. *The quantum physics of atomic frequency standards*. Bristol and Philadelphia: Adam Hilger (1989).

18. Kalliomaki K, Mansten T, Mannermaa J. Short and long term stability of HP Cs standards including environmental effects. In: 18th European Frequency and Time Forum (EFTF 2004); 05-07 April 2004; Guildford: IET (2004). p. 409–10.

19. Chen J, Wang J, Ma P, Guo L, Tu J, Yang W, et al. Test of magnetic-selected cesium atomic clock LIP Cs3000C. *J Time Frequency* (2018) 41(3):190–3. doi:10.13875/j.issn.1674-0637.2018-03-01.90-04

20. Arditi M, Hirano I, Tougne P. Optical pumping of a caesium beam and detection of the 0-0 'clock' transition. *J Phys D Appl Phys* (1978) 11(18):2465–75. doi:10.1088/0022-3727/11/18/005

21. Lewis L, Feldman M. Optical pumping by lasers in atomic frequency standards. In: Thirty Fifth Annual Frequency Control Symposium; 27-29 May 1981; Philadelphia, PA, USA. IEEE (1981). p. 612–24.

22. de Clercq E, de Labachellerie M, Avila G, Cerez P, Tetu M. Laser diode optically pumped caesium beam. *J Phys France* (1984) 45(2):239–47. doi:10.1051/jphys:01984004502023900

23. Zhao X, Chen H, Yang L, Wei Q, Li D, Li Y. Stabilizing the optical frequency by laser-induced fluorescence in optically pumped Cs beam frequency standard. *J Astronautic Metrology Meas* (2020) 40(1):17–22. doi:10.12060/j.issn.1000-7202.2020.01.03

24. Xie W, Wang Q, He X, Chen N, Xiong Z, Fang S, et al. Frequency instability of a miniature optically pumped cesium-beam atomic frequency standard. *Rev Sci Instrum* (2020) 91(7):074705. doi:10.1063/5.0001749

25. He X, Fang S, Yuan Z, Xie W, Chen N, Xiong Z, et al. Compact optically pumped cesium beam atomic clock with a 5-day frequency stability of 7×10^{-15}. *Appl Opt* (2021) 60(34):10761–5. doi:10.1364/AO.443812

26. Liu C, Zhou S, Wang Y. Noise investigation on optical detection in a cesium beam clock with magnetic state selection. In: 2015 Joint Conference of the IEEE International Frequency Control Symposium & the European Frequency and Time Forum (IFCS/EFTF); 12-16 April 2015; Denver, CO, USA. IEEE (2015). p. 483–6.

27. Liu C, Wang S, Chen Z, Wang Y, Jia J, Sun Y, et al. A caesium atomic beam microwave clock detected by distributed feedback laser diodes. In: 2017 Joint Conference of the European Frequency and Time Forum and IEEE International Frequency Control Symposium (EFTF/IFCS); 09-13 July 2017; Besancon, France. IEEE (2017). p. 282–4.

28. Liu C, Chen S, Chen Z, Li L, Xu S, Li Y, et al. Improving the short-term frequency stability of a magnetic-state-selected cesium beam clock with optical detection. *Rev Sci Instrum* (2021) 92(7):073302. doi:10.1063/5.0046575

29. Jones RH, Olander DR, Kruger VR. Molecular-beam sources fabricated from multichannel arrays. I. Angular distributions and peaking factors. *J Appl Phys* (1969) 40(11):4641–9. doi:10.1063/1.1657245

30. Wang Q, Duan J, Qi X-H, Zhang Y, Chen X-Z. Improvement of laser frequency stabilization for the optical pumping cesium beam standard. *Chin Phys Lett* (2015) 32(5):054206. doi:10.1088/0256-307x/32/5/054206

31. Chen Z, Liu C, Wang S, Wang Y. A method on laser power stabilization in optical detection cesium atomic clock. In: China Satellite Navigation Conference (CSNC) 2018 proceedings, Harbin, China, 23 May, 2018. Springer (2018). p. 607–14.

32. Liu C, Wang S, Chen Z, Wang Y, Hou S. Optical detection in magnetic state-selection Cs beam tubes for transportable Cs beam clocks. *Meas Sci Technol* (2019) 30(7):075004. doi:10.1088/1361-6501/ab11af

33. Dimarcq N, Audoin C. Detection of atoms in a beam - filtering of the atomic shot-noise and velocity dispersion contribution. *J Phys B: Mol Opt Phys* (1995) 28(11):2083–94. doi:10.1088/0953-4075/28/11/008

34. Dimarcq N, Giordano V, Cerez P. Statistical properties of laser-induced fluorescence signals. *Appl Phys B* (1994) 59(2):135–45. doi:10.1007/Bf01081164

35. Xu S, Chen S, Liu C, Li Y, Wang J, Wang Y. A new method to suppress the Ac-Stark shift of compact cesium beam atomic clocks. In: China Satellite Navigation Conference (CSNC 2021) 2021 Proceedings, Nanchang, China, 26 May, 2021. Springer (2021). p. 17–25.

36. Xu S, Chen S, Liu C, Li Y, Wang J, Wang Y, et al. Optimization of frequency shifts in optically detected magnetic-state-selection cesium beam atomic clocks. *Europhys Lett* (2022) 136(2):23002. doi:10.1209/0295-5075/ac1bc7

frontiers | Frontiers in Physics

TYPE Original Research
PUBLISHED 15 August 2022
DOI 10.3389/fphy.2022.969921

Detecting the pH-dependent liquid-liquid phase separation of single levitated aerosol microdroplets *via* laser tweezers-Raman spectroscopy

Yu-Kai Tong[1], Xiangxinyue Meng[2], Bo Zhou[1,3], Rui Sun[1], Zhijun Wu[2], Min Hu[2] and Anpei Ye[1]*

[1]Key Laboratory for the Physics and Chemistry of Nanodevices, School of Electronics, Peking University, Beijing, China, [2]State Key Joint Laboratory of Environmental Simulation and Pollution Control, College of Environmental Sciences and Engineering, Peking University, Beijing, China, [3]School of Science, Beijing University of Posts and Telecommunications, Beijing, China

OPEN ACCESS

EDITED BY
Zhiwen Liu,
The Pennsylvania State University (PSU),
United States

REVIEWED BY
Bormashenko Edward,
Ariel University, Israel
Jinda Lin,
Shanghai Institute of Optics and Fine Mechanics, China

*CORRESPONDENCE
Anpei Ye,
yap@pku.edu.cn

SPECIALTY SECTION
This article was submitted to Atomic and Molecular Physics,
a section of the journal
Frontiers in Physics

RECEIVED 15 June 2022
ACCEPTED 11 July 2022
PUBLISHED 15 August 2022

CITATION
Tong Y-K, Meng X, Zhou B, Sun R, Wu Z, Hu M and Ye A (2022), Detecting the pH-dependent liquid-liquid phase separation of single levitated aerosol microdroplets via laser tweezers-Raman spectroscopy.
Front. Phys. 10:969921.
doi: 10.3389/fphy.2022.969921

Ambient atmospheric aerosol particles comprised of various inorganic and organic substances ubiquitously undergo phase transition, such as efflorescence, amorphization, and especially liquid-liquid phase separation (LLPS). Resultant changes of physicochemical properties in aerosols then deeply affect the climate system. However, finely detecting these processes occurring in single aerosol particles, especially under the acidic condition of real atmospheric environment, remains a challenge. In this work, we investigated the pH-dependent phase separation in single levitated microdroplets using a self-developed laser tweezers Raman spectroscopy (LTRS) system. The dynamic process of LLPS in laser-trapped droplets over the course of humidity cycles was detected with the time-resolved cavity-enhanced Raman spectra. These measurements provide the first comprehensive account of the pH-dependent LLPS in single levitated aerosol microdroplets and bring possible implications on phase separation in actual atmospheric particles.

KEYWORDS

single aerosol, pH, liquid-liquid phase separation, Raman spectroscopy, laser tweezers

Introduction

Aerosol particles are prevalent in atmosphere and impact the climate system in two significant ways. One way is that aerosols directly influence solar radiation, e.g., aerosols containing sulfates and nitrates can scatter the solar radiation back into space and then reduce the temperature of atmosphere. The other way is that aerosols can act as cloud condensation nuclei, affect the number density of cloud droplets and indirectly impact the climate. These impacts on climate substantially depend on the critical physicochemical properties of aerosols, including optical properties [1,2], heterogeneous chemistry [3,4], water uptake behavior [5,6], and nucleation activity [7–10]. These properties, in turn, are dictated by the morphology of the aerosols, especially the intern structure and phase state.

The liquid-liquid phase separation (LLPS), a distinctive morphology in aerosol microdroplets, has been investigated under various laboratory and out-field environments [9,11,12]. For laboratory works on LLPS in single aerosol droplets, Kwamena et al. [13] conducted experiments and simulation analysis on decane/NaCl/water droplets and found that the morphology of liquid-liquid phase separated droplets can be explicitly determined once given the values of surface/interface tension of the two phases. Reid et al. [14] investigated the LLPS in microdroplets with NaCl as the hydrophilic component and hydrocarbons, alcohols and fatty acids as the hydrophobic component. With the analysis of surface tension, they found that core-shell morphology predominates in the LLPS of aerosols whose organic components are water insoluble, while partially engulfed morphology predominates in the aerosols with water soluble organics. Stewart et al. [15] put forward three signatures of the time-solved cavity-enhanced Raman spectra to detect the LLPS in aqueous polyethylene glycol (PEG-400)/ammonium sulfate system and aqueous C6-diacids/ammonium sulfate system. Ishizaka et al. [16] used a temperature-responsive ionic liquid as a surrogate of the water insoluble organics and observed the partially engulfed morphology during the dehumidifying process of microdroplets.

For field studies, Pöhlker et al. [17] observed the atmospheric particles collected during the wet season in Amazonian rainforest through scanning electron microscopy, exhibited a LLPS structure with a salt core and an organic coating in the aerosols, and disentangled the impact of rainforests on the climate at the level of aerosols. You et al. [18] presented images that show the coexistence of two noncrystalline phases for real-world samples collected on multiple days in Atlanta. Lee et al. [19] produced primary sea spray aerosols from wave breaking of natural seawater within a wave flume and investigated the evolving heterogeneity within aerosol populations. They found that particles between ca. 0.3 and 1 μm in volume equivalent diameter displayed a LLPS morphology where an inorganic core was coated with an organic shell.

A caveat is that most of present studies focused merely on the influence of chemical composition on LLPS. However, even those works on real-world aerosols used the diluted extracts of filter-collected samples for aerosol generation where the constituent concentration differed from pristine atmosphere aerosols. Recent out-field studies have reported the high acidity found in many ambient aerosol particles [20–25]. Thus, it is imperative to detect the LLPS in microdroplets at their pristine state, that is, in acidic environment. Dallemagne et al. [26] found the variation in pH of aqueous PEG-400/$(NH_4)_2SO_4$ aerosols during LLPS where the pH in two liquid phases was of the same order of magnitude but with a difference of less than 0.4 pH units. Losey et al. [27,28] investigated the LLPS of microdroplets over the course of humidity cycles and found that the separation relative humidity (SRH, the RH level at which LLPS occurs) of organic acids increases as the droplet pH decreases, while the SRH of other organics (e.g., polyols) decreases as pH decreases.

TABLE 1 Information of the mother solutions used to generate aerosol droplets.

Solution ID	Solute	pH
OA-I	Oleic Acid + NaCl	7.07 ± 0.12*
OA-II		1.22 ± 0.08*
HEX-I		6.93 ± 0.11
HEX-II	1,2,6-hexanetriol	4.79 ± 0.08
HEX-III	+ $(NH_4)_2SO_4$	2.85 ± 0.12
HEX-IV		1.13 ± 0.07

*Data reported only for the aqueous compartment.

Such studies on the impact of pH on LLPS are limited. Nearly all used the substrate-deposited droplets as targets, where the influence of the contact coverslip on the morphology of the droplets cannot be excluded [29]. In this study, we investigated the pH-dependent LLPS of single laser-levitated microdroplets. First, we detected the LLPS in inherently separated droplets which were comprised of oleic acid (OA) and sodium chloride, and explored the possible change of LLPS morphology in acidic environment. Then, LLPS in internally miscible 1,2,6-hexanetriol/ammonium sulfate/water droplets with various pH were investigated during dehumidifying process. Finally, we analyzed and compared the influence of pH on phase separation in these aerosol droplets. To the best of the authors' knowledge, it is the first time to investigate the impact of pH on LLPS in single levitated aerosol droplets.

Method and experimental section

Reagents and single aerosol manipulation

Six mother solutions were used in this study to generate aerosol droplets which were grouped into two types, OA/NaCl and 1,2,6-hexanetriol (HEX)/$(NH_4)_2SO_4$. The solutions were prepared by double-distilled water (18.2 MΩ cm; Milli-Q; MilliporeSigma, Burlington, MA, United States). Taking account of that sulfates are one of the major inorganics in ambient aerosols, we adjusted the pH of the solutions by adding different amounts of sulfate acid (guaranteed reagent, Xilong Scientific Co., Ltd., Guangdong, China). Solute NaCl and $(NH_4)_2SO_4$ were purchased from Tong Guang Fine Chemical Co. (Beijing, China). Solute OA (analytical reagent) was purchased from Xilong Scientific Co., Ltd. (Guangdong, China); HEX was purchased from Shanghai Macklin

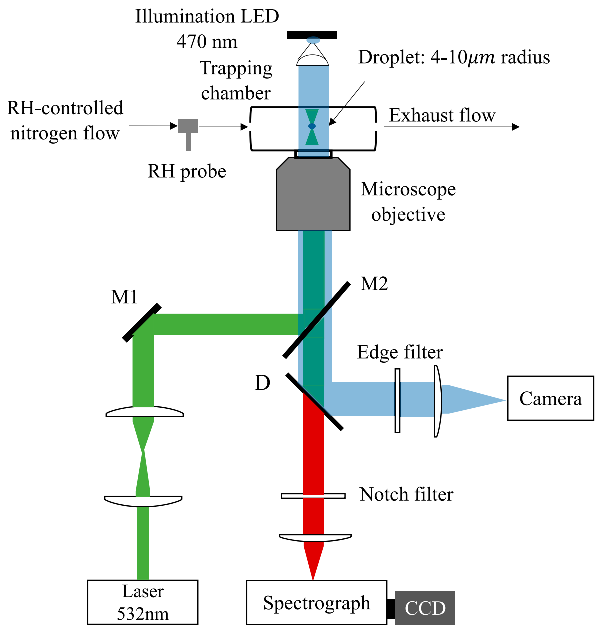

FIGURE 1
Schematic of the laser tweezers Raman spectroscopy (LTRS) system. A laser beam passes through a pair of beam expansion optics and finally couples into an objective to form the laser tweezers. The droplet is imaging using a 470 nm illumination LED and a high frame rate camera. The Raman spectra of the trapped droplets are recorded using a spectrograph/CCD. M1 and M2 are mirrors. D is a long pass dichroic mirror.

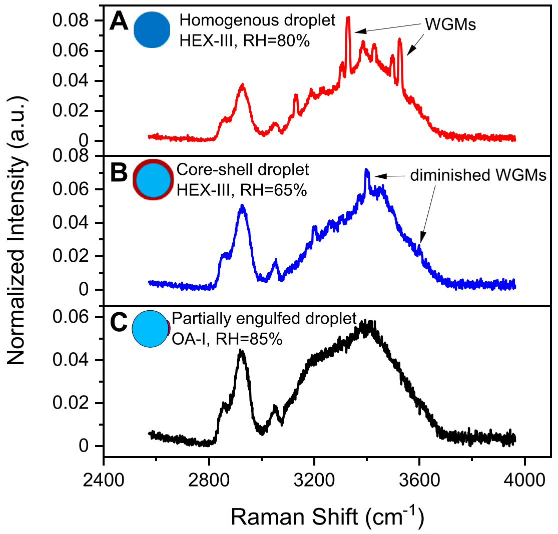

FIGURE 2
Raman spectra snapshots of microdroplets. **(A)** A Raman spectrum extracted from Figure 5A2 at 200 s, a homogenous droplet generated from HEX-III, RH = 80%. **(B)** A Raman spectrum extracted from Figure 5A2 at 1242 s, a core-shell droplet generated from HEX-III, RH = 65%. **(C)** A Raman spectrum extracted from Figure 3A at 613 s, a partially engulfed droplet generated from OA-I, RH=85%. The WGMs are pointed out with arrowed lines.

Biochemical Co.,Ltd. (Shanghai, China). Relevant information of the mother solutions is listed in Table 1. The pH of mother solutions was measured with a pH meter (Mettler Toledo Instruments Co., Ltd., Shanghai, China). All volume fractions of organics in the mother solutions used in this work were 10%. The organic-to-inorganic mass ratios (OIR) of Solution HEX-I ~IV are all 2/1.

A schematic of the laser tweezers Raman spectroscopy (LTRS) system is shown in Figure 1. Details of the single particle technique used here can be seen in our previous work [30,31]. In brief, we generated the aerosol droplets of desired chemical composition by a medical nebulizer (Mint PN100) and used a self-developed laser tweezers to trap a single levitated droplet (4 ~10 μm in radius). The droplet was trapped in a tailored chamber where the relative humidity (RH) could be regulated at a maximum rate of 5% RH/min by mixing dry and humidified nitrogen gas flow; the value of RH was monitored with a RH probe (HC2A-S, ROTRONIC). A laser beam with a wavelength of 532 nm (Excelsior-532-200, Spectra Physics) was used to both trap the aerosol droplet and excite its Raman signal, which was recorded by a spectrograph (SpectaPro 2300i, Acton) equipped with a liquid nitrogen cooled CCD (Spec-10, Princeton Instruments). We observed the LLPS of the single levitated droplet, which was generated from different mother solutions, during a dehumidifying process and determined the SRH according to the readouts of the RH probe.

The disturbance of the RH-controlled nitrogen flow was discussed in the Supplemental Material (Section S1) by calculating relevant dimensionless numbers including the Weber number and the Ohnesorge number. The results indicate that compared with the gravity, inertia and viscosity of the droplet, the surface tension is the dominant factor that impacts the morphology of the droplet. Thus, under the effect of self-surface tension, the single levitated droplet can be considered to be a stationary sphere after achieving a balance with the ambient atmosphere (see an image of the trapped droplet shown in Supplementary Figure S3 in the Supplemental Material).

Detection of liquid-liquid phase separation

The phase separation in substrate-deposited droplets has been directly observed by bright-field imaging or scanning electron microscopy [17–19,32]. However, for levitated droplets, the defocus of the trapped droplets blurs the direct imaging. Instead, the time-resolved Raman spectra of the trapped droplets can be used to detect the LLPS efficiently [13–15,33–36]. The Raman spectra demos from different kinds of microdroplets are shown in Figure 2. The trapped droplet works as an

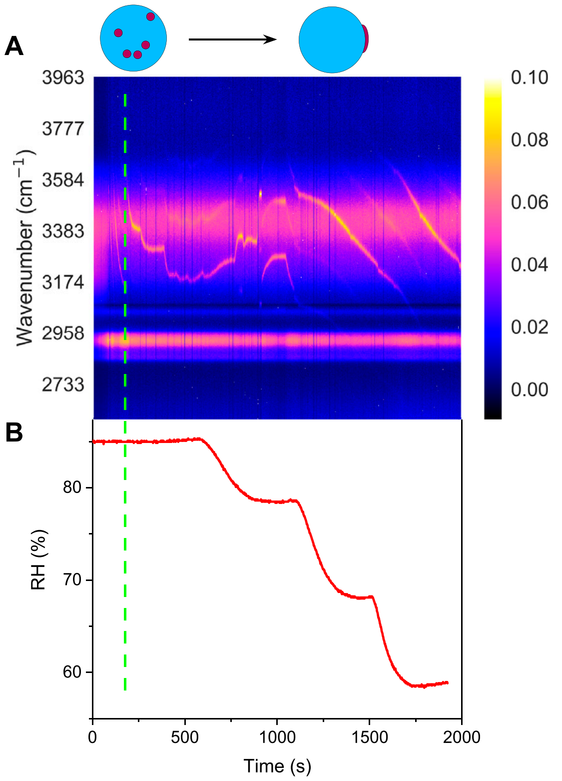

FIGURE 3
Liquid-liquid phase separation of aqueous oleic acid/sodium chloride (OA-I). **(A)** time-resolved Raman spectra and schematic diagram of phase separation, the bright trend dots indicate the position evolution of the detectable peaks (i.e., the WGMs shown in Figure 2). **(B)** RH variation with time in the trapping chamber during the dehumidifying process. The green dashed line indicates the moment when the random motion of inclusions in the droplet stopped and culminated in a stable partially-engulfed structure.

enhancing cavity and will overlap stimulated sharp peaks at wavelengths commensurate with whispering gallery modes (WGMs) on the spontaneous Raman spectra (see Figure 2A). The WGM peaks are extremely sensitive with the morphology of the droplet, indicating that if the droplet undergoes phase separation and becomes nonspherical (e.g., partially engulfed), WGM peaks in the spectra will quench (see Figure 2C). Thus, the moment when WGM peaks start to quench can be determined as the onset of phase separation, particularly for partially engulfed phase separation.

For the other mode of phase separation, the core-shell morphology, the sphericity of the phase separated droplet remains and its Raman spectra still retain WGM peaks (see Figure 2B). Nonetheless, the radial homogeneity is destroyed because of the separation of the hydrophilic core and hydrophobic shell. Thus, fitting the Raman spectra with the Mie scattering model for a homogenous droplet, the fitting errors between the measured and simulated WGM peaks are supposed to increase drastically (i.e. model failure). Therefore, the moment when the homogenous fitting errors start to soar can be determined as the onset of core-shell phase separation. The homogenous Mie scattering fitting model used in this work was developed by Preston et al. [37]. All the Raman spectra used here is normalized by area.

Results and discussion

In this work, we detected the phase separation of microdroplets comprised of various organics and inorganics at room temperature. In details, the aerosol droplets comprised of oleic acid/sodium chloride/water and 1,2,6-hexanetriol/ammonium sulfate/water were included, respectively. The pH of the droplets was adjusted by adding different amounts of sulfate acid. The phase separation of the internally miscible aerosol droplets under different acidic environment was realized by dehydrating the droplets.

Inherently separated aerosols

The number of organic species in a single atmospheric particle is on the order of thousands, among which water insoluble organic compounds (WIOCs) take a quite important part. Here, we used oleic acid as a surrogate of WIOC and detected the phase separation of inherently separated aerosols.

Figure 3A shows the time-resolved Raman spectra of the aerosol droplet generated from Solution OA-I, which vividly depicts the progression of phase separation. The brand range of 3100 ~3600 cm^{-1} corresponds to the bending and stretching modes of O-H of water, while the range of 2,850 ~ 2,950 cm^{-1} corresponds to the C-H mode of organics (OA here). In the beginning, the RH was set at a constant value of 85% for around 650 s to let the freshly trapped droplet reach a stable state. It can be seen that in the beginning (before ~230 s, marked with a green dashed line in Figure 3), there are no pronounced bright dots in the spectra which indicates that no WGMs have emerged in the freshly trapped droplet. It is because that the droplet was generated by nebulizing the mixture of OA/NaCl/Water and a number of emulsions of OA would certainly be contained in the nascent droplet. The random motion of the inclusions destroys the radial homogeneity and gives rise to the absence of the WGMs (see the schematic diagram in Figure 3A). After this, no more than one bright dot presents in each spectral snapshot which indicates that at most one WGM peak has been detected in the spectra of the droplet. It means that the droplet was heterogenous, in other words, phase-separation with a partially engulfed structure took place. The rather complex but very weak resonant structure in the spectra stems from that the volume of the aqueous inorganic phase may be far greater than that of the hydrophobic organic phase because of the

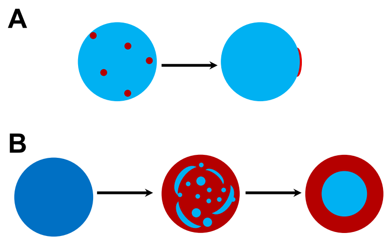

FIGURE 4
Schematic diagram of possible morphologies for the progression of phase separation. **(A)** phase separation of inherently separated aerosols, e.g., OA/NaCl/Water. **(B)** phase separation of internally miscible aerosols in a model of spinodal decomposition during dehumidifying, e.g., HEX/$(NH_4)_2SO_4$/Water. Dark blue: homogenous phase, light blue: hydrophilic phase, dark red: hydrophobic phase.

prior stochastic mixing of OA emulsions and water, and an approximately spherical cavity occurs for the aqueous volume (see the schematic diagram in Figure 4A). The imperfect spherical volume is supposed to lead to complexity in the WGM fingerprint and a low enhancement due to the low quality of the WGMs [14].

After adding sulfate acid, the phase separation of OA-II is shown in Supplementary Figure S1 (see the Supplemental Material). It can be seen that after the transient evolution of the nascent droplet, there are still several weak but non-eliminable WGM peaks in the spectral snapshots (100 ~400 s). It may be explained by that the added sulfate acid worked as a surfactant and reduced the surface tension between air and organic phase and the interface tension between organic and inorganic phase, which then changed the morphology of the phase separated droplet from partially engulfed structure to core-shell structure. However, such core-shell structure was quite fragile and lasted only for a short while. As the RH continued to decrease, the concentration of the inorganics as well as the surface tension between air and inorganic phase increased, which turned the core-shell structure back to partially engulfed structure. This change is shown in the spectral snapshots that as RH decreased, after ~430 s, the droplet was dehydrated and similar low-quality WGMs emerged. Besides, the interim process

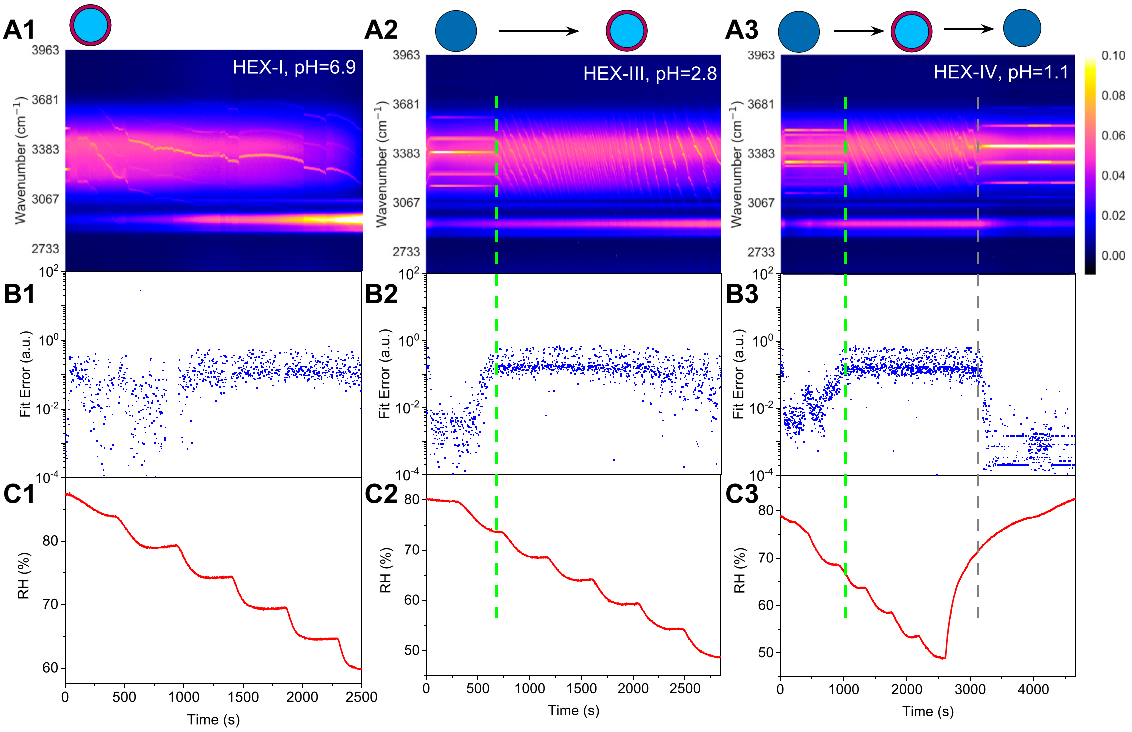

FIGURE 5
Liquid-liquid phase separation of 1,2,6-hexanetriol/ammonium sulfate/water. Top row: time-resolved Raman spectra and schematic diagrams of phase separation, the bright trend dots indicate the position evolution of the peaks. Middle row: fitting errors of the WGMs based on the homogenous Mie scattering model. Bottom row: RH variation with time in the trapping chamber during humidity steps. Panels **(A1–C1)**: aerosol generated from Solution HEX-I. Panels **(A2–C2)**: aerosol generated from Solution HEX-III, green dashed line indicates the moment when phase separation occurred. Panels **(A3–C3)**: aerosol generated from Solution HEX-IV, green dashed line and grey dashed line indicate the moment when phase separation and phase mixing occurred, respectively. Results of HEX-II (pH = 4.8) can be seen in Supplementary Figure S2 in the Supplemental Material.

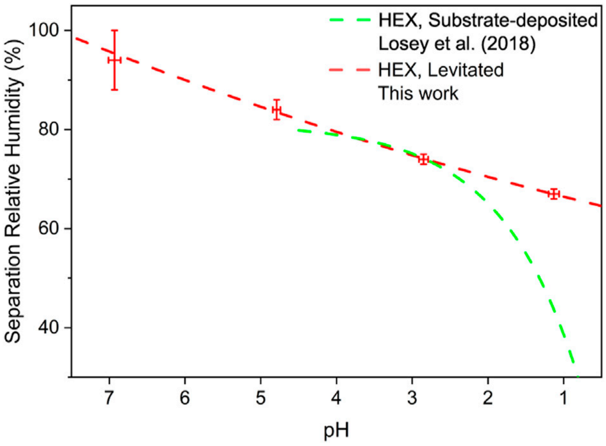

FIGURE 6
Separation relative humidity as a function of pH. Colors: red, droplets from Solution HEX-I ~IV, this work; green, droplets of 1,2,6-hexanetriol/$(NH_4)_2SO_4$, [28]. The uncertainties in pH are the standard deviations resulting from averaging multiple measurements. The uncertainties in SRH mean the range where the exact values of SRH locate. The data points are the mediate values of the SRH ranges.

from partially-engulfed to core-shell is also illustrated in the time-resolved Raman spectra, where no WGMs were recorded during 400 ~430 s.

Internally miscible aerosols

The formation of ambient secondary organic aerosols (SOAs) is inextricable from the generation of organosulfates and nitrooxy-organosulfates [3,38,39], which then contributes to the emergence of various water soluble organic compounds (WSOCs). Most of the WSOCs are humic-like substances, including dicarboxylic acids, polyols, esters, and ethers. We used 1,2,6-hexanetriol as the surrogate of WSOC and detected the phase separation of internally miscible aerosols.

Figure 5 illustrates the phase separations of aerosol droplets generated from aqueous HEX/$(NH_4)_2SO_4$ at different pH levels. For HEX-I (pH = 6.9), from Figure 5A1, we can see that there are numerous WGMs from the beginning of the time-resolved Raman spectra. After the droplet reaches a stable state with the ambient environment, there are still three WGMs in the spectral snapshots, one of which is quite prominent. It means that the droplet could not be partially-engulfed, in other words, the droplet was expected to be either core-shell or homogenous. In Figure 5B1, the fitting errors of the measured WGMs calculated by the homogenous Mie scattering model are on the order of 10^{-1} ~ 10^{0}, which are far greater than those from homogenous droplets (compared with Figure 5B2), time = 0–500 s). It also indicates that although the droplet was generated from a homogenous internally miscible solution, it underwent phase separation just after entering the optical well. Thus, the SRH of HEX-I is presumably higher than the initial RH (88%) in the trapping chamber.

For HEX-III (pH = 2.8), Figure 5A2) shows that before 690 s, the droplet was homogenous with five obvious WGMs in its spectra, and the fitting errors in Figure 5B2 are pretty minor. However, as the RH keeps decreasing, the fitting errors surge promptly (note the logarithmic scale), indicating that the phase state of the droplet changed during 690–700 s (marked with a dashed line in the figure). The corresponding RH shown in Figure 5C2 is in the range of 73%–75%, at which the SRH of HEX-III may locate. Previous works found that the mechanism of phase separation in aerosol microdroplet was mainly determined by the OIR of the droplet. Empirical summaries indicate that when $1/1.5 <$ OIR < 2, the LLPS occurs dominantly via spinodal decomposition [35]. Considering the OIR of HEX-III, the droplet may undergo phase separation by spinodal decomposition and cluster growth and aggregation (see Figure 4B).

For HEX-IV (pH = 1.1), from Figures 5A3–C3, we can see that the SRH of HEX-IV falls within the range of 66%–68%. In the period of 0–2,600 s, the reduction in RH leads to an increase in the Raman intensity from the C-H vibrations and a decrease in the intensity from O-H (this phenomenon is more obvious in Figure 5A1). After that, we elevated the ambient RH; the droplet started to absorb the moisture along with a decrease of C-H mode and an increase of O-H mode. Besides, the convoluted WGMs in the spectra regress to around six main peaks at around 3200 s (marked with a grey dashed line in the figure). It means that the droplet subsequently returned to be homogenous, albeit a hysteresis took place compared with the increase of RH. Moreover, the mixing relative humidity (MRH, the RH level at which phase mixing occurs) can be determined according to the slump of the fitting errors, which is in the range of 72%–75% and mildly higher than the SRH. It is inline with the results of Losey et al. [28]. It also shows that water molecules can go through the hydrophobic shell and be absorbed by the hydrophilic core during the process of water condensation. It might stem from that the molecules of organics are much bigger than the molecules of water so that the latter can transfer through the pores and channels formed in the former.

pH dependence of separation relative humidity

The SRHs of aerosol droplets generated from Solution HEX-I ~IV are illustrated in Figure 6. It can be seen that the SRH of HEX decreases as pH decreases, which means that the acid enhances the miscibility of organics/inorganics. Considering the acidity found in ambient aerosol particles, it is conceivable that aerosols would undergo phase separation at lower RH than the values reported in [17,18]. Moreover, the pH-dependent SRHs reported by Losey et al. [28] are also drawn in the same graph. Our results agree well with that of Losey et al. [28] in the pH range of 3 ~5. The discrepancy occurs when the pH is below 3 and increases in the range of 1 ~2. It may result from the different ambient conditions of the droplets which are laser-levitation (leading to a morphology of sphere) and substrate-deposition (leading to a morphology of spherical crown) respectively. Besides, the researched droplets in our work were also obviously smaller than that in Losey et al. [28]. Considering the realistic size and levitating state, the droplets used in our work better mimicked the natural airborne aerosols Kucinski et al. [40]. found that the size of micro-particles was influential in the phase separation. The smaller size and the spherical morphology enhance the Kelvin effect, making the droplets in our work easier to undergo phase separation.

Conclusion

In this work, we detected the impact of pH on phase separation in multicomponent aerosol droplets, such as OA/NaCl/Water and HEX/$(NH_4)_2SO_4$/Water. To the best of the authors' knowledge, it is the first time to investigate the pH-dependent phase separation at single levitated particle level. The results indicate that pH can change the miscibility of the mixtures, low pH will reduce the SRH of HEX. Besides, pH can also change the phase separated structure, such as pH can change the morphology of OA/NaCl/Water droplet from partially-engulfed to core-shell under certain conditions. Moreover, our results unveil the mass transfer in a core-shell microdroplet that water molecules can go through the hydrophobic shell and be absorbed by the hydrophilic core. This work further informs our understanding of the phase separation of aerosols under real ambient conditions, that the prevalence of phase separation in ambient aerosols perhaps should be reassessed taking account of the acidic environment.

In the future, the phase separation in real acidified ambient aerosols is expected to be further researched, which would provide us with possible implications of the morphology of real aerosols and its impacts on related properties such as the hygroscopicity, homogenous chemistry, and et al.

Data availability statement

The original contributions presented in the study are included in the article/Supplementary Material, further inquiries can be directed to the corresponding author.

Author contributions

Y-KT proposed the idea of the project, performed the measurements, conducted the data analysis, and led in writing the manuscript. AY contributed to funding the research, constructed the optical tweezer system, provided the instruction on the experiment and revised the manuscript. XM discussed the experiment objectives and contents and prepared the aerosol solutions. BZ and RS contributed to the data visualization. ZW was responsible for the conceptualization of aerosol droplets and discussion of methodology.

Funding

This work was supported by the National Natural Science Foundation of China (U19A2007, 32150026 and 92043302) and the National Key Research & Development Program of China (2017YFC0209504).

Acknowledgments

Y-KT gratefully acknowledge Dr Chen Cai for instructive suggestions on experiments.

Conflict of interest

The authors declare that the research was conducted in the absence of any commercial or financial relationships that could be construed as a potential conflict of interest.

Publisher's note

Supplementary material

The Supplementary Material for this article can be found online at: https://www.frontiersin.org/articles/10.3389/fphy.2022.969921/full#supplementary-material

References

1. Du A, Li Y, Sun J, Zhang Z, You B, Li Z, et al. Rapid transition of aerosol optical properties and water-soluble organic aerosols in cold season in fenwei plain. *Sci Total Environ* (2022) 829:154661. doi:10.1016/j.scitotenv.2022.154661

2. Arroyo PC, David G, Alpert PA, Parmentier EA, Ammann M, Signorell R. Amplification of light within aerosol particles accelerates in-particle photochemistry. *Science* (2022) 376:293–6. doi:10.1126/science.abm7915

3. Zhang Y, Chen Y, Lei Z, Olson NE, Riva M, Koss AR, et al. Joint impacts of acidity and viscosity on the formation of secondary organic aerosol from isoprene epoxydiols (iepox) in phase separated particles. *ACS Earth Space Chem* (2019) 3: 2646–58. doi:10.1021/acsearthspacechem.9b00209

4. Lam HK, Xu R, Choczynski J, Davies JF, Ham D, Song M, et al. Effects of liquid–liquid phase separation and relative humidity on the heterogeneous oh oxidation of inorganic–organic aerosols: Insights from methylglutaric acid and ammonium sulfate particles. *Atmos Chem Phys* (2021) 21:2053–66. doi:10.5194/acp-21-2053-2021

5. Pye HOT, Murphy BN, Xu L, Ng NL, Carlton AG, Guo H, et al. On the implications of aerosol liquid water and phase separation for organic aerosol mass. *Atmos Chem Phys* (2017) 17:343–69. doi:10.5194/acp-17-343-2017

6. Li W, Teng X, Chen X, Liu L, Xu L, Zhang J, et al. Organic coating reduces hygroscopic growth of phase-separated aerosol particles *Environ Sci Technol* (2021) 55:16339–46. doi:10.1021/acs.est.1c05901

7. Petters MD, Kreidenweis SM. A single parameter representation of hygroscopic growth and cloud condensation nucleus activity. *Atmos Chem Phys* (2007) 7: 1961–71. doi:10.5194/acp-7-1961-2007

8. Altaf MB, Dutcher DD, Raymond TM, Freedman MA. Effect of particle morphology on cloud condensation nuclei activity. *ACS Earth Space Chem* (2018) 2: 634–9. doi:10.1021/acsearthspacechem.7b00146

9. Freedman MA. Liquid–liquid phase separation in supermicrometer and submicrometer aerosol particles. *Acc Chem Res* (2020) 53:1102–10. doi:10.1021/acs.accounts.0c00093

10. Mikhailov EF, Pöhlker ML, Reinmuth-Selzle K, Vlasenko SS, Krüger OO, Fröhlich-Nowoisky J, et al. Water uptake of subpollen aerosol particles: Hygroscopic growth, cloud condensation nuclei activation, and liquid–liquid phase separation. *Atmos Chem Phys* (2021) 21:6999–7022. doi:10.5194/acp-21-6999-2021

11. You Y, Smith ML, Song M, Martin ST, Bertram AK. Liquid–liquid phase separation in atmospherically relevant particles consisting of organic species and inorganic salts. *Int Rev Phys Chem* (2014) 33:43–77. doi:10.1080/0144235X.2014.890786

12. Freedman MA. Phase separation in organic aerosol. *Chem Soc Rev* (2017) 46: 7694–705. doi:10.1039/C6CS00783J

13. Kwamena N-OA, Buajarern J, Reid JP. Equilibrium morphology of mixed organic/inorganic/aqueous aerosol droplets: Investigating the effect of relative humidity and surfactants. *J Phys Chem A* (2010) 114:5787–95. doi:10.1021/jp1003648

14. Reid JP, Dennis-Smither BJ, Kwamena N-OA, Miles REH, Hanford KL, Homer CJ. The morphology of aerosol particles consisting of hydrophobic and hydrophilic phases: Hydrocarbons, alcohols and fatty acids as the hydrophobic component. *Phys Chem Chem Phys* (2011) 13:15559–72. doi:10.1039/C1CP21510H

15. Stewart DJ, Cai C, Nayler J, Preston TC, Reid JP, Krieger UK, et al. Liquid–liquid phase separation in mixed organic/inorganic single aqueous aerosol droplets *J Phys Chem A* (2015) 119:4177–90. doi:10.1021/acs.jpca.5b01658

16. Ishizaka S, Yamamoto C, Yamagishi H. Liquid–liquid phase separation of single optically levitated water–ionic liquid droplets in air. *J Phys Chem A* (2021) 125:7716–22. doi:10.1021/acs.jpca.1c06130

17. Pöhlker C, Wiedemann KT, Sinha B, Shiraiwa M, Gunthe SS, Smith M, et al. Biogenic potassium salt particles as seeds for secondary organic aerosol in the amazon. *Science* (2012) 337:1075–8. doi:10.1126/science.1223264

18. You Y, Renbaum-Wolff L, Carreras-Sospedra M, Hanna SJ, Hiranuma N, Kamal S, et al. Images reveal that atmospheric particles can undergo liquid–liquid phase separations. *Proc Natl Acad Sci U S A* (2012) 109:13188–93. doi:10.1073/pnas.1206414109

19. Lee HD, Morris HS, Laskina O, Sultana CM, Lee C, Jayarathne T, et al. Organic enrichment, physical phase state, and surface tension depression of nascent core–shell sea spray aerosols during two phytoplankton blooms. *ACS Earth Space Chem* (2020) 4:650–60. doi:10.1021/acsearthspacechem.0c00032

20. Weber RJ, Guo H, Russell AG, Nenes A. High aerosol acidity despite declining atmospheric sulfate concentrations over the past 15 years. *Nat Geosci* (2016) 9: 282–5. doi:10.1038/ngeo2665

21. Song S, Gao M, Xu W, Shao J, Shi G, Wang S, et al. Fine-particle ph for beijing winter haze as inferred from different thermodynamic equilibrium models. *Atmos Chem Phys* (2018) 18:7423–38. doi:10.5194/acp-18-7423-2018

22. Liu M, Huang X, Song Y, Tang J, Cao J, Zhang X, et al. Ammonia emission control in China would mitigate haze pollution and nitrogen deposition, but worsen acid rain. *Proc Natl Acad Sci U S A* (2019) 116:7760–5. doi:10.1073/pnas.1814880116

23. Jia S, Chen W, Zhang Q, Krishnan P, Mao J, Zhong B, et al. A quantitative analysis of the driving factors affecting seasonal variation of aerosol ph in guangzhou, China. *Sci Total Environ* (2020) 725:138228. doi:10.1016/j.scitotenv.2020.138228

24. Angle KJ, Crocker DR, Simpson RMC, Mayer KJ, Garofalo LA, Moore AN, et al. Acidity across the interface from the ocean surface to sea spray aerosol. *Proc Natl Acad Sci U S A* (2021) 118:e2018397118. doi:10.1073/pnas.2018397118

25. Zhang B, Shen H, Liu P, Guo H, Hu Y, Chen Y, et al. Significant contrasts in aerosol acidity between China and the United States. *Atmos Chem Phys* (2021) 21: 8341–56. doi:10.5194/acp-21-8341-2021

26. Dallemagne MA, Huang XY, Eddingsaas NC. Variation in ph of model secondary organic aerosol during liquid–liquid phase separation. *J Phys Chem A* (2016) 120:2868–76. doi:10.1021/acs.jpca.6b00275

27. Losey DJ, Parker RG, Freedman MA. Ph dependence of liquid–liquid phase separation in organic aerosol. *J Phys Chem Lett* (2016) 7:3861–5. doi:10.1021/acs.jpclett.6b01621

28. Losey DJ, Ott E-JE, Freedman MA. Effects of high acidity on phase transitions of an organic aerosol. *J Phys Chem A* (2018) 122:3819–28. doi:10.1021/acs.jpca.8b00399

29. Zhou Q, Pang S-F, Wang Y, Ma J-B, Zhang Y-H. Confocal Raman studies of the evolution of the physical state of mixed phthalic acid/ammonium sulfate aerosol droplets and the effect of substrates. *J Phys Chem B* (2014) 118:6198–205. doi:10.1021/jp5004598

30. Tong Y, Fang T, Liu Y, Zhao D, Ye A. Research on hygroscopicity and volatility of single aerosol droplet. *J Atmos Environ Opt* (2020) 15:486–95. doi:10.3969/j.issn.1673-6141.2020.06.008

31. Tong Y-K, Liu Y, Meng X, Wang J, Zhao D, Wu Z, et al. The relative humidity-dependent viscosity of single quasi aerosol particles and possible implications for atmospheric aerosol chemistry. *Phys Chem Chem Phys* (2022) 24:10514–23. doi:10.1039/D2CP00740A

32. Ma S, Chen Z, Pang S, Zhang Y. Observations on hygroscopic growth and phase transitions of mixed 1, 2, 6-hexanetriol∕(NH<sub>4</sub>)<sub>2</sub>SO<sub>4</sub> particles: Investigation of the liquid–liquid phase separation (LLPS) dynamic process and mechanism and secondary LLPS during the dehumidificationso$_4$ particles: Investigation of the liquid–liquid phase separation (llps) dynamic process and mechanism and secondary llps during the dehumidification. *Atmos Chem Phys* (2021) 21:9705–17. doi:10.5194/acp-21-9705-2021 (nh$_4$)$_2$

33. Gorkowski K, Beydoun H, Aboff M, Walker JS, Reid JP, Sullivan RC. Advanced aerosol optical tweezers chamber design to facilitate phase-separation and equilibration timescale experiments on complex droplets. *Aerosol Sci Technology* (2016) 50:1327–41. doi:10.1080/02786826.2016.1224317

34. Gorkowski K, Donahue NM, Sullivan RC. Emerging investigator series: Determination of biphasic core–shell droplet properties using aerosol optical tweezers. *Environ Sci : Process. Impacts* (2018) 20:1512–23. doi:10.1039/C8EM00166A

35. Gorkowski K, Donahue NM, Sullivan RC. Aerosol optical tweezers constrain the morphology evolution of liquid-liquid phase-separated atmospheric particles. *Chem* (2020) 6:204–20. doi:10.1016/j.chempr.2019.10.018

36. Sullivan RC, Boyer-Chelmo H, Gorkowski K, Beydoun H. Aerosol optical tweezers elucidate the chemistry, acidity, phase separations, and morphology of atmospheric microdroplets. *Acc Chem Res* (2020) 53:2498–509. doi:10.1021/acs.accounts.0c00407

37. Preston TC, Reid JP. Determining the size and refractive index of microspheres using the mode assignments from mie resonances. *J Opt Soc Am A* (2015) 32:2210–7. doi:10.1364/JOSAA.32.002210

38. Mellouki A, Wallington TJ, Chen J. Atmospheric chemistry of oxygenated volatile organic compounds: Impacts on air quality and climate. *Chem Rev* (2015) 115:3984–4014. doi:10.1021/cr500549n

39. Zhang Y, Chen Y, Lambe AT, Olson NE, Lei Z, Craig RL, et al. Effect of the aerosol-phase state on secondary organic aerosol formation from the reactive uptake of isoprene-derived epoxydiols (iepox). *Environ Sci Technol Lett* (2018) 5:167–74. doi:10.1021/acs.estlett.8b00044

40. Kucinski TM, Dawson JN, Freedman MA. Size-dependent liquid–liquid phase separation in atmospherically relevant complex systems. *J Phys Chem Lett* (2019) 10:6915–20. doi:10.1021/acs.jpclett.9b02532

frontiers | Frontiers in Physics

TYPE Mini Review
PUBLISHED 19 August 2022
DOI 10.3389/fphy.2022.970450

OPEN ACCESS

EDITED BY
Yanhui Wang,
Institute of Quantum Electronics,
School of Electronics, Faculty of
Information and Engineering Science,
Peking University, China

REVIEWED BY
Zehuang Lu,
Huazhong University of Science and
Technology, China

*CORRESPONDENCE
Aimin Zhang,
zhangam@nim.ac.cn

SPECIALTY SECTION
This article was submitted to Atomic and
Molecular Physics,
a section of the journal
Frontiers in Physics

RECEIVED 15 June 2022
ACCEPTED 12 July 2022
PUBLISHED 19 August 2022

CITATION
Wang Y, Lin Y, Gao Y and Zhang A
(2022), Traceability of optical frequency
to SI second via UTC(NIM).
Front. Phys. 10:970450.
doi: 10.3389/fphy.2022.970450

Traceability of optical frequency to SI second *via* UTC(NIM)

Yuzhuo Wang, Yige Lin, Yuan Gao and Aimin Zhang*

National Institute of Metrology (NIM), Beijing, China

Absolute frequency measurement of an optical clock is a milestone towards the redefinition of second in the International System of Units. This work summarizes briefly the measurement of frequency ratio between an optical clock and the second, applying the frequency comparison link from UTC(NIM) to International Atomic Time. Some strategies and suggestions are proposed to reduce the uncertainty introduced by the measurement system and dead time, which guided the frequency measurement of three optical clocks at 10^{-16} level in the past 3 years.

KEYWORDS

optical frequency, dead time, SI second, time and frequency, metrology, optical clock

Introduction

Since 1967, the second of the International System of Units (SI) is defined according to the 9,192,631,770 Hz hyperfine transition of ^{133}Cs. Currently, Cesium fountain clocks realize the second to an accuracy of 10^{-16}. It is the most precisely measured unit among the SI units. However, in the last decade, optical frequency standards have achieved accuracies of 10^{-18} or even 10^{-19} [1, 2]. The International Committee for Weights (CIPM) recommends a roadmap for the redefinition of SI second using optical transition [3]. In preparation, the absolute frequency of an optical clock (OC) needs to be accurate to 10^{-16} level. Measuring directly the frequency ratio between an OC and a cesium fountain clock imposes very high demands on local cesium fountain clocks, of which only a few in the world have this capability. Hence, in recent years, some laboratories in the world have performed another scheme, tracing the optical frequency to the International Atomic Time (TAI) to get absolute frequency of an optical clock [4–8].

In China, more than 10 OCs of different types are being developed at several research institutes. At the National Institute of Metrology (NIM), the cesium fountain clock NIM5 with an uncertainty of 9×10^{-16} reports regularly to the International Bureau of Weights and Measures (BIPM) [9]. With its successor NIM6, the uncertainty has been improved to 5.8×10^{-16}. Nevertheless, both are currently unavailable for high-level ($<5 \times 10^{-16}$) precision measurements. We focus on the second feasible scheme, tracing an optical frequency to the SI second using the frequency comparison link from real-time realization of the Coordinated Universal Time (UTC) UTC(NIM) to TAI.

Fundamental scheme

Compared with absolute frequency measurements of an OC obtained directly using a cesium fountain clock, the method discussed below is slightly complicated. Its remarkable advantage is that the measurement uncertainty is no longer limited by the performance of the local cesium fountain clock or even whether such a clock is needed. The traceability link (Figure 1) contains five key nodes: an OC, a local flywheel oscillator (LFO), UTC(NIM), TAI, and SI second definition (SI s). Four procedures are used to measure the frequency ratios between any pair of consecutive nodes. A femtosecond optical frequency comb system measures the frequency ratio of the optical and the microwave frequencies, which originate from the OC and LFO. A dual mixer time difference (DMTD) system is used to measure the frequency difference between multiple hydrogen masersand the reference UTC(NIM). It is therefore the preferred solution of measuring the frequency ratio of a LFO and UTC(NIM). Meanwhile, we maintain remote frequency comparison links by satellite to participate in the TAI cooperation, and to keep time and frequency comparison with the cooperative partners in China. The frequency ratio of the UTC(NIM) and TAI are taken from Circular T, a monthly publication of the BIPM. It uses the weighted average of clock readings to calculate monthly the Échelle Atomique Libre (EAL) from more than 400 atomic clocks in worldwide, and then generate the TAI by steering the EAL frequency to the weighted average frequency of available primary and secondary frequency standards (PSFS) maintained in a few countries. Similarly, the fractional frequency deviation between TAI and the SI second is also published in Circular T, which should be currently the best time reference.

If an OC can continuously run over a complete 1-month period of TAI reporting, its absolute frequency may be evaluated using

$$\frac{y_{\mathrm{OC}}}{y_{\mathrm{SI\,s}}} = \frac{y_{\mathrm{OC}}}{y_{\mathrm{LFO}}} \times \frac{y_{\mathrm{LFO}}}{y_{\mathrm{UTC(NIM)}}} \times \frac{y_{\mathrm{UTC(NIM)}}}{y_{\mathrm{TAI}}} \times \frac{y_{\mathrm{TAI}}}{y_{\mathrm{SI\,s}}}, \tag{1}$$

where y_{OC} and $y_{\mathrm{SI\,s}}$ are respectively the OC frequency and the SI second definition (specifically, 1 Hz), and y_{LFO}, $y_{\mathrm{UTC(NIM)}}$, and y_{TAI} represent respectively the frequencies of the LFO, UTC(NIM), and TAI. In practice, however, the continual running of an OC over a 1-month reporting period is still difficult because of its inherent principle of operation and the state-of-the-art technology. On the right-hand side of Eq. 1, the four factors (the measured frequency ratios) may have potential dead times, implying

$$\begin{aligned}\frac{y_{\mathrm{OC}}}{y_{\mathrm{SI\,s}}} &= \frac{y_{\mathrm{OC}}(\Delta t_1)}{y_{\mathrm{LFO}}(\Delta t_1)} \times \frac{y_{\mathrm{LFO}}(\Delta t_1)}{y_{\mathrm{LFO}}(\Delta t_2)} \times \frac{y_{\mathrm{LFO}}(\Delta t_2)}{y_{\mathrm{UTC(NIM)}}(\Delta t_2)} \\ &\times \frac{y_{\mathrm{UTC(NIM)}}(\Delta t_2)}{y_{\mathrm{UTC(NIM)}}(\Delta t_3)} \times \frac{y_{\mathrm{UTC(NIM)}}(\Delta t_3)}{y_{\mathrm{TAI}}(\Delta t_3)} \times \frac{y_{\mathrm{TAI}}(\Delta t_3)}{y_{\mathrm{TAI}}(\Delta t_4)} \\ &\times \frac{y_{\mathrm{TAI}}(\Delta t_4)}{y_{\mathrm{SI\,s}}(\Delta t_4)},\end{aligned} \tag{2}$$

where Δt_i ($i = 1, 2, 3, 4$) denote the live measurement time intervals for the four frequency ratios to be measured (Eq. 1, right-hand side). Figure 2 shows a schematic of the live measurement time intervals and dead times between the

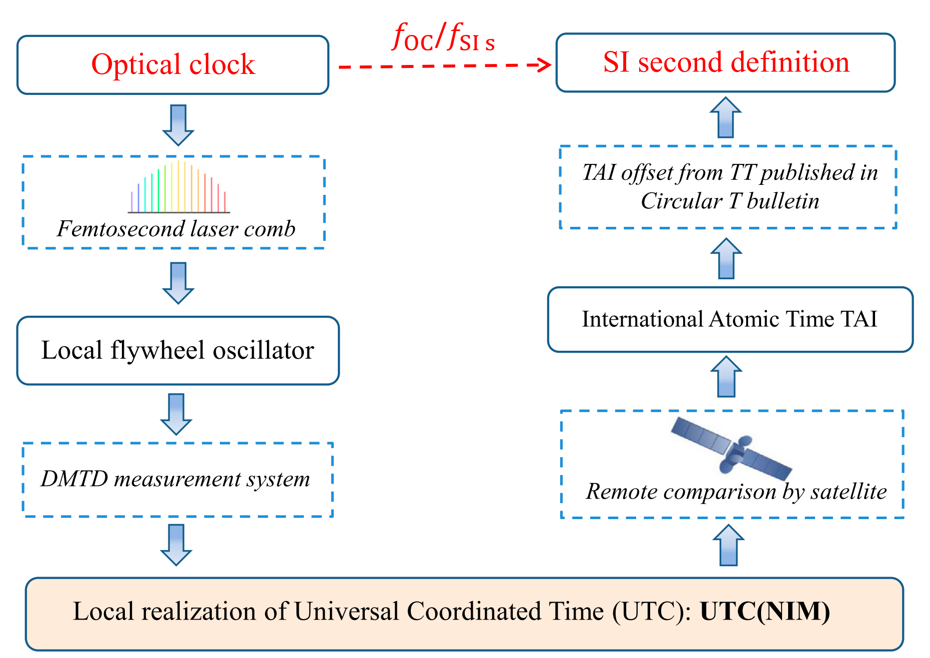

FIGURE 1
Schematic of optical frequency traceability.

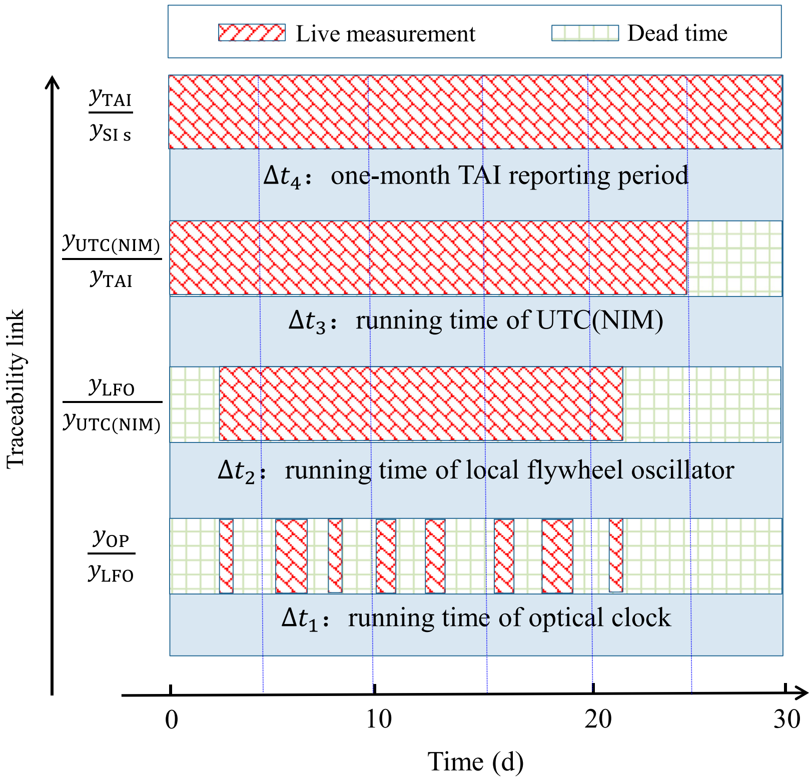

FIGURE 2
Time allocations of live measurements and dead times.

traceability link from the OC frequency to the SI second definition (SI s) *via* the LFO and UTC(k). In principle, we may not need the LFO in this traceability link. Due to its robustness is stronger than that of the UTC(NIM), the hydrogen maser as an LFO is widely used to the traceability of the OC frequency to the SI definition of second.

Measurement of four frequency ratios

Measuring the four frequency ratios appearing in Eq. 1 are key parts in tracing the OC frequency to the SI definition of second by UTC(NIM). Any one ratio measurement contributes to the uncertainty of the final result, specifically, the OC absolute frequency. Each method of measurement as well as its corresponding uncertainty is discussed below.

Femtosecond optical frequency comb

The microwave frequency (10 MHz or 100 MHz) originating from a LFO (in general, a high-performance hydrogen maser) is first synthesized to a higher frequency, which is the frequency reference for the measured OC frequency. Second, the femtosecond optical frequency comb measures accurately the frequency deviation from the higher frequency to the OC frequency. Such frequency ratios between the OC and the LFO may be calculated directly using the frequency deviation. The uncertainty introduced by a femtosecond optical frequency comb may be negligible compared to the 1-part-in-10^{16} accuracy for the frequency ratio measurement. Note that depending on the specific scheme, the microwave frequency distribution and synthesis may introduce a certain uncertainty, which is generally estimated to be close to a few parts in 10^{16} in this measurement.

Dual mixer time difference measurement system

The multi-channel measurement system (TSC MMS, Symmetricom, United States) is based on the DMTD measurement principle and is used in our time keeping laboratory. From the technical specifications, the Allan deviation of the system noise is less than 3×10^{-13} with an averaging time of 1 s. Up until the averaging-time closure of 10^4 s, the Allan deviation theoretically achieves 3×10^{-17}, which is satisfactory for our optical frequency measurements. In contrast, if measurement times are shorter than 10^4 s, the uncertainty with 10^{-16} level could be introduced to measurement result.

Remote comparison by satellite

A physical time scale UTC(NIM) is compared continuously with TAI *via* a time-and-frequency transfer link *via* satellite. BIPM collects clock readings and time comparison data at 5-day intervals from time laboratories around the world and then calculates the monthly UTC. With a delay of 30–45 days, BIPM publishes in the *Circular T* bulletin the time difference between the UTC(NIM) and UTC for the 5-day intervals over the last month. The difference reflects the mean frequency difference between the UTC(NIM) and TAI resulting from having only a difference attributed to a leap second between them. The relationship between the uncertainty associated with frequency transfer and averaging time is reported in detail in reference [10]. Specifically, a ~30-day comparison achieves an uncertainty of ~2×10^{-16} corresponding to a minimum of u_A 0.3 ns.

Fractional frequency deviation of international atomic time relative to SI second

TAI is a realization of Terrestrial Time (TT), a coordinate time with scale unit the SI second in the geocentric reference system [11]. The fractional frequency deviation of TAI relative to TT is published in *Circular T* bulletin monthly. Its uncertainty is generally ~2×10^{-16}, which depends on the number of available primary and secondary frequency standards and the uncertainty of each in that period.

Strategies to reduce the uncertainty introduced by dead times

The absolute frequency measurement of an OC is only at several parts in 10^{16} because of the current performance of cesium fountain clocks. The dead time in this measurement should be rigorously considered because almost all OCs operate only in the intermittent mode, which could introduce the uncertainty of a few parts in 10^{16}. We have focused on using a 1-month TAI reporting period (30 days in general) to complete the absolute frequency measurement and achieve an uncertainty of a few parts in 10^{16}. The continuous running time of the OC is generally much shorter than 30 days (Figure 2). In this traceability link, the uncertainty contributed by live measurements has been considered in the above section. The duration of the dead time in each four-frequency-ratio measurement is closely related to the uncertainty of the final result. In addition, the frequency noise of the LFO, UTC(NIM), and TAI is the main contributor to the uncertainty. In general, the frequency stability of the above-mentioned three in turn become better. Here, Δt_1 is the sum of all running time segments of the OC obtained in actual operations. The total running time of the LFO Δt_2 corresponds to the start- and end-times of the OC and is set to minimize the uncertainty for the frequency ratio $\frac{y_{\mathrm{LFO}}(\Delta t_1)}{y_{\mathrm{LFO}}(\Delta t_2)}$ in Eq. 2. Similarly, Δt_3 is the minimum range covering Δt_2, and its endpoints must satisfy the 5-day interval reported in the *Circular T* bulletin. Finally, Δt_4 is the 1-month TAI reporting period of possibly 30 days.

A more accurate absolute frequency measurement of the OC may be performed based on the above strategy to minimize the uncertainty introduced by dead times. To enhance the measurement capability further, no suitable ideas have been found for TAI and UTC(NIM) because they are relatively unalterable and more complex to perform. The two feasible strategies given below are helpful in optical frequency measurements.

Increasing the operation time of optical clock

In a 1-month TAI reporting period, increasing the operation rate of the OC shortens dead times in the measurements of $\frac{y_{\mathrm{OC}}}{y_{\mathrm{LFO}}}$. In addition, data from more measurements of the fractional frequency difference between OC and LFO are significant in generating more accurate evaluations of noise characteristics of the LFO. Using a weighted method to combine the various measurement results from different 1-month TAI reporting periods is also an optional solution.

Enhancing the frequency stability of local flywheel oscillator

At the fixed operation rate of an OC over a 1-month TAI reporting period, improving the frequency stability of LFO has an extraordinary effect to reduce the uncertainty introduced by measurement dead time between LFO and OC. In our works, the noise model of hydrogen maser as LFO is evaluated accurately by fitting its frequency stability curve respect to sampling time. The short-term frequency stability of hydrogen maser was evaluated by referring to the optical clock based on a continuous measurement period. The middle-term frequency stability was obtained by comparing two identical type hydrogen masers using DMTD system. The long-term frequency stability was measured using UTC as the reference. Therefore, combining several hydrogen masers as a combined LFO will enhance its frequency stability, meanwhile it could be also helpful to decrease the frequency drift of the LFO.

TABLE 1 Uncertainty of optical frequency traceability link.

No.	Ratio	Uncertainty (10^{-16})		
		Transportable Ca$^+$ optical clock [12]	A compact, transportable Ca$^+$ optical clock [13]	^{87}Sr optical clock [14]
1	$\frac{y_{\mathrm{OC}}(\Delta t_1)}{y_{\mathrm{LFO}}(\Delta t_1)}$	2.5	4.6	0.7
2	$\frac{y_{\mathrm{LFO}}(\Delta t_1)}{y_{\mathrm{LFO}}(\Delta t_2)}$	1.3	1.3	1.6
3	$\frac{y_{\mathrm{LFO}}(\Delta t_2)}{y_{\mathrm{UTC(NIM)}}(\Delta t_2)}$	<0.1	<0.1	<0.1
4	$\frac{y_{\mathrm{UTC(NIM)}}(\Delta t_2)}{y_{\mathrm{UTC(NIM)}}(\Delta t_3)}$	0	0	0
5	$\frac{y_{\mathrm{UTC(NIM)}}(\Delta t_3)}{y_{\mathrm{TAI}}(\Delta t_3)}$	2.8	1.7	2.0
6	$\frac{y_{\mathrm{TAI}}(\Delta t_3)}{y_{\mathrm{TAI}}(\Delta t_4)}$	3.6	0	0
7	$\frac{y_{\mathrm{TAI}}(\Delta t_4)}{y_{\mathrm{SI\,s}}(\Delta t_4)}$	1.5	1.4	1.5
Total		5.56	5.26	3.05

Applications

Applying the proposed method, the absolute frequencies of three optical clocks, including two Ca$^+$ optical clocks developed by Innovation Academy for Precision Measurement Science and Technology of Chinese Academy of Sciences (APM) [12, 13], and a ^{87}Sr optical clock developed by NIM [14], were measured at 10^{-16} level in the past 3 years.

The uncertainty details of traceability link about these optical clock are listed in Table 1. In these three measurements, the uptime rates of three optical clocks are respectively ~75% over 20-day period, ~92% over 35-day period and ~56% over 30-day period. Total running time of optical clock is recorded as Δt_1, and then we deliberately arranged $\Delta t_2 = \Delta t_3$ to avoid introducing uncertainty in UTC(NIM) extrapolation, therefore the uncertainty attributed to the fourth term $\frac{y_{\mathrm{UTC(NIM)}}(\Delta t_2)}{y_{\mathrm{UTC(NIM)}}(\Delta t_3)}$ is always zero. The time interval Δt_4 is determined according to the Circular T bulletin corresponding to each measurement time period. In our measurement, Δt_4 is respectively 35 days (Circular T 385), 35 days (Circular T 396) and 30 days (Circular T 391). Both the capability of femtosecond optical frequency comb and dispersion of measurement data are main contributors to the uncertainty of frequency ratio measurement between the OC and the LFO. There is significant difference in the uncertainty of the first term $\frac{y_{\mathrm{OC}}(\Delta t_1)}{y_{\mathrm{LFO}}(\Delta t_1)}$ due to different comb used in each measurement. The noise model of hydrogen maser (VCH-1013M) as LFO used in three measurements were evaluated with DMTD and comb measurement data. The 100 numerical simulated masers according to above the noise model were used to calculate the uncertainty of dead time. In addition, evaluating frequency drift of the maser introduce also a certain uncertainty of the second term $\frac{y_{\mathrm{LFO}}(\Delta t_1)}{y_{\mathrm{LFO}}(\Delta t_2)}$. Due to higher uptime rates of optical clocks, the uncertainty attributed to dead time is smaller in three measurements, but it is still main contributor to final measurement result. Frequency comparison between hydrogen maser and UTC(NIM) is continuously performed using DMTD method, since the uncertainty of that can be ignored ($<1 \times 10^{-17}$). In the Circular T with no. 385, 396 and, 391, the uncertainty u_{A} of the time difference between the UTC(NIM) and TAI is 0.3 ns, attributing to satellite time and frequency transfers. It leads to the uncertainty of the fifth term is 2.8×10^{-16} corresponding to Δt_3 = 20 days, 1.7×10^{-16} corresponding to Δt_3 = 35 days and 2.0×10^{-16} corresponding to Δt_3 = 30 days, respectively. When $\Delta t_3 \neq \Delta t_4$, the extrapolation uncertainty of TAI frequency average over time peirod Δt_3 to Δt_4 need to be evaluated using the above maser frequency extrapolation method. In the first measurement, the uncertainty is 3.6×10^{-16} corresponding to TAI extrapolation 15 days. The uncertainty of the last term $\frac{y_{\mathrm{TAI}}(\Delta t_4)}{y_{\mathrm{SI\,s}}(\Delta t_4)}$ can be directly found in Circular T bulletin.

Summary

Realizing absolute frequency measurements of an OC at low 10^{-16} level remains a challenging task for most research groups. Due to performance limitations in local cesium fountain clocks at NIM, applying the frequency comparison link between UTC(NIM) and TAI to measure precisely the optical frequency is currently a more feasible scheme. This work expressed the principle of absolute frequency measurement, and proposed several strategies to reduce the uncertainty introduced by the measurement system and dead time, according to our practical experience of absolute frequency measurement of three optical clocks at 10^{-16} level.

Author contributions

All authors listed have made a substantial, direct, and intellectual contribution to the work and approved it for publication.

Funding

This research was funded by the National Key R&D Program of China with grant no. 2021YFB3900701 and 2021YFF0600102 and the National Science Foundation of China with grant no. 61905231.

Acknowledgments

The authors would like to thank Professor Yiqiu Wang for his long-term support and guidance to the time and frequency research work of NIM, especially for his effective advises on the reconstruction of UTC(NIM) at NIM new campus. Currently UTC(NIM) has been operating continuously and stably, the work presented in this paper is one of its applications. We sincerely wish Professor Wang a happy 90th birthday.

Conflict of interest

The authors declare that the research was conducted in the absence of any commercial or financial relationships that could be construed as a potential conflict of interest.

Publisher's note

Reference

1. Brewer SM, Chen JS, Hankin AM, Clements ER, Leibrandt DR, Wineland D, et al. Al^{+27} quantum-logic clock with a systematic uncertainty below 10^{-18}. *Phys Rev Lett* (2019) 123:033201. doi:10.1103/physrevlett.123.033201

2. Huang Y, Zhang B, Zeng M, Hao Y, Zhang H, Guan H, et al. *A liquid nitrogen-cooled* Ca^+ *optical clock with systematic uncertainty of* 3×10^{-18} (2021). doi:10.21203/rs.3.rs-333884/v1

3. Riehle F, Gill P, Arias F, Robertsson L. The CIPM list of recommended frequency standard values: Guidelines and procedures. *Metrologia* (2018) 55: 188–200. doi:10.1088/1681-7575/aaa302

4. Hachisu H, Ido T. Intermittent optical frequency measurements to reduce the dead time uncertainty of frequency link. *Jpn J Appl Phys* (2015) 54:112401. doi:10.7567/jjap.54.112401

5. Lodewyck J, Bilicki S, Bookjans E, Robyr JL, Shi C, Vallet G, et al. Optical to microwave clock frequency ratios with a nearly continuous strontium optical lattice clock. *Metrologia* (2016) 53:1123–30. doi:10.1088/0026-1394/53/4/1123

6. Dubé P, Bernard JE, Gertsvolf M. Absolute frequency measurement of the $^{88}Sr^+$ clock transition using a GPS link to the SI second. *Metrologia* (2017) 54:290–8. doi:10.1088/1681-7575/aa5e60

7. Pizzocaro M, Bregolin F, Barbieri P, Rauf B, Levi F, Calonico D, et al. Absolute frequency measurement of the$^1S^0$-$^3F^0$ transition of ^{171}Yb with a link to international atomic time. *Metrologia* (2020) 57:035007. doi:10.1088/1681-7575/ab50e8

8. Kim H, Heo MS, Park CY, Yu DH, Lee WK. Absolute frequency measurement of the ^{171}Yb optical lattice clock at KRISS using TAI for over a year. *Metrologia* (2021) 58:055007. doi:10.1088/1681-7575/ac1950

9. Fang F, Li M, Lin P, Chen W, Liu N, Lin Y, et al. NIM5 Cs fountain clock and its evaluation. *Metrologia* (2015) 52:454–68. doi:10.1088/0026-1394/52/4/454

10. Panfilo G, Parker TE. A theoretical and experimental analysis of frequency transfer uncertainty, including frequency transfer into TAI. *Metrologia* (2010) 47: 552–60. doi:10.1088/0026-1394/47/5/005

11. Arias EF, Panfilo G, Petit G. Timescales at the BIPM. *Metrologia* (2011) 48: S145–53. doi:10.1088/0026-1394/48/4/s04

12. Huang Y, Zhang H, Zhang B, Hao Y, Gao K. Geopotential measurement with a robust, transportable Ca^+ optical clock. *Phys Rev A* (2020) 102:050802. doi:10.1103/PhysRevA.102.050802

13. Cao J, Yuan J, Wang S, Zhang P, Yuan Y, Liu D, et al. A compact, transportable optical clock with 1×10^{-17} uncertainty and its absolute frequency measurement. *Appl Phys Lett* (2022) 120:054003. doi:10.1063/5.0079432

14. Yige L, Q W, Fei M, Cao S, Wang Y, Ye L, et al. A ^{87}Sr optical lattice clock with 2.9×10^{-17} uncertainty and its absolute frequency measurement. *Metrologia* (2021) 58:035010. doi:10.1088/1681-7575/abf33e

Frontiers | Frontiers in Physics

TYPE Original Research
PUBLISHED 24 August 2022
DOI 10.3389/fphy.2022.956719

OPEN ACCESS

EDITED BY
Hendrick L. Bethlem,
VU Amsterdam, Netherlands

REVIEWED BY
Bin Jian,
National Research Council Canada
(NRC-CNRC), Canada
Ben Edward Sauer,
Imperial College London,
United Kingdom

*CORRESPONDENCE
Jinjun Feng,
fengjinjun@tsinghua.org.cn

SPECIALTY SECTION
This article was submitted to Atomic and
Molecular Physics,
a section of the journal
Frontiers in Physics

RECEIVED 30 May 2022
ACCEPTED 29 July 2022
PUBLISHED 24 August 2022

CITATION
Chen H, Yan Y, Chen J and Feng J
(2022), Design of optically pumped
cesium beam tube with hexapole
magnetic system for longer lifetime and
better SNR.
Front. Phys. 10:956719.
doi: 10.3389/fphy.2022.956719

Design of optically pumped cesium beam tube with hexapole magnetic system for longer lifetime and better SNR

Haijun Chen[1], Yufei Yan[1], Jingbiao Chen[2] and Jinjun Feng[1]*

[1]National Key Laboratory of Science and Technology on Vacuum Electronics, Beijing Vacuum Electronics Research Institute, Beijing, China, [2]State Key Laboratory of Advanced Communication System and Networks, School of Electronics, Institute of Quantum Electronics, Peking University, Beijing, China

In order to get a better tradeoff between the long lifetime and high performances of cesium beam atomic clocks, we proposed a design scheme of compact optically pumped cesium beam tube (OPCBT) based on hexapole magnetic focusing (HMF) system for the confinement of cesium. A practical optically pumped cesium beam tube without HMF system has been implemented and tested with high-stability laser by modulation transfer spectroscopy (MTS), and a signal-to-noise ratio (SNR) of 18,000 in 1 Hz bandwidth and Allan deviation of $2 \times 10^{-12}/\sqrt{\tau}$ were obtained. Based on this test, the simulation analysis results of the newly designed tube with HMF show that the predicted lifetime can reach over 20 years without degradation of the performances, and the expected frequency stability of the clock can be $6.5 \times 10^{-13}/\sqrt{\tau}$ with a lifetime of 10 years.

KEYWORDS

compact atomic clock, optically pumped, cesium beam tube, hexapole magnetic focusing, long lifetime, signal-to-noise ratio

Introduction

Continuous atomic beams help to reduce the long-term frequency drift of atomic clocks [1–3]. As a reproduction device of the “definition of seconds”, cesium beam atomic clocks have a wide range of applications, for example, in time keeping, high-speed communication, navigation and fundamental research [4, 5]. As a core device, the cesium beam tube which provides a high vacuum environment for the generation of atomic beams and the interaction of radiation fields with atoms is the most important part affecting the performance and lifetime of cesium beam atomic clocks. For large primary cesium clocks in the laboratory, high performance and long life can be achieved together with big size [6–8]. For example, the resonance width of 62 Hz was obtained in NIST-7, served as the primary time and frequency standard in 1990s, with a Ramsey cavity length of 1.55 m [9–11]. And lifetime can be prolonged through increasing the use of more cesium in the Cs sources or timely supplement of Cs.

However, the length of Ramsey cavity in compact cesium clocks is less than 0.2 m, and the line width is generally around 350–800 Hz [12–14]. Therefore, increasing the atomic beam flux and thus improving the SNR is the most common way to improve the frequency stability of the Cs beam clocks. Unfortunately, the increase in cesium consumption shortens the lifetime of the Cs beam tubes [14]. For example, the compact magnetic state-selected cesium atomic clocks have a 10-years lifetime with the Standard Long-Life Cs Beam Tubes and a 5-years lifetime with the high-performance tubes whose consumption of atoms are large caused by high Cs oven temperature of about 130°C. Compact optically pumped cesium clocks with high atomic utilization have a lifetime of more than 10 years while ensuring high performance. To a certain extent, there has been a better tradeoff between performance and lifetime through optimization. However, the ultra-high-performance cesium clocks together with longer lifetime are expected in some application scenarios such as time keeping [15]. On the other hand, there is also the demand for cesium clocks with ultra-long lifetime of more than 20 years without performance degradation in satellites.

In this paper, commercial OPCBT are shown and tested with the high-stability laser by MTS. The obtained performances are the SNR of 18,000 in 1 Hz bandwidth and the Allan deviation of $2 \times 10^{-12}/\sqrt{\tau}$. While maintaining such high performances, the predicted tube lifetime of 10 years can be guaranteed. The influences of cesium oven temperature on SNR and line width are analyzed. Based on these, a design scheme of compact optically pumped cesium beam tube with HMF system is proposed. Using cesium beam magnetic focusing technology [16, 17], the atomic utilization rate of OPCBT can be further increased by about 9.5 times. The simulation results of the designed Cs beam tubes that with HMF were presented, and the predicted lifetime can reach over 20 years without performance degradation. The expected frequency stability will reach $6.5 \times 10^{-13}/\sqrt{\tau}$ with a lifetime of 10 years. Finally, the challenges that may be encountered in engineering were also discussed.

Experiment on optically pumped cesium beam tube without hexapole magnetic focusing

One type of OPCBT without HMF has been manufactured in BVERI and over 200 tubes have been delivered to our customers and used in Cs beam clocks. The Cs beam tube is composed of Cs oven, Ramsey cavity, magnetic coil, magnetic shield, fluorescence detector, micro ion pump and vacuum shell. The size of the tube is 395 mm × 107 mm × 90 mm. The Cs oven has 200 micro-pores with a depth-to-diameter ratio (DDR) of 60 for the atom emission with a typical working temperature of 100°C. The distance between the two arms of Ramsey cavity is 165.8 mm, and the fluorescence collection efficiency was up to 80% in the reflective fluorescence detector.

The Cs atoms from the heated oven have the ground states of $|F = 3>$ and $|F = 4>$, and are then prepared to $|F = 3>$ by the pumping laser in the region between the oven and the microwave cavity. Those Cs atoms with the state of $|F = 3, m_F = 0>$ will have a transition chance to the state of $|F = 4, m_F = 0>$ through the interaction with the microwave field in the Ramsey cavity. Subsequently, atoms populated on the state of $|F = 4, m_F = 0>$ are detected by the laser probe. The fluorescence excited by the atoms will be converted to a current by the photodetector as frequency offset signal of the Cs beam clocks.

The overall configuration and diagram of the compact optically pumped cesium beam atomic clock based on the tube are shown in Figure 1. In order to reduce the laser frequency noise [18], a high-stability narrow-linewidth 852 nm laser by MTS was used in the experiments. The laser frequency for detection was locked to $|F = 4> \rightarrow |F' = 5>$ cycling transition, and the pumping laser was obtained by frequency shifting 251 MHz via an acousto-optic modulator (AOM), the corresponding energy level is shown in Figure 2A. The intensities of the detection laser and pumping laser are 0.7 mW/cm^2 and 3.3 mW/cm^2, respectively.

The microwave signal applied to the Ramsey cavity comes from the frequency synthesis of a 10 MHz voltage controlled crystal oscillator (VCXO). Detailed design of the microwave source was descripted in [19]. The Ramsey pattern will be detected when the microwave frequency is tuned around 9192631770 Hz corresponding to the transition of ground state $|F = 3, m_F = 0>$ to $|F = 4, m_F = 0>$, as shown in Figure 2B. Linewidth, SNR and figure of merit are the most important indicators of cesium beam tubes, and are also the main factors that determine the frequency stability of cesium beam atomic clocks. The linewidth W and signal intensity A can be directly obtained from Figure 2B. Our cesium beam clocks operate at a microwave modulation frequency of 137 Hz, so the noise in 1 Hz bandwidth at 137 Hz of the cesium beam tubes will be measured by a fast Fourier transform (FFT) spectrum analyzer (Stanford Research Systems, SR770). The SNR is obtained by dividing the signal intensity A by noise N. A SNR of 18,000 in 1 Hz bandwidth was obtained when the Cs oven was operated at the typical temperature of 100°C. It is important to note that the microwave input to the cesium beam tubes is set to a spot frequency of 9192631770 Hz when measuring noise. The figure of merit F that characterizes the comprehensive performance of the tubes is defined by [1].

$$F = \sqrt{\frac{C + A}{2C + A}} \cdot \frac{SNR}{W} \cdot \sqrt{\Delta f}$$

Where A is signal intensity, C is the valley or minimum voltage measured adjacent to the peak, as shown in Figure 2B, Δf is the bandwidth when measuring noise, in this case 1 Hz. Signal intensity, SNR, linewidth, and figure of merit were tested

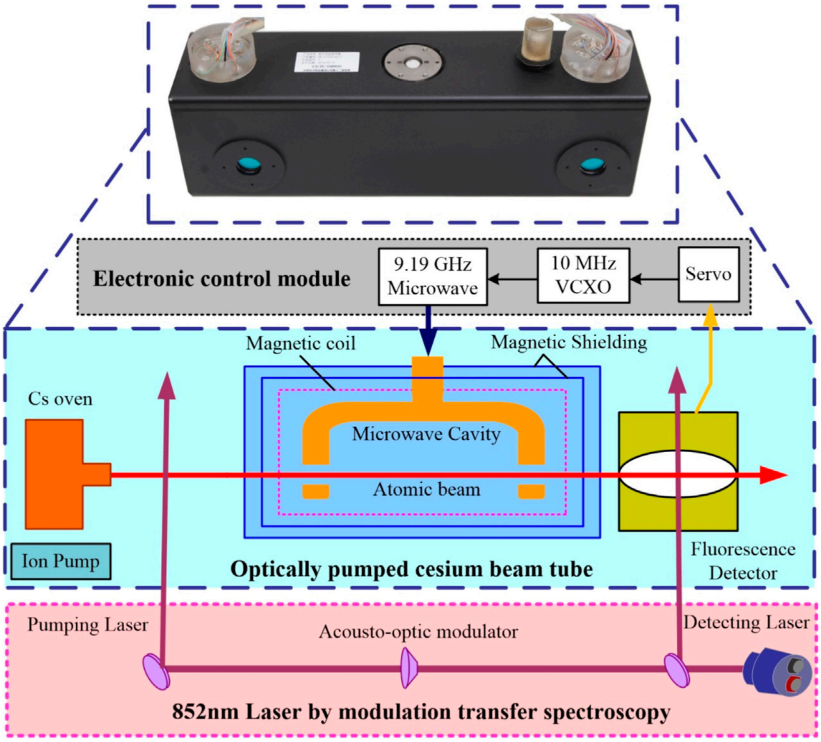

FIGURE 1
Overall configuration of the compact optically pumped cesium beam atomic clock. The cyan box is the diagram of the practical OPCBT made in BVERI, and the photograph is shown as above. The pink box is the 852 nm laser by MTS. The gray box is the electronic control module.

separately at different oven temperatures, as shown in Figures 2C,D. The curves fitted with the polynomial functions give the trend of these data with oven temperature.

As the Cs oven temperature rises from 70 to 130°C, the signal intensity rises exponentially. At the same time, the increase of the oven temperature means a large consumption of cesium and a significant reduction in the lifetime of Cs beam tubes. However, the growth of the SNR in 1 Hz bandwidth gradually slowed down and is shown in Figure 2C. This may be caused by useless atoms that are not absorbed by graphite getters. The linewidth of the central fringe increases linearly with the increase of the oven temperature, while the figure of merit F increase gradually, as shown in Figure 2D. It can be seen that constantly increased temperature does not keep the performance rising, but makes the life drop rapidly.

After modulating and demodulating the Ramsey fringes, an error signal is produced to lock the frequency of the 10 MHz VCXO. The output of the clock is also derived from the 10 MHz VCXO. Comparing with the 10 MHz sine output of a Hydrogen maser (VREMYA-CH, VCH-1003M, option L) by a high-performance phase noise and Allan deviation test set (Microsemi, 5120A), the Allan deviation of the compact optically pumped cesium beam atomic clock based on the tube without HMF is measured to be $2 \times 10^{-12}/\sqrt{\tau}$, as shown in Figure 3. The Allan deviation of the Hydrogen maser comes from the calibration certificate of The National Institute of Metrology, China, which is better than the nominal value provided by the manufacturer.

According to the 8 g of cesium loaded in the oven and the typical working temperature of 100°C, the lifetime of the tubes without HMF is estimated to be more than 10 years. Although this has not been fully verified, some tubes have been running continuously for 9 years and show stable operation without any degradation of the performances.

Design of hexapole magnetic focusing for optically pumped cesium beam tubes

As is known, the cesium atomic beam emitted from the micro-hole array of oven is divergent, and most of the atoms are not utilized efficiently, and some even become the source of noise. Therefore, based on the above test results, reducing the oven temperature and increasing the atomic utilization rate is critical for improving the performance and lifetime. On the basis of the practical OPCBTs, a new tube that would realize a high flux of cesium atomic beam at low oven temperature has been

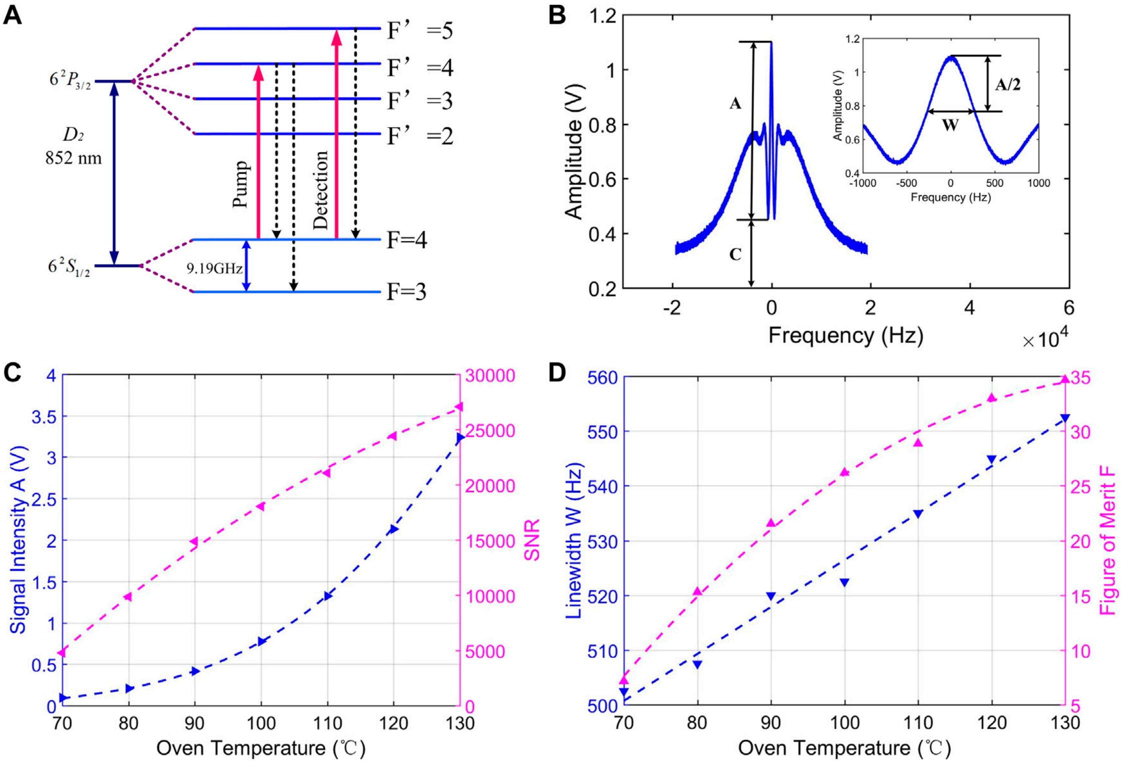

FIGURE 2
Energy levels and experimental results of OPCBT without HMF. **(A)** Relevant energy levels of cesium, |F = 4>→|F' = 5> is cycling transition. **(B)** Ramsey fringes of the microwave clock transition, |F = 3, m_F = 0>→ |F = 4, m_F = 0>. **(C)** Measured signal intensity A (blue triangles) and SNR (purple triangles) in 1 Hz bandwidth at the Cs oven temperature of 70–130°C. **(D)** Measured linewidth W (blue triangles) and Figure of merit F (purple triangles) at the Cs oven temperature of 70–130°C.

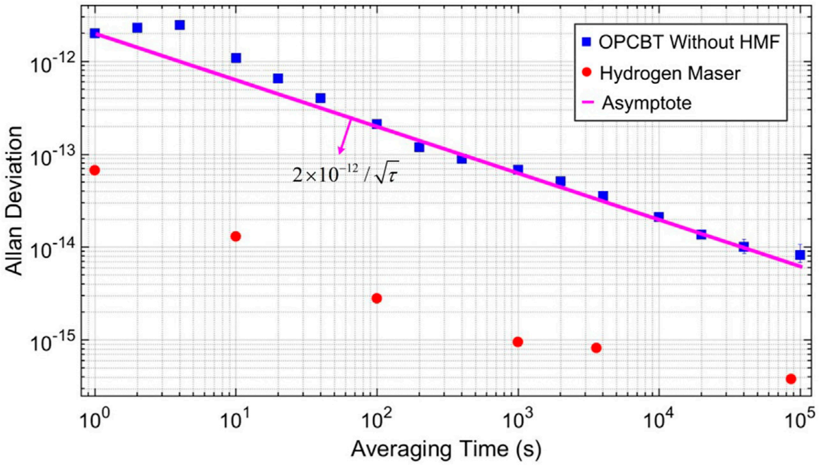

FIGURE 3
Allan deviation of the compact Cs beam clock based on the OPCBT without HMF (blue squares). The purple-solid line is the asymptote fitted with $2\times10^{-12}/\sqrt{\tau}$. Red circles are the frequency instability of the reference Hydrogen maser.

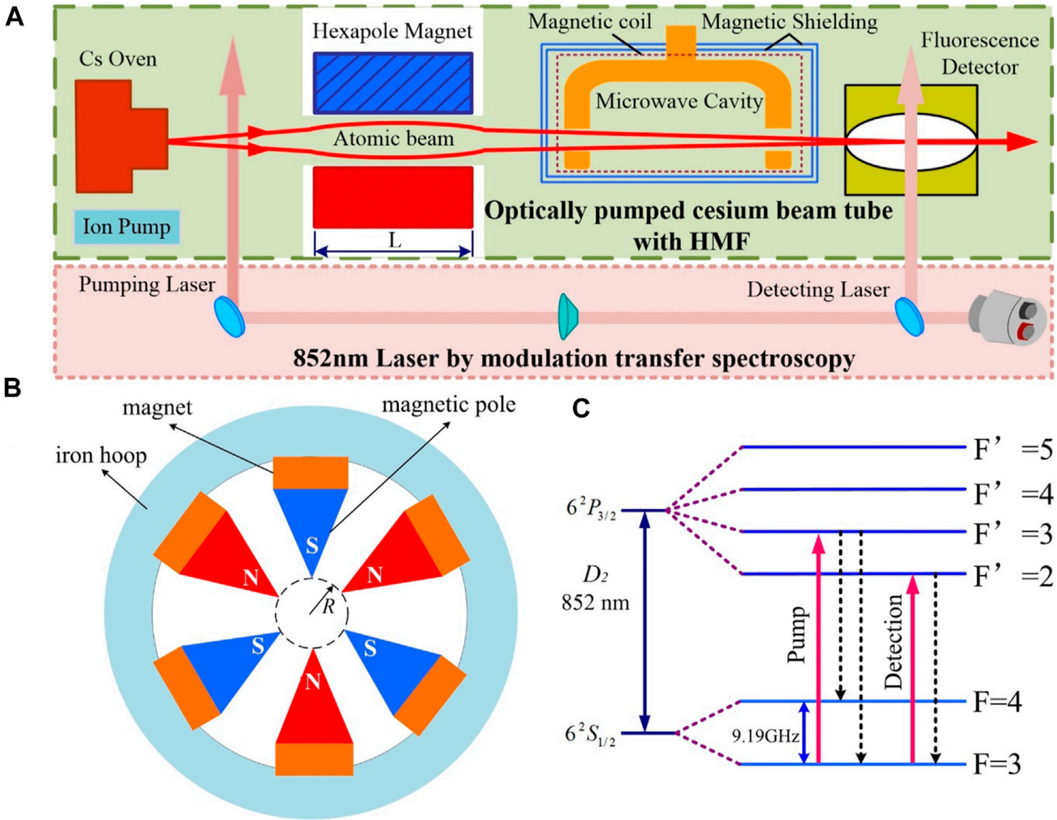

FIGURE 4
Energy levels and overall approach of OPCBT based on HMF. **(A)** The green box is the diagram of OPCBT with HMF system, L is the length of the hexa-pole magnets. The pink box is the 852 nm laser by MTS. **(B)** The cross-section of the HMF system, R is the bore radius of the hexa-pole magnets. **(C)** Relevant energy levels of cesium, |F = 3>→|F' = 2> is cycling transition.

designed. Figure 4 shows the overall approach, where two main measures are used to achieve the goals of "the low temperature operation of the Cs oven" and "the generation of high atomic beam flux".

First, the DDR of the micro-pores for emitting atoms is increased from 60 to 100, which will reduce the divergence angle of the atomic beam and improve the atomic utilization rate. Limited by the magnetic field space inside the dipole magnetic state-selected cesium beam tube, the shape of the emission cross-section of the atomic beam is usually designed to be rectangular to form a sheet beam. In fact, although the shape of the emission cross-section is only limited by the laser beam diameter and the cutoff waveguide size of the microwave cavity in the OPCBT, the rectangular section is still used in the first generation of products considering the versatility of the cesium oven. In this protocol, a cross-section of emitted Cs atomic beam is nearly a square.

Second, a HMF system was added between the pumping area and the microwave cavity, as shown in Figure 4A. The HMF can confine the |F = 4 > atoms of large emission angles, which is similar to that a convex lens converges light. From the 1960s to the 1980s, the HMF system was studied to achieve the separation of cesium atoms with different energy states in the magnetic state-selected cesium beam clock [20–22], but was not ultimately chosen in compact cesium clocks. However, the HMF plays a new role of focusing the |F = 4 > atoms with a large divergence angle into the microwave cavity in this scheme. The cross-section of the HMF system is shown in Figure 4B.

It is important to note that only the cesium atoms of |F = 4 > state can be focused by the HMF, while those of |F = 3 > state are divergent. Therefore, in order to prepare the cesium atoms to |F = 4 > state, the pumping laser frequency will be locked to |F = 3>→|F' = 3 > transition. In the microwave cavity region, a small magnetic field of about 0.06 G is applied to separate the state of |F = 4, m_F = 0>. The clock transition |F = 4, m_F = 0>→|F = 3, m_F = 0 > will occurs under the excitation of the microwave. To obtain as much atomic fluorescence as possible, the detecting laser frequency will be locked to |F = 3>→|F' = 2 > cycling transition, as shown in Figure 4C. It is worth noting that the locked frequency of the pumping and detecting lasers with 852 nm used here are different from the conventional optically pumped cesium beam frequency standards.

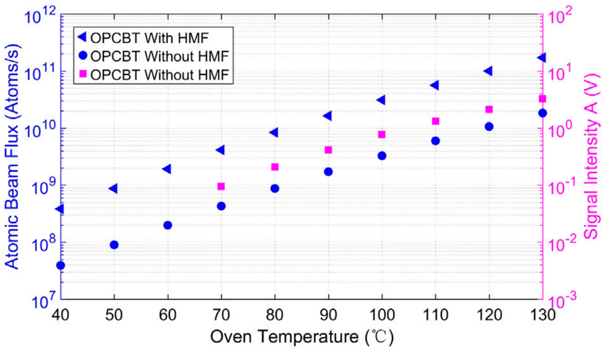

FIGURE 5
The calculated atomic beam flux of $|m_F = 0>$ in OPCBT with HMF (blue triangles) and OPCBT without HMF (blue circles). The measured signal intensity of OPCBT without HMF (purple squares).

The beam flux of those Cs atoms with the state of $|m_F = 0>$ in the detecting region determines the signal intensity and the maximum SNR of OPCBT. The atomic beam flux in the detecting region of the OPCBT without HMF at temperatures from 40 to 130°C are calculated and shown together with the measured signal intensity of the OPCBT without HMF at temperatures from 70 to 130°C in Figure 5. It can be seen that the trend of signal intensity with oven temperature is consistent with that of atomic beam flux. Therefore, calculating the atomic beam flux in the detecting region can intuitively reflect the improvement effect of HMF on the OPCBT. We have developed a dedicated code to simulate the atomic trajectories and optimize various parameters such as the magnetic induction B at the pole cone end, the length L and the bore radius R of the hexa-pole magnets. Taking the maximum number of atoms that can reach the detecting region per second as the goal, the influence of various parameters was analyzed. Simulation model, magnet structure, magnetic field distributions, atomic trajectories, and parameter optimization processes were described in detail in our other paper [16]. Briefly, on the basis of fully considering the space size inside the existing Cs beam tube, a set of optimized parameters, L = 20mm, R = 3.2mm, B = 2.6T, was obtained. The materials of the magnets are Sm2Co17, and the materials of the magnetic poles are DT8A iron.

The calculated atomic beam flux in the detecting region of the OPCBT with HMF at temperatures from 40 to 130°C are also shown in Figure 5. According to the calculation results, the same beam flux can be achieved at about 70°C in the new design, compared with 100°C in the current tube without HMF. Combined with the test results of Figure 2, the line width is expected to be narrowed to about 500 Hz, and the life expectancy will reach 20 years without changing the amount of cesium loaded in the oven. At the same operating temperature of 100°C, the signal intensity of the new tube with HMF will be about 9.5 times higher than that of the first generation tube. And when the laser by MTS is used for pumping and detecting on the new tube, the expected Allan deviation of the new compact clock will reach $6.5 \times 10^{-13}/\sqrt{\tau}$.

In order to directly measure the increase in atomic utilization, an experiment is designed with a HMF system outside the vacuum shell of a conventional slightly longer OPCBT. And the test experiments will be carried out after the assembled tube is finished soon.

Discussion

Although the HMF has brought about an improvement in the utilization of atoms, its strong magnetic field may destroy the uniformity of the C field located in the microwave cavity region, which is used to separate the $|F = 4, m_F = 0>$ magnetic sublevels. The OPCBT shown in Figure 2 has installed two layers of permalloy magnetic shields around the microwave cavity, but it can only ensure the uniformity of the C field when the ambient magnetic field is not greater than 2 Gauss. Combining the feasible scheme for shielding strong magnetic fields in the dipole magnetic state-selected cesium beam tube, a magnetic shield using industrial pure iron is designed to reduce the leakage of the hexapole magnetic field. In practice, other surrounding materials may interfere with the effect of shielding, which requires attention in experiments.

Scattered light entering the microwave cavity will cause frequency shift, which has always been a challenge for the optically pumped cesium beam atomic clocks [23]. The HMF system separates the laser pumping region and the microwave cavity, which can reduce the light frequency shift to a certain extent. The specific value of light frequency shift will be evaluated in the follow-up experimental.

In addition, calculations show that atoms with an emission angle of less than 3.95° will be detected, compared to those with a much smaller angle of 0.92° without the hexapole magnetic system. A significant increase in atomic utilization means fewer stray atoms, which will help reduce the noise of the Ramsey pattern.

If necessary, increasing the oven temperature to 130°C can achieve the expected frequency stability of $3 \times 10^{-13}/\sqrt{\tau}$, but the tube life will be reduced to 5 years accordingly, which can meet the application needs of some special scenarios.

Conclusion

In summary, we first implement a commercial optically pumped cesium beam tube without HMF. Tested with the high-stability laser by MTS, the SNR of 18,000 in 1 Hz bandwidth were obtained at the typical operating temperature of 100 C. As the oven temperature rises from 70 to 130°C, the variation laws of the signal amplitude, the SNR in 1 Hz bandwidth, the linewidth W and the figure of merit F are tested and analyzed. It can be seen that constantly increasing the temperature does not keep the performance rising, but makes the life drop rapidly. By comparing with a Hydrogen maser, the Allan deviation of the compact optically pumped cesium beam atomic clock based on this type of tubes is measured to be $2 \times 10^{-12}/\sqrt{\tau}$. And according to the 8 g of cesium loaded and the typical working temperature of 100°C, the life expectancy of the compact cesium clock is estimated to be more than 10 years.

Then we proposed a design scheme of OPCBT based on HMF. A dedicated code is programed to simulate the atomic trajectories. Calculations show that the atomic utilization of OPCBT with HMF can be increased by about 9.5 times. This tube can be operated in ultra-long life or ultra-high-performance mode. When the oven temperature is operated at about 70°C, the life expectancy can reach more than 20 years with an Allan deviation of $2 \times 10^{-12}/\sqrt{\tau}$. When at the operating temperature of 100°C, the signal intensity of the new tube with HMF will be about 9.5 times higher than that of the first generation tube, and the expected Allan deviation of the new compact clock will reach $6.5 \times 10^{-13}/\sqrt{\tau}$ with a lifetime of 10 years being acceptable. An OPCBT with a HMF system outside the vacuum shell was designed for direct comparison with the tube without HMF in experiments, and specific experiments will be carried out after it is manufactured. Although magnetic shielding is designed, the effect of possible leakage of magnetic field on C-field and pumping efficiency still needs to be paid attention to in experiments. After the experiment is completed, we will further design the new OPCBT with HMF system inside the vacuum shell and make it a practical tube.

HMF-based OPCBT and MTS-based high-stability laser can greatly improve the performance and lifetime of cesium clocks. The performance of the new compact optically pumped cesium beam atomic clock will be close to that of Hydrogen maser while maintaining a small volume, which will promote the fields such as metrology, timekeeping and space.

Data availability statement

The original contributions presented in the study are included in the article/Supplementary Material, further inquiries can be directed to the corresponding author.

Author contributions

HC: Conceptualization, Methodology,Validation, Formal Analysis, Writing—Original Draft; YY: Data Curation, Software,Visualization, Validation JC: Conceptualization, Writing—Review and Editing JF: Conceptualization, Writing—Review and Editing, Project Administration, Resources, Supervision.

Acknowledgments

We express our most sincere wishes on the occasion of Professor Prof. Yiqiu Wang's 90th birthday. The authors would like to thank Prof. Wang for his selfless help in the development of the optically pumped cesium beam tube. As early as the 1980s, Prof. Wang carried out theoretical and experimental research on the optically pumped cesium beam frequency standard, which laid a solid foundation for our later work. HC sincerely thanks Prof. Wang for many useful discussions on the realization of the optically pumped cesium beam tube based on hexapole magnetic focusing. In order to answer our questions in a timely manner, he often worked late into the night, and we sometimes even received emails from him at 2 a.m. Prof. Wang's rigorous attitude to scientific investigation and diligence in his work motivate us to keep moving forward.

Conflict of interest

The authors declare that the research was conducted in the absence of any commercial or financial relationships that could be construed as a potential conflict of interest.

Publisher's note

References

1. Vanier J, Audoin C. *The quantum Physics of atomic frequency standards*. Bristol: Adam Hilger (1989).

2. Audoin C, Dimarcq N, Giodano V, Viennet J. Physical origin of the frequency shifts in cesium beam frequency standards: Related environmental sensitivity. *IEEE Trans Ultrason Ferroelectr Freq Control* (1992) 39:412–21. doi:10.1109/58.143175

3. Audoin C, Vanier J. Atomic frequency standards and clocks. *J Phys E* (1976) 9: 697–720. doi:10.1088/0022-3735/9/9/001

4. Vanier J, Audoin C. The classical caesium beam frequency standard: Fifty years later. *Metrologia* (2005) 42:S31. doi:10.1088/0026-1394/42/3/s05

5. Marlow BLS, Scherer DR. A review of commercial and emerging atomic frequency standards. *IEEE Trans Ultrason Ferroelectr Freq Control* (2021) 68: 2007–22. doi:10.1109/tuffc.2021.3049713

6. Becker G. Recent progress in primary Cs beam frequency standards at the PTB. *IEEE Trans Instrum Meas* (1976) 25:458–65. doi:10.1109/tim.1976.6312264

7. DeMarchi A, Shirley J, Glaze DJ, Drullinger RE. A new cavity configuration for cesium beam primary frequency standards. *IEEE Trans Instrum Meas* (1988) 37: 185–90. doi:10.1109/19.6049

8. Drullinger RE, Glaze DJ, Lowe L, Shirley JH. The NIST optically pumped cesium frequency standard. *IEEE Trans Instrum Meas* (1991) 40:162–4. doi:10.1109/tim.1990.1032906

9. Drullinger RE, Lowe JP, Glaze DJ, Shirley JH. NIST-7, the new US primary frequency standard. *Proc IEEE Int Freq Control Symp* (1993) 71.

10. Drullinger RE, Shirley JH, Lowe JP, Glaze DJ. Error analysis of the NIST optically pumped primary frequency standard. *IEEE Trans Instrum Meas* (1993) 42: 453–6. doi:10.1109/19.278603

11. Lee WD, Shirley JH, Lowe JP, Drullinger RE. The accuracy evaluation of NIST-7. *IEEE Trans Instrum Meas* (1995) 44:120–3. doi:10.1109/19.377788

12. Huang LY, Chen J, Wang J, Zhang DX. Influence of rod tuner position on resonance frequency of Ramsey cavity in compact cesium atom clock. In: International Conference on Microwave and Millimeter Wave Technology (ICMMT) (2012). p. 1.

13. Mueller LF, Dull DB, Kusters JA. A new high-performance cesium beam tube compensated for Ramsey pulling. In: Proceedings of the 45th Annual Symposium on Frequency Control (1991). p. 554.

14. Hyatt RC, Mueller LF, Osterdock TN. A high-performance beam tube for cesium beam frequency standards. *Hewlett Packard J* (1973) 14:14.

15. Qu LL, Li B, Gao Z. Research on the relation between frequency stability and timekeeping clock allocation. In: 12th IEEE Int. Conf. Electron. Meas. Instrum. (ICEMI) (2015). p. 888.

16. Yan YF, Chen HJ, Pan D, Liu TY, Chen JB, Feng JJ. Enhancing the signal-to-noise ratio in optically pumped cesium beam tubes using a hexapole magnetic system. In: 2021 Joint Conference of the European Frequency and Time Forum and IEEE International Frequency Control Symposium (EFTF-IFCS) (2021). p. 1.

17. Liu TY, Pan D, Chen JB. Optical pumped cesium atomic clock with multi-pole magnet. In: 2020 Joint Conference of the IEEE International Frequency Control Symposium and International Symposium on Applications of Ferroelectrics (IFCS-ISAF) (2020). p. 1.

18. Shang HS, Zhang TY, Miao JX, Shi TT, Pan D, Zhao XW, et al. Laser with 10^{-13} short-term instability for compact optically pumped cesium beam atomic clock. *Opt Express* (2020) 28:6868. doi:10.1364/oe.381147

19. Cao Y, Zhao X, Xie W, Wei Q, Yang L, Chen H, Zhang S. A merchandized optically pumped cesium atomic clock. In: Proceedings of Joint European Frequency and Time Forum and International Frequency Control Symposium (2017). p. 618–21.

20. Emons DA, Rogers PJ. New cesium beam tube utilizing hexapole/double-dipole optics. In: 33rd Annual Symposium on Frequency Control (1979). p. 490.

21. Dorenwendt K. Development and performance of the PTB's CS1 primary clock. *Proc IEEE* (1986) 74:137–40. doi:10.1109/proc.1986.13421

22. Bauch A, Dorenwendt K, Fischer B, Heindorff T, Müller EK, Schröder R. CS2: The PTB's new primary clock. *IEEE Trans Instrum Meas* (1987) 36:613–6. doi:10.1109/tim.1987.6312751

23. Shirley J. Fluorescent light shift in optically pumped cesium standards. In: 39th Annual Symposium on Frequency Control (1985). p. 22.

frontiers | Frontiers in Physics

TYPE Original Research
PUBLISHED 25 August 2022
DOI 10.3389/fphy.2022.971099

EDITED BY
Xuzong Chen,
Peking University, China

REVIEWED BY
Kaikai Huang,
Zhejiang University, China
Yuan Sun,
Shanghai Institute of Optics and Fine Mechanics (CAS), China

*CORRESPONDENCE
Jin He,
frankhe@pku.edu.cn
Yiqun Wei,
weiyq@ier.org.cn
Lianshan Gao,
gaolianshan258@126.com

SPECIALTY SECTION
This article was submitted to Atomic and Molecular Physics,
a section of the journal
Frontiers in Physics

RECEIVED 16 June 2022
ACCEPTED 22 July 2022
PUBLISHED 25 August 2022

CITATION
Wang X, He J, Wang Y, Wang Y, Wang W, Wang W, Li S, Zhu X, Liu G, Liu S, Wang Y, Wang L, Liu Y, Yang T, Cao C, Wei Y, Yue Y, Hu G, Liu Z, Pan Y and Gao L (2022), Construction of optical system for an atomic clock-beyond atomic fountain.
Front. Phys. 10:971099.
doi: 10.3389/fphy.2022.971099

Construction of optical system for an atomic clock-beyond atomic fountain

Xiumei Wang[1,2], Jin He[1]*, Yifei Wang[2], Yunjia Wang[2], Wenming Wang[2], Weili Wang[2], Shiguang Li[2], Xi Zhu[2], Guodong Liu[2], Shuo Liu[2], Ye Wang[2], Liang Wang[2], Yaxuan Liu[2], Tongmin Yang[2], Chunyan Cao[2], Yiqun Wei[3]*, Yutao Yue[3], Guoqing Hu[1], Zhenfeng Liu[4], Yimin Pan[4] and Lianshan Gao[2]*

[1]Shen Zhen SoC Key Laboratory, PKU-HKUST Shen Zhen-Hong Kong Institution, Shenzhen, China, [2]Time-Frequency Research and Development Center, Beijing Institute of Radio Metrology and Measurement, Beijing, China, [3]Peking University Shenzhen Institute, Shenzhen, China, [4]Zhejiang Faraday Laser Technology Co.,Ltd, Wenzhou, China

We demonstrate the construction of the optical system in the atomic clock-beyond atomic fountain based on ^{87}Rb atom. The optical system includes a high-stability laser system and an optical lattice. The high-stability laser system with the new scheme of frequency locking and shift is introduced in detail, which is an important laser source for laser cooling. The optimized frequency and intensity stability are achieved to $4 \times 10^{-14}\boldsymbol{\tau}^{-1/2}$ ($\boldsymbol{\tau}$ is the averaging time) and $4 \times 10^{-5}\boldsymbol{\tau}^{-1/2}$, respectively, which are highly stable. On the basis of the conventional atomic fountain clock, the optical lattice is specially investigated along the direction of gravity and its characteristics are studied systematically. For the optimized and novel exploration, we predict the achievable stability of $3.6 \times 10^{-14}\boldsymbol{\tau}^{-1/2}$ and it has the potential to be improved to $3.6 \times 10^{-15}\boldsymbol{\tau}^{-1/2}$. The realizability of the construction due to the stabilized laser and optical lattice makes the beyond fountain promising candidate for the next-generation high performance microwave atomic clock.

KEYWORDS

laser cooling, cold atom, laser stabilization, optical lattice, atomic fountain clock

1 Introduction

Laser cooling can produce the cold atoms with low temperature and high density, which has been widely used in different fields, such as atomic clocks [1–5], atomic interferometer [6–8], atomic optics [9], Bose-Einstein condensate (BEC) [10, 11], quantum computing [12], quantum communication [13], etc. The atomic clocks can provide the unprecedented precision in the determination of time and the SI second is experimentally determined by measuring the ^{133}Cs hyperfine transition with atomic fountain clocks [14]. However, due to the gravity, the usual coherent interrogation time of the atomic fountain clock reaches around one second. The more longer coherent interrogation time in the atomic fountain clock on Earth seems impractical. However, the cold atoms trapped in the optical traps can be stored with a long lifetime even up to hundreds of seconds with negligible optical scattering and minimal laser-noise-induced heating [15, 16]. Using this method, the optical trapping without affecting the internal energy-level of the atoms is desirable, which is attractive particularly in the atomic fountain clock. Some authors have proposed a novel microwave atomic clock, combining the atomic fountain clock and optical lattice configurations [17, 18]. Compared with the conventional atomic fountain clock, the new microwave atomic clock with higher frequency stability and accuracy can be achieved. This new microwave atomic clock is called beyond atomic fountain clock, which is abbreviated to the "beyond fountain" [17]. In the beyond fountain, not only the coherent interrogation time is increased to improve the frequency stability of 10^{-15} at one second, but also the frequency accuracy of 10^{-15} to 10^{-17} is feasible, due to the dramatic elimination or suppress of the cavity related shifts, the collision shift and the Doppler effect [18]. They have proven that we can attempt to overcome the limitation of coherent interrogation time, when the cold atoms are trapped in the optical lattice. This microwave atomic clock provides an easy way to improve the atomic fountain clock performance by adding a trapping laser beam in the conventional atomic fountain clock without any further complicated modifications. It is still feasible to achieve the microwave atomic clock for ^{87}Rb or ^{133}Cs cold atoms with a high accuracy even though no magic wavelength exists [18], in contrast to the optical lattice clocks employing a dipole trap at a magic wavelength to suppress the differential light shift. Besides, based on the proposal of the beyond fountain, several approaches have been predicted to further suppress the differential light shift, such as magic wavelengths on microwave transitions for Al and Ga [19], the laser traps of particular polarization combined with a specific magnetic field [20, 21] and the cancellation at the expense of a small magnetic-field sensitivity [22].

The beyond fountain has attracted much attention and it is of great practical significance to develop to broaden the field of microwave atomic clock. However, in the beyond fountain, the preparation of cold atoms is primary to provide the atomic medium and the optical lattice is utilized to trap the cold atoms for long coherent interrogation time. On the basis of conventional atomic fountain clock, the beyond fountain can prepare the cold atoms in the magneto-optical trap (MOT) zone directly and the optical lattice can be specially designed with the upward movement of cold atoms. For the cold atoms, the quality of laser frequency locking and the fluctuation of cold atoms number caused by the laser intensity are still problems, because they seriously determine the hyperfine transition of laser cooling and the stability of cold atom number. For the optical lattice, it should be investigated to optically load and trap atoms along the gravity, which coincides with the atomic trajectory from the conventional atomic fountain clock. It is obtained that the construction of the optical system including a high-stability laser system and an optical lattice is very necessary in the beyond fountain, which will meet the laser cooling and optical trapping requirements of cold atoms.

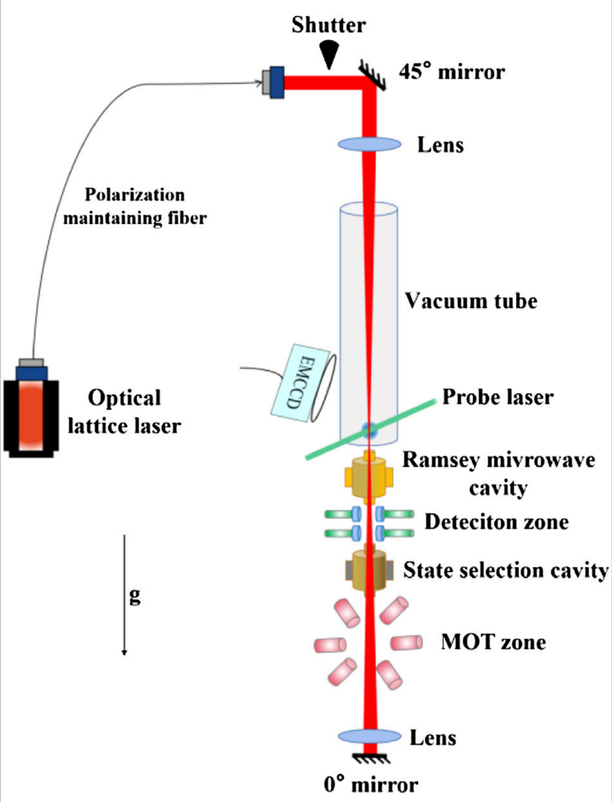

FIGURE 1
The experimental scheme of 1D optical lattice in the physical package of the beyond fountain.

In this paper, the construction of the optical system in the beyond fountain based on ^{87}Rb atom is proposed. The high-stability laser system with the new scheme of frequency locking and shift is introduced in detail, which is an important laser source for laser cooling. In the high-stability laser system, we have built the diode laser with narrow linewidth and measured the optimized frequency and intensity stability. Together with the MOT, the laser system is expected to capture the cold atoms with μK temperature by Doppler and sub-Doppler cooling mechanism. These cold atoms are prepared to be loaded into the optical lattice. On the basis of the conventional atomic fountain clock, the optical lattice is specially investigated along the direction of gravity, which is located above the Ramsey microwave cavity. This engineered scheme can realize the optical lattice and the performance for trapping can be observed directly. It is predicted that the cold atoms can be loaded into the optical lattice by an appropriate time sequence successfully. Thus, the investigation on the construction of the optical system will effectively promote the development of the beyond fountain.

2 Principle

2.1 Physical package of beyond fountain

As shown in Figure 1, we consider an experimental scheme of 1D optical lattice in the physical package of the beyond fountain, which is the combination of atomic fountain clock and optical lattice configurations. In contrast to the complexity of 2D and 3D optical lattices [23], the 1D optical lattice is formed by two counter-propagating laser beams [24–26], which is uncomplicated and can be integrated with the atomic fountain clock along the direction of gravity by the standing wave. Compared with the optical dipole trap (ODT) formed by a traveling wave, the potential well depth at the laser beam waist of the 1D optical lattice is four times larger than the ODT, with the identical laser intensity. The 1D optical lattice can cause the more attractive force for the cold atoms than the ODT, which will contribute the more tightly confining cold atoms. So the 1D optical lattice is chosen over the ODT. To facilitate the integration, the optical lattice laser is injected above the vacuum tube of the atomic fountain clock by an optical cage structure and reflected by the mirror at the bottom of MOT zone. Using the 1D standing wave, the optical lattice can be produced above the Ramsey microwave cavity. The launching cold atoms from the MOT zone can be loaded into the 1D optical lattice and trapped for a long time before releasing. The 1D optical lattice is designed to minimize any structure distortion, which hardly affects the vacuum environment and microwave oscillation. Two optical windows are established at the top of the vacuum tube and the bottom of the MOT zone for the injection and reflection of laser. Several windows are established at the sides of the vacuum tube for the injection of probe laser and the observation of fluorescence from cold atoms in the optical lattice. These optical windows are vacuum sealed and nonmagnetic. An electronic multiple charge coupled device (EMCCD) needs to be installed outside of the vacuum tube to observe the fluorescence from the cold atoms.

In order to load the cold atoms into the optical lattice as much as possible, the potential well depth is predicted to tens of microkelvin temperature and the cold atoms should be cooled to several microkelvin temperature in MOT zone. In addition, we assume that the velocity of cold atoms is almost zero, when the cold atoms reach to the position of optical lattice. That means the cold atoms are loaded under static condition and then trapped in the ultra-high vacuum environment. It is worth noting that the cold atoms launching from the MOT zone should have a good stability to ensure the uniformity of trapped cold atoms in every duty cycle. The coherent interrogation time are mainly determined by the optical lattice depth, the beam waist and the vacuum environment.

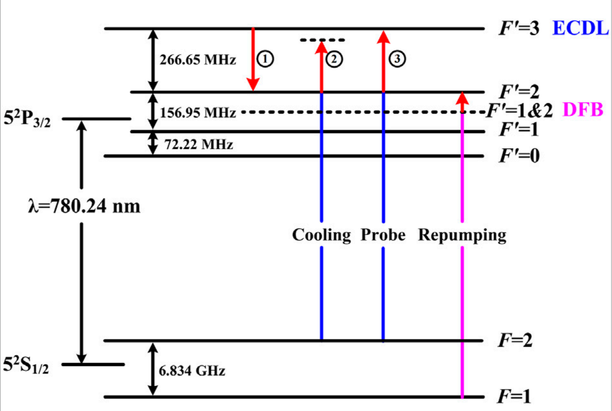

FIGURE 2
The scheme of laser frequency locking and shift for ^{87}Rb.

2.2 The high-stability laser system

2.2.1 Scheme of laser system

In the MOT zone, the laser system including the cooling and repumping light [3, 27, 28] is used in the cold atom experiments. These lights interact with the hyperfine energy level of atoms, so the linewidth of them should be reduced preferably to hundreds of kHz or tens of kHz. The stability of cold atom number are determined by the stability of cooling light, so the cooling light requires the sufficient stability of laser wavelength, single mode and intensity. The factors affecting the laser stability can be divided into the external and internal factors. The external factors include mechanical vibration, temperature, pressure, magnetic field, etc. The internal factors include spontaneous emission, power supply circuit, aging, etc. Therefore, it is very important to reduce the linewidth and improve the laser stability by the locking technology. There are many frequency locking schemes, such as dichroic atomic vapour laser lock (DAVLL) [29], polarization spectroscopy [30], frequency modulation spectroscopy [31], Pound-Drever-Hall (PDH) [32], saturation absorption spectroscopy (SAS) [33] and modulation transfer spectroscopy (MTS) [34]. Among them, the usual SAS modulates the laser frequency by current and the laser frequency is locked by the negative feedback loop, in which the additional laser noise will be introduced to the output laser. Compared with the widely used SAS, the MTS with the external modulation can avoid the modulation disturbance to the output laser. Here, we develop the MTS technology to achieve the frequency stabilization. This technology does not modulate the frequency of the output laser, so it will not bring the additional noise. Besides, the slope of the error signal is large and the background noise is small, which is beneficial for the frequency locking. For the stabilization of laser intensity, in order to achieve the desired performance, it is necessary to select an appropriate device as the feedback actuator and an acousto-optic modulator (AOM) will be suitable.

TABLE 1 The requirement of laser beams in the laser system with^{87}Rb.

Parameters	Cooling	Repumping	Probe
Power/mW	~66	~2	~1
Energy level of D2 line	2→3′	1→2′	2→3′
Detuning	0~-10Γ	0	+0.5Γ
Linewidth	~100 kHz	~1 MHz	~100 kHz

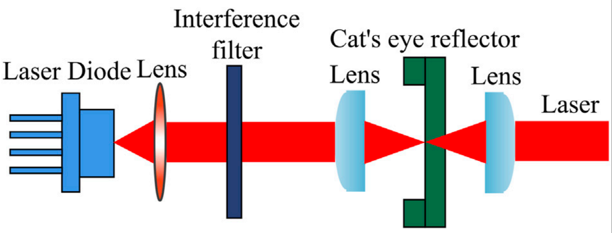

FIGURE 3
The scheme of IF-ECDL.

To achieve the narrow linewidth and improve the stability of laser frequency, the laser system for laser cooling is optimized. As shown in Figure 2, the new scheme of laser frequency locking and shift is proposed. In the scheme, an external cavity diode laser (ECDL) and a distribution feedback Bragg (DFB) laser allow us to minimize the number of laser source and simplify the laser frequency shift processes. The frequency of the ECDL is locked to the ^{87}Rb D2 line F = 2→F' = 3 by MTS and then shifted to form the frequency of the cooling and probe lights simultaneously. One basic light resonant with D2 line F = 2→F' = 2 is formed by the negative frequency shift from the locked frequency of the ECDL. The cooling light (red-detuning of D2 line F = 2→F' = 3) is formed by the positive frequency shift from the basic light. The probe light (near resonance of D2 line F = 2→F' = 3) is also formed by the positive frequency shift from the basic light. The DFB laser offers the repumping light, whose frequency is locked to the D2 line F = 1→F' = 1&2 by SAS. The repumping light is formed by the positive frequency shift from the DFB laser, because its frequency is resonant with D2 line F = 1→F' = 2. The scheme of the optical path with four laser frequency shift processes will be realized by the acoustic-optical modulators (AOMs). In the above process, the expected characteristics of lights in the laser system is shown in Table 1. It is worth noting that the cooling light has different detuning and power in the different laser cooling stage.

2.2.2 IF-ECDL

In the laser system, an interference-filter-type ECDL (IF-ECDL) offers an ultra-narrow interference filter to replace the alignment-sensitive diffraction grating in the conventional Litman-Metcalf-type and Littrow-type [35, 36]. It is easier to achieve the narrow linewidth and the sufficient stability of laser frequency, due to the insensitivity to the pressure, mechanical, thermal strain, etc. As shown in Figure 3, instead of the diffraction grating, a narrow bandwidth interference filter and a cat's eye mirror are placed for wavelength selection and optical feedback, respectively. The emitted light from the laser diode is collimated using an aspheric lens and the collimated beam passes through an interference filter. The collimated beam is then focused on the surface of the cat's eye mirror by an aspheric lens. The piezoactuator having external threads on one side is attached to the cat's eye mirror with a threaded cap. Finally, the output laser is collimated by an additional aspheric lens. All the optical components are integrated and the length of the external cavity is about 73 mm. The output single mode and the laser wavelength are fine-tuned by the voltage applied to the piezoactuator. Not only the output laser with the wavelength 780 nm, the frequency no-hopping range 5–20 GHz and the linear polarization has been obtained, but also the laser linewidth well below 100 kHz has been achieved successfully.

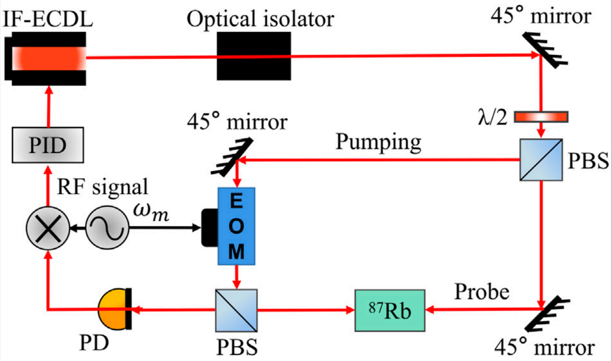

FIGURE 4
The experimental set-up for the frequency stabilization by MTS.

2.2.3 Frequency stabilization

To stabilize the laser frequency of the IF-ECDL, the MTS is applied. Figure 4 shows the experimental set-up for the frequency stabilization by MTS. This modulation transfer is described as an example of four-wave mixing, which only takes place when the sub-Doppler resonance condition is satisfied. This leads to the flat, zero background signal and the position of the zero-crossing always falls on the centre of the sub-Doppler resonance. The IF-ECDL is used to provide the laser at 780 nm with an optical isolator to prevent the laser being reflected back into the IF-ECDL. Two counter-propagating laser beams can be referred as the pumping and probe lights as in SAS [37], and two polarizing beam splitters (PBSs) are utilized to split and then overlap the two lights. A free-space electro-optic modulator (EOM) is driven by an oscillator at the modulation frequency ω_m and applied as the phase modulator to provide the sideband-offset for pumping light. The transmission of the EOM is greater than 98% and its aperture is 3 × 3 mm for easy alignment. The transmitted phase-modulated pumping light can be represented in terms of the carrier and sidebands frequency separated by the modulation frequency ω_m. The phase modulated pumping light and the counter-propagating, unmodulated probe light are aligned through an ^{87}Rb vapour cell. If the interaction of the pumping and probe lights with the atomic vapour are sufficiently nonlinear, the modulation will appear on the unmodulated probe light. After passing through the vapour cell, the probe light is incident on a photo-detector (PD). The sidebands frequency of the probe light generated in the vapour beats with the carried frequency of the probe light to produce an alternating signal at the modulation frequency ω_m. This alternating signal is mixed with the RF signal to generate the MTS signal, and the MTS signal can be used to feedback the IF-ECDL. The size of optical components in Figure 4 has been miniaturized and the optical simplification of the experimental setup is convenient for the integration with the IF-ECDL to be locked.

2.2.4 Power stabilization

To stabilize the laser power of the IF-ECDL, an AOM can be used with an electrical drive signal [38]. It is based on the acousto-optic effect, i.e., the modification of the refractive index of the crystal material by the oscillating mechanical strain of a sound wave. A piezoelectric transducer attached to the crystal obtains a strong oscillating electrical signal from a RF driver and is used to excite a sound wave. The sound wave generates a traveling strain wave in the crystal material. The photo-elastic effect leads to a traveling refractive index grating, at which the light can experience the Bragg diffraction. The angle of Bragg diffraction θ_d can be expressed as

$$\sin\theta_d \approx \theta_d = (\lambda_0/v) f_1 \tag{1}$$

where λ_0 is the wavelength of laser, v is the velocity of sound wave and f_1 is the frequency of sound wave. The Bragg first-order diffraction efficiency η is

$$\eta = I_1/I_T = \sin^2\left[(\pi/\lambda_0)\sqrt{2LM_2P_a/H}\,/2\right] \tag{2}$$

where I_1 is the intensity of the first-order diffracted light, I_T is the intensity of the incident light, L is the length of the acousto-optic interaction, M_2 is the quality factor of the acousto-optic materials, P_a is the power of the sound wave and H is the height of the acousto-optic interaction. It is obtained that the first-order diffraction efficiency η changes with the power of sound wave P_a, that is, as the power of the applied RF signal is varied, the amount of diffracted light varies proportionally. So the AOM can be used as a feedback device, and the intensity of the first-order diffracted light can be controlled by the external signal acting on the RF drive.

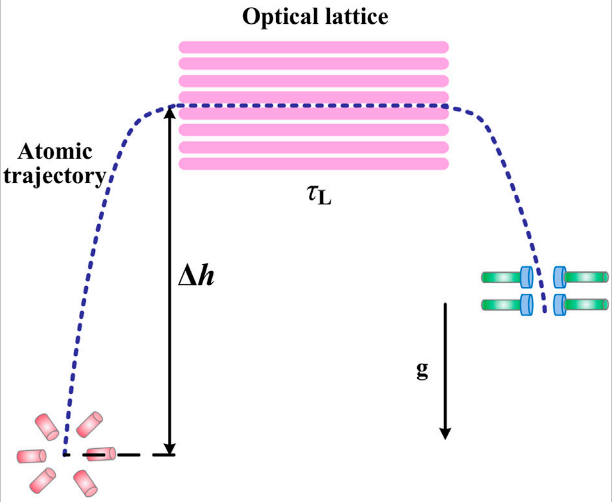

FIGURE 5
Space-time atomic trajectory for loading.

2.3 Optical lattice

2.3.1 Loading

The optical lattice is the periodic dipole trap formed by the opposite laser beams, which is located above the Ramsey microwave cavity. The space-time atomic trajectory for loading is shown in Figure 5. The ^{87}Rb atoms are laser-cooled to about 2 μK, prepared in the D2 line F = 2 state, and then launched into the free fall. After the launch, the atomic trajectory includes the upper half part of MOT zone, selection microwave cavity, detection zone and Ramsey microwave cavity. The launched cold atoms reach the apex after 400 ms of free fall time (corresponding to height from the center of MOT zone to the optical lattice $\Delta h \approx 800$ mm). At the apex, the counter-propagating laser beams are turned on and the cold atoms are loaded into the optical lattice. Then the cold atoms will be stored for a time τ_L. If the cold atoms with kinetic energy lower than the potential well depth, they will be trapped for a long time. Upon turning off the counter-propagating laser beams, the optical lattice will disappear and the cold atoms will be released into the free fall, due to the gravity.

2.3.2 Trapping

Let us consider the two counter-propagating laser beams of linear polarization and of the same wavelength. The potential well depth experienced by the cold atoms U_0 is

$$U_0 = \alpha \frac{4P}{\varepsilon_0 c \pi \omega_0^2}, \tag{3}$$

where P is the laser power, α is the atomic polarizability, ε_0 is the permittivity of vacuum, c is the speed of light and ω_0 is the beam waist. The potential well depth can also be written as

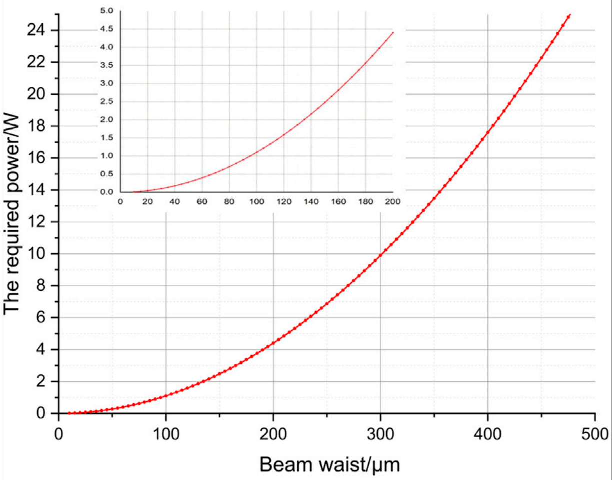

FIGURE 6
The required power versus the beam waist in case of potential well depth U_0 = 20 μK.

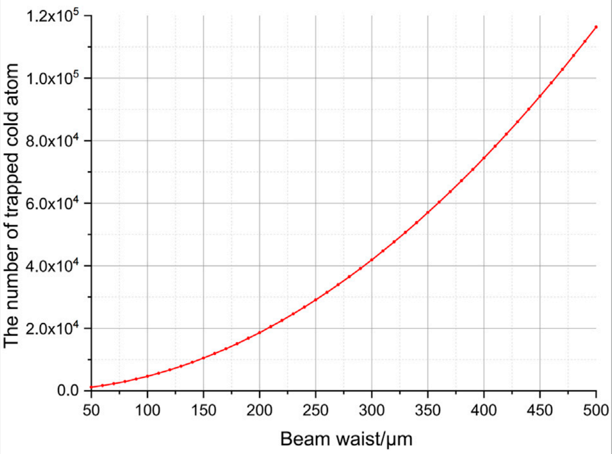

FIGURE 7
The number of trapped cold atom versus the beam waist of the optical lattice.

$$T = \frac{U_0}{\mathrm{k_B}}, \tag{4}$$

where T is the temperature and $\mathrm{k_B}$ is the Boltzmann constant. Here, the temperature of cold atoms is about 2 μK, and the potential depth U_0 will be expected to be about 20 μK, similar to the ^{87}Sr optical lattice clock [26]. It is easy to obtain that $P = 1.1\times 10^8 \omega_0^2$ and Figure 6 shows the required laser power P versus the beam waist ω_0 in case of potential well depth U_0 = 20 μK. It can be seen that the condition of $\omega_0 \geq 100\,\mu$m needs the laser power $P \geq 1$ W, and the condition of $\omega_0 \geq 300\,\mu$m needs the laser power $P \geq 10$ W, in which the laser power are in high Watt-range for diode laser. In this paper, the condition of $\omega_0 \geq 100\,\mu$m is easier to achieve, which will be shown in the next section.

The radius of cold atom cloud in the MOT zone $\sigma(0)$ at time $t_0 = 0$ is assumed to be 1 mm and the total cold atom number is assumed to 1×10^7, so the density of cold atoms in MOT zone n_0 is estimated to 2.4×10^6/mm^3. After launching, the cold atom cloud is expanding gradually at the free fall and its radius $\sigma(t)$ can be expressed as

$$\sigma^2(t) = \sigma^2(0) + (v_{rms} t)^2, \tag{5}$$

where t is time at the free fall and v_{rms} is the velocity of cold atoms (v_{rms} = 14 mm/s corresponding the temperature of cold atoms about 2 μK). Once the cold atoms reach to the apex at time t_1, the radius $\sigma(t_1)$ is increased to 5.7 mm and the density of cold atoms n_L is decreased to 1.3×10^4/mm^3. Some cold atoms will be loaded into the optical lattice at this density. The volume for trapping V_C is determined by the cross volume of the cold atoms and optical lattice at the apex. Therefore, it is necessary to compare the radius of cold atom cloud at the apex $\sigma(t_1)$ and the Rayleigh length $z_R = \pi\omega_0^2/\lambda$. It is calculated that the Rayleigh length is larger than $\sigma(t_1)$, once the beam waist ω_0 is increased to 40 μm. Here, it is expected that the beam waist is at the hundreds of micrometers, so the volume for trapping V_C is determined by the radius of cold atom cloud at the apex $\sigma(t_1)$, not the Rayleigh length z_R. Then the volume for trapping V_C is approximately expressed as

$$\mathrm{V_C} = 2\sigma(t_1)\pi\omega_0^2 \tag{6}$$

and the number of trapped cold atom will take the form

$$N_T = n_L V_C = 2 n_L \sigma(t_1)\pi\omega_0^2. \tag{7}$$

As shown in Figure 7, the larger beam waist leads to the more number of trapped cold atom. However, a large number of cold atom trapped will require much more laser power. Therefore, it is necessary to take the appropriate beam waist and laser power for the optical lattice in the experiment. Under our experimental conditions, it would be proper to take the laser power about P = 1 W, the beam waist about ω_0 = 100 μm and the number of cold atoms will be N_T =4,650.

3 Experimental set-up

3.1 Optical path for laser system

3.1.1 Optical path for laser cooling

Figure 8 shows the schematic diagram of the optical path for laser cooling. Details on the energy level and the specifications of the IF-ECDL have been described in Section 2.2. For the experimental set-up, an IF-ECDL and a DFB laser at the same wavelength 780 nm are applied, whose frequencies are locked to D2 line F = 2→F' = 3 by MTS and D2 line F = 1→F' = 1&2 by

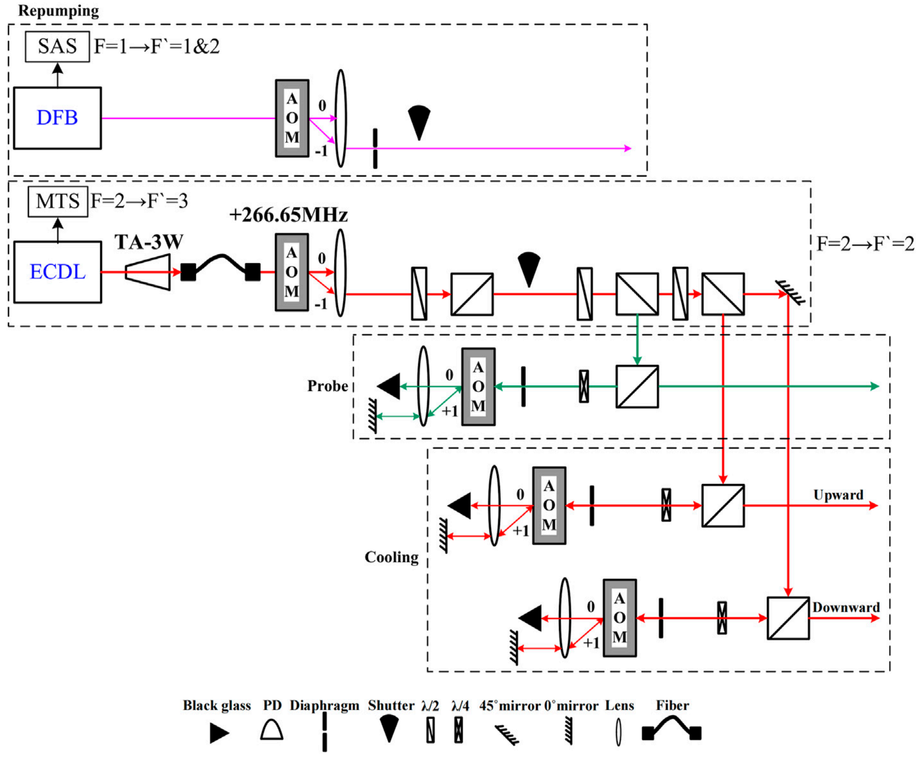

FIGURE 8
The schematic diagram of the optical path for laser cooling.

SAS, respectively. The power IF-ECDL is about 100 mW, which is necessary to be amplified to provide the cooling and probe lights. Considering the difficulty of optical tuning, the power is amplified sufficiently to 3 W and a single-mode polarization-maintaining fiber is applied to introduce the laser beam to the optical bench. After the fiber, the laser beam is collimated and beam diameter is about 1 mm. This laser beam is then shifted to F = 2→F' = 2 by an AOM, which is divided into three lights: one cooling light in the upward direction at the bottom half of MOT zone, one cooling light in the downward direction at the upper half of MOT zone, and one probe light for fluorescence detection. These lights require the different RF frequency and power driving on AOMs for the control of their detuning. In addition, these AOMs allow the laser frequency to be tuned without optical path changing. The repumping light is achieved by the DFB laser and an AOM, which is the usual approach in the atomic fountain clock. Some fiber beam splitters will be applied to introduce these lights to the MOT or detection zone to interact with atoms in the vacuum. All lasers can be continuously monitored by the PD and two mechanical shutters are installed for the time sequence.

3.1.2 Stabilizing laser power

The laser power of IF-ECDL for laser cooling is strongly dependent on the diffraction of AOM, so the AOM is selected as a feedback device for the control of laser power. Figure 9 shows the scheme of stabilizing the laser power with an AOM. The first-order diffraction beam is picked up by a 0° mirror and turned back for the second pass-through of the AOM. Some of them are reflected by a PBS and monitored by the PD in the in-loop. The in-loop signal of the PD is compared to a reference voltage issued from a voltage reference with low noise and low drift. After the

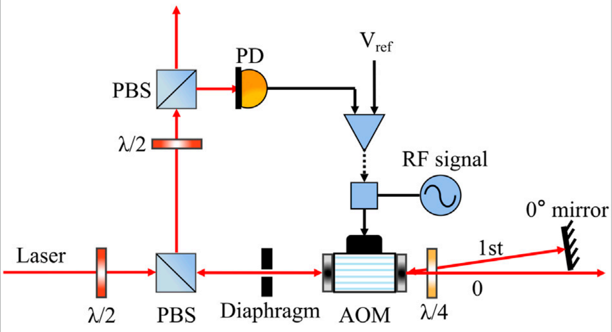

FIGURE 9
The scheme of stabilizing the laser power with an AOM.

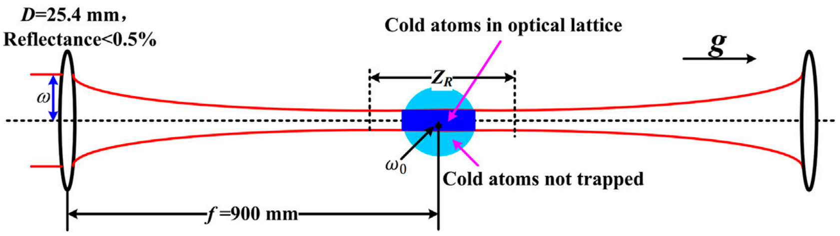

FIGURE 10
The schematic diagram of optical path for optical lattice.

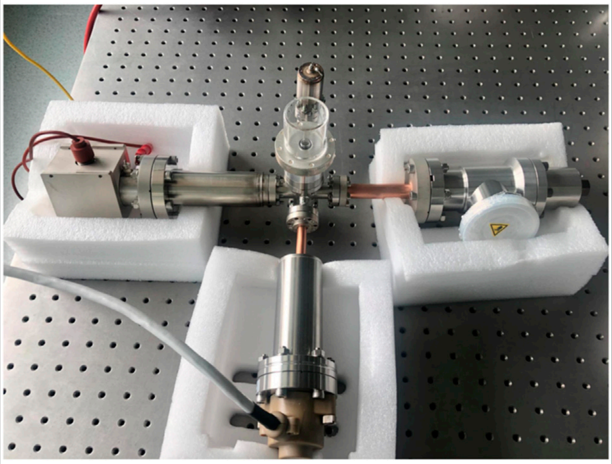

FIGURE 11
The miniaturized vacuum system.

comparison, the error signal shows the difference between the PD signal and the voltage reference and it will be applied to the diffraction efficiency of the AOM. Due to this procedure, the fluctuation of laser power can be decreased.

3.2 Optical path for optical lattice

The optical lattice employs the large red-detuning from resonance to achieve the long trapping time, in which the cold atoms are trapped at antinodes. In our experiment, an amplified tunable diode laser with high power up to 3 W is applied, whose wavelength is 852 nm. After the fiber coupling, the laser power is estimated to be 1 W. We can build the optical lattice with this power value. From Figure 6 and Figure 7, it is obtained that the beam waist is about 100 μm and the number of trapped cold atom is about 4,650. Although the number of trapped cold atom is not large enough for the clock signal, it is still beneficial for loading and observing the cold atoms in the optical lattice. If the diode laser with higher power is offered, the more cold atoms will be trapped. Figure 10 shows the optical path for trapping in the optical lattice built by the available laser. According to Figure 1, it is difficult to focus at the apex of the free fall with the usual lens, because of the long distance between the center of MOT zone and the Ramsey microwave cavity. Therefore, the lens is specially customized with the diameter of D = 25.4 mm and focal length f = 900 mm, which is designed to meet the beam diameter for two counter-propagating laser beams. For the lens, if the radius of curvature is much greater than the focal length, the beam waist ω_0 can be expressed as

$$\omega_0 \approx \frac{\lambda_L f}{\pi \omega}, \tag{8}$$

where λ_L is the wavelength of optical lattice laser, and ω is the radius of beam on the lens. In our experiment, the ω_0 =100 μm leads to the ω ≈2.4 mm, which means the laser beam from the single-mode polarization-maintaining fiber should be collimated and its beam diameter is about 4.8 mm for focusing.

Once the optical lattice is home-built successfully, the centers of the optical lattice and cold atom cloud should coincide as much as possible. It is necessary to be carefully adjusted in the experiment. The atomic transition in optical lattice is excited by the probe light, and we observe the fluorescence image of cold atoms from the EMCCD to evaluate the coincidence. When the fluorescence image of the trapped cold atom cloud reaches to the brightest, and the width of the cold atom cloud is close to the beam waist, it can be considered that the centers of the optical lattice and cold atom cloud accurately coincide [39]. For the coarse adjustment, the center of the optical lattice can be moved by the two lenses along the direction of gravity. When the coarse adjustment is completed, more fine adjustment and calibration on the angle of the incident light are required. Recently, we have built a miniaturized vacuum system with about 2 × 10^{-7}Pa for ^{133}Cs shown in Figure 11. Although it is not for ^{87}Rb, it can also be used for laser cooling and applied as an apparatus to optically trap cold atoms by the optical lattice.

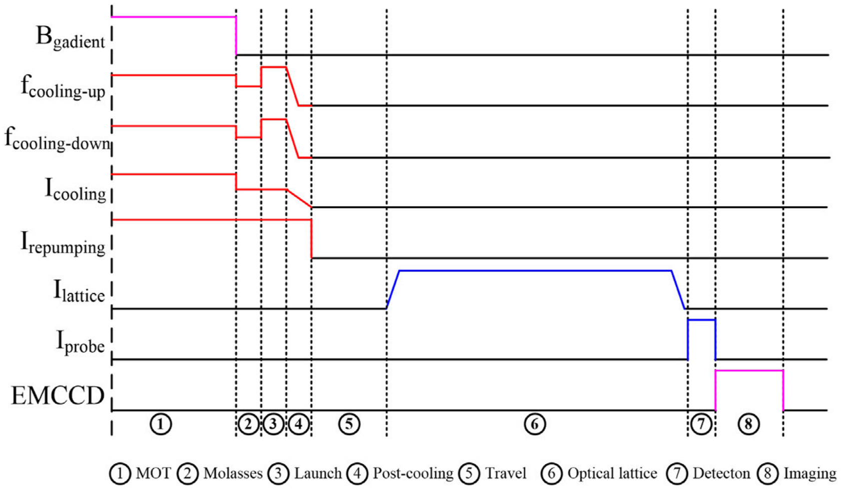

FIGURE 12
Time sequence for the preparation and loading of cold atoms for optical lattice.

3.3 Time sequence

As shown in Figure 12, the time sequence for the preparation and loading of cold atoms is proposed from the atomic fountain clock, which is used for the experiments of cold atoms. The atoms are laser-cooled to about 10 μK at the MOT and Molasses cooling stage, and launched into the free fall. At the beginning of the free fall, the post-cooling further reduces the temperature of atoms to about 2 μK. Then at the free fall, the cold atoms will travel through the upper half part of MOT zone, selection microwave cavity, detection zone and Ramsey microwave cavity. At the apex of the free fall, the cold atoms just pass the Ramsey microwave cavity and are loaded into the optical lattice. The cold atoms will be trapped into the optical potential well for a long time. This trapping time is the desired parameter to evaluate the performance the optical lattice. Then the cold atoms trapped in the optical lattice are detected by the pulsed probe light (near resonance of D2 line F = 2→F' = 3). At the same time, in order to observe the fluorescence image from optical lattice, an EMCCD is placed outside of the vacuum tube. The experimental detuning and power parameters of probe light can be optimized by observing the fluorescence image. In this time sequence, the mechanical shutters are turned on and off for the time control.

4 Results and discussion

4.1 Highly stable laser

4.1.1 Stable laser frequency

The laser frequency of the IF-ECDL depends on the temperature and diode current. The temperature has an impact on the length of the external cavity, which is actively monitored by a negative temperature coefficient (NTC) thermistor and controlled by a thermo electric cooler (TEC). This active temperature control will be combined with the external cavity length feedback to stabilize the laser frequency. As shown in Figure 13A, the output laser power of the IF-ECDL versus the diode current has been measured. Once the current is higher than the specific threshold 25 mA, the output laser power is almost linear to the diode current and can be over 100 mW. During operation, the diode current should be set above the threshold and well below the nominal maximum. Besides, we must effectively narrow the laser linewidth to avoid mode hopping and drift, because the laser cooling require the laser with low noise and high frequency stability. As shown in Figure 13B, the frequency beat-note signal of our laser with another IF-ECDL shows that the laser frequency noise is suppressed effectively, and the linewidth of about 75 kHz is achieved. A master oscillator power amplifier (MOPA) is applied to amplify the output laser of the IF-ECDL, which is used as the seed laser. The power of the seed laser between 10 and 30 mW can be amplified up to nearly diffraction limited power values in the Watt-range. Here, the temperature of the MOPA is lower than the room temperature and the difference between them should be as small as possible, which is beneficial to avoid the condensation on the surface of the MOPA.

According to the scheme of laser frequency locking and shift shown in Figure 2, the frequency of the IF-ECDL should be locked to the ^{87}Rb D2 line F = 2→F' = 3 by MTS. The scanned MTS signal is shown in Figure 14. After optimization, the slope of the F = 2→F' = 3 spectral line is very sensitive to the fluctuation of the frequency, which can improve the accuracy of frequency locking. As shown in Figure 15, the laser frequency is stabilized on the ^{87}Rb D2 line F = 2→F' = 3, and the frequency stability is achieved to $4 \times 10^{-14}\boldsymbol{\tau}^{-1/2}$ and reaches about 2×10^{-13} at $\boldsymbol{\tau} = 1 \times$

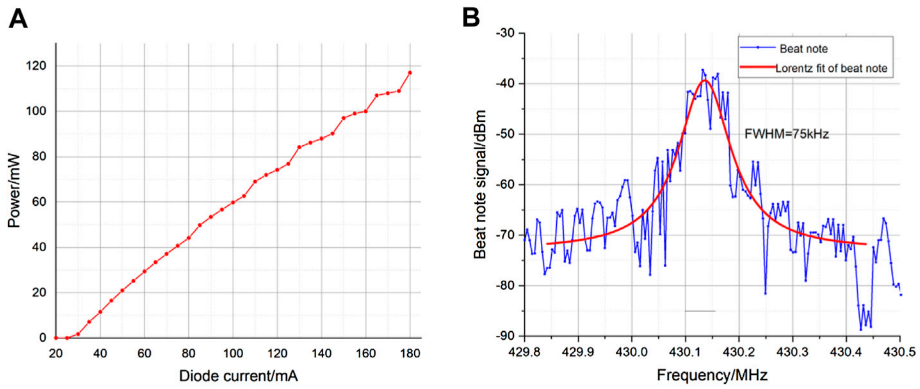

FIGURE 13
The characteristic of the IF-ECDL **(A)** the output laser power versus the diode current **(B)** the frequency beat-note signal with another IF-ECDL.

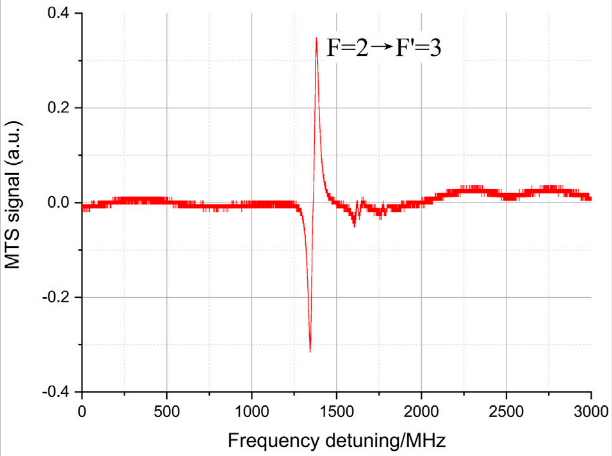

FIGURE 14
The scanned MTS signal of ^{87}Rb D2 line.

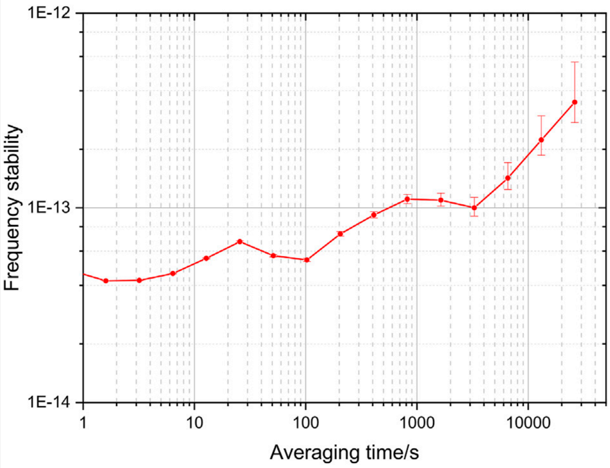

FIGURE 15
The frequency stability of IF-ECDL with MTS.

10^4 s by self comparison. The observed experimental results show an excellent frequency stability, which can fully meet the requirement of laser cooling in MOT zone.

By positioning a PD to monitor the diffraction light produced by the AOM, the stabilized laser light is achieved. Here the PD is home-built, whose gain is 1.8×10^5V/W and the maximum output voltage is 5 V. Using this PD, the intensity stability of the monitored laser is shown in Figure 16. The intensity stability of $4 \times 10^{-5}\tau^{-1/2}$ is achieved, which reaches about 3×10^{-6} at $\tau = 500$ s and begins to drift after about 1,000 s. The long term drift is mainly caused by the factors such as environmental temperature, voltage fluctuation of the voltage reference and the position offset of the optical components. The excellent performance shows the stability of output laser with stabilization has been greatly improved, which is over two orders of magnitude better than the stability without stabilization. The cold atom number is nearly proportional to the laser intensity of cooling light in MOT zone, so the fluctuation of cold atom number caused by the laser intensity can also be suppressed effectively about two orders of magnitude. Here, the relative fluctuation of cold atom number is conservatively estimated to 10^{-4} level due to the laser intensity stabilization.

4.2 Performance evaluation of trapping

4.2.1 Lifetime

The optical lattice that shifts from the focused laser beam red-detuned about 72 nm below an atomic dipole resonance

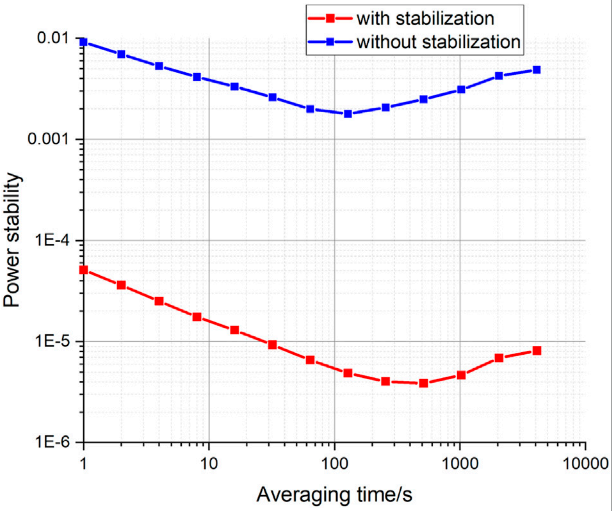

FIGURE 16
The intensity stability of the monitored laser with and without stabilization.

using the ac Stark, is designed to trap the ^{87}Rb cold atoms. The cold atoms in ground state F = 2 can be trapped when the optical lattice laser is turned on. The lifetime of cold atoms in the trap will be determined by the interactions of the cold atoms with photons, and the collisions with other atoms [40]. During the interaction between the cold atoms with light, an atom will absorb a photon and emits a photon spontaneously. The direction of the emitted photon and the recoil momentum of atoms are random, which will cause the heating rate due to the momentum diffusion. When the accumulated collision between cold atoms and background gas atoms exceeds the potential well depth, the cold atoms will escape from the well and the lifetime will be limited. In addition, the accumulated heating caused by the fluctuation of potential well depth can raise the temperature of the cold atoms. Once the temperature of the cold atoms exceeds the optical depth, the cold atoms will also escape from the well.

4.2.1.1 Momentum diffusion

Although the heating rate due to the momentum diffusion may be small at large detuning, the diffusive heating always introduces an upper limit on the lifetime. As described in Section 3.3, the detuning $|\delta| = 5.5 \times 10^6 \Gamma$ and the Rabi frequency $\Omega = 1.03 \times 10^3 \Gamma$ are calculated, where Γ is the natural linewidth. The calculated data satisfies the conditions $|\delta| \gg \gamma, \Omega$. Under these conditions, the lifetime limited by the momentum diffusion can be expressed as

$$\tau_h = \frac{U_0}{2R\gamma_s}, \tag{9}$$

where U_0 is the potential well depth, $\gamma_s = \Gamma\Omega^2/4\delta^2$ is the scattering rate and R is the recoil energy of ^{87}Rb. The recoil energy R is expressed as

$$R = \frac{(\hbar k)^2}{2m} = \frac{k_B T_R}{2}, \tag{10}$$

where ħ is the Planck constant, k is the wave number, m is the mass of ^{87}Rb atom, and T_R is the recoil temperature. It can be seen that the lifetime τ_h is directly proportional to the ratio of the potential well depth to the scattering rate. However, since the potential well depth U_0 and the scattering rate γ_s are directly proportional to the light intensity [16], the lifetime τ_h is independent of the light intensity and only related to the detuning. In our experimental set-up, the scattering rate γ_s is 0.33 and the recoil temperature T_R is 361 nK, which leads to the lifetime τ_h estimated to about 230 s.

4.2.1.2 Collisions

The optical lattice is performed in a vacuum tube attached to an ion pump. The lifetime of cold atoms in the trap is also limited by the collisions with other atoms. The lifetime limited by the collisions τ_coll depends on the collision cross section σ_c, the density of the residual gas n and the thermal velocity of the background gas u. The lifetime limited by the collision τ_coll can be expressed as

$$\tau_\mathrm{coll} \cong \frac{1}{\sigma_c n u}. \tag{11}$$

It is assumed that the collision cross section σ_c is 8×10^{-15} cm^2, the density n is 5×10^6/cm^3 at background gas pressure 2×10^{-7} Pa and the thermal velocity u is 240 m/s at room temperature. Therefore, the lifetime limited by the collision τ_coll is estimated to about 80 s.

4.2.1.3 Heating due to optical lattice laser

When the cold atoms are trapped in a noisy optical lattice, we have to consider the heating rate caused by the fluctuation of optical lattice laser power and polarization. The fluctuation of potential well depth arises naturally due to the fluctuations of the optical lattice laser, which is time-dependent. The accumulated heating caused by the fluctuation of potential well depth can raise the temperature of the cold atoms. Once the temperature of the cold atoms exceeds the optical depth, the cold atoms will also escape from the well and the lifetime will be limited. The heating process caused by the fluctuation of optical lattice laser power and polarization is related to the noise spectrum and the many-body dynamics. Here, we ignore the lifetime limited by the fluctuations of optical lattice laser, and it will be studied in the future.

4.2.2 Vibration

The potential in the optical lattice can be approximated by the harmonic trap in both the longitudinal and radial dimensions yielding the vibrational frequencies. The theoretical calculation formulas of the longitudinal ν_z and radial vibrational frequency ν_r are $\nu_z = \frac{1}{\lambda_L}\sqrt{\frac{2U_0}{m}}$ and $\nu_r = \frac{1}{\pi\omega_0}\sqrt{\frac{U_0}{m}}$, respectively. Under the conditions mentioned in Section 3.3, the two vibrational frequencies can be estimated to 48 kHz and 200 Hz, respectively. Note that the two vibrational frequencies can also be measured unambiguously by modulating the intensity of the optical lattice. The ratio of the trap frequencies $\frac{\nu_z}{\nu_r} = \frac{\sqrt{2}\pi\omega_0}{\lambda_L}$ yields the information about the beam waist without knowledge of laser power or atomic polarizability. This can be very useful for checking the position of the cold atoms relative to minimum waist of the optical lattice.

4.2.3 Contribution for beyond fountain

To determine the stabilized laser system and optical lattice contributions, the frequency stability is calculated by the Ramsey spectroscopy. We present the frequency stability of

$$\sigma_y(\tau) = \frac{1}{\pi}\frac{1}{C}\frac{1}{\nu_0/\Delta\nu}\frac{1}{SNR}\sqrt{\frac{T_c}{\tau}}, \tag{12}$$

where $C = 1$ is the contrast, ν_0 is the center frequency, $\Delta\nu = 1/(2\tau_L)$ is the linewidth of Ramsey fringe, SNR is the signal-to-noise, T_c is the cycle time, and τ is the integration time. The relative fluctuation of cold atom number has been conservatively suppressed to 10^{-4} level due to the laser intensity stabilization, so the noise on the Ramsey signal caused by this fluctuation can be ignored. The frequency stability is mainly limited by the quantum project noise, which is related to the $\sqrt{N_T}$. So the SNR can be estimated to 68, when the number of cold atoms N_T is 4,650. In addition, assuming the coherent interrogation time is τ_L is 80 s and the cycle time is about 80.5 s, the frequency stability can be improved $3.6 \times 10^{-14}\tau^{-1/2}$. Furthermore, if the power of the optical lattice is improved to 100 W, the cold atoms trapped will be increased by two orders of magnitude and the SNR will be increased by one order of magnitude. Under this condition, we infer the frequency stability has the potential to be improved to $3.6 \times 10^{-15}\tau^{-1/2}$. From the above analysis of our exploration, it is predicted that the presented frequency stability will be superior to the stability of the conventional atomic fountain clock.

5 Conclusion

In conclusion, the construction of the optical system in the atomic clock-beyond atomic fountain based on ^{87}Rb atom is investigated. By optimizing the laser frequency locking and shift, we demonstrate the stabilized and simple laser system for laser cooling. The frequency and intensity stability are achieved to $4 \times 10^{-14}\tau^{-1/2}$ and $4 \times 10^{-5}\tau^{-1/2}$, respectively, which are highly stable. The frequency stability combined with the narrow linewidth is beneficial for laser cooling. The stabilized intensity can reduce the fluctuation of cold atom number effectively. Besides, the engineered scheme of optical lattice along the direction of gravity using the available 852 nm laser is achieved and its characteristics are studied systematically. For the optimized and novel exploration, we predict the achievable stability of $3.6 \times 10^{-14}\tau^{-1/2}$, and it has the potential to be improved to $3.6 \times 10^{-15}\tau^{-1/2}$ in the future. Therefore, the construction of the optical system due to stabilized laser and optical lattice makes the beyond fountain promising candidate for the next-generation high performance microwave atomic clock.

Data availability statement

The original contributions presented in the study are included in the article/Supplementary Material, further inquiries can be directed to the corresponding authors.

Author contributions

XW, JH, YWe, and LG developed the principle, designed the Experimental set-up and wrote the manuscript; YiW, YuW, WW (5th author), WW (6th author), SLi, XZ, GL, SLiu, and YeW carried out the experiments and tests; YYu and GH analyzed the calculation data; ZL and YP analyzed the spectroscopy and data; LW, YL, TY, and CC revised the manuscript.

Funding

This work was funded by the Fundamental Research Project of Shenzhen Sci. & Tech. Fund (JCYJ20210324115812036, JCYJ20200109144612399, JCYJ20200109144601715), 2021Szvup002, IERF202002 and IERF202105.

Acknowledgments

We give our best wishes to Prof. Yiqiu Wang and congratulate him on his achievements in quantum precision measurement and cold atom physics on the occasion of his 90th birthday. We are also grateful to Yige Lin and Qiang Wang (National Institute of Metrology, China) for fruitful discussions in this paper.

Conflict of interest

ZL and YP were employed by Zhejiang Faraday Laser Technology Co.,Ltd.

The remaining authors declare that the research was conducted in the absence of any commercial or financial relationships that could be construed as a potential conflict of interest.

Publisher's note

References

1. Gibble K, Chu S. Laser-cooled Cs frequency standard and a measurement of the frequency shift due to ultracold collisions. *Phys Rev Lett* (1993) 70:1771–4. doi:10.1103/physrevlett.70.1771

2. Santarelli G, Laurent P, Lemonde P, Clairon A, Mann AG, Chang S, et al. Quantum projection noise in an atomic fountain: A high stability cesium frequency standard. *Phys Rev Lett* (1999) 82:4619–22. doi:10.1103/physrevlett.82.4619

3. Liu L, Lü DS, Chen WB, Li T, Qu QZ, Wang B, et al. In-orbit operation of an atomic clock based on laser-cooled ^{87}Rb atoms. *Nat Commun* (2018) 9:2706. doi:10.1038/s41467-018-05219-z

4. Liu P, Meng YL, Wan JY, Wang XM, Wang YN, Xiao L, et al. Scheme for a compact cold-atom clock based on diffuse laser cooling in a cylindrical cavity. *Phys Rev A* (2015) 92:062101. doi:10.1103/physreva.92.062101

5. Nicholson TL, Campbell SL, Hutson RB, Marti GE, Bloom BJ, McNally RL, et al. Systematic evaluation of an atomic clock at 2 × 10−18 total uncertainty. *Nat Commun* (2015) 6:6896. doi:10.1038/ncomms7896

6. Hardman KS, Kuhn CCN, McDonald GD, Debs JE, Bennetts S, Close JD, et al. Role of source coherence in atom interferometry. *Phys Rev A* (2014) 89:023626. doi:10.1103/physreva.89.023626

7. Peters A, Chung KY, Chu S. Measurement of gravitational acceleration by dropping atoms. *Nature* (1999) 400:849–52. doi:10.1038/23655

8. Gustavson TL, Bouyer P, Kasevich MA. Precision Rotation Measurements with an atom interferometer gyroscope. *Phys Rev Lett* (1997) 78:2046–9. doi:10.1103/physrevlett.78.2046

9. Adams CS. Atom optics. *Contemp Phys* (1994) 35:1–19. doi:10.1080/00107519408217492

10. Anderson MH, Ensher JR, Matthews MR, Wieman CE, Cornell EA. Observation of Bose-Einstein condensation in a dilute atomic vapor. *Science* (1995) 269:198–201. doi:10.1126/science.269.5221.198

11. Davis KB, Mewes MO, Andrews MR, van Druten NJ, Durfee DS, Kurn DM, et al. Bose-Einstein condensation in a gas of Sodium atoms. *Phys Rev Lett* (1995) 75:3969–73. doi:10.1103/physrevlett.75.3969

12. Monroe C. Quantum information processing with atoms and photons. *Nature* (2002) 416:238–46. doi:10.1038/416238a

13. Duan LM, Lukin MD, Cirac JI, Zoller P. Long-distance quantum communication with atomic ensembles and linear optics. *Nature* (2001) 414:413–8. doi:10.1038/35106500

14. Wynands R, Weyers S. Atomic fountain clocks. *Metrologia* (2005) 42:S64–S79. doi:10.1088/0026-1394/42/3/s08

15. Takekoshi T, Knize RJ. CO_2 laser trap for cesium atoms. *Opt Lett* (1996) 21:77–9. doi:10.1364/ol.21.000077

16. O'Hara KM, Granade SR, Gehm ME, Savard TA, Bali S, Freed C, et al. Ultrastable CO_2 laser trapping of lithium Fermions. *Phys Rev Lett* (1999) 82:4204–7.

17. Chen JB, Zhou XJ, Chen XZ. *Beyond fountain*. Miami, FL: Institute of Electrical and Electronics Engineers (2006). 281–3.

18. Zhou XJ, Chen XZ, Chen JB, Wang YQ, Li JM. Microwave atomic clock in the optical lattice with specific fre quency. *Chin Phys Lett* (2009) 26:090601. doi:10.1088/0256-307X/26/9/090601

19. Beloy K, Derevianko A, Dzuba VA, Flambaum VV. Micromagic clock: Microwave clock based on atoms in an engineered optical lattice. *Phys Rev Lett* (2009) 102:120801. doi:10.1103/physrevlett.102.120801

20. Derevianko A. "Doubly magic" conditions in magic-wavelength trapping of ultracold alkali-metal atoms. *Phys Rev Lett* (2010) 105:033002. doi:10.1103/PhysRevLett.105.033002

21. Chicireanu R, Nelson KD, Olmschenk S, Lundblad N, Derevianko A, Porto JV. Differential light-shift cancellation in a magnetic-field-insensitive transition of 87rb. *Phys Rev Lett* (2011) 106:063002. doi:10.1103/PhysRevLett.106.063002

22. Lundblad N, Schlosser M, Porto JV. Experimental observation of magic-wavelength behavior of ^{87}Rb atoms in an optical lattice. *Phys Rev A* (2010) 81:031611. doi:10.1103/physreva.81.049904

23. Campbell SL, Hutson RB, Marti GE, Goban A, Darkwah Oppong ND, McNally RL, et al. A Fermi-degenerate three-dimensional optical lattice clock. *Science* (2017) 358:90–4. doi:10.1126/science.aam5538

24. Li X, Li XP, Sarma SD. Mobility edges in one-dimensional bichromatic incommensurate potentials. *Phys Rev B* (2017) 96:085119. doi:10.1103/physrevb.96.085119

25. Lüschen HP, Scherg S, Kohlert T, Schreiber M, Bordia P, Li X, et al. Single-particle mobility edge in a one-dimensional quasiperiodic optical lattice. *Phys Rev Lett* (2018) 120:160404. doi:10.1103/PhysRevLett.120.160404

26. Blatt S, Thomsen JW, Campbell GK, Ludlow AD, Swallows MD, Martin MJ, et al. Rabi spectroscopy and excitation inhomogeneity in a one-dimensional optical lattice clock. *Phys Rev A* (2009) 80:052703. doi:10.1103/physreva.80.052703

27. Fang F, Chen WL, Liu K, Liu NF, Suo R, Li TC. Design of the new NIM6 fountain with collecting atoms from a 3D MOT loading optical molasses. *IEEE Int Frequency Control Symp* (2015) 2015:492–4. doi:10.1109/fcs.2015.7138891

28. Fang F, Li MS, Lin PW, Chen WL, Liu NF, Lin YG, et al. NIM5 Cs fountain clock and its evaluation. *Metrologia* (2015) 52:454–68. doi:10.1088/0026-1394/52/4/454

29. Corwin KL, Lu ZT, Hand CF, Epstein RJ, Wieman CE. Frequency-stabilized diode laser with the Zeeman shift in an atomic vapor. *Appl Opt* (1998) 37:3295–8. doi:10.1364/ao.37.003295

30. Wieman C, Hänsch TW. Doppler-free laser polarization spectroscopy. *Phys Rev Lett* (1976) 36:1170–3. doi:10.1103/physrevlett.36.1170

31. Bjorklund GC. Frequency-modulation spectroscopy: A new method for measuring weak absorptions and dispersions. *Opt Lett* (1980) 5:15–7. doi:10.1364/ol.5.000015

32. Black ED. An introduction to Pound-Drever-Hall laser frequency stabilization. *Am J Phys* (2001) 69:79–87. doi:10.1119/1.1286663

33. Preston DW. Doppler-free saturated absorption: Laser spectroscopy. *Am J Phys* (1996) 64:1432–6. doi:10.1119/1.18457

34. Shirley JH. Modulation transfer processes in optical heterodyne saturation spectroscopy. *Opt Lett* (1982) 7:537–9. doi:10.1364/ol.7.000537

35. Baillard X, Gauguet A, Bize S, Lemonde P, Laurent P, Clairon A, et al. Interference-filter-stabilized external-cavity diode lasers. *Opt Commun* (2006) 266:609–13. doi:10.1016/j.optcom.2006.05.011

36. Jiang ZJ, Zhou Q, Tao ZM, Zhang XG, Zhang SN, Zhu CW, et al. Diode laser using narrow bandwidth interference filter at 852 nm and its application in faraday anomalous dispersion optical filter. *Chin Phys. B* (2016) 25:083201. doi:10.1088/1674-1056/25/8/083201

37. Qi XH, Chen WL, Lin Y, Zhou DW, Zhou T, Xiao Q, et al. Ultra-stable rubidium-stabilized external-cavity diode laser based on the modulation transfer spectroscopy technique. *Chin Phys Lett* (2009) 26:044205. doi:10.1088/0256-307X/26/4/044205

38. Tricot F, Phung M, Lours S, Guérandel ED, de Clercq E. Power stabilization of a diode laser with an acousto-optic modulator. *Rev Scientific Instr* (2018) 89:113112. doi:10.1063/1.5046852

39. Wei Chun-Hua CH, Yan Shu-Hua SH, Yang Jun J, Wang Guo-Chao GC, Jia Ai-Ai AA, Luo Yu-Kun YK, et al. Design and control of large-detuned optical lattice based on 87Rb atoms. *Acta Phys Sin* (2017) 66:010701. doi:10.7498/aps.66.010701

40. Balykin VI, Minogin VG, Letokhov VS. Electromagnetic trapping of cold atoms. *Rep Prog Phys* (2000) 63:1429–510. doi:10.1088/0034-4885/63/9/202

frontiers | Frontiers in Physics

TYPE Original Research
PUBLISHED 02 September 2022
DOI 10.3389/fphy.2022.959343

OPEN ACCESS

EDITED BY
Xuzong Chen,
Peking University, China

REVIEWED BY
Xuan He,
Peking University, China
Wang Qing,
Peking University, China

*CORRESPONDENCE
Jiang Chen,
chernjiang@aliyun.com

SPECIALTY SECTION
This article was submitted to Atomic and Molecular Physics,
a section of the journal
Frontiers in Physics

RECEIVED 01 June 2022
ACCEPTED 18 July 2022
PUBLISHED 02 September 2022

CITATION
Chen J, Wang J, Guo L, Yang J, Ma P, Huang L and Liu Z (2022), Characteristics analysis of compact cesium atomic clock with magnetic state selection.
Front. Phys. 10:959343.
doi: 10.3389/fphy.2022.959343

Characteristics analysis of compact cesium atomic clock with magnetic state selection

Jiang Chen[1,2]*, Ji Wang[1,2], Lei Guo[1,2], Jun Yang[1,2], Pei Ma[1,2], Liangyu Huang[1,2] and Zhidong Liu[1]

[1]Science and Technology on Vacuum Technology and Physics Laboratory, Lanzhou, China, [2]Lanzhou Institute of Physics, Lanzhou, China

This paper introduces a compact magnetic state-selection cesium atomic clock called LIP Cs-3000 and analyses its characteristics. The test results reveal that the ranges of the line width, peak-to-valley ratio and signal-to-noise ratio of Ramsey pattern are 340–410 Hz, 2–13 and 2,000–8,000 respectively. The corresponding distributions of these parameters are derived by using statistical methods. According to these results, some suggestions are put forward for the further development of the clock. It is also pointed out that the most important factor affecting the accuracy of LIP Cs-3000 atomic clock is the uncertainty of cavity phase shift. In addition, the method to estimate the lifetime of a clock has been proposed. In the end, the paper gives some environmental adaptability designs of the clock, which enable the clock to be used in complex environments.

KEYWORDS

cesium atomic clock, cesium beam tube, accuracy, stability, ramsey pattern, electron multiplier

Introduction

The function of a compact cesium atomic clock with magnetic state selection is to realize the definition of SI second in a continuous and reliable manner, providing the user with frequency signals with high stability and accuracy. Thus this kind of clock has been widely used in time keeping, navigation, positioning, communication, and other fields in the world [1–7].

Presently, there are several brands of such atomic clock that can be available on the market. The cesium clock 5071A has specifications with an accuracy of $\pm 5 \times 10^{-13}$ and a stability of 2.7×10^{-14} at 100,000 s [8]. OSA 3235B Cesium Clock has a specified accuracy of $\pm 1 \times 10^{-12}$ and a stability of 8.5×10^{-14} at 100,000 s [9]. Although these clocks show excellent performance in many applications, the analysis of their characteristics is rarely discussed in the literature. This situation is not conducive to the development of cesium atomic clocks with magnetic state selection.

To solve this problem, the paper introduces a compact magnetic state-selection cesium clock called LIP Cs-3000 which was developed at Lanzhou Institute of

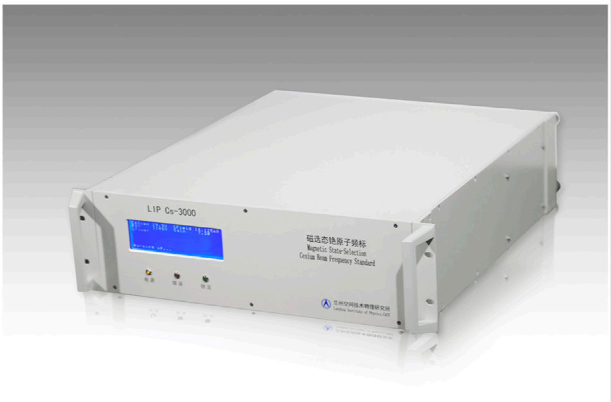

FIGURE 1
LIP Cs-3000 cesium atomic clock. The overall dimension of the LIP Cs-3000 is 435 mm × 133 mm × 500 mm. It is the standard dimension of the 3U case. Thus the LIP Cs-3000 could easily been installed on the standard 19 inch cabinet.

Physics in China [10, 11]. The paper adopts statistical methods to obtain the distributions of the line width, signal-to-noise and peak-to-valley ratio of Ramsey pattern. Based on the results, the range of stability of LIP Cs-3000 is calculated and the further development of the clock is suggested. The paper also analyzes various factors affecting accuracy and points out that the most important factor is the uncertainty of cavity phase shift. We expect that this conclusion will help improve the accuracy of the atomic clock in the future. In addition, the paper studies how to estimate the lifetime of LIP Cs-3000 clock and derives that the lifetime of the clock is larger than 5 years. The formula for assessing lifetime can be also used in other brands of cesium atomic clocks. In the end, the paper gives some environmental tests of LIP Cs-3000, which show that the clock can be applied to some complex environments. The contents of this paper not only contribute to the further development of LIP Cs-3000, but also can be applied to other brands of compact cesium atomic clocks to improve performance.

Principle and scheme

LIP Cs-3000 (see Figure 1) uses an identical two-wire magnetic field which realized by Stern-Gerlach magnet to prepare and detect atomic states and Ramsey-separated field excitation to achieve the state transitions [6, 7]. The transition signal is sent to a servo system to tune a voltage controlled crystal oscillator (VCXO).

Figure 2A shows a schematic diagram of the cesium atomic clock of LIP Cs-3000. A beam of atoms emerges from the oven at a temperature near 110°C and travels through the state-preparation region (the A magnet in Figure 2A), where the beam is split into two beams of atoms with different atomic states. These states are characterized by two quantum number F and m_F, where $F = 3$ or 4 and m_F can have integer values between $-F$ and $+F$ (see Figure 2B). Therefore, there are 16 possible states of cesium, but only the transition between the $|4,0\rangle$ and $|3,0\rangle$ states is used to define SI second. One of the beams where the atoms are in $F = 4$ with $m_F \neq -4$ states is absorbed by getter, but the other where the atoms are in $|F = 3, m_F\rangle$ and $|F = 4, m_F = -4\rangle$ states is deflected into the Ramsey cavity where the technique of separated oscillating fields is realized. The cavity is bent in a way shown in Figure 2A and the atomic beam enters and leaves the two end sections of the cavity through small holes near the end plates. The atoms in $|F = 3, m_F = 0\rangle$ state will change their state to $|F = 4, m_F = 0\rangle$ with probability [12]

$$P = \frac{b^2 \sin\left(2qt\right)^2}{q^2}\left(\cos\left(\Delta T + \frac{\theta}{2}\right) - \frac{\Delta}{q}\sin\left(\Delta T + \frac{\theta}{2}\right)\tan\left(qt\right)\right)^2 \tag{1}$$

where $\Delta = (\omega - \omega_0)/2$, $\omega_0 = 2\pi\nu_0$, $\nu_0 = 9192631770$ Hz, ω is the angular microwave excitation frequency, t is the transit time through a cavity end, T is the transit time in the drift region between the cavity ends, θ is the phase angle lead of the microwaves in the second cavity end with respect to that in the first, $2b$ is the Rabi frequency of the cesium in the microwave magnetic field and $q = (\Delta^2 + b^2)^{1/2}$. After leaving the Ramsey cavity, the atoms pass through the second two-wire magnetic field (the B magnet in Figure 2A). The two-wire field directs only the atoms in changed state $|F = 4, m_F = 0\rangle$ to the hot-wire ionizer where the atoms are changed into ions; the other atoms are directed to getter and absorbed. The electron multiplier amplifies the ion flow as an electric current signal which contains the frequency offset of the RF signal that comes from the VCXO. Signal amplifier makes the current signal to the level that the servo system can operate. The servo system calculates the frequency offset of the VCXO and tunes the VCXO to lock to cesium resonance. Then standard output frequencies, such as 5 MHz, and 10 MHz, are derived from the output amplifier and used as reference signals.

Performance and analysis

Important performance aspects of compact cesium atomic clocks include the stability and accuracy. The stability is the degree to which the atomic clock produces the same value of frequency throughout a specified time interval. The accuracy reflects the degree to which atomic clock output frequency agrees with the value corresponding to the definition of the SI second.

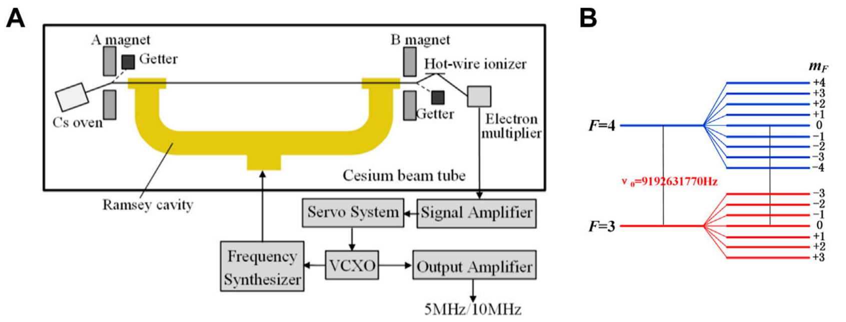

FIGURE 2
Principle of LIP Cs-3000 cesium atomic clock. **(A)** Schematic of LIP Cs-3000. **(B)** Cesium ground state sublevels in a magnetic field.

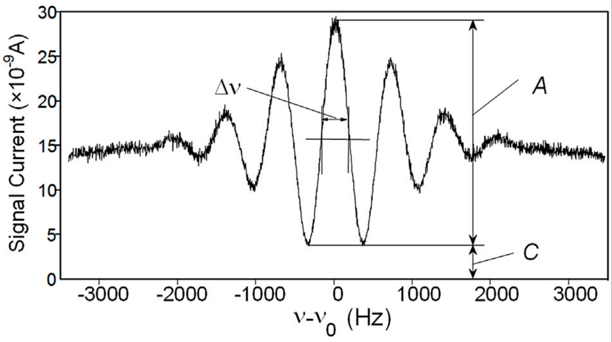

FIGURE 3
The Ramsey pattern of the CBT of LIP Cs-3000 (ν_0 = 9192631770 Hz).

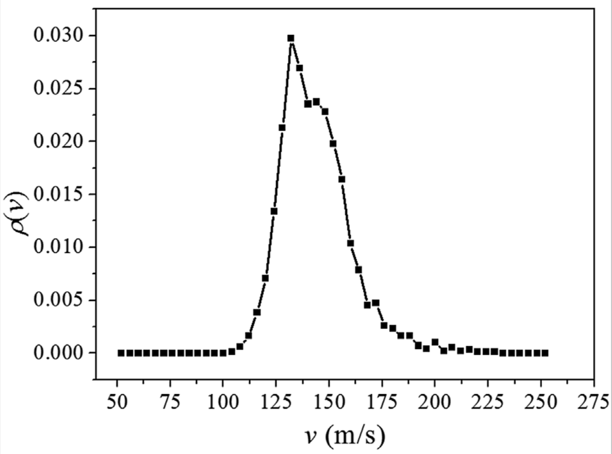

FIGURE 4
Velocity distribution of the signal atoms in CBT of LIP Cs-3000 clock.

Stability

The frequency stability depends on the averaging time and on the Ramsey pattern of the cesium beam tube (CBT) of an atomic clock. The typical curve of Ramsey pattern of LIP Cs-3000 is shown in Figure 3. The curve can be described by three parameters including line width, peak-to-valley ratio and signal-to-noise ratio, which determine the Allan deviation σ_f according to the formula as follows [13]

$$\sigma_f = 0.55\sqrt{\frac{2 + A/C}{1 + A/C}}\,\frac{\Delta\nu}{\nu_0}\,\frac{1}{S/N}\,\frac{1}{\sqrt{\tau}} \tag{2}$$

where $\Delta\nu$ is line width, A is the amplitude of the signal, C is the average valley value of the signal, $(A + C)/C$ is peak-to-valley ratio, S/N is signal-to-noise ratio and τ is the averaging time in seconds.

The line width $\Delta\nu$ is defined as the full width at half maximum of the central fringe. It can be derived from Eq. 1 as follows [14, 15]

$$\frac{\Delta\nu}{\nu_0} \approx \frac{1}{t_d \nu_0} \tag{3}$$

where $t_d = L/\langle v\rangle$ is the transit time through the cavity, L is the drift length between microwave interaction regions, $\langle v\rangle = \int v\rho(v)\mathrm{d}v$, $\rho(v)$ is the velocity distribution of the signal atoms in changed state $|4, 0\rangle$. Figure 4 shows the velocity distribution of LIP Cs-3000, which derived by Monte Carlo method. Obviously, not every atom in state $|3, 0\rangle$ is selected to finish the transition within CBT. Only the atoms with velocity located in the range from 100 to 200 m/s have a chance to interact with the microwave. According to $\rho(v)$ given in Figure 4, the line width of the Ramsey pattern for LIP Cs-3000 is less than 400 Hz. Figure 5 shows the line width of over one hundred cesium beam tubes produced in nearly 4 years. The line widths of these tubes meet

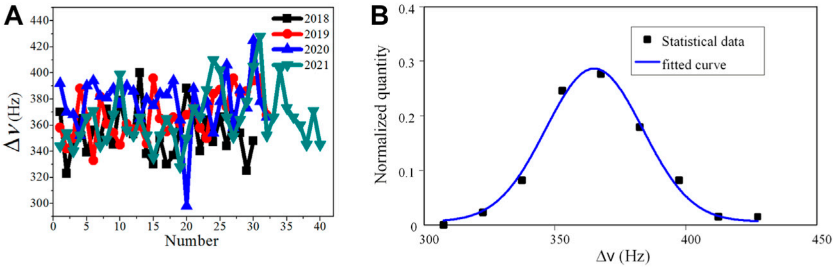

FIGURE 5
The line widths of CBTs. **(A)** Statistical chart of the line widths of CBTs from 2018 to 2021, and there are about 30 or 40 tubes every year considered. **(B)** Normal distribution fitting for line width of all tubes.

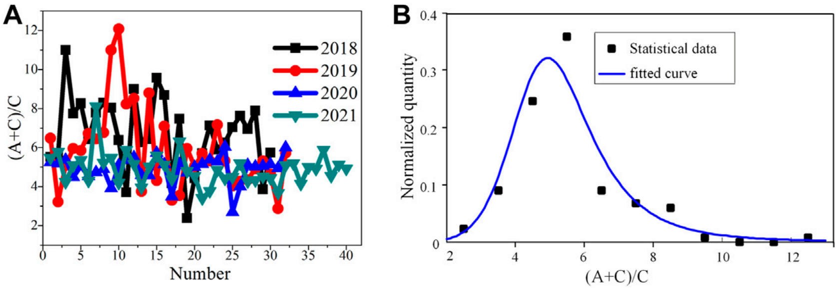

FIGURE 6
The peak-to-valley ratios of CBTs. **(A)** Statistical chart of the peak-to-valley ratios of CBTs from 2018 to 2021. **(B)** Burr type XII distribution fitting for the peak-to-valley ratios of all tubes.

with the normal distribution with the mean value of 365 Hz and standard deviation of 18 Hz.

The peak-to-valley ratios of these clocks lie in the range of 2–13 in Figure 6. It can be seen that the peak-to-valley ratios approximately obey the Burr type XII distribution [16] with shape parameters of 0.8 and 7.0 and a scale parameter of 5.0 respectively. The peak-to-valley ratio of a cesium beam tube reveals the relative position of ionization detector (Hot-wire ionizer in Figure 2A) to the state-selection magnet where cesium atoms pass through. A higher peak-to-valley ratio represents a more accurate position of ionization detector where less cesium atoms without clock transition are collected. This wide distribution implies that the position of ionizer needs more accurate control in the manufacturing process.

The signal-to-noise ratio is the root mean square noise of the signal with 1 Hz bandwidth. Because square wave frequency modulation is employed near the central peak of Ramsey pattern, the signal of CBT is DC signal at each modulation frequency. The signal-to-noise ratio of the DC signal with noise depends on the bandwidth of measurement. The signal is filtered with the 1 Hz low pass filter centered at the frequency 0 Hz. In general, the signal-to-noise ratio increases with the increase of cesium oven temperature. For the convenience of comparison, we fixed the oven temperature at 110°C in the signal-to-noise ratio test of cesium beam tubes. The signal-to-noise ratio lies in 2,000–8,000 shown in Figure 7, which resulting in upmost predicted Allan deviation of less than $5 \times 10^{-12}/1\text{s}$. The signal-to-noise ratio in Figure 7 is also approximately fitted with the Burr type XII distribution with shape parameters of 1.2 and 6.7 and a scale parameter of 4039.5 respectively. It is worth noting that the high signal-to-noise ratio of more than 7,000 can be obtained for the magnetic state-selection CBT. Higher signal-to-noise ratio means better collimation of the atomic beam in CBT. However the proportion of cesium beam tubes with high signal-to-noise ratio is less than 5%. This means that we need to improve the accuracy of beam optical parameters in the manufacturing process of CBT. In particular, considering that the magnetic field is the largest source of atomic beam divergence, we should improve the assembly accuracy of A and B magnets.

If we take $\Delta\nu \approx 340 \sim 400$ Hz, $(A + C)/C \approx 3.5 \sim 10$ and $S/N \approx 2500 \sim 6000$ into Eq. 2, we immediately get

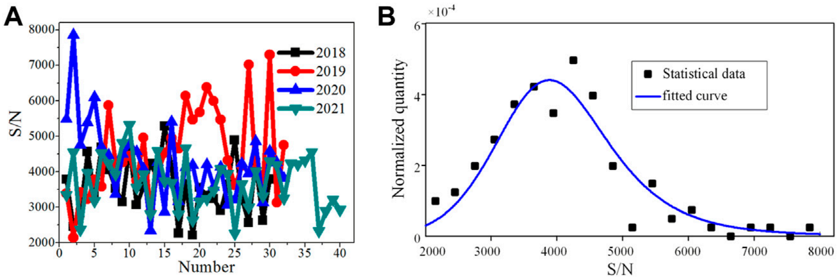

FIGURE 7
The signal-to-noise ratios of the CBTs. **(A)** Statistical chart of the signal-to-noise ratios of CBTs from 2018 to 2021. **(B)** Burr type XII distribution fitting for the signal-to-noise ratio of all tubes.

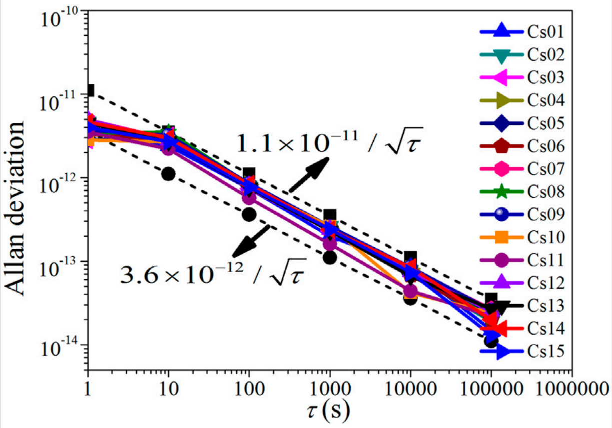

FIGURE 8
The Allan deviation data of LIP Cs-3000 atomic clocks. Cs*nn*–LIP Cs-3000 clocks. The dotted lines are corresponding to $1.1 \times 10^{-11}/\sqrt{\tau}$ and $3.6 \times 10^{-12}/\sqrt{\tau}$.

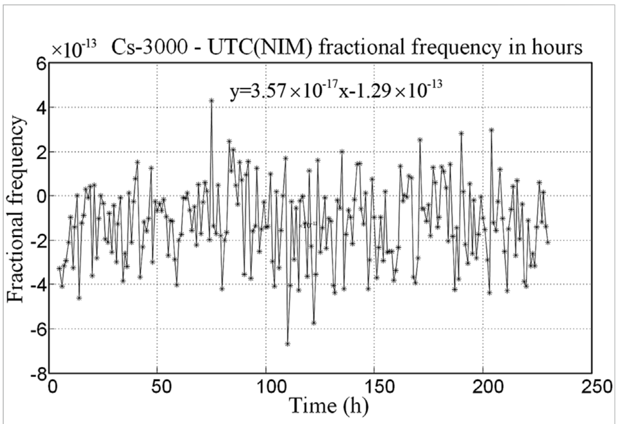

FIGURE 9
The fractional frequency of LIP Cs-3000 cesium atomic clock.

$\sigma_f \approx 1.1 \times 10^{-11} \sim 3.6 \times 10^{-12}/\sqrt{\tau}$. Figure 8 shows the Allan deviation data of 15 cesium atomic clocks during 15-days continuous measurement at the National Institute of Metrology (NIM) of China. The frequency reference of 10 MHz signal is atomic time scale of NIM. The typical frequency stability of the clock is 5×10^{-12}/1s, 3.5×10^{-12}/10 s, 8.5×10^{-13}/100 s, 2.7×10^{-13}/1000 s, 8.5×10^{-14}/10000 s and 2.7×10^{-14}/100000 s. As a supplement, we also give the 5-days stability of LIP Cs-3000 here, which ranges from 9.0×10^{-15} to 2.0×10^{-14}.

Accuracy

The accuracy of the LIP Cs-3000 clock is within the range of $\pm 3 \times 10^{-13}$. Figure 9 shows the fractional frequency in hours of one of the clock with the accuracy of -1.29×10^{-13} compared with UTC (NIM). There are several factors that influence the accuracy of LIP Cs-3000 clocks. The most important factors include the uncertainty in the derivation of the second-order Zeeman frequency shift, the second-order Doppler effect and the uncertainty in the measurement of the cavity and others.

The second-order Zeeman frequency shift is given by [17].

$$\boldsymbol{\nu = \nu_0 + 427.45B^2}, \tag{4}$$

where B is the C field and $\nu_0 = 9192631770$ Hz. If B has an increment dB, then ν has an increment d$\nu = 854.9B$dB. For LIP Cs-3000 clocks, $B = 0.06$G and d$B/B < 1 \times 10^{-4}$. Thus we have $\frac{d\nu}{\nu_0} < 3.35 \times 10^{-14}$.

The second-order Doppler effect originates from the time dilation phenomenon of relativity. For an atom of velocity v, the fractional frequency shift is given by the equation (17)

TABLE 1 Summary of frequency shifts and their uncertainties in LIP Cs-3000.

Origin of shift	Typical size ($\times 10^{-14}$)	Typical uncertainty achieved ($\times 10^{-14}$)
Magnetic field	~10,000	3.4
Second-order Doppler effect	~10	1.2
Black body radiation	~2	0.03
Cavity pulling	~0.5 to 1	0.06
Bloch-Siegert effect	~0.1	<0.03
Majorana transitions	~0.2	<0.13
Rabi and Ramsey pulling	<0.2	0.002
Microwave spectrum	<4	0.4
Microwave leakage	~0.1	<0.1
Electronic system	~0.3	0.3
Cavity phase shift	~10	20–30

$$\frac{\nu - \nu_0}{\nu_0} = -\frac{v^2}{2c^2}, \tag{5}$$

where c is the speed of light. Considering the velocities of the atoms are spread according to the distribution $\rho(v)$ (see Figure 4), so the v in (5) should be displaced by average v_{avg}. For LIP Cs-3000, $\mathrm{d}v_{avg}/v_{avg} < 0.1$, therefore $\frac{\mathrm{d}\nu}{\nu_0} = -(v_{avg}^2/c^2)\ (\mathrm{d}v_{avg}/v_{avg}) < -1.2 \times 10^{-14}$.

The end-to-end cavity phase shift φ also introduces a frequency shift as follows [17]

$$\delta\nu = -\frac{\varphi}{2\pi T}, \tag{6}$$

where T is the transit time in the drift region between the cavity ends. The phase shift comes from the energy losses occurring in the cavity wall and in the two terminations and unequal lengths of the two cavity-arms. In general, the relative frequency shift amounts to the level of 10^{-13} for compact cesium clocks [17, 18]. But the relative frequency variation is difficult to determine from the energy losses, which limit the accuracy to which the phase asymmetry in the Ramsey cavity can be determined. To estimate the relative frequency variation, we had to consider other effects including black body radiation, Bloch-Siegert effect etc. These effects, however, introduce smaller uncertainties than those mentioned above. Table 1 lists the various frequency shifts and the accuracy in the determination of these shifts for LIP Cs-3000. We find that the combined uncertainty of the clock is less than 5×10^{-14} if we consider all origin shifts but the cavity phase shift. Considering the accuracy of the clock is $\pm 3 \times 10^{-13}$, we can conclude that the uncertainty of the cavity distributed phase shift exceeds $\pm 2 \times 10^{-13}$. Therefore it is easy to find that cavity phase shift is actually the greatest cause of inaccuracy. If we want to improve the accuracy of LIP Cs-3000 further, we must select a higher performance microwave cavity.

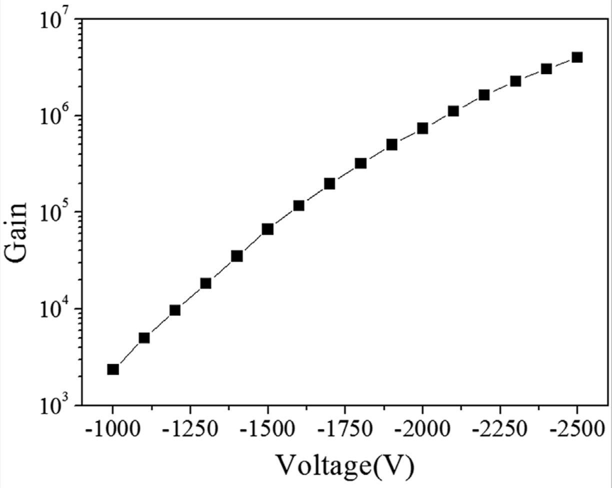

FIGURE10
The curve of the gain value of the electron multiplier changing with operating voltage.

Lifetime evaluation

At present, the lifetime of LIP Cs-3000 cesium atomic clock is almost equal to that of electron multiplier. The multiplier is used to amplify the signal current of about 1 pA to tens or even hundreds of nA. However, this amplification ability will gradually decrease over time [19]. When it reduces to a certain extent, the life of multiplier, that is, the life of cesium clock, will end [20].

The lifetime of electron multiplier depends on two parameters called gain and decay rate of gain [21, 22]. The higher gain and lower decay rate of gain mean the longer

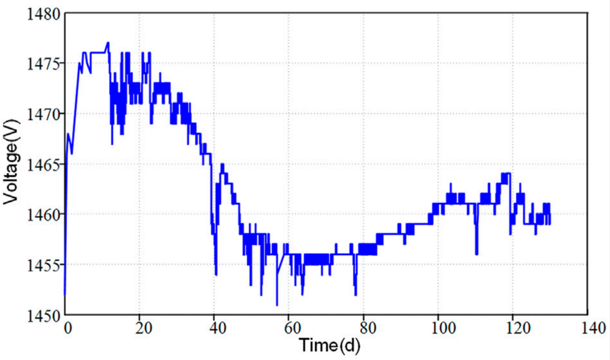

FIGURE11
The curve of the operating voltage of the electron multiplier with time in the early stage.

lifetime of a electron multiplier. Gain is a multiple factor by which the electron multiplier amplifies the current signal. One of the characteristics of electron multiplier is that its gain value changes exponentially with the increase of the working voltage. Figure 10 shows the curve of the gain value of the electron multiplier of the LIP Cs-3000 clock changing with operating voltage. We can find from Figure 10 that under the working voltage of −2500 V, the gain value can reach 4×10^6. Decay rate refers to the average daily decrease of the gain of the electron multiplier. The decay of gain makes signal current of CBT lower and lower and therefore deteriorates the long-term stability of the clock.

To solve the deterioration problem, the function of automatically regulating the voltage of the electron multiplier is added into the circuit of LIP Cs-3000. When the gain of the multiplier varies, the circuit will changes its voltage accordingly to keep the current stable. Therefore, we can expect that as the gain continues to decrease, the voltage will continue to rise. It should be pointed out that in the initial stage of electron multiplier, one usually observes that the voltage does not increase but decreases (Figure 11). This is because at this stage, the dynode surface of the electron multiplier is covered with a layer of impurities, which will be gradually removed under the bombardment of electrons, so that the gain of the multiplier became higher and higher. This process lasts about 1 month to half a year.

The added function that introduced to automatically regulate the voltage of the electron multiplier improves the long-term stability of the cesium atomic clock. In addition, it brings another advantage that the lifetime of an electron multiplier can be evaluated. When the cesium atomic clock enters the stable working stage, it can be observed that the voltage increases in a nearly linear form (see Figure 12). Consequently, as long as the daily voltage increase of a multiplier is measured, the lifetime of the multiplier can be calculated according to the following formula approximately

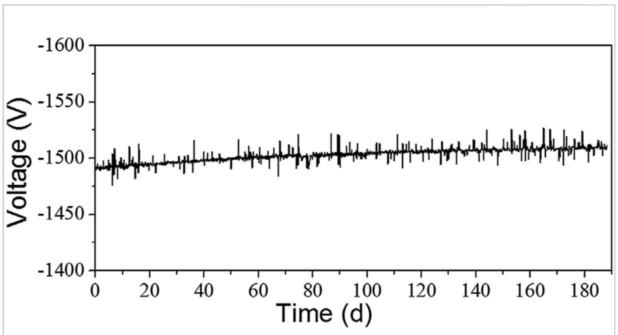

FIGURE12
The curve of the operating voltage of the electron multiplier with time after it enters the stable working stage.

$$\boldsymbol{T_{life}} = \frac{\boldsymbol{V_{max}} - \boldsymbol{V_{min}}}{\boldsymbol{\Delta V}} \tag{7}$$

where T_{life} represents the lifetime of a multiplier, V_{min} is the starting working voltage of a multiplier, V_{max} is the maximum voltage that the circuit can provide, and ΔV represents the daily increase of the voltage.

If the initial stage life of the multiplier is considered, the lifetime Eq. 4 will be modified as follows

$$\boldsymbol{T_{life}} = \boldsymbol{T_0} + \frac{\boldsymbol{V_{max}} - \boldsymbol{V_{min}}}{\boldsymbol{\Delta V}} \tag{8}$$

where T_0 represents multiplier initial stage life which is in 1 month to half a year. At present, these parameters of the clock are as follows $T_0 \approx 1 \sim 6$ month, $V_{min} \sim -1200$ V, $V_{max} = -2600$ V and $\Delta V < -0.7$ V/day. According to Eq. 5, the lifetime of the clock can be estimated to be more than 5 years.

Environmental adaptability

In order to meet the requirements for the application of LIP Cs-3000 cesium clock in different environments, we have carried out a series of designs and tests on the environmental adaptability. These works ensure the quality characteristics of the clock in different environments during operation, transportation and storage. Up to now, the designs and tests are mainly related to mechanical vibration environment, thermal environment and electromagnetic field environment.

For the mechanical vibration environment, the finite element analysis method is adopted. The structure of the whole machine is analyzed, the weak area is found and the reinforcement is completed, highly reliable components of beam optics in CBT were designed. On this basis, a random vibration test with road-level was carried out with vibration frequency in the range of 10–500 Hz and the vibration order 1.04 g. As shown in Table 2,

TABLE 2 Frequency stability before and after the random vibration test.

Averaging time (s)	Stability	
	Before test	After test
1	3.8×10^{-12}	3.64×10^{-12}
10	1.6×10^{-12}	1.58×10^{-12}
100	4.85×10^{-13}	4.90×10^{-13}

there is no significant change in the stability before and after the vibration test.

A variety of measures have been adopted in the thermal design. Using the thermal imaging technology, it was found that the module with the largest heat sources in a cesium atomic clock is the power supply. Thus the power supply module is installed on the side wall of the case to accelerate heat exchange. In addition, different passages of heat dissipation are designed in the clock. For example, the modules with high power such as microwave source and 1PPS source are also installed on the case wall, and the VCXO is positioned near CBT where temperature variation is relatively smaller. Meanwhile, the clock adopts constant-temperature VCXO with "SC-cut", which has good temperature characteristics and small temperature coefficient. Therefore the clock can start up and operate normally after low and high temperature storage tests carried out at −40°C and +70°C. The temperature coefficient measured in range of −20 ~+55°C is 1.4×10^{-14}/°C compared with 5.4×10^{-14}/°C without the design of heat dissipation. The frequency curves under the different temperatures are shown in Figure 13.

In terms of electromagnetic field environment, shielding technology is mainly used. By establishing the relation between magnetic sensitivity and permeability of magnetic shield in a cesium clock, a magnetic shield system with high permeability more than 150,000 is designed in CBT. As a result, the total shielding efficiency is greater than 2×10^6 and the remanence in C field zone is less than 1nT, which can resist the influence of external magnetic field on the uniform of C field. Therefore the magnetic sensitivity of the clock measured by Helmholtz coil at room temperature is less than 2.25×10^{-14}/G (−2G~+2G). In addition, each module is shielded by metal screen independently to avoid electromagnetic interference, which made the clocks be passed by some electromagnetic compatibility test items including CE102, CS101, CS114, CS115, Cs116, RE102 and RS103 [23].

Although the clock has passed the above tests, some other tests, such as drop, functional shock and temperature shock, need to be completed in the future. We expect that these new tests will help improve the adaptability of the clocks further and make the clocks be applied to the more complex environments such as vehicles and ships and so on.

Summary

This paper has studied and analyzed the performance of LIP Cs-3000 cesium clocks according to their technical characteristics and test data. The statistical data show that the range of value of line width, peak-to-valley ratio and signal-to-noise ratio of Ramsey pattern are 340–410 Hz, 2–13 and 2,000–8,000 respectively. These values assure that the Allan deviations of the clocks lies in the range of $1.1 \times 10^{-11} \sim 3.6 \times 10^{-12}/\sqrt{\tau}$, which are consistent with the test results (see Figure 8). The statistical data also show that the line widths subject to the normal distribution, while the peak-to-valley ratio and signal-to-noise ratio approximately obey Burr type XII distribution. Their ranges are relatively wide, indicating that the consistency of the manufacture process needs to be improved. In addition, the paper analyzed various factors affecting accuracy and pointed out that LIP Cs-3000 clock has a specified accuracy of 3×10^{-13}. At the same time, the most important factor affecting accuracy is the uncertainty caused by

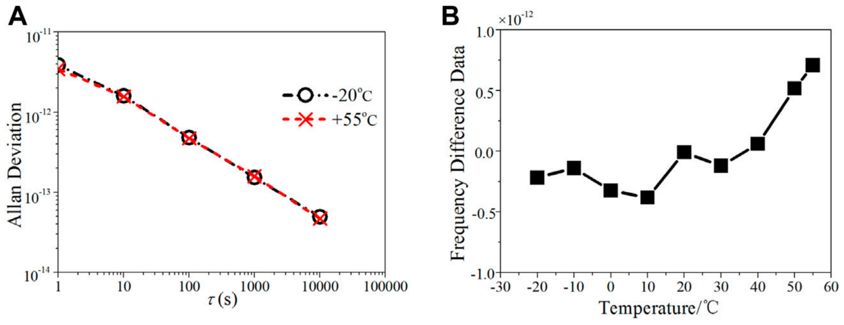

FIGURE 13
The frequency curves under the different working temperatures. **(A)** Frequency stability. **(B)** Relative frequency difference at different temperatures.

the cavity phase shift. This means that if we want to improve the accuracy of LIP Cs-3000 further, we must select a higher performance microwave cavity. The paper also studied how to estimate the lifetime of LIP Cs-3000 clock. Considering that lifetime of the clock is almost equal to that of electron multiplier and the multiplier lifetime is related to its voltage variation, we proposed to use the trend of the voltage variation to estimate the clock lifetime. According to this method we obtained that the lifetime of the clock is larger than 5 years. To improve the lifetime further, we need to prepare and adopt such a secondary electron emission film in the multiplier, which is more insensitive to the environment. In the end, the paper introduced some environmental adaptability designs of the clock, which ensure that the temperature coefficient and magnetic sensitivity reach 1.4×10^{-14}/°C and 2.25×10^{-14}/G respectively. In order to get a lower temperature coefficient, we need to carry out the optimization of thermal design of the clock.

Data availability statement

The original contributions presented in the study are included in the article/supplementary material, further inquiries can be directed to the corresponding author.

Author contributions

JC: conception and idea. JW: testing of CBT. LG: testing of electronic multiplier. JY: testing of environment. PM: testing of circuit. LH: pictures production. ZL: funding acquisition. Data analysis and writing of the paper by JC, JW, LG, JY, and PM.

Funding

National Defense Key Laboratory Stabilization Support Program of China under Grant No. HTKJ2020KL510006. National Natural Science Foundation of China under Grants No. 61971209.

Acknowledgments

The authors thank Professor Wang Yiqiu for his helpful discussions in developing LIP Cs-3000 clocks. The authors also thank the support from National Defense Key Laboratory Stabilization Support Program of China and National Natural Science Foundation of China.

Conflict of interest

Publisher's note

References

1. BIPM. *BIPM annual report on time activities, volume 15* (2020). Available from: https://www.bipm.org/en/search?p_p_id=search_portlet&p_p_state=normal&p_p_mode=view&_search_portlet_javax.portlet.action=search&_search_portlet_source=BIPM&p_p_lifecycle=0 (Accessed April 24, 2022).

2. Yuan Hb., Qu LL, Dong SW, Li W, Zhang H. The hydrogen maser and cesium clocks in time keeping at NTSC. In: 2009 Joint Meeting of the European Frequency and Time Forum (EFTF'09) and the IEEE International Frequency Control Symposium (FCS'09) (2009). p. 639–42. doi:10.1109/FREQ.2009.5168261

3. Breakiron LA. Kalman filter characterization of cesium clocks and hydrogen masers. In: Proceedings of the 34th Annual Precise Time and Time Interval Systems and Applications Meeting (2002). p. 511–26. Available from: https://www.ion.org/publications/abstract.cfm?articleID=13966 (Accessed August 1, 2022).

4. Vannicola F, Beard R, White J, Seni K, Largay M, Buisson J. GPS block IIF atomic frequency standard analysis. In: 42nd Annual Precise Time and Time Interval (PTTI) Meeting (2010). p. 181–95. Available from: https://www.ion.org/publications/abstract.cfm?articleID=10732 (Accessed August 1, 2022).

5. Vannicola F, Beard R, Koch D, Kubik A, Wilson D, White J. GPS block IIF atomic frequency standard analysis. In: Proceedings of the 45th Annual Precise Time and Time Interval Systems and Applications Meeting (2013). p. 244–9. Available from: https://www.ion.org/publications/abstract.cfm?articleID=11597 (Accessed August 1, 2022).

6. Vanier J, Audoin C. *The quantum Physics of atomic frequency standards.* New York: Adam Hilger (1989). Available from: http://www.crcpress.com/The-Quantum-Physics-of-Atomic-Frequency-Standards/Vanier-Audoin/p/book/9781420050851 (Accessed August 1, 2022).

7. Fritz Riehle. *Frequency standards: Basics and applications.* Weinheim: WILEY-VCH Verlag GmbH (2004). doi:10.1109/MIM.2005.1578626

8. Microchip. *Microchip* (2022). Available from: https://www.microsemi.com/document-portal/doc_download/133269-5071a-datasheet (Accessed August 1, 2022).

9. Oscilloquartz. *Oscilloquartz* (2022). Available from: https://www.oscilloquartz.com/en/resources/downloads/data-sheets/osa-3235b-cesium-clock (Accessed August 1, 2022).

10. Chen J, Ma P, Wang J, Guo L, Liu ZD, Yang J, et al. Progress in commercialization of compact magnetically selected cesium atomic clocks. *J Astronautic Metrology Meas* (2020) 40(3):12–6. doi:10.12060/j.issn.1000-7202.2020.03.03

11. Chen J, Ma P, Wang J, Guo L, Tu JH, Yang W. Test of magnetic-selected cesium atomic clock LIP Cs3000C. *J Time Frequency* (2018) 41(3):190–3. doi:10.13875/j.issn.1674-0637.2018-03-0190-04

12. Cutler LS. Fifty years of commercial caesium clocks. *Metrologia* (2005) 42(3):90–9. doi:10.1088/0026-1394/42/3/S10

13. Wang YQ, Wang QJ, Fu JS, Dong TQ. *The theory of frequency standards*. Beijing: Science Press (1986). p. 168–73.

14. Sullivan DB, Bergquist JC, Bollinger JJ, Drullinger RE, Itano WM, Jefferts SR, et al. Primary atomic frequency standards at NIST. *J Res Natl Inst Stand Technol* (2001) 106(1):47. doi:10.6028/jres.106.004

15. Lombardi MA, Heavner TP, Jefferts SR. NIST primary frequency standards and the realization of the SI second. *NCSLI Measure* (2007) 2(4):74–89. doi:10.1080/19315775.2007.11721402

16. Burr IW. Cumulative frequency functions. *Ann Math Statist* (1942) 13(2): 215–32. doi:10.1214/aoms/1177731607

17. Vanier J, Audoin C. The classical caesium beam frequency standard: Fifty years later. *Metrologia* (2005) 42(3):31–42. doi:10.1088/0026-1394/42/3/S05

18. Audoin C, Dimarcq N, Giodano V, Viennet J. Physical origin of the frequency shifts in cesium beam frequency standards-related environmental sensitivity. *IEEE Trans Ultrason Ferroelectr Freq Control* (1992) 39(3):412–21. doi:10.1109/58.143175

19. Hirashima M, Miyashiro S. Some factors affecting the decay of secondary electron emission of silver-magnesium alloys. *J Phys Soc Jpn* (1957) 12(7):770–7. doi:10.1143/JPSJ.12.770

20. Brock C, Tolman BW, Taylor RE. End-of-life indicators for nima's high-performance cesium frequency standards. In: Proceedings of the 34th Annual Precise Time and Time Interval Systems and Applications Meeting (2002). p. 117–26. Available from: https://www.ion.org/publications/abstract.cfm?articleID=13932 (Accessed August 1, 2022).

21. Straka ER. Performance characteristics of cesium beam tube electron multipliers. In: 36th Annual Frequency Control Symposium (1982). p. 230–5. doi:10.1109/FREQ.1982.200575

22. Kusters JA, Cutler LS, Powers ED. Long-term experience with cesium beam frequency standards. In: 1999 Joint Meeting EFTF - IEEE IFCS (1999). p. 159–63. doi:10.1109/FREQ.1999.840733

23. GJB-151B. *Electromagnetic emission and susceptibility requirements and measurements for military equipment and subsystems* (2013). p. 12–80. Available from: http://www.bzko.com/std/201059.html (Accessed August 1, 2022).

frontiers | Frontiers in Physics

TYPE Review
PUBLISHED 06 September 2022
DOI 10.3389/fphy.2022.957151

The manipulation of ultracold atoms of high orbitals in optical lattices

Shengjie Jin, Xuzong Chen and Xiaoji Zhou*

State Key Laboratory of Advanced Optical Communication System and Network, School of Electronics, Peking University, Beijing, China

OPEN ACCESS

EDITED BY
Andrea Bertoldi,
ParisTech Institut d'Optique Graduate School, France

REVIEWED BY
Santiago F. Caballero-Benitez,
Instituto de Física, Universidad Nacional Autónoma de México, Mexico
Xin Zheng,
University of Wisconsin-Madison, United States

*CORRESPONDENCE
Xiaoji Zhou,
xjzhou@pku.edu.cn

SPECIALTY SECTION
This article was submitted to Atomic and Molecular Physics,
a section of the journal
Frontiers in Physics

RECEIVED 30 May 2022
ACCEPTED 09 August 2022
PUBLISHED 06 September 2022

CITATION
Jin S, Chen X and Zhou X (2022), The manipulation of ultracold atoms of high orbitals in optical lattices.
Front. Phys. 10:957151.
doi: 10.3389/fphy.2022.957151

Ultracold atoms in optical lattices are a powerful tool for quantum simulation, precise measurement, and quantum computation. A fundamental problem in applying this quantum system is how to manipulate the higher bands or orbitals in Bloch states effectively. Here we mainly review our methods for manipulating high orbital ultracold atoms in optical lattices with different configurations. Based on these methods, we construct the atom-orbital qubit under nonadiabatic holonomic quantum control and Ramsey interferometry with trapped motional quantum states. Then we review the observation of the novel quantum states and the study of the dynamical evolution of the high orbital atoms in optical lattices. The effective manipulation of the high orbitals provides strong support for applying ultracold atoms in the optical lattice in many fields.

KEYWORDS

high orbitals, optical lattice, ultracold atoms, quantum manipulation, quantum simulation

1 Introduction

Ultracold atoms confined in optical lattices are a powerful tool for quantum simulation [1–3, 3–6], precision measurement [7], and quantum computation [8]. An optical lattice is formed by the interference of laser beams, creating a spatially periodic potential for ultracold atoms. The periodic potential generates the Bloch bands and Bloch states corresponding to different orbitals. Different to the study of ground band of optical lattice, by effectively manipulating the orbital degrees of freedom of ultracold atoms in the optical lattice, novel quantum states are found [9–12], and new qubits [8] and interferometers [13] based on the atomic orbitals are realized. In applying these high orbital ultracold atoms in optical lattices, a fundamental problem is how to manipulate the orbitals. Unlike internal states of atoms, the effective manipulation of Bloch states in optical lattices is complex because of the lack of selection rules [14]. Recently, methods to effectively manipulate Bloch states and high orbitals of optical lattices have been proposed, such as stimulated Raman transitions [15], shortcut method [14, 16–21], phase imprint [22], moving lattices [23], and band swapping technique [9, 11, 12, 24].

In this paper, we review our practical methods for manipulating high orbital atoms in optical lattices. These methods contain the shortcut method [14], band swapping technique [9, 11, 12, 24], and the amplitude modulation method to manipulate atoms in optical lattices [25].

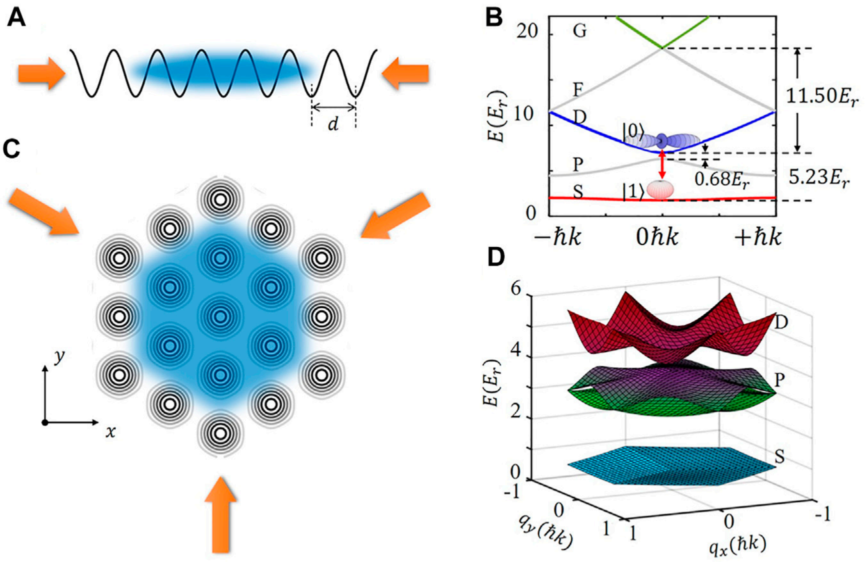

FIGURE 1
Schematic diagram and band structure of optical lattices. **(A)** is a 1D optical lattice with the lattice constant *d*. **(B)** The band-gap structures of 1D optical lattice for lattice depth $V = 5E_r$ with laser wavelength 1,064 nm. **(C)** is a triangular optical lattice, with the corresponding band structure **(D)** for lattice depth $V = 3E_r$.

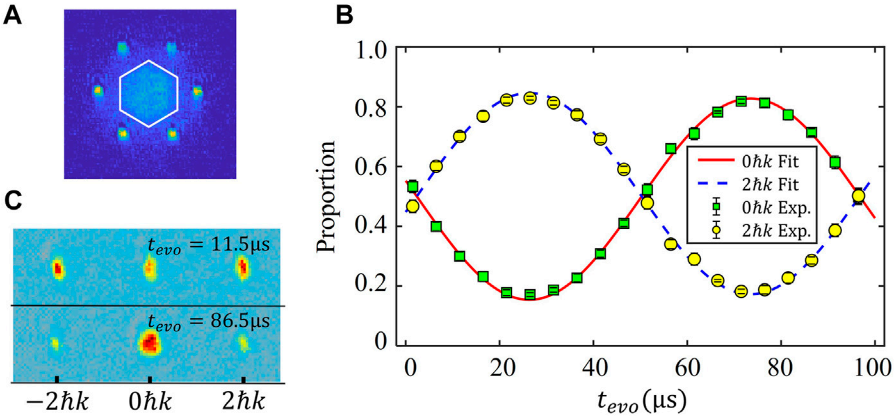

FIGURE 2
(A) Experimental result of atoms in D-band after band mapping process. The white hexagon is the boundary of the first Brillouin zone of the triangular lattice. The atoms are mainly distributed in the fourth Brillouin zone. **(B)** TOF quantum state tomography process. The initial state is a superposition Bloch state of the 1D optical lattice. After different evolution time t_{evo}, the atom number proportion at $0\hbar k$ and $\pm 2\hbar k$ are shown by the green and yellow points. **(C)** The momentum distribution of atoms at $t_{evo} = 11.5\mu s$ and $86.5\mu s$. The lattice depth is $V = 5E_r$.

The shortcut is a nonadiabatic coherent control composed of lattice pulse sequences [14]. The band swapping technique refers to quickly switching the structure of deep and shallow composite lattice, realizing the inversion of Bloch bands, and pumping atoms to the target band [9]. The manipulation of atoms in an optical lattice by amplitude modulation is another flexible way to control Bloch states coherently. In this method, the modulation with more than one frequency is applied to the lattice, couples the different orbitals, and realizes a large-momentum-transfer beam splitter [25]. We can manipulate any Bloch state of optical lattices with different configurations based on these methods. All the experiments in this paper are based on a Bose-Einstein-Condensate (BEC) of ^{87}Rb prepared in a hybrid trap with the harmonic trap frequencies $(\omega_x, \omega_y, \omega_z) = 2\pi \times (28, 55, 60)$ Hz [21]. The

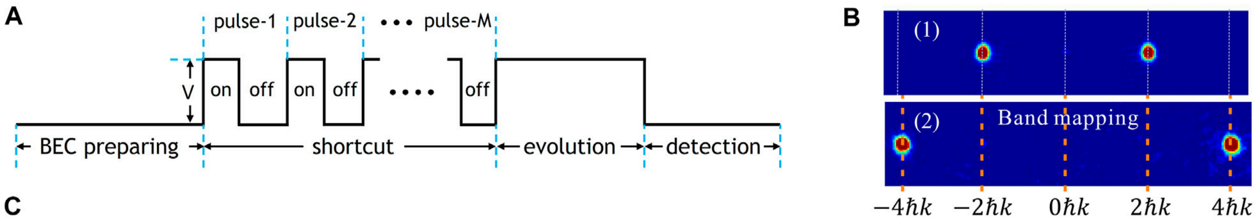

C

Target state	Lattice	Fidelity	pulse-1		pulse-2		pulse-3		pulse-4		pulse-5		pulse-6		pulse-7		pulse-8	
			on	off	on	off	on	off	on	off	on	off	on	off	on	off	on	off
D	1D 10Er	0.9999	25.0	28.1	39.0	2.7	X	X	X	X	X	X	X	X	X	X	X	X
D	Tri. 3Er	0.9995	13.5	11.5	49.0	9.5	8.5	56.5	11.0	11.0	X	X	X	X	X	X	X	X
G	1D 5Er	0.9919	32.0	39.0	40.0	14.0	41.0	13.0	13.0	14.0	13	13	13	14	11	43	11	12
S+D	1D 5Er	0.9999	47.0	35.0	3.0	17.0	X	X	X	X	X	X	X	X	X	X	X	X
P	1D 5Er	0.9869	31.2	39.4	28.8	20.0	24.4	20.0	20.0	24.0	X	X	X	X	X	X	X	X
F	1D 10Er	0.9948	27.0	15.0	30.0	42.0	12.0	13.0	62.0	13.0	18.0	57.0	15.0	42.0	X	X	X	X

unit: µs

FIGURE 3
(A) The timing diagram of the shortcut. **(B)** The band mapping result of D-band (top) and G-band (bottom) with zero quasi-momentum for 1D optical lattice. **(C)** The parameters of shortcut for different target states and optical lattice. The red time parameter is for the sequence of misplacement lattice for the P-band and F-band sequences. The quasi-momentum of all target states in this figure is zero. This symbol X indicates that there is no pulse.

experiments are mainly carried out in one dimensional (1D) and two dimensional (2D) triangular optical lattices. For 1D lattice, atoms are confined in more than 50 discrete pancakes with each pancakes containing 2000 atoms on average [10]. For triangular lattice, there are around 800 tubes with each tube containing 60 atoms on average [12].

The structure of this review is organized as follows. In section 2, we introduce the Bloch bands of atoms in optical lattices and review three methods for manipulating high orbital atoms in optical lattices. Then, we review the related applications based on these methods in section 3, including the atom-orbital qubit under nonadiabatic holonomic quantum control, Ramsey interferometry with trapped motional quantum states of the optical lattice. In section 4, we review the observations of exotic quantum states of p-orbital ultracold atoms. In section 5, we analyze the dynamical character of high orbital atoms in optical lattices. Finally, section 6 is the summary of this paper.

2 Manipulation of high orbital atoms in optical lattices

2.1 Bloch bands of atoms in optical lattice

An optical lattice is formed by the interference of a set of laser beams with electric field amplitude $\vec{E}_i$, which provides a spatially periodic potential for atoms:

$$V(\boldsymbol{r}) = \alpha \sum_{i,j} \boldsymbol{E}_i \cdot \boldsymbol{E}_j \cos\left(\left(\boldsymbol{k}_i - \boldsymbol{k}_j\right) \cdot \boldsymbol{r} + \left(\beta_i - \beta_j\right)\right) \tag{1}$$

where $\boldsymbol{k}_i$ is the wave number and β_i is the initial phase of laser beams i, and α is the coefficient related to detuning, atomic energy level, etc. For red detuned beams, α is negative. After neglecting the interactions between atoms, the Hamiltonian for single atom in optical lattice is $\hat{H} = \frac{\hat{p}^2}{2m} + V(\boldsymbol{r})$. According to the Bloch's theorem, the periodic potential can generate Bloch bands and Bloch states $\Psi_{n,q}$, which can be expressed by

$$\Psi_{n,\boldsymbol{q}}(\boldsymbol{r}) = u_{n,\boldsymbol{q}}(\boldsymbol{r}) e^{i\boldsymbol{q}\cdot\boldsymbol{r}}, \tag{2}$$

where $n = 1, 2, 3\ldots$ is the index of the Bloch bands, $\boldsymbol{q}$ is the quasi-momentum, and $u_{n,\boldsymbol{q}}$ is a periodic function. The bloch states $\Psi_{n,q}$, or the eigenstates of $\hat{H}$ can be projected onto a series of momentum eigenstates:

$$\Psi_{n,\boldsymbol{q}} = \sum_{\ell_1,\ell_2,\ell_3} c^{n,\boldsymbol{q}}_{\ell_1,\ell_2,\ell_3} \left|\hbar\left(\ell_1 \boldsymbol{b}_1 + \ell_2 \boldsymbol{b}_2 + \ell_3 \boldsymbol{b}_3\right) + \boldsymbol{q}\right\rangle \tag{3}$$

where $\boldsymbol{b}_i$ is the reciprocal lattice vector.

Figure 1 shows two different configurations of optical lattices, 1D lattice and triangular lattice. As for the 1D lattice in Figure 1A, the lattice constant is $d = \lambda/2$ and the band spectrum is shown in Figure 1B (when lattice depth $V = 5E_r$, where $E_r = \hbar^2 k^2/2m$ is the recoil energy and $k = 2\pi/\lambda$). From the bottom to the top of the spectrum, the Bloch bands are S-, P-, D-, F-, and G-band, corresponding to $n = 1, 2, 3, 4, 5$, respectively. In Figure 1C, the triangular lattice with lattice constant $2/3\lambda$, is constructed by three laser beams. The spectrum of this triangular lattice is different from that of the 1D lattice, where Bloch bands split

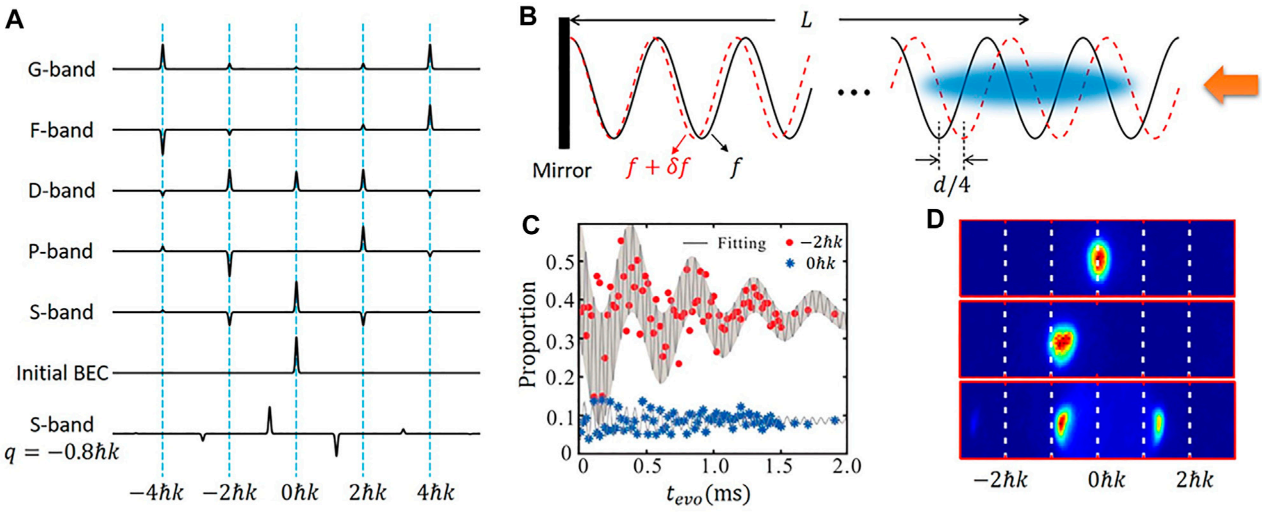

FIGURE 4
(A) From the bottom to the top, the solid lines represent the momentum distributions of different states (S-band with $q = -0.8\hbar k$, initial BEC with $p = 0$, S-, P-, D-, F-, and G-band with zero quasi-momentum). **(B)** Two 1D lattices with a $d/4$ position shift. **(C)** Population oscillations around momenta $-2\hbar k$ (red points) and $0\hbar k$ (blue stars). The solid lines are the fitting curves. **(D)** The experimental images: from top to bottom, the images are for the initial BEC with $p = 0$, the BECs with $p_0 = -0.8\hbar k$ after acceleration, and the final states $\Psi_{1,-0.8\hbar k}$.

into some different bands, as shown in Figure 1D (when the lattice depth is $3E_r$).

Before introducing the manipulation of the atoms in Bloch bands, we review the methods used in our experiments to probe the Bloch states. The first method is the band mapping technique [14, 15, 26–28]. In the experiment, if we switch off the lattice adiabatically within around 1 ms, the atoms in different bands can be mapped to different momentum components, measured after the time of flight (TOF). In addition, the value of quasi-momentum can be obtained from the position of atoms in corresponding Brillouin zones after the band mapping process and TOF. Figure 2A shows the band mapping result of atoms in a triangular lattice. Atoms are mainly distributed in the fourth Brillouin zone, corresponding to the D-band.

The band mapping method is easy to implement in the experiment, and the atomic population of different Bloch bands can be obtained. However, in this mapping process, the phase information of the Bloch state is lost. Then we use a TOF quantum state tomography (TOFQST) method to extract full information about the Bloch states [8]. For example, we use the TOFQST to detect the superposition of Bloch states in a 1D optical lattice with depth $V = 5E_r$. In the experiment, we let the state evolve in the static lattice for a certain time t_{evo}. Then we turn off the lattice diabatically and measure the momentum distribution after 31 ms TOF, which is shown in figure 2BC. By fitting the experimental data, we can obtain the full information of the states $\psi = \sqrt{0.493}\Psi_{1,0} + \sqrt{0.507}e^{i\cdot 0.987\pi}\Psi_{3,0}$.

2.2 Shortcut to manipulating atoms in optical lattice

2.2.1 Introduction of the shortcut method

This section demonstrates a shortcut method for manipulating atoms in different Bloch bands [14, 16–21]. This method is characterized by short time and high fidelity, which can directly transfer ultracold atoms from the ground state in the harmonic trap to any Bloch state, and accurately manipulate atoms of different orbitals in optical lattices. The shortcut is composed of a series of optical lattice pulse sequences, which is shown in 3A. Each pulse pulse-i consists of two parts. First, the lattice is turned on for t_j^{on}, and then the interval is t_j^{off}. The time $\{t_j^{\mathrm{on}}, t_j^{\mathrm{off}}\}$ are optimized to achieve the goal of manipulating quantum states.

We consider a general situation for transferring an arbitrary initial state $|\psi_i\rangle$ to a target state $|\psi_t\rangle$, where the states $|\psi_i\rangle$ and $|\psi_t\rangle$ can be the Bloch eigenstates or the superposition states. This shortcut applied to the initial state can be expressed as an evolution operator $\hat{U}_s = \prod_{j=M}^{1}\hat{U}_j^{t_j^{\mathrm{on}},t_j^{\mathrm{off}}}$. Here $\hat{U}_j$ represents evolution operator of the jth pulse, $\hat{U}_j = e^{-i(\hat{H}_j^{\mathrm{on}}t_j^{\mathrm{on}}+\hat{H}_j^{\mathrm{off}}t_j^{\mathrm{off}})}$, with $\hat{H}_j^{\mathrm{on}} = \frac{\hat{p}^2}{2m} + V(\boldsymbol{r})$ and $\hat{H}_j^{\mathrm{off}} = \frac{\hat{p}^2}{2m}$. The final state after the shortcut is $|\psi_f\rangle = \hat{U}_s|\psi_i\rangle$. Then we define the fidelity F of the manipulation

$$F = |\langle\psi_f|\psi_t\rangle| = |\langle\psi_f|\prod_{j=M}^{1}\hat{U}_j^{t_j^{\mathrm{on}},t_j^{\mathrm{off}}}|\psi_i\rangle|. \tag{4}$$

By optimizing the pulse sequences $\{t_j^{\mathrm{on}}, t_j^{\mathrm{off}}\}$ to maximize F, the operation process with high fidelity for manipulating Bloch states or high orbital atoms in an optical lattice is obtained.

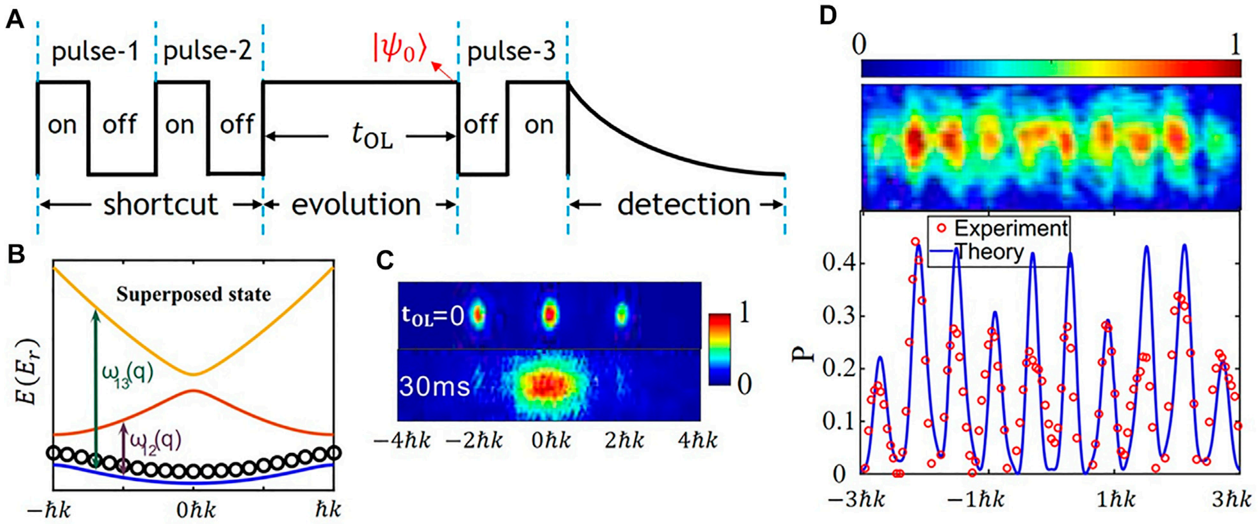

FIGURE 5
(A) Time sequence: after the first two pulses and the 30 ms holding time in the optical lattice, the state becomes the superposition of the Bloch states in S-band with quasi-momentum taking the values throughout the first Brillouin zone, denoted as $|\psi(0)\rangle$. **(B)** The superposition of Bloch states of S-band spreading the whole S-band. **(C)** The comparison of the experimental results between t_{OL} = 0 ms and t_{OL} = 30 ms. These results are obtained after the sequence in **(A)** but without pulse-3. **(D)** Patterns with ten main peaks for the experimental measurements (the red circles) and the theoretical curves (the solid blue line).

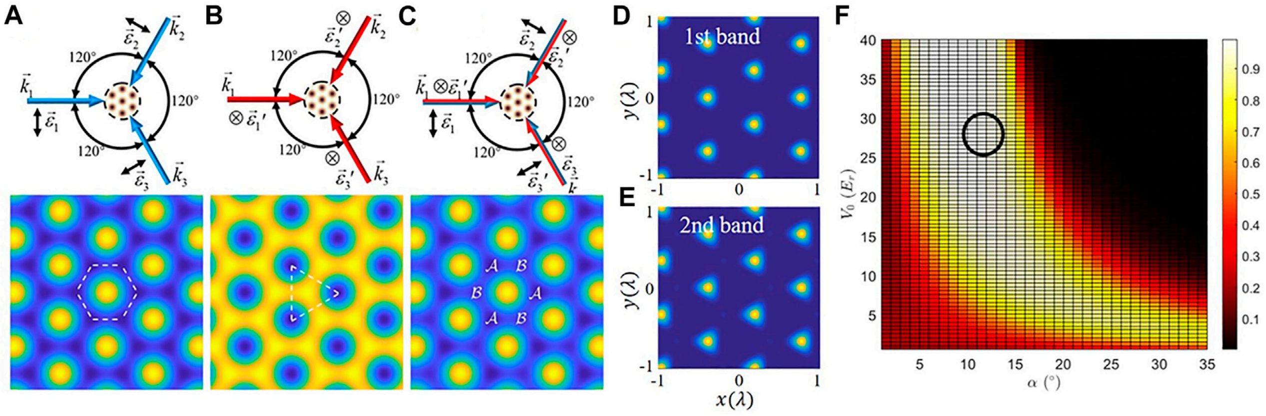

FIGURE 6
The arrangement of the laser beams forms the honeycomb **(A)** and triangular **(B)** lattice. The two groups of sublattices form a composite hexagonal lattice **(C)**, which consists $\mathcal{A}$ and $\mathcal{B}$ wells. **(D)** and **(E)** represent the wave function distributions in the real space of the ground band and the second band with zero quasi-momentum, respectively. **(F)** The wavefunction overlap with different lattice depth and light intensity ratios.

To verify the effectiveness of the shortcut, we demonstrate some experimental results in Figures 2, 3. In Figure 3C, we list some pulse sequences for manipulating Bloch states, where the initial states are all the ground states of the harmonic trap, $|p = 0\rangle$ zero momentum state. For 1D optical lattice, we achieve to transfer atoms from zero momentum state to D-band, G-band, and the superposition states of S and D band with zero quasi-momentum, which corresponds to Figure 3B1B2, and Figure 2BC, and this theory fidelity is more than 99% [14]. For the D-band of the triangular optical lattice with depth $V = 3E_r$, we give the shortcut sequence with 99.95% fidelity in Figure 3C, and the experimental band mapping results is shown in Figure 2A [21].

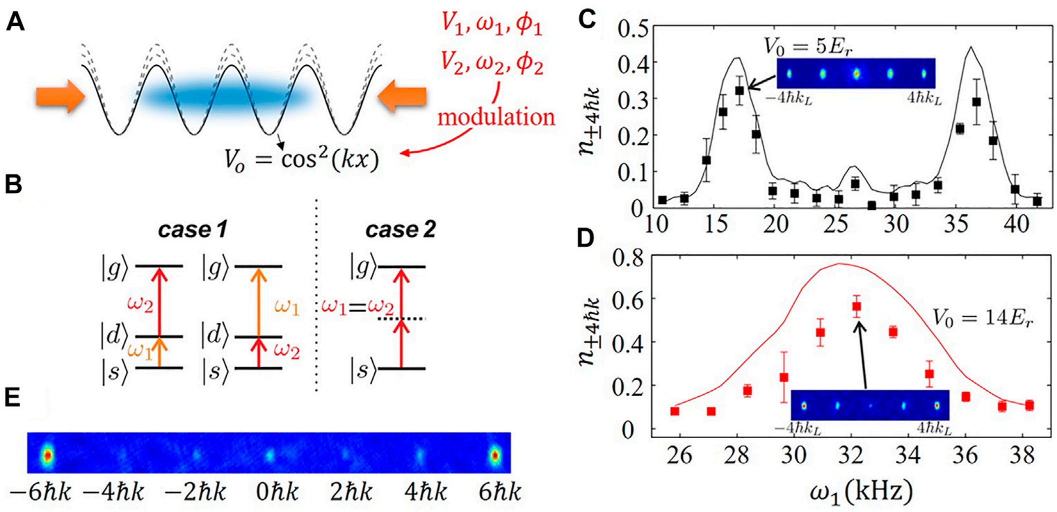

FIGURE 7
(A) Schematic diagram of the polychromatic amplitude modulation lattice. **(B)** Two special cases in detecting the transfer population spectrum. In case 1, absorption of photons with ω_1 or ω_2 is resonant with D-band. In case 2, two frequencies are equal. Spectrum for the population on $\pm 4\hbar k$ states with increasing of modulation frequency ω_1 for **(C)** $V_0 = 5E_r$ with $V_1 = 1.4E_r$, $V_2 = 1.6E_r$, modulation time $t = 300\mu s$, and for **(D)** $V_0 = 14E_r$ with $V_1 = V_2 = 2.5E_r$, and $t = 150\mu s$. **(E)** A large-momentum-transfer beam splitter with a separation of $12\hbar k$.

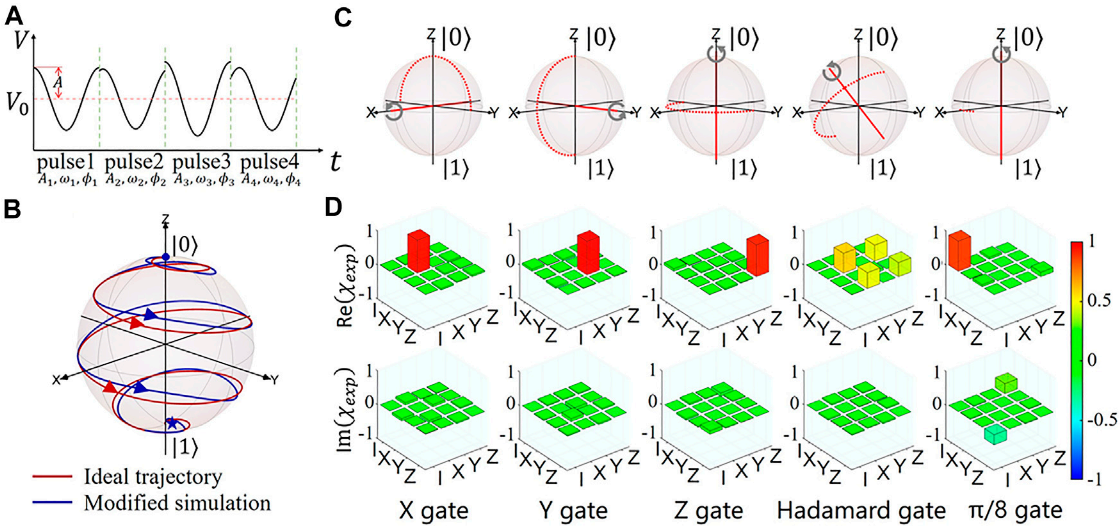

FIGURE 8
(A) The pulse sequence of the holonomic gate. **(B)** Simulated time evolution of the $|0\rangle$ on the Bloch sphere under the holonomic X gate. **(C)** The schematic illustration of the quantum process. **(D)** Process matrices of the implemented holonomic X, Y, Z, Hadamard, and $\pi/8$ gates by quantum process tomography measurements.

2.2.2 Manipulating bloch states with different symmetries

The symmetry of Bloch states with different energy bands and quasi momentum is different. For example, in the 1D optical lattice, Eq. 3 is rewritten as

$$\Psi_{n,q} = \sum_{\ell} c_{\ell}^{n,q} |\ell \cdot 2\hbar k + q\rangle. \tag{5}$$

The parity of Bloch states on S-, D-, and G-bands with zero quasi-momentum is even, which is shown in Figure 4A. On the contrary, the P- and F-bands with zero quasi-momentum

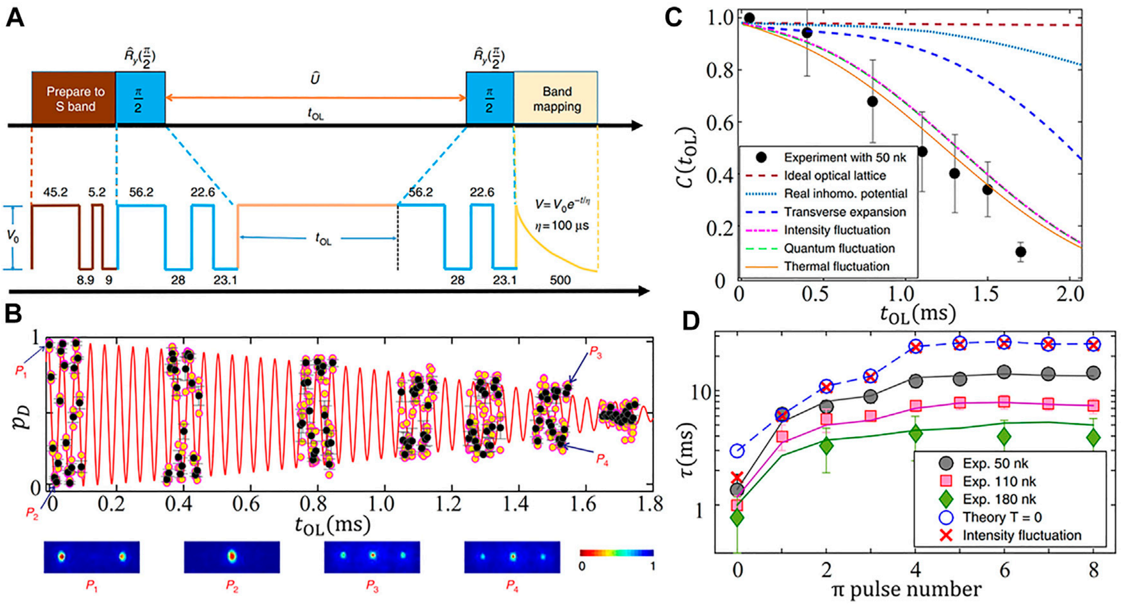

FIGURE 9
(A) Time sequences for the Ramsey interferometry. The atoms are first loaded into the S-band, followed by the RI sequence $\pi/2$-pulse, holding time t_{OL}, and the second $\pi/2$-pulse. Finally, band mapping is used to detect the number of atoms in the different bands. The used sequences designed by the shortcut method are shown in the figures (unit: μs). **(B)** The oscillation of the population of atoms in the D-band p_D. The images below show typical time of flight pictures after band mapping. **(C)** The experimental contrast (black points) and the theoretical calculation for $V_0 = 10E_r$. In theory, we begin with an ideal optical lattice and gradually add the effect of lattice inhomogeneity, transverse expansion of atom cloud, intensity fluctuation of laser amplitude, quantum fluctuation, and thermal fluctuation. **(D)** Coherence time τ vs the number of applied π-pulse n with different temperatures.

are odd parity. Moreover, the symmetries of Bloch states with non-zero quasi-momentum are also different from that of zero quasi-momentum states. On the other hand, the symmetries of the 1D optical lattice and the initial states $|\boldsymbol{p} = 0\rangle$ are even. Hence, we can easily prepare and manipulate even parity Bloch states, such as S-, D-, and G-bands with zero quasi-momentum. However, it is challenging to prepare states with different parity or change the symmetry. In order to expand the application scope of the shortcut, we propose two methods.

The first method is to use two misplacement lattices [10, 14, 18]. In experiments, we realize this configuration through a reflective optical path and two laser beams with frequency difference δf, as shown in Figure 4B. When the distance L between BECs and mirror and laser frequency f are fixed, we can realize the misplacement of $d/4$ of the two sets of standing wave optical lattices by adjusting the frequency difference δf. Because $\delta f \ll f$, the lattice constants of the two lattices can be regarded as the same. As an example, we transfer atoms from $|\boldsymbol{p} = 0\rangle$ to P-band with zero quasi-momentum $\Psi_{2,0}$. We apply two sets of shortcut sequences in turn. The first one is of the lattice with frequency $f + \delta f$, and the second is of f. When the first sequence is switched to the second, each momentum state component $c_\ell|\ell \cdot 2\hbar k\rangle$ will be attached with a phase and becomes $e^{i\cdot\frac{\pi}{2}\ell}c_\ell|\ell\cdot 2\hbar k\rangle$. We design the first sequence to make $c_\ell = 0$ for $\ell = 2, 4, 6 \ldots$ and keep only c_ℓ for $\ell = 1, 3, 4 \ldots$. So the result is that after the first sequence, the quantum state changes to odd parity, $c_\ell = -c_{-\ell}$ for all ℓ. Finally, we use the second sequence to adjust this odd parity state to $\Psi_{2,0}$. In the experiment, we use TOFQST to detect the final state in the 1D lattice with depth $V = 5E_r$, shown in Figure 4C, and the experimental fidelity is more than 90%. The parameters of these sequences are shown in Figure 3C [18]. Similarly, we can also use this scheme to load atoms into the F-band [14], and the sequence is shown in Figure 3C.

The second method is to change the symmetry of the initial state. For example, we demonstrate how to transfer atoms from initial BEC to non-zero quasi-momentum Bloch state in S-band. As shown in Figure 4D, the atoms with $p = 0$ is accelerated to obtain a momentum $p_0 = -0.8\hbar k$. Immediately afterward, the designed shortcut sequence is used to transfer atoms into the S-band at $-0.8\hbar k$ quasi-momentum. The bottom figure of 4D is the momentum distribution of the final state in the experiment [14].

Hence, our shortcut method can be applied to manipulate arbitrary Bloch states in any Bloch band within a very short time and with high fidelity. Moreover, This shortcut can be applied to optical lattices with different configurations.

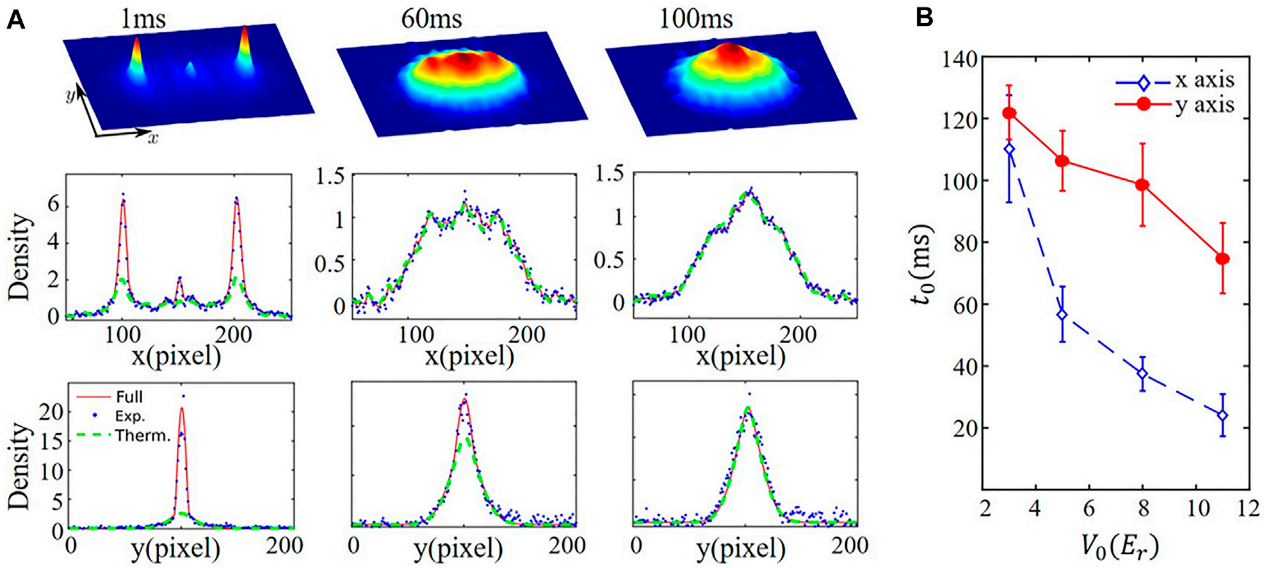

FIGURE 10
(A) Momentum distributions measured at three different holding times t_{evo} = 1, 60, 100 ms, along different directions (with V_0 = 5E_r). The corresponding distribution along the *x*-direction is given in the second row with blue dots. The solid red line gives a full fitting line, while the green dashed line gives the distribution of the thermal component. The third row shows the atomic distribution in the *y*-direction for images measured by probe 2. **(B)** The time t_0 for the atoms to lose coherence in lattice and pancake directions with different optical-lattice depths. The blue diamonds are for the *x*-direction (lattice) by probe one and the dotted points are for the *y*-direction (pancake). The optical lattice is the 1D lattice.

2.2.3 Atomic momentum patterns with narrower intervals

The previous method is mainly for the Bloch state with a certain single quasi-momentum, and the intervals of the momentum peaks are $2\hbar k$ (for 1D optical lattice). The manipulation of the entire Bloch band and the preparation of narrow momentum peak distribution will also appear in many applications, such as the atom interferometer [29–31]. However, the manipulation of this superposition state with different quasimomenta is seldom studied [19]. In this section, we expand the shortcut to manipulating the superposed Bloch states with different quasi-momenta. Figure 5A shows the time sequence for the manipulating process of the superposed states. The first challenge is to prepare the superposition states $|\psi(0)\rangle$ with different quasi-momentum that spread the whole S-band, as shown in Figure 5B. In the experiment, we first prepare a superposed state $\frac{1}{\sqrt{2}}(\Psi_{1,0}+\Psi_{3,0})$ by shortcut and hold the lattice for a time t_{OL}. When t_{OL} = 30 ms, the atoms are almost all in the first Brillouin zone of S-band, which is due to collisions during the holding time, as shown in Figure 5C [19].

The next challenge is how to design the pulse-3 in Figure 5A for atomic momentum patterns with narrower intervals. First, we analyze the action of the pulse on $|\psi(0)\rangle$. The initial state can be expressed as

$$|\psi(0)\rangle = \frac{1}{\sqrt{N}}\sum_{q=-\hbar k}^{\hbar k}\Psi_{1,q}. \tag{6}$$

After the pulse-3 (with interal t_3^{off} and duration t_3^{on}), the momentum distribution $P(0, q)$ is

$$P(0,q) \approx C_1 + C_2\cos\left(W_{1,0}t_3^{\mathrm{off}}\right) + C_3\cos\left(W_{-1,0}t_3^{\mathrm{off}}\right) + C_4\cos\left(\omega_{1,2}t_3^{\mathrm{on}}\right) + C_5\cos\left(\omega_{1,3}t_3^{\mathrm{on}}\right), \tag{7}$$

where C_i is the corrresponding amplitudes from the numerical calculations, $W_{\ell,\ell'} = \hbar^2\,[(2\ell k+q)^2-(2\ell' k+q)^2]/2m$ and $\omega_{n,n'} = E^{n,q} - E^{n',q}$ (the band gap between n and n' band at quasi-momentum q) corresponds to the energy difference between different momentum states and Bloch states, respectively. By designing the t_3^{off} and t_3^{on}, we can get the momentum patterns $P(0, q)$ with narrower intervals. In Figure 5D, we use the sequence $t_3^{\mathrm{off}} = 118\mu s$ and $t_3^{\mathrm{on}} = 19\mu s$, and obtain ten main peaks with $0.6\hbar k$ interval for lattice depth $10E_r$ [19].

2.3 Band swapping tecnique for loading atoms into high bands

The band swapping technique is another method for loading atoms into high Bloch bands, which can be used to study the characteristics of Bloch bands and orbits. This technique is first proposed in [9] to load atoms into the P-band of a checkerboard

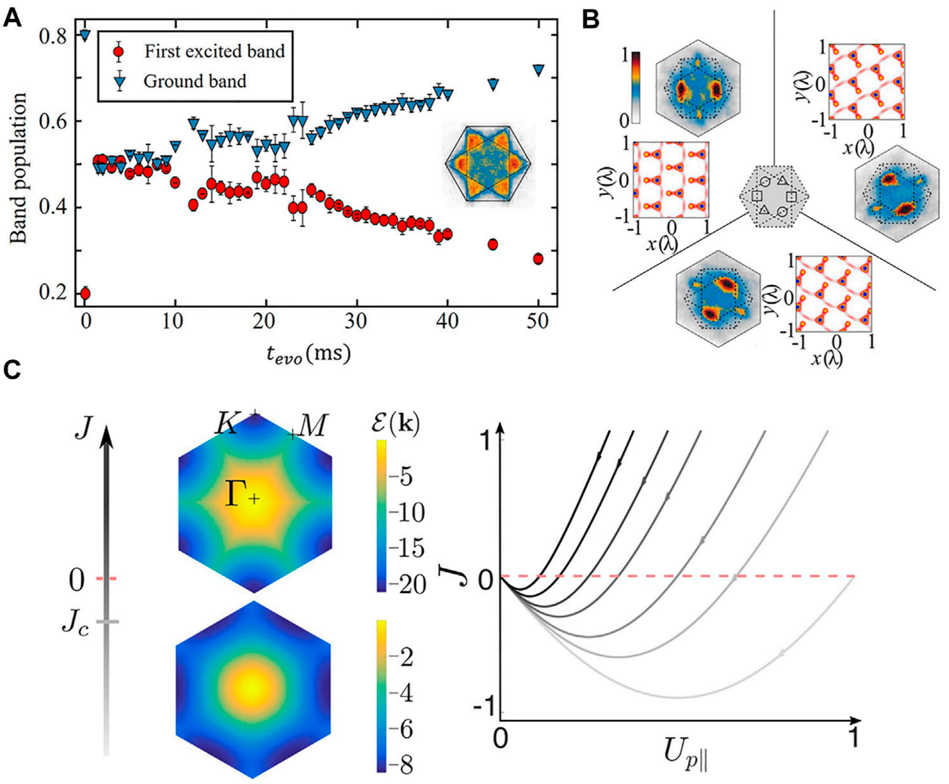

FIGURE 11
(A) The measured time evolution of the atomic population in the ground and the second bands of the hexagonal optical lattice. **(B)** The averaged momentum distribution for three symmetries. **(C)** Theoretical quantum phase transitions varying the orbital Josephson coupling. The energy $\varepsilon(\boldsymbol{k})$ for a plane-wave condensate at a lattice momentum $\boldsymbol{k}$. The energy $\varepsilon(\boldsymbol{k})$ has minima at K (M) points for $J > J_c$ ($J < J_c$). The right figure is the sketch of the renormalization of the p-orbital couplings to low energy.

square lattice and is also applicable to other configurations of optical lattices. The key to realizing this technology is constructing a controllable composite optical lattice, including deep and shallow wells. Compared with the shortcut method, the band swapping technique is more suitable for the study of ground state or metastable state.

Here, we take a hexagonal lattice as an example to show the process of band swapping [12]. We choose triangle lattice because it is more complex than square lattice, and it is impossible to separate variables in two directions directly. Three intersecting far-red-detuned laser beams form the hexagonal lattice in the $x-y$ plane with an enclosing angle of 120°. Each beam is formed by combining two linearly polarized lights with polarization directions oriented in the $x-y$ plane (denoted as ϵ light) and along the z axis (denoted as ϵ' light), respectively. The ϵ light form a honeycomb lattice as shown in Figure 6A. The ϵ' light form a triangular lattice as shown in Figure 6B. The superposition of the two groups of optical lattices is the configuration shown in Figure 6C, which consists of two wells with different depths (denoted as $\mathcal{A}$ and $\mathcal{B}$). The optical potential takes the form

$$V(\boldsymbol{r}) = -V_{\epsilon'}\sum_{i,j}\cos\left[\left(\boldsymbol{k}_i-\boldsymbol{k}_j\right)\cdot\boldsymbol{r}+\theta_j-\theta_i\right] + \frac{1}{2}V_{\epsilon}\sum_{i,j}\cos\left[\left(\boldsymbol{k}_i-\boldsymbol{k}_j\right)\cdot\boldsymbol{r}\right], \tag{8}$$

where $\boldsymbol{k}_1 = (\sqrt{3}\,\pi, -\pi)/\lambda$, $\boldsymbol{k}_2 = (-\sqrt{3}\,\pi, -\pi)/\lambda$, $\boldsymbol{k}_3 = (0, 2\pi)/\lambda$, and V_ϵ ($V_{\epsilon'}$) is the depth of the honeycomb (triangular) lattice. The depth difference between the two wells $\mathcal{A}$ and $\mathcal{B}$ can be adjusted by the ϵ-to-ϵ' light intensity ratio (denoted as $\tan^2\alpha = V_{\epsilon'}/V_\epsilon$), and the relative phases $\theta_{1,2,3}$. First, we adiabatically load the BEC into the ground band with zero quasi-momentum of the optical lattice. The phase differences are initially set to be $\theta_{1,2,3} = (2\pi/3, 4\pi/3, 0)$, for which the $\mathcal{B}$ wells are deeper than the $\mathcal{A}$ wells. In real space, atoms mainly reside in the s orbitals of $\mathcal{B}$ wells as shown in Figure 6D. Then we switch the relative phases rapidly to $\theta_{1,2,3} = (4\pi/3, 2\pi/3, 0)$, making $\mathcal{A}$ wells much lower than $\mathcal{B}$. In this way, the atomic sample is directly projected onto the excited band. The key is to select appropriate parameters (ϵ' and ϵ) to make the distribution of the wave function (Figure 6D) of the ground band before the switch consistent with that (Figure 6E) of the second band after the switch (at zero quasi-momentum). In

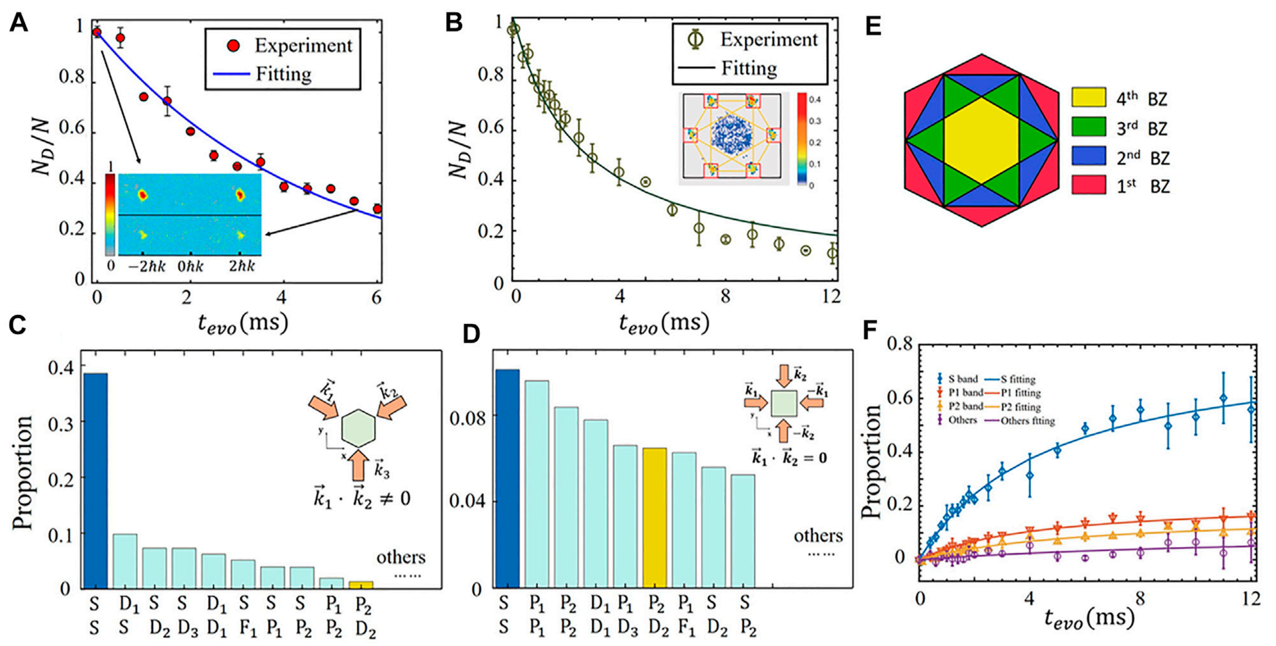

FIGURE 12
(A) The proportion of D-band over the evolution time in 1D lattice. **(B)** The proportion of the first D-band (D1-band) in the triangular lattice. The proportions of several main scattering channels are shown in **(C)** (triangular lattice) and **(D)** (square lattice). The inserts show the diagram of a square optical lattice and triangular optical lattice. **(E)** Schematic diagram of the first four Brillouin zones of a triangular optical lattice. Yellow, green, blue, and red areas represent 1*st*, 2*nd*, 3*rd*, 4*th* BZ, respectively. **(F)** The atomic proportion in S (P1, P2 band, and others), of which the solid lines with the same color fit lines.

our experiment, the range of parameter selection is in the black circle of Figure 6F, where the total lattice depth is $30E_r$ and $\alpha = 14°$. As shown in Figure 11A, after this band swapping process, the atoms are pumped into the second band [12].

2.4 Manipulation of atoms in optical lattice by amplitude modulation

The modulation with more than one frequency component to optical lattices provides a flexible way to control quantum states coherently [25]. In this section, we demonstrate bi-frequency modulations, which can be used to couple the S- and G-band of 1D optical lattice and realize a large-momentum-transfer beam splitter.

For atoms in an amplitude modulated lattice system along the x axis, as schematically shown in Figure 7A, the time-dependent Hamiltonian can be written as

$$H(t) = \frac{p_x^2}{2m} + V_0 \cos^2(kx) + \sum_i V_i \cos(\omega_i t + \phi_i) \cos^2(kx). \quad (9)$$

The second term on the right hand represents optical lattice potential without modulation. The last term is the amplitude modulation with modulation amplitude V_i, the frequency ω_i, and the phase ϕ_i of each frequency component [25].

According to the Floquet's theorem, a bi-frequency modulation induced two-photon process between S- and D-band is described by an effective Hamiltonian H_{SG} as

$$H_{SG} = \begin{pmatrix} E_S & e^{i\phi_1} V_1 \Omega_{SD} & e^{i\phi_2} V_2 \Omega_{SD} & 0 & 0 & 0 \\ e^{-i\phi_1} V_1 \Omega_{SD}^* & E_D - \hbar\omega_1 & 0 & e^{i\phi_2} V_2 \Omega_{DG} & e^{i\phi_1} V_1 \Omega_{DG} & 0 \\ e^{-i\phi_2} V_2 \Omega_{SD}^* & 0 & E_D - \hbar\omega_2 & e^{i\phi_1} V_1 \Omega_{DG} & 0 & e^{i\phi_2} V_2 \Omega_{DG} \\ 0 & e^{-i\phi_2} V_2 \Omega_{DG}^* & e^{-i\phi_1} V_1 \Omega_{DG}^* & E_G - \hbar(\omega_1 + \omega_2) & 0 & 0 \\ 0 & e^{-i\phi_1} V_1 \Omega_{DG}^* & 0 & 0 & E_G - 2\hbar\omega_1 & 0 \\ 0 & 0 & e^{-i\phi_2} V_2 \Omega_{DG}^* & 0 & 0 & E_G - 2\hbar\omega_2 \end{pmatrix}, \quad (10)$$

where $\Omega_{nn'} = \langle \Psi_{n,0} | \cos^2(kx) | \Psi_{n',0} \rangle$ with $\Psi_{n,0}$ the Bloch states on n band at zero quasi-momentum. We include six nearly degenerate states considering four main process in the excitation, which are $|E_S\rangle$, $|E_D - \hbar\omega_1\rangle$, $|E_D - \hbar\omega_2\rangle$, $|E_G - \hbar(\omega_1 + \omega_2)\rangle$, $|E_G - 2\hbar\omega_1\rangle$, and $|E_G - 2\hbar\omega_2\rangle$. Using this basis a general state $(\nu_1, V_2, V_3, V_4, \nu_5, \nu_6)^T$ gives complex coefficient of the six dressed states. Population on S-band is $|\nu_1|^2$, while population on G-band is $|\nu_4 e^{i(\omega_1+\omega_2)t} + \nu_5 e^{2i\omega_1 t} + \nu_6 2i\omega_2 t|^2$, given by coherent superposition of all G band states dressed with different Floquet photons. This effective model provides us a better understanding of the mutiphoton process. However, in the calculation more states associated with higher order processes could be included to get a more accurate result.

In the experiment, we keep the frequences ω_1 and ω_2 satisfying $\omega_1 + \omega_2 = \omega_{SG}$. According to Eq. 10, there are two cases which would benefit the excitation process (shown in Figure 7B).

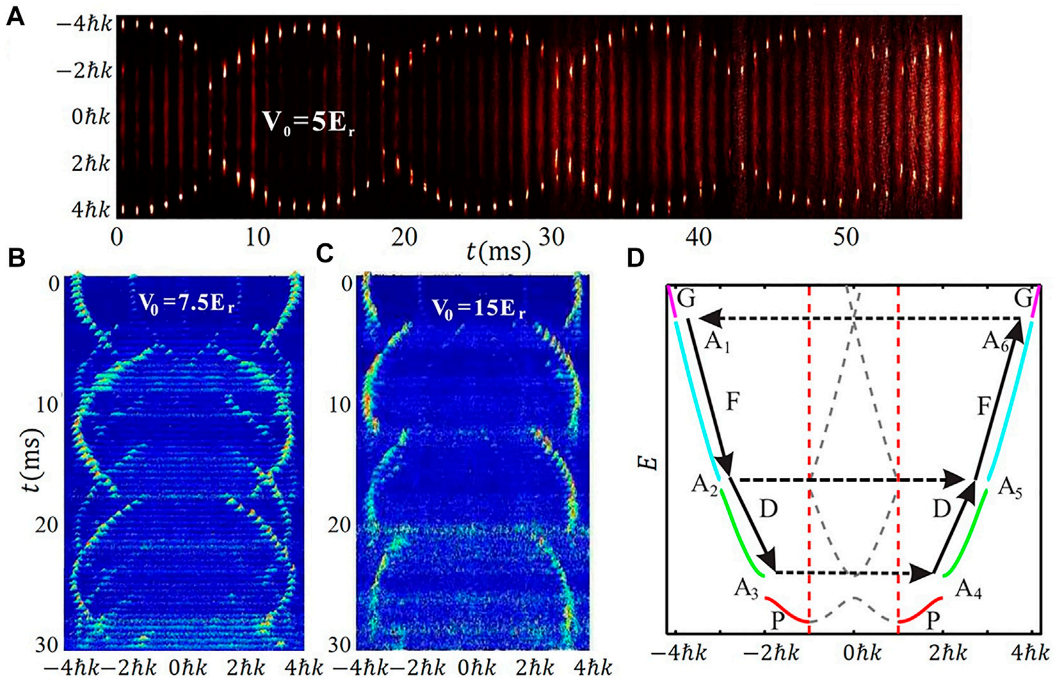

FIGURE 13
Quantum oscillations of the BECs in higher bands of the 1D optical lattice. Experimental results in momentum space with lattice depth **(A)** $5E_r$, **(B)** $7.5E_r$, and **(C)** $15E_r$. **(D)** Schematic of extended Bloch bands of the 1D optical lattice.

Case 1: Resonant two-photon process. When $\omega_1 = \omega_{\mathrm{SD}}$ or $\omega_2 = \omega_{\mathrm{SD}}$, atoms are transferred from $\Psi_{1,0}$ to $\Psi_{5,0}$ with the assistance of D band as an intermediate band.

Case 2: Equal frequency two-photon process. When $\omega_1 = \omega_2 = \omega_{SG}/2$, two modulations with the same frequency can be added together, and the coupling strength of the process is doubled.

In the experiments, we sweep the frequency ω_1 for different lattice depth $V = 5E_r$ and $14E_r$, and measure the population on momentum states $\pm 4\hbar k$ that relect the transfer rate to G-band. For $V = 5E_r$, in Figure 7C, two peaks appear at $\omega_1 = \omega_{\mathrm{SD}}$ and $\omega_2 = \omega_{\mathrm{SD}}$ follows **Case 1**. And the central peak at frequency $\omega_1 = \omega_2 = \omega_{SG}/2$ following **Case 2** is much lower than **Case 1**. For $V = 14E_r$, only one peak is measured in Figure 7D, which means **Case 1** and **Case 2** are fulfilled simultaneously. Under this condition, the coupling is greatly enhanced. This bi-frequency modulation can also be applied to realize a large-momentum-transfer beam splitter, such as a distribution at $\pm 6\hbar k$. We choose the frequency $\omega_1 = \omega_{\mathrm{SD}} = \omega_{DG}$ and $\omega_2 = \omega_{GI}$ (with I the seventh Bloch band). The experimental result is shown in Figure 7E [25].

This polychromatic amplitude modulation can be further improved to achieve more complex manipulation. We can control each period of the modulation waveform separately. Each period can be regarded as a pulse, which is shown in Figure 8A. The modulation amplitude A_i, phase ϕ_i, and frequency ω_i are optimized to achieve more accurate Bloch states manipulation, such as holonomic quantum control [8], which will be discussed in detail next section.

In this section, we list three methods for manipulating ultracold atoms of high orbitals in optical lattices. The shortcut method is characterized by short time and high fidelity, which can directly transfer ultracold atoms from the ground state in the harmonic trap to any Bloch state, and accurately manipulate atoms of different orbitals in optical lattices. This method can be used to construct atomic orbital interferometers and qubits and to study the dynamic properties of high orbital atoms in optical lattices. The band swapping technique considers the interaction between atoms and the additional potential trap (such as harmonic trap) besides the optical lattice, which is more suitable for studying the ground and metastable states of the system. The amplitude modulation focuses on coupling different Bloch bands and can be used to realize quantum gates and the large-momentum-transfer beam splitter.

3 Application of manipulating high orbital atoms in optical lattices

3.1 Atom-orbital qubit under nonadiabatic holonomic quantum control

In section 2.4, we mentioned that the amplitude modulation pulses could realize the holonomic quantum control. This section

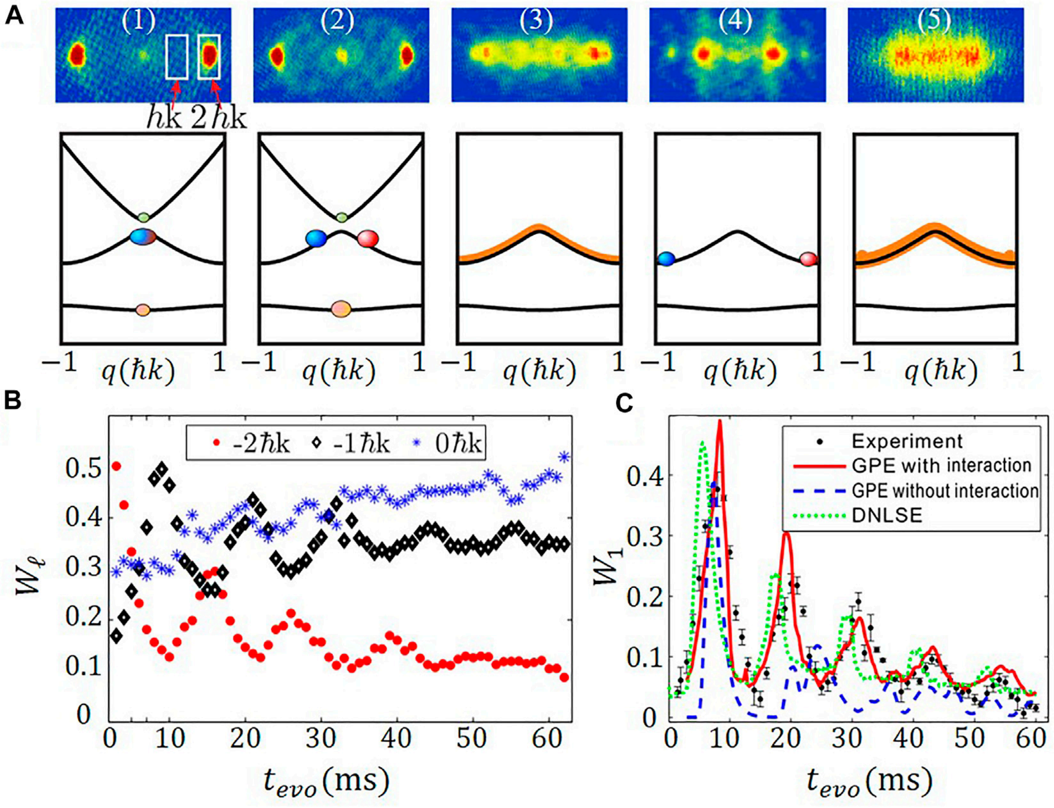

FIGURE 14
(A) First row: the measured momentum distributions of the BEC in the P-band of the 1D lattice at different holding times (0 ms, 2 ms, 5 ms, 7 ms, and 30 ms), and the white rectangles are the region for us to calculate the proportion of different momentum states; the second row: schematic illustration of the corresponding population distributions in the Bloch band. **(B)** Population oscillations around momenta $0\hbar k$ (blue stars), $-\hbar k$ (black diamonds), and $-2\hbar k$ (red dots) with $t > 2$ ms. The oscillation period is about 14.9 ms with $V = 5E_r$. **(C)** Population for $\hbar k$ vs. time t_{evo}. The experimental results and theoretical simulations with and without the interaction correspond to the black dots with an error bar, red solid curves, and blue dashed curves, respectively.

demonstrates an atom-orbital qubit by manipulating the s and d orbitals of BECs in the 1D optical lattice. Moreover, we achieve noise-resilient single-qubit gates by performing holonomic quantum control, allowing geometrical protection. The atom-orbital qubit and quantum control are based on the shortcut and amplitude modulation methods [8].

As shown in Figure 1A, the band gap between S and D band ($5.23E_r$) is much smaller than that between D and G band ($11.50E_r$) for optical lattice depth $V = 5E_r$. With leakage to other bands neglected, the system corresponds to a two-level system, defining our atom-orbital qubit, $\Psi_{3,0}$ and $\Psi_{1,0}$ being orbital states identified as the qubit basis states $|0\rangle$ and $|1\rangle$. The 1D optical lattice potential is $V_p(x) = V_0 \cos^2(kx)$, which is formed by 1,064 nm laser beams. We use shortcut method to initialize the qubit to an arbitrary state, $|\psi\rangle = \cos\theta|0\rangle + \sin\theta e^{i\varphi}|1\rangle$. By TOFQST, we extract the fidelities of initial states $\{|0\rangle, |1\rangle, \frac{1}{\sqrt{2}}(|0\rangle + |1\rangle), \frac{1}{\sqrt{2}}(|0\rangle - |1\rangle), \frac{1}{\sqrt{2}}(|0\rangle + i|1\rangle), \frac{1}{\sqrt{2}}(|0\rangle - i|1\rangle)\}$, and the averaged fidelity is 99.72 (7)%. The relaxation time and dephasing time are 4.5 ± 0.1 ms and 2.1 ± 0.1 ms, respectively [8].

The modulation pulses on potential takes form

$$\Delta V(x,t) = A\sin(\omega t + \phi)V_p(x), \tag{11}$$

where amplitude A, phase ϕ and frequency ω programmable in our experiment. After a rotating wave approximation, we have a qubit control Hamiltonian $H(t)$

$$H(t) = \frac{1}{2}\Delta\sigma_z + \frac{1}{2}\lambda\left[-\cos(\omega t + \phi)\sigma_y + \sin(\omega t + \phi)\sigma_x\right], \tag{12}$$

with Δ the gap between the S and D bands at zero quasi-momentum, and the induced coupling by the lattice modulation

$$\lambda = A\int dx V_p(x)\Psi_{3,0}(x)\Psi_{1,0}(x), \tag{13}$$

We implement nonadiabatic holonomic orbital control base on dynamical invariant of the Hamiltonian in Equation (12). To exploit the geometrical protection, the dynamical phase has to be canceled, which corresponds to

$$\lambda^2 + \Delta(\Delta - \omega) = 0. \tag{14}$$

Then, we calculate a control sequence of lattice modulation frequency, amplitude, and phase, denoted by $\Theta \equiv (\omega_i, A_i, \phi_i)$. After orbital leakage elimination, the gate fidelity is improved to above 98% in the multiorbital numerical simulation. The simulated time evolution of the $|0\rangle$ on the Bloch sphere under the holonomic X gate is shown in Figure 8B. Besides, we also design the holonomic X, Y, Z, Hadamard, and $\pi/8$ gates. We further perform quantum process tomography to characterize the holonomic quantum gates, which is shown in Figure 8D. The measured quantum process fidelities are 98.47(9)%, 98.35(11)%, 97.81(13)%, 98.53(8)%, 98.63(15)%, and 98.63 (15)%, for the X, Y, Z, Hadamard, and $\pi/8$ gates, respectively [8]. There are four main factors limiting fidelities: a) orbital leakage: although we have greatly eliminated the band leakage, there are still a small number of atoms in high bands that affect the current fidelities. b) De-phasing mechanism: the quasi-momentum broadening of BEC and the non-uniformity of light intensity of optical lattice will lead to the de-phasing effect, which causes the decrease of fidelity. c) Atom interaction: As discussed in section 5.1, atoms in the D band will be scattered to the ground band due to collision, which will affect the fidelities. d) Error caused by measurement: It is mainly caused by the vibration of the imaging system during the absorption imaging process. For a) and b), we can overcome them through super lattice or more complex lattice. We can construct a more perfect two-level so that the G-band is far away from the D-band. Further, by constructing flat bands, the dephasing effect brought by momentum broadening and non-uniformity of the light can be suppressed, so as to greatly improve the fidelity. If we want to further improve the fidelity, we need to consider the factors of c) and d). We can use Feshbach resonance technology to reduce the atomic interaction, and reduce the imaging error through the improvement of the mechanical structure of the imaging system.

3.2 Ramsey interferometry with trapped motional quantum states of the optical lattice

Ramsey interferometry (RI) using internal electronic or nuclear states find wide applications in science and engineering [32]. In this section, we review a new RI with the S- and D-bands in an optical lattice [13], similar to Figure 1B (in this section, the laser wavelength of the optical lattice is 852 nm, and the lattice depth is $10E_r$). A key challenge for constructing this RI is to realize π-pulse and $\pi/2$-pulse analogous to those in conventional RIs. In section 3.1, we have achieved the arbitrary holonomic quantum control, which ensures the noise-resilient but increases the control time. However, we want to study the quantum many-body lattice dynamics by this RI, which requires the time duration of the π-pulse and $\pi/2$-pulse to be as short as possible. Hence, we use the shortcut method to design these pulse sequences.

The full time sequence for RI with two shortcut $\pi/2$-pulses $\hat{R}(\pi/2)$ we use in experiments is shown in Figure 9A. First the atoms in the harmonic trap are transferred into the S-band by shortcut, then the first pulse $\hat{R}(\pi/2)$ is applied to prepare an initial superposition state $\frac{1}{\sqrt{2}}(\Psi_{1,0} + \Psi_{3,0})$. After evolution in the optical lattice for time t_{OL} and a second $\pi/2$-pulse, the final state can be expressed as $\Psi_f = a_S\Psi_{1,0} + a_D\Psi_{3,0}$. Then we apply band mapping to read out the final state, and obtain the population of atoms in S (D) band, denoted as N_S (N_D). We define the signal of this RI as $p_D(t_{OL}) = N_D/(N_S + N_D)$. For the ideal single-atom system, where the imperfection and decoherence can be neglected, the signal $p_D(t_{OL}) = [1 + \cos(\omega t_{OL} + \phi)]/2$, with ω corresponding to the energy difference between $\Psi_{1,0}$ and $\Psi_{3,0}$. However, when t_{OL} gets longer, the oscillation amplitude decays, as shown in Figure 9B. The contrast $C(t_{OL})$ can be obtained by fitting the amplitude of oscillation $p_D(t_{OL})$ with

$$p_D(t_{OL}) = [1 + C(t_{OL})\cos(\omega t_{OL} + \phi)]/2. \tag{15}$$

In order to improve the performance of the RI, we now investigate the mechanisms that lead to RI signal attenuation. The decay of the contrast, shown by the black points in Figure 9C, mainly comes from de-phasing and de-coherence mechanisms. These mechanisms are caused by the imperfect design of the $\pi/2$ pulse, non-uniform potential distribution of the Gaussian beam in the radial direction, atom-atom interaction leading to transverse expansion, intensity fluctuation of the lattice, and thermal fluctuations of the system. The theoretical calculation with different mechanisms is shown in Figure 9C, which is consistent with the experimental results. The expansion leads to a significant reduction in contrast (blue dashed line in Figure 9C). In our experiment, the influence of the quantum fluctuation is not significant.

To further improve the contrast of the RI, we develop a matter-wave band echo technique. A π-pulse is designed, which swaps the atom population in the S- and D-band. The π-pulse is inserted into the center of the evolution process. After implementing one π-pulse, the intensity fluctuation can be well suppressed. After applying six echo pulses, the effects of non-uniform lattice potential and transverse expansion are eliminated. The coherence times τ (defined as the time when the contrast $C(t_{OL})$ drops to $1/e$) with different echo pulses are shown in Figure 9D. The coherent time is increased from 1.3 to 14.5 ms by the echo pulses [13].

4 Exotic quantum states of p-orbital ultracold atoms in optical lattices

4.1 Observation of a dynamical sliding phase superfluid with P-Band bosons

The Sliding phase [33], which is introduced to characterize intricate phase transitions in a wide range of the many-body system, appears under extreme conditions for thermal equilibrium systems or quantum ground states, causing a grievous challenge in experimental implementation [34–40]. Here, we review the observation of a sliding phase superfluid in a dynamical system of ultracold atoms in the P-band [10]. We load the atoms into P-band with zero quasi-momentum by the shortcut as shown in Figure 4. The quantum system is driven to a far-out-of-equilibrium but a phase-coherent state. We hold the condensate in the P-band for a certain time t_{evo}. Then the TOF images are taken in two probe directions with probe light along the z-axis (denoted as probe-1) and along the x-axis (denoted as probe-2). The distribution in different probe directions is analyzed via a bimodal fitting, as shown in Figure 10A. We extract the coherent fraction from the bimodal fitting so that the phase coherence of the dynamical many-body state can be inferred [10].

From the time evolution, we identify three distinct dynamical regions. At an early time, the system has superfluid phase in all directions, as shown in Figure 10A at $t_{evo} = 1$ ms. In the second state, the phase coherence of the quantum gas survives partially. The bimodal fitting in Figure 10A at $t_{evo} = 60$ ms shows that there is a finite condensed component in the pancake directions, but no such component in the lattice direction, which is called the sliding phase. At the last state, the quantum gas has rethermalized with a complete loss of phase coherence. The bimodal fitting shows that all atoms are thermal in the complete absence of any condensed component. We define the lifetime t_0 for the atoms to lose coherence in lattice and pancake directions, which is shown in Figure 10B for different lattice depth. We find that with the total atom number fixed in the experiment, a critical lattice depth appears beyond which the sliding phase superfluid starts to emerge. Moreover, we also verify that P-band is necessary to realize the dynamical sliding phase in our experiment, and the sliding phase is absent for cold atoms in the S-band at equilibrium [10].

4.2 Observation of a potts-nematic superfluidity in a hexagonal *sp*^{2} optical lattice

In this section, we review the observation of a Potts-nematic quantum state in a system of cold atoms loaded into the second band of a hexagonal optical lattice [12]. We use the band swapping method to load the atoms into the second band, as shown in section 2.3. After the atoms are transferred into the band maximum of the second band, the phase coherence in the state will immediately disappear. After a few milliseconds, the phase coherence reemerges, and the quantum state spontaneously chooses one orientation, giving rise to a three-state Potts nematicity. We divide the experimental TOF images into three classes and take the average within each class [12]. The post-classification averaged results are shown in Figure 11B.

To gain insight into the mechanism supporting the Potts-nematic order in the sp^2-orbital hybridized band, we provide a mean-field theory analysis assuming a plane-wave condensate. The interaction can be expressed as

$$H_{int} = \frac{1}{2}\sum_{\boldsymbol{r}\in\mathcal{B}} U_s \hat{s}_{\boldsymbol{r}}^\dagger \hat{s}_{\boldsymbol{r}}^\dagger \hat{s}_{\boldsymbol{r}} \hat{s}_{\boldsymbol{r}} + \sum_{\boldsymbol{r}\in\mathcal{A}} \left\{ J\left[\hat{p}_{x,\boldsymbol{r}}^\dagger \hat{p}_{x,\boldsymbol{r}}^\dagger \hat{p}_{y,\boldsymbol{r}} \hat{p}_{y,\boldsymbol{r}} + H.c. \right] \right\} + \frac{1}{2}\sum_{\boldsymbol{r}\in\mathcal{A}} \times \sum_{\alpha,\beta\in\{x,y\}} U_{p,\alpha\beta} \hat{p}_{\alpha,\boldsymbol{r}}^\dagger \hat{p}_{\beta,\boldsymbol{r}}^\dagger \hat{p}_{\beta,\boldsymbol{r}} \hat{p}_{\alpha,\boldsymbol{r}} \tag{16}$$

where $\hat{s}$ and $\hat{p}$ represent quantum mechanical annihilation operators for s and p orbitals, and the p-orbital couplings are constrained by $U_{p,xx} = U_{p,yy} \equiv U_{p_\parallel}$, $U_{p,xy} = U_{p,yx} \equiv U_{p_\perp}$, $J = U_{p_\parallel - U_{p_\perp}}/2$. Taking a trial condensate wave function with $\langle s_{\boldsymbol{r}} \rangle = \phi_s e^{i\boldsymbol{k}\cdot\boldsymbol{r}}$, $\langle p_{x,y,\boldsymbol{r}} \rangle = \phi_{x,y} e^{i\boldsymbol{k}\cdot\boldsymbol{r}}$, with ϕ_s, $\phi_{x,y}$ the variational parameters. For each lattice momentum $\boldsymbol{k}$, we minimize the energy by varying $\phi_{s,x,y}$, and the resultant energy is denoted as $\varepsilon(\boldsymbol{k})$ and shown in Figure 11C. With the orbital Josephson coupling $J > 0$, both the kinetic and interaction energies favor a condensate at K points which breaks the time-reversal symmetry but respects the rotation symmetry. With the Josephson coupling $J < 0$, minimizing the kinetic and interaction energies meets frustration, as interaction favors p-orbital polarization. Figure 11C shows the possible value range of J considering renormalization effects [12].

5 Dynamical evolution for atoms in high bands of optical lattices

5.1 The scattering channels induced by two-body collision of D-band atoms in optical lattices

The mechanism of atomic collisions in excited bands plays an essential role in the atomic dynamics in high bands of optical lattices and the simulation of condensed matter physics [21]. Atoms distributed in an excited band of an optical lattice can collide and decay to other bands through different scattering channels [17, 21]. The decay rate and scattering channels of optical lattices with different configurations are different. Here, we first compare the lifetime of atoms in the D-band for one-dimensional lattice and triangular lattice. In experiments, we utilize the shortcut method to load BECs to the D (D1) band of the 1D optical lattice (triangular optical lattice). Then the BECs in the optical lattice evolve for a certain time t_{evo}. Finally, we apply band mapping to measure the proportion p_D (t_{OL}) of atoms in the D-band, which is shown in Figure 12A for 1D lattice and 12B for triangular lattice. We define the lifetime τ of atoms in the D-band as the proportion p_D reduces to $1/e$. The lifetime for the triangular lattice is 5.0 ms, which is much longer than that of the 1D lattice, 2.1 ms. The difference in collisional scattering cross-section leads to the difference of a lifetime. Next, we will carefully analyze the scattering cross-section and the scattering channels [21].

We take triangular and square lattices as examples to study the difference in the scattering process. We use the scattering theory to calculate the cross-section of each scattering channel in those two types of lattices. Two-body collisional scattering cross section for two atoms initially at the Γ point ($(q_x, q_y)=(0,0)$) of D1 band jumping to band n_1 and n_2 can be written as:

$$\sigma(n_1, n_2) = \frac{4\pi m\hbar}{v_a} \int d\boldsymbol{q} \times |-2\pi i \frac{4\pi a_s}{m} \zeta_{n_1,n_2}(0,0;\boldsymbol{q},-\boldsymbol{q})|^2, \quad (17)$$

where v_a is the atomic velocity and a_s is atomic s-wave scattering length. And the overlapping integral of eigenstates $\zeta_{n_1,n_2}(0,0;\vec{q},-\vec{q})$ is given by:

$$\zeta_{n_1,n_2}(0,0;\boldsymbol{q},-\boldsymbol{q}) = \int d\boldsymbol{r} \times \Psi^*_{n_1,\boldsymbol{q}}(\boldsymbol{r}) \Psi^*_{n_2,-\boldsymbol{q}}(\boldsymbol{r}) \Psi_{d,0}(\boldsymbol{r}) \Psi_{d,0}(\boldsymbol{r}) \quad (18)$$

where $\Psi_{n,\boldsymbol{q}}(\boldsymbol{r})$ is Bloch function of the eigenstate at quasi-momentum $\boldsymbol{q}$ in the n band. In the calculation, we assume the periodic boundary conditions, and consider that $|\zeta_{n_1,n_2}(0,0;\boldsymbol{q},-\boldsymbol{q})|^2 = \int d\boldsymbol{r} \times |\Psi^\star_{n_1,\boldsymbol{q}}(\boldsymbol{r}) \Psi^\star_{n_2,-\boldsymbol{q}}(\boldsymbol{r}) \Psi_{d,0}(\boldsymbol{r}) \Psi_{d,0}(\boldsymbol{r})|^2$. After neglecting the scattering channels of higher bands, we calculate the scattering channels, as shown in Figure 12CD. In the square lattice, the cross-section of the strongest channel SS, P_1P_1 and P_2P_2 are all around 10% of the total cross-section respectively. Besides, there are many smaller channels included in 'Others.' There is no significant difference in scattering cross-section values among the first six channels, which means no dominant scattering channel in a square lattice. By contrast, in the triangular lattice, the proportion of scattering cross-section of the SS channel is 38.5%, while that of the second strong channel D_1S is only 9.8%. Besides, the proportion of other channels is much lower than that of channel SS. Consequently, the channel SS is dominant in the two-body scattering process of the triangular optical lattice. The experimental results are consistent with the theoretical results, as shown in Figure 12F. For example, at time $t_{evo} = 12$ ms, the experimental proportion of the S-band is 55.8%, which is roughly equal to the theoretical prediction of 57.3% [21].

5.2 Quantum dynamical oscillations of ultracold atoms in the F and D bands

Here we review the observation of quantum dynamical oscillations of ultracold atoms in the F and D bands of the 1D optical lattice [20]. We can control the Bragg reflections at the Brillouin-zone edge up to the third order and observe three different types of quantum oscillations [20].

The BECs is initially loaded in the G band, where the atoms mostly populate at momenta $4\hbar k$, as shown in Figure 3B(2). Then the atoms fall into the F-band due to the small gap between G- and F-bands. The following trace of the atoms is shown in the extended band structures as shown in Figure 13D. Once the BECs are in the F-band, it loses momentum while gaining potential energy from the harmonic confinement ($A_1 \rightarrow A_2$). Once arriving A_2, the atoms face different dynamics depending on the lattice depth. When the depth is small ($\sim 5E_r$), and the Bragg reflections at A_2 are weak, the BECs will continue into the D-band by a Landau-Zener transition and reach A_3. Then the atoms will be Bragg reflected to A_4 and reverse its dynamics ($A_4 \rightarrow A_5 \rightarrow A_6$). This oscillation is shown in Figure 13A. When the lattice is strong ($\sim 15E_r$), and the gap at A_2 is large, the Bragg reflection can dominate the dynamics, forbidding the atoms from tunneling from the F band to the D band. Instead, the atoms at A_2 will transfer to A_5 and oscillate only within the F-band, which is shown in Figure 13C. For intermediate depth ($\sim 7.5E_r$), these two oscillation modes exist simultaneously, as shown in Figure 13B [20].

5.3 Nonlinear dynamical evolution for P-band ultracold atoms in 1D optical lattice

The dynamical evolution for atoms in P-band is different from that of F- and D-bands [18]. After loading the BECs into the P-band with zero quasi-momentum for the lattice depth $5E_r$, we hold the BECs for time t_{evo} and then measure the momentum distribution. The momentum distributions at different holding time t_{evo} are shown in Figure 14A. We use the normalized populations $W_\ell(t_{evo})$ of momentum states $|\ell \cdot 2\hbar k + q\rangle$ to better quantify the dynamical evolution of atoms. At the beginning of the evolution process $t_{evo} < 1.5$ ms, we find $W_\ell(t_{evo})$ oscillating rapidly, as shown in Figure 4C and Figure 14A(1) [2]. Then, after a short transition time, a different type of oscillation begins to emerge around $t_{evo} = 2$ ms. The period of this oscillation is 14.9 ms, which is shown in Figures 14A,B [3-5].

The short-period oscillations shown in Figure 4C are beating signals due to the coherent superposition of different bands. From the numerical analysis, the superposed state is close to $|\psi(t_{evo} = 0) = \sqrt{0.9}\Psi_{2,0} + \sqrt{0.05}\Psi_{1,0} + \sqrt{0.05}\Psi_{3,0}$. The rapid oscillations disappear at about 1.5 ms. Then a long-period oscillation begins to emerge at around 2 ms. There are five cycles of the long-period oscillation in Figure 14C. The long-period oscillation reflects the random phase between neighboring lattice sites, which can be well captured by the simulation with the Gross-Pitaevskii equation (shown by the red line in Figure 14C). This experiment paves the way to study the long-time dynamical evolution of the high orbital physics for other novel quantum states, such as the sliding phase [18].

6 Discussion and conclusion

In this review, we concentrate on the methods to prepare and control the BEC in optical lattices linked to one-body physics. The many-body interactions also play an important role in the system of ultracold atoms in the optical lattices. For the control methods mentioned in this review, such as the shortcut method, amplitude modulation, and nonadiabatic holonomic control, the operation time (< 1 ms) is much shorter than the time when the interaction has a significant effect. Therefore, the control schemes designed ignoring the influence of many-body interaction is still very successful. The effects of the interaction mainly occur in the long-term evolution process in the optical lattice after we manipulate or prepare the Bloch states, such as the de-coherence in the Ramsey interferometry with motional states, the two-body collision of D-band atoms, and the emergency of the exotic quantum states of p-orbitals. On the other hand, we can also utilize the interactions to expand the methods of atomic manipulation in optical lattices. For example, a two-qubit gate can be achieved by adapting the interaction scheme based on the method shown in section 3.1. Considering two nearby sites, denoted as a and b, the orbital states are $|s_a s_b\rangle$, $|d_a d_b\rangle$, $|d_a s_b\rangle$, $|s_a d_b\rangle$. The relevant interactions between neighboring sites contain this term $U_0 (s_a^\dagger d_b^\dagger d_b s_a + d_a^\dagger s_b^\dagger s_b d_a)$. A $\sqrt{\text{swap}}$ gate control can be reached by letting atoms interact for a time duration $\pi\hbar/(4U_0)$. In a word, we can use these control methods to observe the special dynamic mechanism and novel quantum states produced by the interaction of different orbitals of optical lattices, and we can also use the interactions to achieve more manipulation.

In summary, we review our practical methods for manipulating the high orbitals of ultracold atoms in optical lattices. The shortcut method is characterized by short time and high fidelity, which can directly transfer ultracold atoms from the ground state in the harmonic trap to any Bloch state, and accurately manipulate atoms of different orbitals in optical lattices. This method can be used to construct atomic orbital interferometers and qubits and to study the dynamic properties of high orbital atoms in optical lattices. The band swapping technique considers the interaction between atoms and the additional potential trap (such as harmonic trap) besides the optical lattice, which is more suitable for studying the ground and metastable states of the system. The amplitude modulation focuses on coupling different Bloch bands and can be used to realize quantum gates and the large-momentum-transfer beam splitter. Based on these methods, the atom-orbital qubit under nonadiabatic holonomic quantum control and Ramsey interferometry with trapped motional quantum states of the optical lattice can be constructed. Many exotic quantum states of the high orbital atoms have been observed. Then we study the quantum dynamical evolution of atoms in high bands. The effective manipulation of the high orbitals provides strong support for applying the ultracold atoms in the optical lattice in quantum simulation, quantum computing, and quantum precision measurement.

Author contributions

SJ: Drafting the manuscript XC: Revising the manuscript XZ: Revising the manuscript.

Funding

This work is supported by the National Natural Science Foundation of China (Grants No. 12104020, No. 61727819, and No. 11334001), the National Basic Research Program of China (Grants No. 2021YFA0718300 and No. 2021YFA1400901), the Project funded by China Postdoctoral Science Foundation (Grant No. 2020TQ0017), the Science and Technology Major Project of Shanxi (No. 202101030201022), and the Space Application System of China Manned Space Program.

Acknowledgments

Thank Yiqiu Wang for establishing this experimental group of ultra-cold atoms in China. In completing the above work, thank Xiaopeng Li, Jörg Schmiedmayer, Biao Wu, Hongwei Xiong, Guangjiong Dong, Peng Zhang, and Lan Yin.

Conflict of interest

The authors declare that the research was conducted in the absence of any commercial or financial relationships that could be construed as a potential conflict of interest.

Publisher's note

References

1. Greiner M, Mandel O, Esslinger T, Hänsch TW, Bloch I. Quantum phase transition from a superfluid to a mott insulator in a gas of ultracold atoms. *Nature* (2002) 415:39–44. doi:10.1038/415039a

2. Bloch I, Dalibard J, Nascimbène S. Quantum simulations with ultracold quantum gases. *Nat Phys* (2012) 8:267–76. doi:10.1038/nphys2259

3. Bloch I, Dalibard J, Zwerger W. Many-body physics with ultracold gases. *Rev Mod Phys* (2008) 80:885–964. doi:10.1103/RevModPhys.80.885

4. Goldman N, Budich JC, Zoller P. Topological quantum matter with ultracold gases in optical lattices. *Nat Phys* (2016) 12:639–45. doi:10.1038/nphys3803

5. Georgescu IM, Ashhab S, Nori F. Quantum simulation. *Rev Mod Phys* (2014) 86:153–85. doi:10.1103/RevModPhys.86.153

6. Gross C, Bloch I. Quantum simulations with ultracold atoms in optical lattices. *Science* (2017) 357:995–1001. doi:10.1126/science.aal3837

7. Moan ER, Horne RA, Arpornthip T, Luo Z, Fallon AJ, Berl SJ, et al. Quantum rotation sensing with dual sagnac interferometers in an atom-optical waveguide. *Phys Rev Lett* (2020) 124:120403. doi:10.1103/PhysRevLett.124.120403

8. Shui H, Jin S, Li Z, Wei F, Chen X, Li X, et al. Atom-orbital qubit under nonadiabatic holonomic quantum control. *Phys Rev A (Coll Park)* (2021) 104: L060601. doi:10.1103/PhysRevA.104.L060601

9. Wirth G, Ölschläger M, Hemmerich A. Evidence for orbital superfluidity in the p-band of a bipartite optical square lattice. *Nat Phys* (2011) 7:147–53. doi:10.1038/nphys1857

10. Niu L, Jin S, Chen X, Li X, Zhou X. Observation of a dynamical sliding phase superfluid with *p*-band bosons. *Phys Rev Lett* (2018) 121:265301. doi:10.1103/PhysRevLett.121.265301

11. Wang XQ, Luo GQ, Liu JY, Liu WV, Hemmerich A, Xu ZF. Evidence for an atomic chiral superfluid with topological excitations. *Nature* (2021) 596:227–31. doi:10.1038/s41586-021-03702-0

12. Jin S, Zhang W, Guo X, Chen X, Zhou X, Li X. Evidence of potts-nematic superfluidity in a hexagonal sp^2 optical lattice. *Phys Rev Lett* (2021) 126:035301. doi:10.1103/PhysRevLett.126.035301

13. Hu D, Niu L, Jin S, Chen X, Dong G, Schmiedmayer J, et al. Ramsey interferometry with trapped motional quantum states. *Commun Phys* (2018) 1:29. doi:10.1038/s42005-018-0030-7

14. Zhou X, Jin S, Schmiedmayer J. Shortcut loading a Bose-Einstein condensate into an optical lattice. *New J Phys* (2018) 20:055005. doi:10.1088/1367-2630/aac11b

15. Müller T, Fölling S, Widera A, Bloch I. State preparation and dynamics of ultracold atoms in higher lattice orbitals. *Phys Rev Lett* (2007) 99:200405. doi:10.1103/PhysRevLett.99.200405

16. Liu X, Zhou X, Xiong W, Vogt T, Chen X. Rapid nonadiabatic loading in an optical lattice. *Phys Rev A (Coll Park)* (2011) 83:063402. doi:10.1103/PhysRevA.83.063402

17. Zhai Y, Yue X, Wu Y, Chen X, Zhang P, Zhou X. Effective preparation and collisional decay of atomic condensates in excited bands of an optical lattice. *Phys Rev A (Coll Park)* (2013) 87:063638. doi:10.1103/PhysRevA.87.063638

18. Hu D, Niu L, Yang B, Chen X, Wu B, Xiong H, et al. Long-time nonlinear dynamical evolution for *p*-band ultracold atoms in an optical lattice. *Phys Rev A (Coll Park)* (2015) 92:043614. doi:10.1103/PhysRevA.92.043614

19. Yang B, Jin S, Dong X, Liu Z, Yin L, Zhou X. Atomic momentum patterns with narrower intervals. *Phys Rev A (Coll Park)* (2016) 94:043607. doi:10.1103/PhysRevA.94.043607

20. Wang Z, Yang B, Hu D, Chen X, Xiong H, Wu B, et al. Observation of quantum dynamical oscillations of ultracold atoms in the *f* and *d* bands of an optical lattice. *Phys Rev A (Coll Park)* (2016) 94:033624. doi:10.1103/PhysRevA.94.033624

21. Guo X, Yu Z, Peng P, Yin G, Jin S, Chen X, et al. Dominant scattering channel induced by two-body collision of *d*-band atoms in a triangular optical lattice. *Phys Rev A (Coll Park)* (2021) 104:033326. doi:10.1103/PhysRevA.104.033326

22. Taie S, Ozawa H, Ichinose T, Nishio T, Nakajima S, Takahashi Y. Coherent driving and freezing of bosonic matter wave in an optical lieb lattice. *Sci Adv* (2015) 1:e1500854. doi:10.1126/sciadv.1500854

23. Browaeys A, Häffner H, McKenzie C, Rolston SL, Helmerson K, Phillips WD. Transport of atoms in a quantum conveyor belt. *Phys Rev A (Coll Park)* (2005) 72: 053605. doi:10.1103/PhysRevA.72.053605

24. Ölschläger M, Wirth G, Hemmerich A. Unconventional superfluid order in the *f* band of a bipartite optical square lattice. *Phys Rev Lett* (2011) 106:015302. doi:10.1103/PhysRevLett.106.015302

25. Niu L, Hu D, Jin S, Dong X, Chen X, Zhou X. Excitation of atoms in an optical lattice driven by polychromatic amplitude modulation. *Opt Express* (2015) 23: 10064–74. doi:10.1364/OE.23.010064

26. Köhl M, Moritz H, Stöferle T, Günter K, Esslinger T. Fermionic atoms in a three dimensional optical lattice: Observing fermi surfaces, dynamics, and interactions. *Phys Rev Lett* (2005) 94:080403. doi:10.1103/PhysRevLett.94.080403

27. Kastberg A, Phillips WD, Rolston SL, Spreeuw RJC, Jessen PS. Adiabatic cooling of cesium to 700 nk in an optical lattice. *Phys Rev Lett* (1995) 74:1542–5. doi:10.1103/PhysRevLett.74.1542

28. Greiner M, Bloch I, Mandel O, Hänsch TW, Esslinger T. Exploring phase coherence in a 2d lattice of bose-einstein condensates. *Phys Rev Lett* (2001) 87: 160405. doi:10.1103/PhysRevLett.87.160405

29. de Saint-Vincent MR, Brantut JP, Bordé CJ, Aspect A, Bourdel T, Bouyer P. A quantum trampoline for ultra-cold atoms. *Europhys Lett* (2010) 89:10002. doi:10.1209/0295-5075/89/10002

30. Impens F, Santos FPD, Bordé CJ. The theory of quantum levitators. *New J Phys* (2011) 13:065024. doi:10.1088/1367-2630/13/6/065024

31. Cronin AD, Schmiedmayer J, Pritchard DE. Optics and interferometry with atoms and molecules. *Rev Mod Phys* (2009) 81:1051–129. doi:10.1103/RevModPhys.81.1051

32. Riehle F, Kisters T, Witte A, Helmcke J, Bordé CJ. Optical ramsey spectroscopy in a rotating frame: Sagnac effect in a matter-wave interferometer. *Phys Rev Lett* (1991) 67:177–80. doi:10.1103/PhysRevLett.67.177

33. O'Hern CS, Lubensky TC, Toner J. Sliding phases in *XY* models, crystals, and cationic lipid-dna complexes. *Phys Rev Lett* (1999) 83:2745–8. doi:10.1103/PhysRevLett.83.2745

34. Granato E, Kosterlitz JM. Critical behavior of coupled xy models. *Phys Rev B* (1986) 33:4767–76. doi:10.1103/PhysRevB.33.4767

35. Choi MY, Doniach S. Phase transitions in uniformly frustrated xy models. *Phys Rev B* (1985) 31:4516–26. doi:10.1103/PhysRevB.31.4516

36. Feigel'man M, Geshkenbein V, Larkin A. Pinning and creep in layered superconductors. *Physica C: Supercond* (1990) 167:177–87. doi:10.1016/0921-4534(90)90502-6

37. Klemm RA, Luther A, Beasley MR. Theory of the upper critical field in layered superconductors. *Phys Rev B* (1975) 12:877–91. doi:10.1103/PhysRevB.12.877

38. Stoebe T, Mach P, Huang CC. Unusual layer-thinning transition observed near the smectic-*a*-isotropic transition in free-standing liquid-crystal films. *Phys Rev Lett* (1994) 73:1384–7. doi:10.1103/PhysRevLett.73.1384

39. Cheng M, Ho JT, Hui SW, Pindak R. Electron-diffraction study of free-standing liquid-crystal films. *Phys Rev Lett* (1987) 59:1112–5. doi:10.1103/PhysRevLett.59.1112

40. O'Hern CS, Lubensky TC. Sliding columnar phase of dna-lipid complexes. *Phys Rev Lett* (1998) 80:4345–8. doi:10.1103/PhysRevLett.80.4345

frontiers | Frontiers in Physics

TYPE Original Research
PUBLISHED 07 September 2022
DOI 10.3389/fphy.2022.971059

OPEN ACCESS

EDITED BY
Andrea Bertoldi,
ParisTech Institut d'Optique Graduate School, France

REVIEWED BY
Nassim Zahzam,
Office National d'Études et de Recherches Aérospatiales, France
Guglielmo Tino,
University of Florence, Italy

*CORRESPONDENCE
Xuzong Chen,
xuzongchen@pku.edu.cn

SPECIALTY SECTION
This article was submitted to Atomic and Molecular Physics,
a section of the journal
Frontiers in Physics

RECEIVED 16 June 2022
ACCEPTED 19 August 2022
PUBLISHED 07 September 2022

CITATION
Li H, Yu J, Yuan X, Wu B, Xie Y, Li L, Liang A, Huang M, Jin S, Xiong W, Wang B, Chen D, Li T, Hou X, Liu L, Zhou X, Chen W and Chen X (2022), Deep cooling scheme of quantum degenerate gas and ground experimental verification for chinese space station.
Front. Phys. 10:971059.
doi: 10.3389/fphy.2022.971059

Deep cooling scheme of quantum degenerate gas and ground experimental verification for chinese space station

Hui Li[1], Jiachen Yu[1], Xiaolong Yuan[1], Biao Wu[1], Yu Xie[2], Lin Li[2], Angang Liang[2], Mingshan Huang[2], Shengjie Jin[1], Wei Xiong[1], Bin Wang[2], Dijun Chen[2], Tang Li[2], Xia Hou[2], Liang Liu[2], Xiaoji Zhou[1], Weibiao Chen[2] and Xuzong Chen[1]*

[1]Institute of Quantum Electronics, School of Electronics, Peking University, Beijing, China, [2]Aerospace Laser Engineering Department, Shanghai Institute of Optics and Fine Mechanics, Chinese Academy of Sciences, Shanghai, China

The Cold Atom Physics Rack (CAPR) of Chinese space station will be launched at the end of 2022. The important goal of CAPR is to achieve BEC at 100 pk. In order to obtain ultracold atoms in microgravity of space station, we propose a two-stage cooling scheme using all-optical trap with different waist beams. The cold atom cloud obtained by this scheme is composed of condensate and thermal atoms around condensate. The design of our two-stage cooling scheme will effectively reduce the temperature of the thermal atom cloud and the effective temperature generated by the interaction energy of the condensate. The atomic temperature of 5 nk is obtained from the ground test experiment, and the corresponding temperature under the microgravity condition of the space station is theoretically predicted to be less than 100 pk. Taking the advantages of ultracold temperature and long-time detection, many scientific experiments will be arranged. In this paper, the ground test experiments based on ground principle prototype and pre-prototype for CAPR are also introduced.

KEYWORDS

space station, cold atom physics rack, two-stage cooling, picokelvin, microgravity

Introduction

Ultra-low temperature has always been the tireless pursuit of scientists in the field of atomic and molecular physics since the beginning of the last century. The lower the atomic temperature, the more impetus and representative significance for the verification of many physical theories [1–3]. The sensitivity and accuracy of atomic interferometers, gravimeters, and gyroscopes can also achieve an order of magnitude leap in cooler degenerate gases [4–7]. In 1908, Kamerlingh Onnes produced liquid Helium, of which the temperature is below 4.2K [8]. In 1911, he found superconductivity in mercury at 4.1K [9]. The development of laser cooling overwrote the record to micro Kelvin [10, 11]. The success of Bose-Einstein Condensation (BEC) paves the way for lowering temperatures in nano-Kelvin [12–14], and adiabatic release of degenerate gases pushes the limit to sub-nanometer Kelvin [15]. Further atomic deep cooling is limited by gravity. Continuously reducing the depth of the potential well can theoretically obtain lower temperature trapped atoms, but the shallower potential well will not be able to resist the effect of the atom's own gravity, causing the atoms to leak out of the well, resulting in a substantial loss of the number of atoms and a decrease in the collision rate between atoms. Thus the evaporative cooling process tends to be ineffective.

Thanks to microgravity, degenerate atomic gases can be cooled to lower temperature than ever before. Germany, France, the United States and China have all carried out cold atom experiments under microgravity conditions. In the QUANTUS project in Germany, Rasel's research team used an atomic chip to realize BEC with atomic kinetic energy of 9 nk in the Bremen drop tower experiment in 2010 [16]. In 2013, they used delta-kick cooling (DKC) method to reduce the atomic temperature to about 1 nk and conducted interference experiments [17]. And in the German MAIUS-1 mission in 2018, they achieved a rubidium BEC of about 1 nk for a longer experimental time under the 6-min microgravity conditions created by the sounding rocket [18]. In France, Bouyer's research team created a microgravity environment by flying the parabolic plane in 2011, using a velocity-selective Raman light pulse carrying two counter-propagating laser fields and cooled the atoms to a temperature of 300 nK in the longitudinal velocity distribution and obtained an improvement in the sensitivity of the interferometer at 0 g [19]. The JPL team of NASA in the United States installed the Cold Atom Laboratory (CAL) experimental module on the International Space Station (ISS) in 2018, using the atom chip to conduct the deep cooling experiment of degenerate gas of rubidium and potassium [20–23]. One of the aim of the CAL is to break the limit of atomic temperature on the ground and realize ultra-low temperature of pK or even fK. Limited by the experimental system and mechanical vibration disturbances in the space station, the current cold atom temperature is on the order of 10 nK. China is scheduled to launch the space station experimental module by the end of 2022, which will be equipped with a Cold Atom Physics Rack (CAPR). The atomic deep cooling adopts the two-stage cooling (TSC) scheme proposed by Peking University [24–27]. In the first stage, atoms undergo the runaway evaporation cooling process in an optical trap formed by two crossed laser beams with narrow beam diameter and high power. In the second stage, low temperatures atoms are loaded into the other optical trap formed by two crossed laser beams with wide waist and weak power. The TSC scheme has been validated to effectively reduce the thermal atomic cloud temperature. The atomic temperature of 5 nk is obtained from the ground verification test, and it is theoretically predicted that the corresponding atomic temperature under the microgravity condition of the space station is less than 100 pk. The project for CAPR includes three stages: ground principle prototype, pre-prototype, formal prototype. We have achieved ground principle prototype, pre-prototype, and completed the test experiments based on pre-prototype.

This article firstly emphasizes the necessity of conducting ultra-cold atomic physics experiments in the microgravity environment. And then introduces the structure, modules, key technologies of ground principle prototype and pre-prototype, as well as ground test experiments for the CAPR on Chinese Space Station. The atomic deep cooling scheme of TSC is introduced through physical principles, theoretical simulation results, ground verification experiments, and the reduction of thermodynamic temperature. Finally, it is concluded that the space station ultra-cold atomic experiment using the two-stage cooling scheme is of great significance to the advancement of atomic and molecular physics research under the conditions of ultra-low temperature and long-term detection.

Cold atom physics rack of chinese space station

Currently, the main factor limiting further temperature reductions is the acceleration of earth's gravity. For DKC cooling and pulsed optical lattice momentum filter, the atoms cannot be trapped by the external potential field during the cooling process, otherwise the external potential field will heat the atomic gas. But the existence of gravitational acceleration will make the atoms leave off the optical trap in the direction of gravity. Therefore, the cooling of the atomic gas by these cooling technologies on the ground only reduces the momentum width of the atomic gas in some dimensions, but does not reduce the average kinetic energy of the atomic gas. Hence, the realization of microgravity conditions is crucial for the reduction of atomic temperature [28], and the long-term gravity-free gradient environment of the space station is very beneficial to the implementation of precise physical experiments.

Chinese space station has been launched in 2021, and the science module II is due to launch in late 2022 with the Cold Atom Physics Rack. The goal of CAPR is to achieve the quantum degenerate gas of picokelvin ultra-low temperature and conduct a series of scientific experiments for quantum simulations and precise verification of physical laws in microgravity conditions on the space station. The CAPR is based on the constraints of external mechanical, electrical, thermal, information, measurement and control resources. Due to the particularity of space station and rocket carrying, CAPR must be small in volume (1.5 cubic meters), light in weight (500 kg) and low in power consumption (1,000 W). There are five units in the miniaturized and highly integrated CAPR system: 1) Physics module; 2) Laser and optics module; 3) Electronics module; 4)

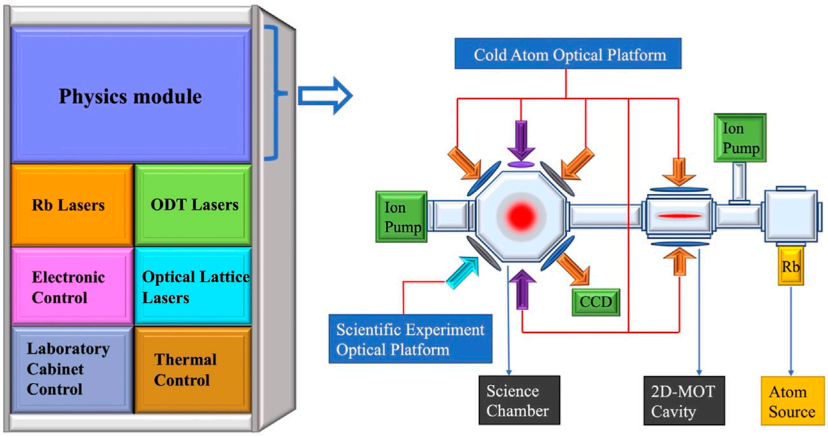

FIGURE 1
The structure of Cold Atom Physics Rack (CAPR) on the Chinese space station. There are five units in the miniaturized and highly integrated CAPR system: (1) Physics module; (2) Laser and optics module; (3) Electronics module; (4) Remote control module; (5) Rack support module.

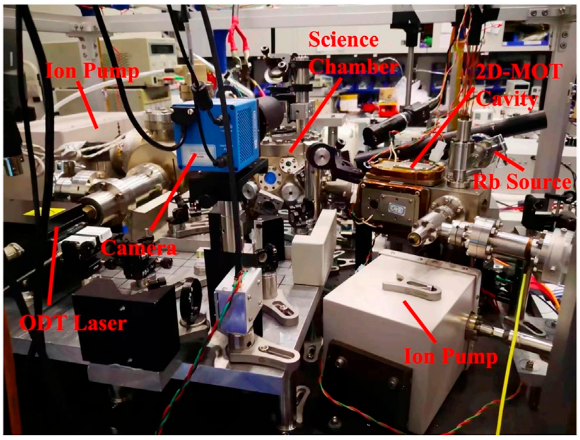

FIGURE 2
Ground principle prototype for CAPR. The purpose of the ground principle prototype is to verify that some technical solutions adopted on CAPR are available.

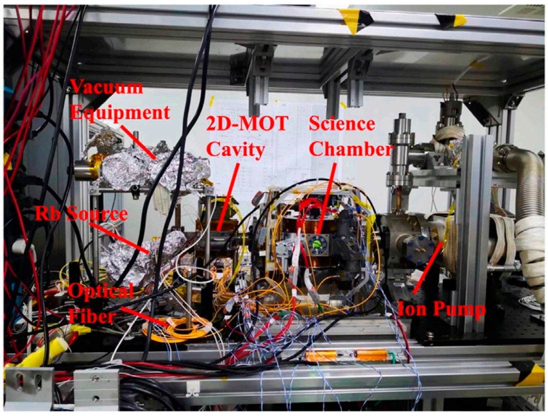

FIGURE 3
Pre-prototype for CAPR (2D-MOT and 3D-MOT parts). The size is almost same of the formal one. All laser transmissions on the pre-prototype use optical fiber, which is different from the space optical path transmission on the ground-based prototype. Various tests are also carried out on the pre-prototype to make reference and backup for the real launched one.

Remote control module; 5) Rack support module. As shown in Figure 1.

Our ground-based verification system for CAPR is a Rb quantum gas system for physical experiments in space microgravity. In order to achieve the goal of miniaturization and low power consumption in the space station, there are several key techniques in the process of preparing Bose-Einstein condensation. High frequency laser phase lock technology is used to produce a tunable frequency-stabilized laser to cool atoms. The tuning range is ±12 GHz (dynamic range 500 MHz). Optical phase lock loop (OPLL) avoids the larger volume and high power consumption of the traditional AOM complex optical path. The complex programmable logic device (CPLD) is used to replace the LabVIEW board card (not available in space) to realize the control of system time sequence. It is just a 10 cm × 10 cm circuit board programmed through a computer, which realize the switch control of shutter driver, AOM driver, magnetic coil driver, laser power variation curve of optical dipole trap, camera trigger and so on. And high current magnetic trap control technology enables a high-current coil to have a current of 500 A and a magnetic field of 600 Gs.

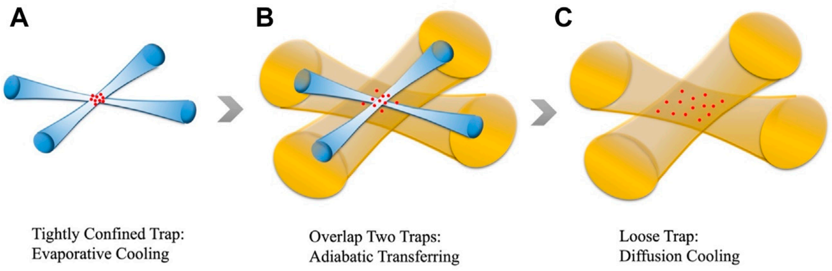

FIGURE 4
Schematic diagram of the experimental process of the two-stage cooling (TSC) scheme. **(A)** Atoms (red dots) trapped in the tightly confined optical dipole trap formed by two thin-waisted crossed beams for evaporative cooling. **(B)** Adiabatic transfer of atoms from the thin-waisted optical trap (blue beams) to the thick-waisted optical trap (yellow beams). **(C)** Atoms are diffusively cooled in the loose optical trap while decreasing the intensity of the thick-waisted beams. After decompression cooling process, the temperature of atoms below 1e-10K is expected to be achieved.

Ground test experiments was performed first from the ground principle prototype for CAPR (see Figure 2), which demonstrated that the principle of two-stage cooling is correct and some experimental techniques are available. The pre-prototype for CAPR (see Figure 3) adopts an all-optical scheme, which is almost identical to the launched one in the future. It needs to use the specified components available in aerospace. The following verification experiments were implemented on the pre-prototype. It tested that the techniques and approaches for two-stage cooling and the subsequent experiments are available for the CAPR in microgravity.

Compared with the Cold Atom Laboratory of the US International Space Station, which uses the atom chip and magnetic trap plus microwave cooling, the CAPR on Chinese space station adopts all-optical trap two-stage cooling scheme. Theoretical and ground-based experiments show that our scheme can obtain lower temperature. In addition, the CAPR system is developed to support the research of space ultracold atom physics and carry out quantum simulation experiments. Four fundamental physics experiments based on quantum gas will be implemented on Chinese space station in first 3 years: 1) Quantum Magnetism [29]; [30]; [31]; 2) Exotic material [32]; [33]; 3) Acoustic black hole [34]; 4) Efimov effect [35].

Two-stage cooling scheme

When directly applying evaporation cooling method [36–38] to break through to a lower temperature (pico-Kelvin), a major difficulty is that when the groups of atoms are cooled to a temperature of the order of nK, its internal collision rate per unit time will be greatly reduced. Such a low collision rate is not sufficient to maintain an effective evaporative cooling process. And the longer the cooling process continues, the more atomic number loss is caused by inelastic collisions. Therefore, how to introduce a more efficient mechanism so that the cooling can continue when the atomic gases enter the temperature of the order of nK is a key question. In order to ensure that the temperature of pK magnitude can be reached within an acceptable time, our experimental group proposed the two-stage cross beam cooling method in 2013 [24], and applied it to the ultra-cold atomic physics experiments on Chinese space station launched at the end of 2022.

Here, we deduce the feasibility of the two-stage cooling scheme from physical principles. Without regard to gravity, the potential of the crossed optical dipole trap can be expressed as

$$U(r) = \frac{U_0}{w^2}\left(2z^2 + x^2 + y^2\right) \tag{1}$$

Where w is the waist of the beams, U_0 is the optical trap depth. The far-detuned crossed laser beam traps are approximated as simple harmonic potential traps near the center of the trap. Then, U_0 can be described as

$$U_0 = \frac{3\pi c^2}{\omega_0^3}\frac{\Gamma}{\Delta}\frac{2P}{\pi w^2} = \alpha\frac{P}{w^2} \tag{2}$$

Where $\alpha = \frac{6\pi c^2 \Gamma}{\omega_0^3 \Delta\pi}$, c is the speed of light in vacuum, Γ is the atomic spontaneous emission rate, ω_0 is the atomic center transition frequency, Δ is the detuning difference between the optical dipole trap (ODT) laser frequency and the atomic resonance frequency, and P is the ODT laser power of a single beam.

Taking the x-direction as an example, the potential energy at the center of the simple harmonic trap can be written as

$$E_P(x) = \frac{1}{2}m\omega_x^2 x^2 = U(x) = \frac{U_0}{w^2}x^2 \tag{3}$$

Where m is the mass of the atom, ω_x is the harmonic frequency of the trap in the x direction. From Eqs. 2, 3, we can get trap frequency

$$\omega_x = \sqrt{\frac{2U_0}{mw^2}} = \sqrt{\frac{12c^2\Gamma}{\Delta\omega_0^3 m}}\ \frac{P^{1/2}}{w^2} \tag{4}$$

Similarly, the harmonic trap frequencies in the y and z directions are $\omega_y = \sqrt{\frac{2U_0}{mw^2}}$ and $\omega_z = 2\sqrt{\frac{U_0}{mw^2}}$, respectively.

The critical temperature of atoms is directly related to the potential trap frequency, which can be obtained from the following equation

$$k_B T_c \approx 0.94\hbar\bar{\omega}N^{1/3} \tag{5}$$

Where k_B is the Boltzmann constant, $\hbar = \frac{h}{2\pi}$ is the reduced Planck constant, $\bar{\omega} = (\omega_x\omega_y\omega_z)^{1/3}$ is the mean frequency of three-dimensional harmonic oscillatory traps, N is the number of atoms.

The relationship between the ground state atomic ratio and temperature is $\frac{T}{T_c} = (1 - \frac{N_0}{N})^{1/3}$, where T_c is the critical temperature and N_0 is the number of atoms in the ground state, or at the state of Bose-Einstein Condensation. From the above formulas, we can get the relationship between the temperature of atomic cloud and ODT laser power and waist width:

$$\begin{aligned} k_B T &= k_B T_c\left(1 - \frac{N_0}{N}\right)^{1/3} \\ &= 0.94\hbar\bar{\omega}(N - N_0)^{1/3} = 0.94\,\hbar\,(N - N_0)^{1/3}\sqrt{\frac{12c^2\Gamma}{\Delta\omega_0^3 m}}\ \frac{P^{1/2}}{w^2} \end{aligned} \tag{6}$$

From Eq. 6, we can get that the atomic temperature is proportional to the root square of the laser power and inversely proportional to the square of the beam waist size. The reduction of ODT laser power P corresponds to the well-known all-optical trap evaporative cooling. Since the exponent of w is larger than the exponent power of P, the effect of increasing the laser waist w on reducing the atomic temperature is more significant. When the laser power continues to decrease until the cooling effect of evaporative cooling is not obvious, increasing the beam waist size will further reduce the temperature of atomic cloud.

The experimental process of the two-stage cooling scheme is shown in Figure 4. First, the atoms of micro-Kelvin temperature are loaded into the tightly confined optical dipole trap formed by two thin-waisted crossed beams. Atoms undergo the runaway evaporation cooling process with decreasing laser intensity. In the first stage the atoms will be cooled to tens of nanokelvin temperature in about 5 s. Next, overlap the loose optical dipole trap consisting of a pair of thick-waisted intersecting beams. With the continuous weakening of the laser intensity of the thin-waisted optical trap and the continuous increase of the intensity of the thick-waisted optical trap, the atoms undergo adiabatic transfer in these two optical traps. Afterwards, continuously reducing the intensity of the thick-waisted beams, the atoms are diffusively cooled in the loose trap to the picokelvin temperature. A deeply cooled quantum degenerate gas is thus formed.

Ground experimental verification

In order to provide reference and verification for the space station experiment, we did a series of tests on the ground. Figure 5 shows the illustrations of experimental parameter settings for the TSC scheme in the ground verification experiments towards Chinese space station.

In the experiment, we used a pair of 1,064 nm far-detuned lasers with the waist radius of 30 μm to form an optical dipole trap, which trapped the ^{87}Rb atoms. The initial power of a single laser beam is 5 W, and the intensity is ramped down to 23 mW in 5,700 m by the exponential curve

$$P(t) = P_0\left(1 + \frac{t}{\tau}\right)^{-\beta}, \qquad (7$$

Where P_0 is the initial laser power, τ and β are the characteristic parameters associated with the ramping curve. This process reduces the depth of the optical dipole trap gradually in order to allow the atoms to undergo runaway evaporation cooling. After the atomic clouds are cooled in the thin-waisted optical trap in the first stage, the BEC with an atomic number of 6.75×10^4 and a temperature of 74 nk is formed (see Figure 6A). Then, the laser power of the thin-waisted optical trap is kept unchanged for the next 200 m, during which the thick-waisted optical trap laser is turned on for adiabatic loading to the maximum power of 200 mW and the waist width of each beam is 300 μm. At the same time, the lifting magnetic field is gradually turned on at this stage in order to counteract the effect of the gravitational field in the subsequent decompression cooling. After that, the laser power of the thin-waisted optical trap was gradually turned off, and the laser intensity is slowly decreased from 23 to 7 mW within 400 m. During this period, the thick-waisted optical trap first kept the laser power value unchanged for 50 m, and then reduced the laser power to 74 mW at the next 350 mW according to Eq. 7 by setting different parameters. In the meantime, after holding the value of the lifting magnetic field unchanged for 50 m, the gradient of the magnetic field is slowly decreased in a linear form for 300 m, and remains unchanged for the last 50 m. To minimize the effects of ground gravity, we use gradient magnetic fields to lift the atoms. But after many experiments, we found that when the second-stage potential well is shallow, the gradient magnetic field will heat the atoms. So in the later stage we gradually weaken the gradient of the magnetic field. At the end, after 20 m of TOF (time-of-flight), the equivalent temperature of BEC energy is measured to be 5 nk, and the number of ^{87}Rb atoms is 2.81×10^4. The image of BEC after deep cooling in the ground verification experiments are shown in the insert of Figure 7.

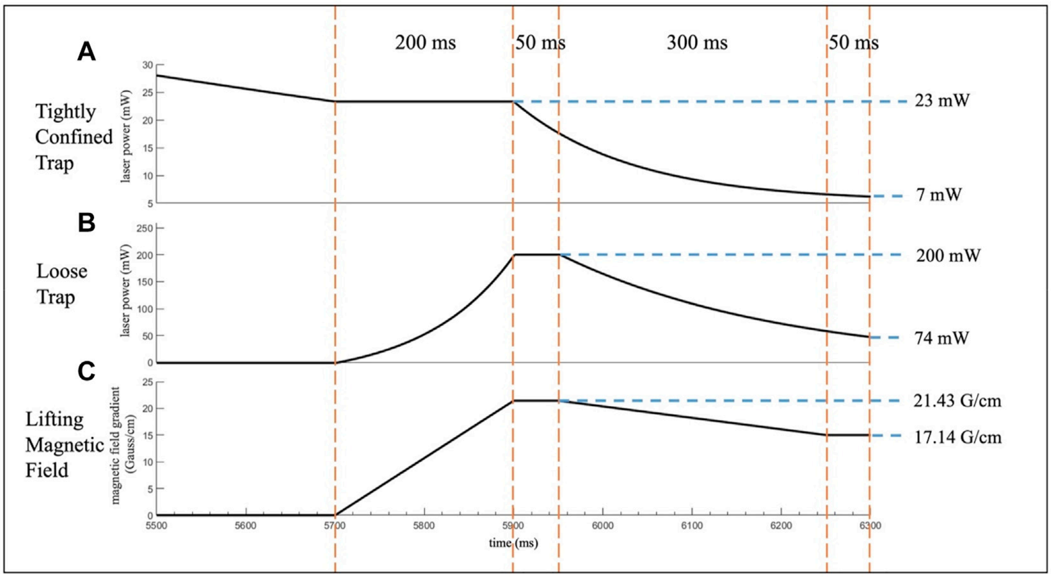

FIGURE 5
Experimental parameter settings for the two-stage cooling scheme in the ground verification experiments towards Chinese space station. Illustrations **(A,B)** show the variation of laser power with time for the thin-waisted ODT and the thick-waisted ODT, respectively, during the implementation of the TSC scheme. **(C)** The gradient of the lifting magnetic field (compensating for gravitational effects) changes as the experiment progresses.

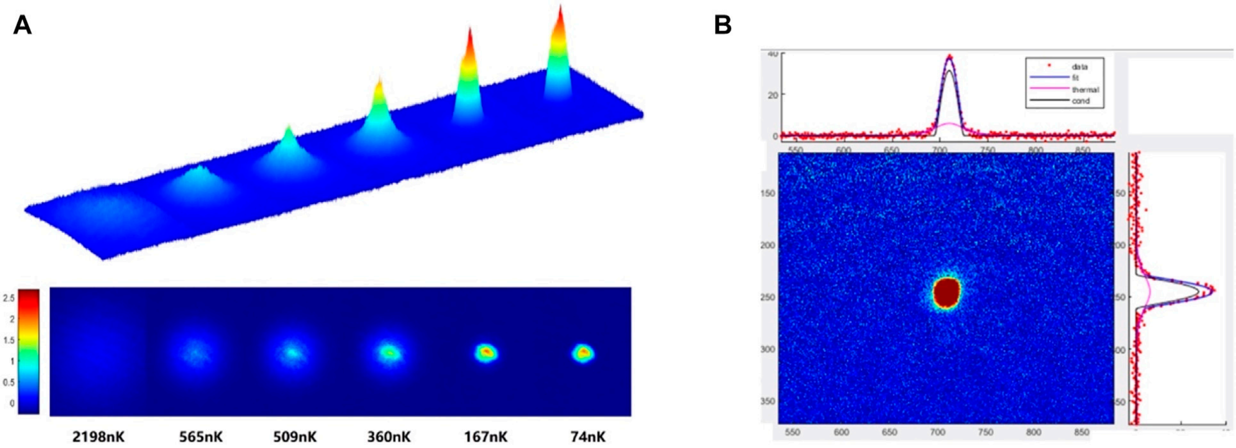

FIGURE 6
(A) First stage cooling with tight crossed beam trap. The temperature of BEC reached to 74 nK; **(B)** Second stage cooling with loose crossed beam trap. The temperature of BEC reached to 5 nK. Corresponding 100 pK in the microgravity.

Our group has previously performed multiple numerical simulations using the direct simulation Monte Carlo (DSMC) method [25, 39]. The simulation results theoretically confirm that the atomic temperature can be reduced to 100 pK when the TSC process is carried out for about 7.3 s in the microgravity on the space station [39]. This includes 5 s of evaporative cooling in the first stage and about 2.3 s of adiabatic diffusion cooling in the second stage. Simultaneously, the numerical simulation results show that if the CAPR on the Chinese space station are isolated from vibration, the temperature of quantum gas can be below

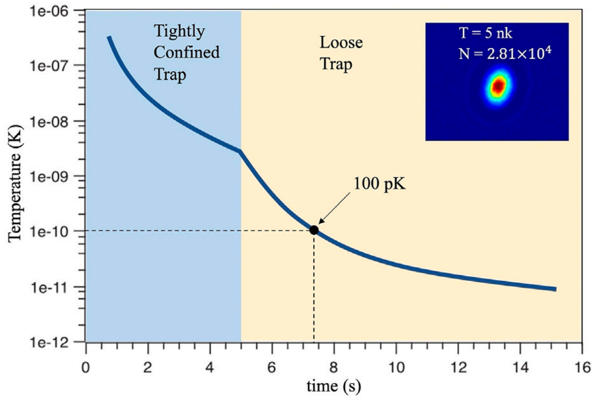

FIGURE 7
The schematic diagram of the numerical simulation results of TSC scheme. It is theoretically confirmed that the atomic temperature can be reduced to 100 pK when the TSC process is proceeded around 7.3 s in microgravity on the space station [39]. The insert shows the image of BEC after deep cooling in the ground verification experiments. The equivalent temperature of BEC is T = 5 pK and the number of ^{87}Rb atoms is n = 2.81 × 10^4.

10 pK around 15 s [39]. The schematic diagram of simulation results of TSC scheme is shown in Figure 7.

Conclusion

Mankind is making continuous efforts in the pursuit of low temperature. From the preparation of liquid helium to cold atomic gases, the level of low temperature continued to improve from K (liquid helium) to 1 × 10^{-3} K (magneto-optical trap), 1 × 10^{-6}K (molasses), 1 × 10^{-9} K (quantum degenerate gas), and possibly even 1 × 10^{-12} K (deeply cooled quantum gas). Further cooling is a key area of competition. It has been widely recognized in the international physics community that ultra-cold atomic experiments in microgravity can achieve this goal. The purpose of the Cold Atom Physics Rack on Chinese space station is to achieve ultra-low temperature Bose-Einstein Condensation on the scale of pico-Kelvin (pK) and carry out a series of physical experiments. Two-stage cooling is proved to be a reliable and operational solution that can meet the requirements of physical experiments towards CAPR. Cold atoms of 5 nK on the ground have been obtained in verification experiments, and the equivalent temperature will be less than 100 pK in the microgravity environment of the space station in the future. Ultracold atoms in space are about to open up new avenues for quantum simulation and precision measurements.

Data availability statement

The original contributions presented in the study are included in the article/Supplementary Material, further inquiries can be directed to the corresponding author.

Author contributions

HL, JY, XY, BW, YX, LL, AL, MH, SJ, WX, BW, DC, TL, XH, LL, XZ, WC, and XC participated in the construction of prototypes. XC, WX, and WC directed the research. HL and BW performed the experiments and measured experimental data. LL, AL, MH, and SJ assisted the experiments. JY and XY contributed to the analysis of data. YX contributed to the numerical simulation. HL wrote the manuscript. XC revised the manuscript.

Funding

This work is supported by the National Natural Science Foundation of China (Grants Nos. 11920101004, 11334001, 61727819, 61475007) and the National Key Research and Development Program of China (Grant Nos. 2021YFA1400900, 2021YFA0718300).

Acknowledgments

Thanks to all the project staff for the construction and promotion of the Cold Atomic Physics Rack on the Chinese Space Station. Thanks to Tian Luan and Bo Fan for their previous simulation studies on the two-stage cooling scheme.

Conflict of interest

The authors declare that the research was conducted in the absence of any commercial or financial relationships that could be construed as a potential conflict of interest.

Publisher's note

References

1. Bergmann P, Sabbata V. *Advances in the interplay between quantum and gravity physics*, 103-33. Boston: Kluwer (2002). p. 317–39.

2. Bloch I, Dalibard J, Nascimbène S. Quantum simulations with ultracold quantum gases. *Nat Phys* (2012) 8(4):267–76. doi:10.1038/nphys2259

3. Rosi G, Sorrentino F, Cacciapuoti L, Prevedelli M, Tino GM. Precision measurement of the Newtonian gravitational constant using cold atoms. *Nature* (2014) 510:518–21. doi:10.1038/nature13433

4. Bouyer P, Kasevich MA. Heisenberg-limited spectroscopy with degenerate Bose-Einstein gases. *Phys Rev A (Coll Park)* (1997) 56(2):R1083–6. doi:10.1103/physreva.56.r1083

5. Dowling JP. Correlated input-port, matter-wave interferometer: Quantum-noise limits to the atom-laser gyroscope. *Phys Rev A (Coll Park)* (1998) 57(6): 4736–46. doi:10.1103/physreva.57.4736

6. Gupta S, Dieckmann K, Hadzibabic Z, Pritchard DE. Contrast interferometry using bose-einstein condensates to measureh/mandαand. *Phys Rev Lett* (2002) 89(14):140401. doi:10.1103/physrevlett.89.140401

7. Eckert K, Hyllus P, Bruß D, Poulsen UV, Lewenstein M, Jentsch C, et al. Differential atom interferometry beyond the standard quantum limit. *Phys Rev A (Coll Park)* (2006) 73(1):013814. doi:10.1103/physreva.73.013814

8. Onnes HK. The resistance of pure mercury at helium temperatures. *Comm Phys Lab Univ Leiden* (1911) 12.

9. Onnes HK. *The superconductivity of mercury*. Leiden, Netherlands: Comm. Phys. Lab. Univ. Leiden (1911). p. 122–4.

10. Chu S, Hollberg L, Bjorkholm JE, Cable A, Ashkin A. Three-dimensional viscous confinement and cooling of atoms by resonance radiation pressure. *Phys Rev Lett* (1985) 55:48–51. doi:10.1103/physrevlett.55.48

11. Dalibard J, Cohen-Tannoudji C. Laser cooling below the Doppler limit by polarization gradients: Simple theoretical models. *J Opt Soc Am B* (1989) 6(11): 2023–45. doi:10.1364/josab.6.002023

12. Anderson MH, Ensher JR, Matthews MR, Wieman CE, Cornell EA. Observation of bose-einstein condensation in a dilute atomic vapor. *Science* (1995) 269(5221):198–201. doi:10.1126/science.269.5221.198

13. Davis KB, Mewes MO, Andrews MR, van Druten NJ, Durfee DS, Kurn DM, et al. Bose-einstein condensation in a gas of sodium atoms. *Phys Rev Lett* (1995) 75(22):3969–73. doi:10.1103/physrevlett.75.3969

14. Bradley CC, Sackett CA, Tollett JJ, Hulet RG. Evidence of bose-einstein condensation in an atomic gas with attractive interactions. *Phys Rev Lett* (1995) 75(9):1687–90. doi:10.1103/physrevlett.75.1687

15. Leanhardt AE, Pasquini TA, Saba M, Schirotzek A, Shin Y, Kielpinski D, et al. Cooling Bose-Einstein condensates below 500 picokelvin. *Science* (2003) 301(5639): 1513–5. doi:10.1126/science.1088827

16. Van Zoest T, Gaaloul N, Singh Y, Ahlers H, Herr W, Seidel ST, et al. Bose-Einstein condensation in microgravity. *Science* (2010) 328(5985):1540–3. doi:10.1126/science.1189164

17. Müntinga H, Ahlers H, Krutzik M, Wenzlawski A, Arnold S, Becker D, et al. Interferometry with Bose-Einstein condensates in microgravity. *Phys Rev Lett* (2013) 110:093602. doi:10.1103/physrevlett.110.093602

18. Becker D, Lachmann MD, Seidel ST, Ahlers H, Dinkelaker AN, Grosse J, et al. Space-borne Bose-Einstein condensation for precision interferometry. *Nature* (2018) 562:391–5. doi:10.1038/s41586-018-0605-1

19. Geiger R, Ménoret V, Stern G, Zahzam N, Cheinet P, Battelier B, et al. Detecting inertial effects with airborne matter-wave interferometry. *Nat Commun* (2011) 2(1):474. doi:10.1038/ncomms1479

20. Sackett CA, Lam TC, Stickney JC, Burke JH. Extreme adiabatic expansion in micro-gravity: Modeling for the cold atomic laboratory. *Microgravity Sci Technol* (2018) 30, 155–63. doi:10.1007/s12217-017-9584-3

21. Gibney E. Universe's coolest lab set to open up quantum world. *Nature* (2018) 557:151–2. doi:10.1038/d41586-018-05111-2

22. Elliott ER, Krutzik MC, Williams JR, Thompson RJ, Aveline DC. NASA's cold atom lab (CAL): System development and ground test status. *npj Microgravity* (2018) 4(1):16. doi:10.1038/s41526-018-0049-9

23. Aveline DC, Williams JR, Elliott ER, Dutenhoffer C, Kellogg JR, Kohel JM, et al. Observation of bose–einstein condensates in an earth-orbiting research lab. *Nature* (2020) 582(7811):193–7. doi:10.1038/s41586-020-2346-1

24. Wang L, Zhang P, Chen X, Ma Z. Generating a picokelvin ultracold atomic ensemble in microgravity. *J Phys B: Mol Opt Phys* (2013) 46:195302. doi:10.1088/0953-4075/46/19/195302

25. Yao H, Luan T, Li C, Zhang Y, Ma Z, Chen X. Comparison of different techniques in optical trap for generating picokelvin 3D atom cloud in microgravity. *Opt Commun* (2016) 359:123–8. doi:10.1016/j.optcom.2015.09.065

26. Luan T, Li Y, Zhang X, Chen X. Realization of two-stage crossed beam cooling and the comparison with Delta-kick cooling in experiment. *Rev Sci Instrum* (2018) 89:123110. doi:10.1063/1.5046815

27. Chen X, Fan B. The emergence of picokelvin physics. *Rep Prog Phys* (2020) 83: 076401. doi:10.1088/1361-6633/ab8ab6

28. Deppner C, Herr W, Cornelius M, Stromberger P, Sternke T, Grzeschik C, et al. Collective-mode enhanced matter-wave optics. *Phys Rev Lett* (2021) 127(10): 100401. doi:10.1103/physrevlett.127.100401

29. LeBlanc L. Physics.APS. *Physics* (2018) 11:131. Available at: https://physics.aps.org/articles/v11/131.

30. Stamper-Kurn D, Ueda M. Spinor Bose gases: Symmetries, magnetism, and quantum dynamics. *Rev Mod Phys* (2013) 85(3):1191–244. doi:10.1103/revmodphys.85.1191

31. Wang W, Zhu H, Wang L, Bai W, Chen X, Liu W. Precise measurements of quantum magnetism of cold atoms in ground and microgravity environment. *Sci Sin -Phys Mech Astron* (2021) 51:074207. doi:10.1360/sspma-2020-0475

32. Banerjee A, Bridges CA, Yan JQ, Aczel AA, Li L, Stone MB, et al. Proximate Kitaev quantum spin liquid behaviour in a honeycomb magnet. *Nat Mater* (2016) 15(7):733–40. doi:10.1038/nmat4604

33. Jin S, Zhang W, Guo X, Chen X, Zhou X, Li X. Evidence of potts-nematic superfluidity in a hexagonal sp^2 optical lattice. *Phys Rev Lett* (2021) 126:035301. doi:10.1103/physrevlett.126.035301

34. Muñoz de Nova JR, Golubkov K, Kolobov VI, Steinhauer J. Observation of thermal Hawking radiation and its temperature in an analogue black hole. *Nature* (2019) 569(7758):688–91. doi:10.1038/s41586-019-1241-0

35. Helfrich K, Hammer H. Resonant atom-dimer relaxation in ultracold atoms. *Europhys Lett* (2009) 86:53003. doi:10.1209/0295-5075/86/53003

36. Ketterle W, Van Druten N. Evaporative cooling of trapped atoms. *Adv Mol Opt Phys* (1996) 37:181–236.

37. Barrett MD, Sauer JA, Chapman MS. All-optical formation of an atomic bose-einstein condensate. *Phys Rev Lett* (2001) 87(1):010404. doi:10.1103/physrevlett.87.010404

38. Condon G, Rabault M, Barrett B, Chichet L, Arguel R, Eneriz-Imaz H, et al. All-optical bose-einstein condensates in microgravity. *Phys Rev Lett* (2019) 123(24): 240402. doi:10.1103/physrevlett.123.240402

39. Fan B, Zhao L, Zhang Y, Sun J, Xiong W, Chen J, et al. Numerical study of evaporative cooling in the space station. *J Phys B: Mol Opt Phys* (2020) 54:015302. doi:10.1088/1361-6455/abc72d

Frontiers in Physics

TYPE Original Research
PUBLISHED 12 August 2022
DOI 10.3389/fphy.2022.967255

OPEN ACCESS

EDITED BY
Andrea Bertoldi,
ParisTech Institut d'Optique Graduate School, France

REVIEWED BY
Shayne Bennetts,
University of Amsterdam, Netherlands
Georgy Kazakov,
Vienna University of Technology, Austria

*CORRESPONDENCE
Tiantian Shi,
tts@pku.edu.cn

SPECIALTY SECTION
This article was submitted to Atomic and Molecular Physics,
a section of the journal
Frontiers in Physics

RECEIVED 12 June 2022
ACCEPTED 18 July 2022
PUBLISHED 12 August 2022

CITATION
Shi T, Miao J, Zhang J and Chen J (2022), Active optical clock lasing on the Cs $7S_{1/2}$-$6P_{3/2}$ transition under a weak magnetic field.
Front. Phys. 10:967255.
doi: 10.3389/fphy.2022.967255

Active optical clock lasing on the Cs $7S_{1/2}$-$6P_{3/2}$ transition under a weak magnetic field

Tiantian Shi[1]*, Jianxiang Miao[1], Jia Zhang[1] and Jingbiao Chen[1,2]

[1]State Key Laboratory of Advanced Optical Communication Systems and Networks, Institute of Quantum Electronics, School of Electronics, Peking University, Beijing, China, [2]Hefei National Laboratory, Hefei, China

In the bad-cavity limit, the collective atomic dipole is highly coherent, resulting in the phase information of an active optical clock (AOC) laser primarily stored in the atomic gain medium. Therefore, compared with the good-cavity laser, the sensitivity of an AOC laser to cavity fluctuations is greatly reduced, as characterized by the suppressed cavity-pulling effect. In this work, the AOC lasing on the cesium $7S_{1/2}$-$6P_{3/2}$ clock transition with a natural linewidth of 1.81 MHz under a weak magnetic field is achieved. We calculate the Zeeman spectra of upper and lower states of clock transition, and measure the beat-note spectrum between different Zeeman-sublevel transitions of $7S_{1/2}$-$6P_{3/2}$. Moreover, the cavity-pulling, temperature, power, and linewidth characteristics of the AOC laser are demonstrated under a weak magnetic field. Such an emerging laser can be applied as a narrow-linewidth local oscillator, as well as an active optical frequency standard, which is promising for the field of precision measurement.

KEYWORDS

bad-cavity limit, suppressed cavity-pulling effect, quantum-limited linewidth, Zeeman effect, beat-note spectrum, active optical frequency standard

1 Introduction

The ultranarrow-linewidth laser with long coherence time has an irreplaceable status in the field of precision measurement. One of the most important applications is the measurement of time or frequency realized by the state-of-the-art optical atomic clocks [1–3], with implications for the geodetic surveys [4], searching for the variation of fundamental constants [5], gravitational wave detection [6], and test of general relativity [7].

Consequently, great efforts have been put into the development of extremely coherent light sources. Three of the most widely used techniques include the Pound–Drever–Hall (PDH) technique using highly stable optical Fabry-Pérot (F-P) resonators [8,9], the spectral-hole burning in cryogenic crystals [10,11], and the stimulated emission of radiation from the atomic gain medium of the active optical clock (AOC) technique to realize mHz-linewidth superradiant lasers [12–18] and frequency stabilized bad-cavity lasers [19,20]. In the first approach, the laser frequency is stabilized to an optical reference cavity with the ultra-stable length to narrow the laser linewidth, which has realized the most-coherent oscillator with the narrowest linewidth of 10 mHz [9]. However, the mirrors of the reference cavity inevitably vibrate due to the thermal Brownian motion noise, limiting the narrowing of laser linewidth and increasing the system complexity. With the second method, frequency stabilizes to a steady-state pattern of spectral holes in cryogenically cooled crystals. The frequency stability has reached $1 \times 10^{-15}/\sqrt{\tau}$ [10], but further optimization is limited to the temperature instability, Doppler shifts, and residual amplitude modulation. Comprehensively, in this work, we choose the AOC technique to realize the extremely coherent laser sources.

For the bad-cavity laser, the coherence is stored in the collective atom dipole, that is, the gain medium, and the stimulated emission of radiation can be realized when driven by the weak intracavity photon field. Working in the bad-cavity limit, where the atomic decay rate Γ_{gain} is much smaller than the cavity dissipation rate κ, only weak cavity-induced feedback on the atomic dipole. Consequently, the laser frequency is mainly determined by the atomic radiation rather than the cavity-mode frequency, which is similar to the hydrogen maser in the microwave domain [21]. The cavity-pulling coefficient is reduced to $P = \frac{\Gamma_{\text{gain}}}{\Gamma_{\text{gain}}+\kappa} \ll 1$ [12], while $P \approx 1$ in the good-cavity limit. In addition, the Schawlow–Townes quantum–limited linewidth of the AOC laser can be much reduced to the mHz-level [22]; [14]. AOC is emerging as a technology that can optimize the frequency stability of optical standards and enhance the coherence of laser sources. Using the clock transition of cold strontium atoms, Thompson's group observed a fractional Allan deviation of 6.7×10^{-16} at 1 s of the superradiant laser [15]. Schäffer [17] and Laske [16] investigated the characteristics of superradiant lasing in cold thermal strontium and cold calcium ensembles, respectively. A few achievements have been acquired, but using the cold atom as a gain medium, the current AOCs are limited to the pulse-mode operation and low output power. This problem can be solved by the thermal-atom scheme. Liu et al. proposed a superradiant laser based on the hot atomic-beam method, which has advantages of continuous-wave operation [18]. Moreover, using the thermal cesium ensemble as a gain medium, Chen [20] experimentally realized a continuous-wave active optical frequency standard with power of 100 μW, based on the experimental scheme proposed in 2010 [23].

In this work, we demonstrated the AOC lasing on the cesium $7S_{1/2}$-$6P_{3/2}$ clock transition under a weak magnetic field using the thermal atomic ensemble. Due to the Zeeman effect, level splitting of $7S_{1/2}$ and $6P_{3/2}$ states occurs under the action of a magnetic field, which is calculated in the Section 3.1.1. Moreover, the cavity-pulling, temperature, power, magnetic field, and linewidth characteristics of the AOC laser under a weak magnetic field are analyzed in Section 3.2.1, Section 3.2.2, Section 3.2.3, Section 3.2.4, and Section 3.2.5, respectively.

2 Experimental methods

The experimental scheme and relevant energy levels are depicted in Figures 1A,B, respectively. A cloud of thermal cesium atoms in a vapor cell provided the gain medium, which was pumped by the linearly polarized 459 nm interference filter configuration–extended cavity diode laser (IF-ECDL). Moreover, the frequency of the IF-ECDL was stabilized to cesium $6S_{1/2}(F = 4)$—$7P_{1/2}(F = 3)$ hyperfine transition by the modulation transfer spectrum (MTS). The natural linewidth of cesium $6S_{1/2}$-$7P_{1/2}$ transition at the wavelength of 459.3 nm is $2\pi \times 126$ kHz [24], while the laser linewidth of the IF-ECDL is around 13.3 kHz [25], which is much smaller than that of the corresponding atomic natural linewidth. Moreover, the cesium atoms were pumped by the 459 nm laser through the velocity-selective mechanism. In this work, the pumping power was adjustable in the range of 8–13 mW. Assuming that the pumping light intensity was $I = 10$ mW/mm^2, only atoms in the direction of the cavity mode with a velocity of $|\vartheta| \leq \Delta\vartheta/2 = 6.05$ m/s could be pumped to the $7S_{1/2}$ excited state. The relevant calculation is given in [26]. Therefore, the inhomogeneous Doppler broadening is $\Delta\omega_D = \frac{\vartheta}{c}\omega_0 = 2\pi \times 4.12$ MHz, where c is the speed of light, and ω_0 is the transition frequency of $7S_{1/2}$-$6P_{3/2}$.

The realization of 1,470 nm lasing is shown in Figure 1B. First, the cesium atoms are pumped from the $6S_{1/2}$ ($F = 4$) ground state to the $7P_{1/2}$ ($F = 3$) state by the 459 nm laser, and then decay to the $7S_{1/2}$ ($F = 4$) upper level by spontaneous radiation. Second, the atoms at the $7S_{1/2}$ ($F = 4$) state decay to $6P_{3/2}$ ($F = 5, 4, 3$) lower levels. Third, the atoms at $6P_{3/2}$ ($F = 5, 4, 3$) levels return to the $6S_{1/2}$ ground state and then pumped to the $7P_{1/2}$ state again by the continuous-wave 459 nm laser. In the steady state, the population inversion can be built up between $7S_{1/2}$ ($F = 4$) and $6P_{3/2}$ ($F = 5$), $7S_{1/2}$ ($F = 4$) and $6P_{3/2}$ ($F = 4$), and $7S_{1/2}$ ($F = 4$) and $6P_{3/2}$ ($F = 3$) levels, respectively. This result is experimentally demonstrated in our previous work, as given in [27]. In this work, we chose the $7S_{1/2}$ ($F = 4$) to $6P_{3/2}$ ($F = 5$) transition as the clock-transition laser, because the power of stimulated emission between this transition is biggest.

Through the weak feedback of a low-finesse optical cavity consisting of a plane mirror M_1 and a plano-concave mirror M_2 separated by a distance $L = 18$ cm, the stimulated emission of radiation on the $7S_{1/2}$-$6P_{3/2}$ transition at a wavelength of 1,470 nm was achieved. The reflectivities of M_1 and M_2 at the wavelength of 1,470 nm were, separately, 46.5% and 24.5%, and both with anti-reflective coatings at 459 nm. The spontaneous decay rate of cesium $7S_{1/2}$-$6P_{3/2}$ transition is $\Gamma_0 = 2\pi \times 1.81$ MHz [28], and the Doppler broadening of the $7S_{1/2}$ excited state is $\Gamma_D = 2\pi \times 8.23$ MHz under the condition of pumping light intensity of $I = 10$ mW/mm^2 [26]. Therefore, the atomic decay rate is $\Gamma_{\text{gain}} = \Gamma_0 + \Gamma_D = 2\pi \times 10$ MHz, which is much smaller than the cavity dissipation rate $\kappa = 2\pi \times 244$ MHz.

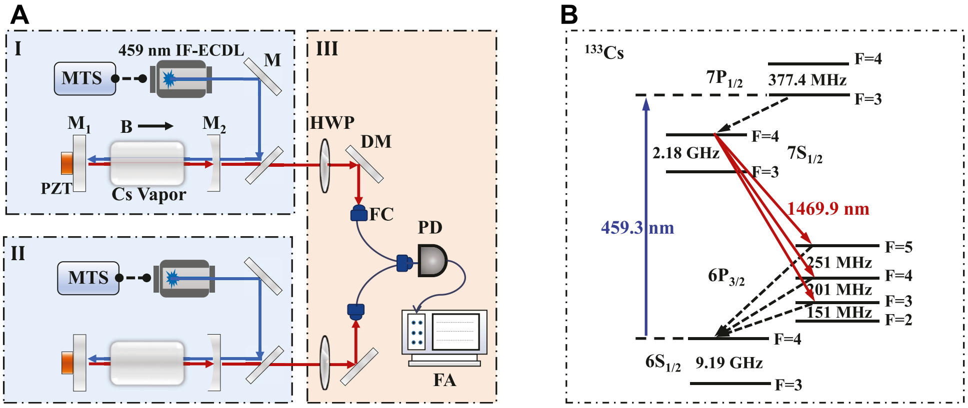

FIGURE 1
Working principle of the 1,470 nm AOC laser. **(A)** Sketch of the experimental setup for AOC lasing under a weak magnetic field. MTS, modulation transfer spectroscopy; IF-ECDL, interference filter configuration extended cavity diode laser; M, high-reflection coated mirror; M$_1$ and M$_2$, cavity mirrors; PZT, piezoelectric ceramic; HWP, half-wave plate; DM, dichroic mirror coated with anti-reflection at 1,470 nm and high-reflection at 459 nm; FC, fiber coupler; PD, photodetector; FA, frequency analyzer. **(B)** Hyperfine level scheme for the ^{133}Cs atom shows the 1,470 nm transition as the AOC lasing using 459 nm transition for pumping.

To study the characteristics of active optical frequency standard at a weak external magnetic field, we built two 1,470 nm laser systems, as shown as parts I and II in Figure 1A. A weak magnetic field was induced axially in the vapor cell of part I, while another vapor in part II without applying an additional magnetic field. A double-layer mu-metal magnetic shielding was applied outside each vapor cell to isolate the geomagnetic field. The 1,470 nm laser output from part II only had one frequency mode used as the frequency reference. In part I, the upper and lower levels of 1,470 nm clock transition split under the weak magnetic field, which led to different clock transitions between Zeeman levels of 7S$_{1/2}$ and 6P$_{3/2}$ states. The beat-note signal between clock transitions of Zeeman levels input a polarization-maintaining fiber, then was detected by the photodetector (PD) connecting a frequency analyzer (FA). Meanwhile, the beat-note signal between lasers from part I and part II were also measured by the FA. A half-wave plate (HWP) in front of the fiber coupler (FC) was used to adjust the laser power for optical heterodyning.

3 Results

3.1 Theory results

3.1.1 Zeeman spectra of clock-transition levels

Under the weak magnetic field, considering $|Fm\rangle$ as a basis, the Hamiltonian matrix elements for each value of magnetic quantum number m, which is the projection of the total angular momentum F along the direction of external magnetic field B, are given by [29,30]

$$\begin{aligned}\langle IJFm|H|IJF'm\rangle = {} & \frac{1}{2}\delta_{FF'}\left\{AK + B\left[\frac{3K(K+1) - 2I(I+1)2J(J+1)}{2I(2I-1)2J(2J-1)}\right]\right\} \\ & + \mu_B g_J B_z (-1)^{I+J+m+1} \times \sqrt{J(J+1)(2J+1)(2F+1)(2F'+1)} \times \begin{Bmatrix} J & 1 & J \\ F' & I & F \end{Bmatrix}\begin{pmatrix} F & 1 & F' \\ -m & 0 & m \end{pmatrix} \\ & - \mu_N g_I B_z (-1)^{I+J+m+1} \times \sqrt{I(I+1)(2I+1)(2F+1)(2F'+1)} \times \begin{Bmatrix} I & 1 & I \\ F' & J & F \end{Bmatrix}\begin{pmatrix} F & 1 & F' \\ -m & 0 & m \end{pmatrix}.\end{aligned} \tag{1}$$

The Hamiltonian matrix element H is in megahertz. I and J are the nuclear spin and angular momentum, $K = F(F+1) - J(J+1) - I(I+1)$, and A and B represent the magnetic dipole and electric quadrupole constants, respectively. μ_B and g_J are the Bohr magneton and the Lange g factor, respectively, and μ_N and g_I are the nuclear Bohr magneton and the nuclear g factor, respectively. The first term, second term, and the third therm of Eq. 1 depict the contribution from the zero field, electron Zeeman effect, and nuclear Zeeman effect, respectively. The contribution of nuclear spin is negligible because g_I is much smaller than g_J of the cesium atom.

For the 7S$_{1/2}$ state of cesium, $I = 7/2$, $J = 1/2$, the total angular momentum $F = I - J = 3$ and $F = I + J = 4$. Under an external magnetic field, the 7S$_{1/2}$ state splits into $(2J + 1)(2I + 1) = 16$ Zeeman sublevels. $g_J \approx 2$ and $A = h \cdot 545.90$ MHz [31]. The electric quadrupole constant B is zero for the state with $J = 1/2$. Therefore, the Hamiltonian of the cesium 7S$_{1/2}$ state for each value of m is expressed as follows:

$$\begin{aligned}\langle Fm|H|F'm\rangle = {} & \frac{1}{4}\delta_{FF'}A[2F(F+1) - 33] + \mu_B g_J B_z (-1)^{m+1} \times \sqrt{\frac{3}{2}(2F+1)(2F'+1)} \\ & \times \begin{Bmatrix} \frac{1}{2} & 1 & \frac{1}{2} \\ F' & \frac{7}{2} & F \end{Bmatrix}\begin{pmatrix} F & 1 & F' \\ -m & 0 & m \end{pmatrix}.\end{aligned} \tag{2}$$

For the 6P$_{3/2}$ state of cesium, $I = 7/2$, $J = 3/2$. The total angular momentum $|J - I| \le F \le J + I$, thus F can take any value of 2, 3, 4, or 5. Under an external magnetic field, the 6P$_{3/2}$ state splits into $(2J + 1)(2I + 1) = 32$ Zeeman sublevels. $g_J \approx \frac{4}{3}$, $A = h \cdot 50.28827$ MHz, and the electric quadrupole constant $B = -h \cdot 0.4934$ MHz

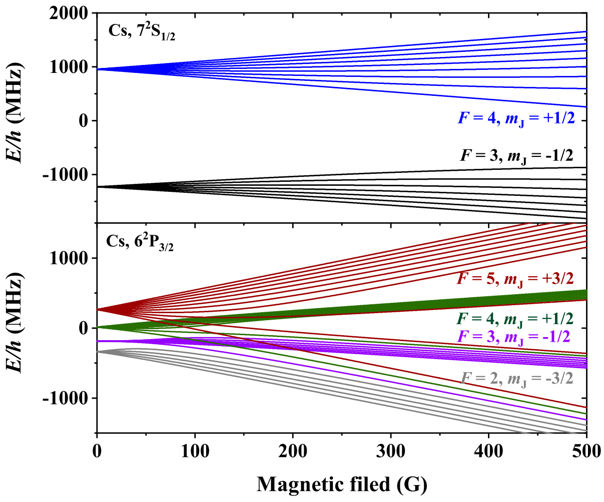

FIGURE 2
Splitting of the energy levels as a function of magnetic-field strength for the $7S_{1/2}$ upper level and the $6P_{3/2}$ lower level of clock transition. The blue and black lines represent the Zeeman sublevels of $7S_{1/2}$ $F = 4$ and $F = 3$. The red, green, purple, and gray lines are the Zeeman sublevels of $6P_{3/2}$ $F = 5$, $F = 4$, $F = 3$, and $F = 2$.

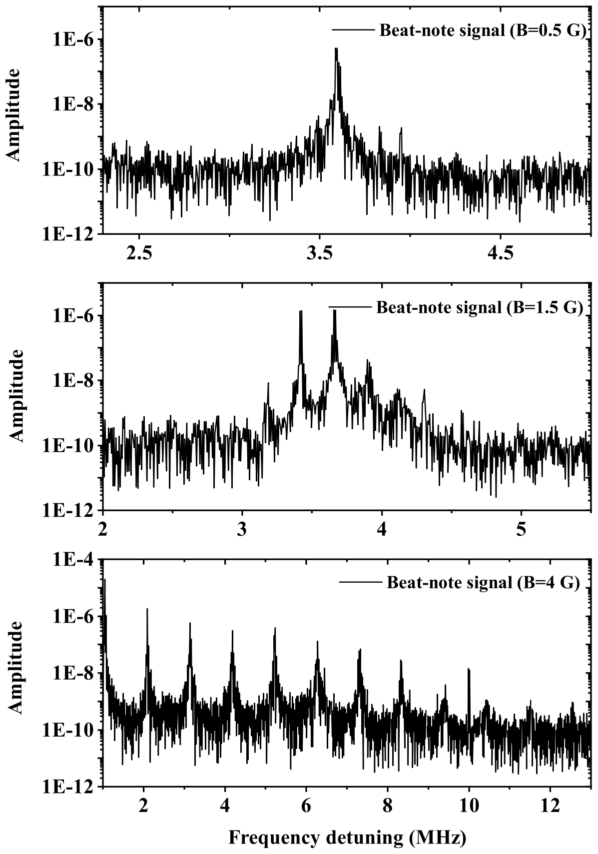

FIGURE 3
Beat-note signal between Zeeman sublevels of 1,470 nm clock-transition output from part I of Figure 1A under different external magnetic fields. The subgraphs from top to bottom represent the results with an external magnetic field of 0.5 G, 1.5 G, and 4 G, respectively.

for the $6P_{3/2}$ state [32]. Therefore, the Hamiltonian of the cesium $6P_{3/2}$ state for each value of m becomes

$$\begin{aligned}\langle Fm|H|F'm\rangle &= \frac{1}{8}\delta_{FF'}\left\{A[4F(F+1)-78] + B\frac{[2F(F+1)-39][2F(F+1)-37]-315}{84}\right\}\\ &+\mu_B g_J B_z(-1)^m \times \sqrt{15(2F+1)(2F'+1)} \times \begin{Bmatrix} \frac{3}{2} & 1 & \frac{3}{2} \\ F' & \frac{7}{2} & F \end{Bmatrix}\begin{pmatrix} F & 1 & F' \\ -m & 0 & m \end{pmatrix}.\end{aligned} \tag{3}$$

The Hamiltonian of $7S_{1/2}$ and $6P_{3/2}$ states for each value of m can be separately expressed in the following matrix form.

$$H = \begin{pmatrix} \langle 3m|H|3m\rangle & \langle 3m|H|4m\rangle \\ \langle 4m|H|3m\rangle & \langle 4m|H|4m\rangle \end{pmatrix}, \tag{4}$$

and

$$H = \begin{pmatrix} \langle 2m|H|2m\rangle & \langle 2m|H|3m\rangle & 0 & 0 \\ \langle 3m|H|2m\rangle & \langle 3m|H|3m\rangle & \langle 3m|H|4m\rangle & 0 \\ 0 & \langle 4m|H|3m\rangle & \langle 4m|H|4m\rangle & \langle 4m|H|5m\rangle \\ 0 & 0 & \langle 5m|H|4m\rangle & \langle 5m|H|5m\rangle \end{pmatrix}, \tag{5}$$

Solving the eigenvalues of the matrices, we obtain the splitting of energy levels as a function of the magnetic field strength for $7S_{1/2}$ and $6P_{3/2}$ states, as shown in Figure 2.

3.1.2 Laser linewidth

Working in the bad-cavity limit, the AOC laser has the advantage of the suppressed cavity-pulling effect expressed as the smaller cavity-pulling coefficient, that is, the rate of change of the laser frequency ω with respect to the cavity-mode frequency ω_c [12,33].

$$P = d\omega/d\omega_c = \Gamma_{\text{gain}}/\left(\Gamma_{\text{gain}} + \kappa\right), \tag{6}$$

where the cavity-pulling coefficient is $p = 0.039$ in this work. The laser frequency mainly depends on the atomic transition and is robust to the change of the cavity length caused by the environmental noise.

Contrary to the good-cavity lasers, AOC utilizes a bad cavity with the cavity dissipation rate being much wider than the atomic decay rate. Therefore, the frequency is insensitive to the cavity-length noise, which helps to narrow the laser linewidth. Without considering the influence of inhomogeneous Doppler broadening and the homogeneous power broadening, and according to the Shawlow–Townes quantum–limited linewidth in the bad-cavity regime [34], the laser linewidth can be expressed as

$$\Delta\nu_L = \frac{\kappa}{4\pi n}N_{\text{sp}}\left(\frac{\Gamma_{\text{gain}}}{\Gamma_{\text{gain}} + \kappa}\right)^2, \tag{7}$$

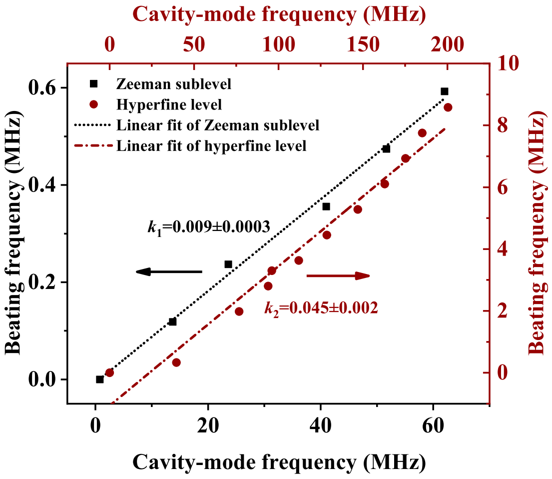

FIGURE 4
Beat-note frequency with the change of cavity-mode frequency. The black square dots are the experimental data of beat-note signal between Zeeman sublevels generated in the part I of Figure 1A under a magnetic field of 0.5 G. The data are fitted linearly with a slope of 0.009 ± 0.0003 (black dotted line). The red dots represent the experimental data of beat-note signal between AOC lasers generated in the part I and part II of Figure 1A without an applied magnetic field. Its linear fitting result is indicated by the red dotted line with a slope of 0.045 ± 0.002.

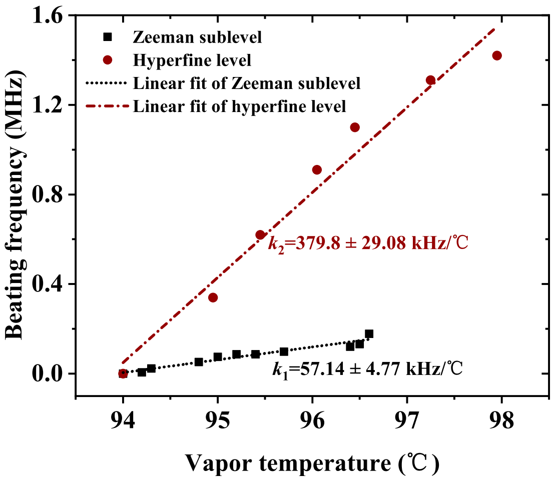

FIGURE 5
Beat-note frequency with the change of vapor temperature. The black square dots are the experimental data of beat-note signal between Zeeman sublevels generated in the part I of Figure 1A under a magnetic field of 0.5 G. The data are fitted linearly with a slope of 57.14 ± 4.77 kHz/°C (black dotted lines). The red dots represent the experimental data of the beat-note signal between AOC lasers generated in the part I and part II of Figure 1A without applied magnetic field. Its linear fitting result is indicated by the red dotted line with a slope of 379.8 ± 29.08 kHz/°C.

where n is the average intracavity photon number, and $N_{sp} = \frac{N_e}{N_e - N_g}$ is the spontaneous emission factor, N_e and N_g are the populations of the upper and lower laser levels, respectively. Here, $N_{sp} \approx 1$ for the four-level structure is shown in Figure 1B. Assuming that laser power can reach 50 μW, that is, $n = 2.4 \times 10^5$, the quantum-limited linewidth of the 1,470 nm laser is around 0.8 Hz.

3.2 Experimental results

Applying a weak magnetic field along the direction of light propagation to the vapor cell in part I of Figure 1A, of which intensity is between 0 and 4 G, the beat-note spectra between different Zeeman sublevels of 1,470 nm clock transition are observed. The subgraphs from top to bottom in Figure 3 represent the beat-note spectrum under a magnetic field of 0.5 G, 1.5 G, and 4 G, respectively. Obviously, under the zero magnetic field, the AOC laser output from the optical cavity of part I contains only one frequency component, and no beat-note signal can be observed by PD in Figure 1A. However, according to Figure 2, the energy levels of $7S_{1/2}$ and $6P_{3/2}$ split under an external magnetic field. Therefore, there are different transitions between Zeeman sublevels of $7S_{1/2}$ $F = 4$ and $6P_{3/2}$ $F = 5$. With the increase in the magnetic field, the splitting of energy level increases, resulting in the increase of frequency components of the AOC laser and the peaks of beating signal splitting from one to multiple.

Next, we analyze the cavity-pulling, temperature, power, magnetic field, and linewidth characteristics of the beat-note signal between Zeeman sublevels of 1,470 nm clock transition under the magnetic field of 0.5 G. In addition, the characteristics of the beat-note signal between 1,470 nm laser output from part I and part II of Figure 1A are studied simultaneously for comparison.

3.2.1 Cavity-pulling effect

According to Eq. 6, the bad-cavity coefficient is 0.039, which means that the influence of cavity-pulling noise on the laser frequency is suppressed by a factor of around 25. First, under zero magnetic field, we measured the central frequency of the beat-note signal between AOC laser, separately, output from part I and part II with the change of cavity-mode frequency of part I, as shown in the red dots in Figure 4. The experimental data were fitted linearly with a slope of 0.045 ± 0.002, which is close to the theoretical value of 0.039. For comparison, under a magnetic field of 0.5 G, the central frequency of the beat-note signal between Zeeman sublevels generated from part I with the change of its cavity-mode frequency is also depicted by the black square dots in Figure 4. Because the lasing generated from part I shared one optical cavity, the influence of common-mode noise induced by cavity-length fluctuation on the central frequency of the beat-note spectrum is greatly suppressed with the fitted cavity-pulling coefficient being only 0.009 ± 0.0003 depicted by the black dotted line.

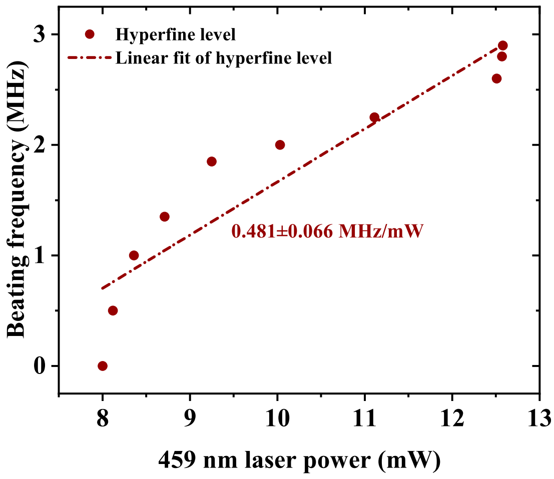

FIGURE 6
Beat-note frequency with the change of power of 459 nm laser. The red dots are the experimental data of the beat-note signal between AOC lasers generated in the part I and part II of Figure 1A without an applied magnetic field. Its linear fitting result is indicated by the red dotted line with a slope of 0.481 ± 0.066 MHz/mW.

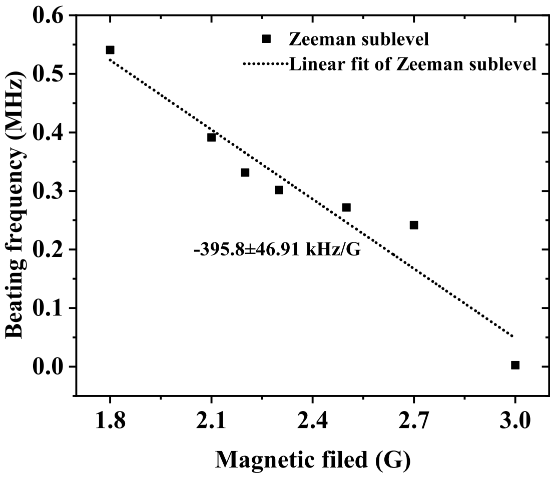

FIGURE 7
Beat-note frequency with the change of an external magnetic field. The black square dots are the experimental data of beat-note signal between Zeeman sublevels generated in the part I of Figure 1A. The data are fitted linearly with a slope of −395.8 ± 46.91 kHz/G (black dotted lines).

3.2.2 Temperature characteristic

Moreover, we measured the change of beat-note frequency with the temperature of atomic vapor placed in part I. The red dots in Figure 5 represent the beat-note signal of laser, separately, output from part I and part II, of which frequency is almost linearly changed with the vapor temperature and the slope is 379.8 ± 29.08 kHz/°C. The change in vapor temperature causes the cavity-length variation, which leads to the change in the beat-note frequency [35]. As for the result, as shown by the black square dots in Figure 5, of the beat-note signal between Zeeman sublevels, the fitted slope is only 57.14 ± 4.77 kHz/°C. The smaller slope is owing to the lasers sharing one cavity, which will reduce the influence of temperature change in the beat-note frequency. In addition, this result is similar to the experimental value reported in [20], where the cavity length is stabilized by the optical phase–locking loop technique.

3.2.3 Power characteristic

Next, we measured the beat-note frequency versus the power of the 459 nm laser. Figure 6 depicts the beating signal between laser output from part I and part II with a fitted slope of 0.481 ± 0.066 MHz/mW. Here, the experimental result of Zeeman sublevels is not shown, because the central frequency is almost constant with the change of pumping power. However, the pumping power greatly influences the output power of each transition between Zeeman sublevels. The beat-note signal disappears if the laser power changes by more than 1 mW.

3.2.4 Magnetic field characteristic

Under a weak magnetic field, we measured the central frequency of the beat-note signal between Zeeman sublevels with the change in the magnetic field, as depicted in the black square dots in Figure 7. The slope is − 395.8 ± 46.91 kHz/G using linear fitting. At present, the continuous variation range of the beat-note signal with the magnetic field is very small at around 2 MHz. According to Figure 3, the frequency component of the beat-note spectrum becomes complex, and it is difficult to continuously measure the frequency change of one of the beating spectra.

In this work, $7S_{1/2}$ ($F = 4$)-$6P_{3/2}$ ($F = 5$) transition is used to realize 1,470 nm lasing. Under an external magnetic field, the $7S_{1/2}$ ($F = 4$) and $6P_{3/2}$ ($F = 5$) hyperfine levels are split into 9 and 11 Zeeman sublevels, respectively. The transition selection rule under a weak field satisfies the condition of $\Delta F = 0, \pm 1$ (except for $F = 0 \rightarrow F = 0$), $\Delta m_F = 0, \pm 1$. Therefore, there are 27 kinds of Zeeman transitions. Because the result shown in Figure 7 of the study is measured by the heterodyne beat, there are many beat-note signals between different Zeeman sublevels. It is difficult to distinguish which transition corresponds to each beat-note signal. We can only measure the change in the center frequency of one of the beat-note signals with the magnetic field. Limited by the measurement method, we cannot give a direct theoretical result of the beat-note frequency with the change in the magnetic field in the current study. We leave this problem for future investigations.

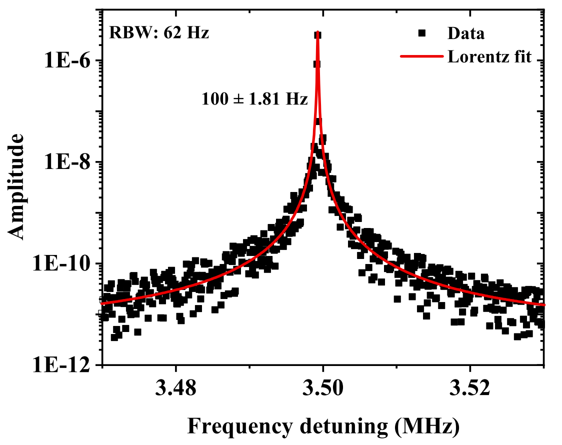

FIGURE 8
Typical beat-note spectrum between Zeeman sublevels of 1,470 nm clock-transition output from part I of Figure 1A under an external magnetic field of 0.5 G (RBW: 62 Hz). The linewidth of the experimental data (black square dots) is obtained by using the Lorentzian fit (red line).

3.2.5 Linewidth characteristic

Finally, we analyzed the linewidth characteristic of the beat-note signal between Zeeman sublevel transition between $7S_{1/2}$ and $6P_{3/2}$ states under an external magnetic field of 0.5 G. A typical beat-note signal is shown in Figure 8 with the resolution bandwidth of 62 Hz. The relative Lorentzian fit linewidth of the power spectrum of the beat-note signal is 100 Hz. It indicates that the relative noise between two modes of Zeeman sublevels is 70 Hz. Although this value is much wider than the quantum-limited linewidth calculated by Eq. 7, it is narrower than the linewidth measured by beating between two identical 1,470 nm lasers [35]. This is because the lasing share one common cavity, and the impact of noises induced by the cavity-length fluctuation, vapor temperature change, and pumping power fluctuation on the linewidth broadening is greatly suppressed. Although the common noise is largely reduced, the residual technical noises, such as the fluctuations of vapor-cell temperature, external magnetic field, and pumping laser power, still influence the laser linewidth. The influence of each type of technical noise on linewidth broadening is analyzed as follows.

First, the residual temperature fluctuations of the atomic vapor cell are the main factor resulting in the linewidth broadening. According to Figure 5, the slope of the beat-note frequency between different Zeeman sublevels with the change in vapor temperature is 57.14 ± 4.77 kHz/°C. The temperature stability of the vapor cell at a short-time scale is better than 1×10^{-5}. Therefore, after eliminating the most common- mode noise, the influence of residual temperature fluctuations on the relative noise is around 50 Hz at the vapor temperature of 95°C. Second, the contribution of residual power fluctuations of a pumping laser to linewidth broadening is negligible. Third, the applied magnetic field on the atomic vapor is 0.5 G. We installed two layers of mu-metal shield to isolate external magnetic field disturbance, for which the expected stability of magnetic field exceeds $\times 1\ 10^{-4}$ at a short-time scale. According to Figure 7, the slope of the beat-note frequency with the change of magnetic field is around − 395.8 ± 46.91. Consequently, the linewidth broadening induced by residual fluctuations of the magnetic field is smaller than 20 Hz. In summary, the linewidth broadening induced by the residual technical noises is estimated to be around 70 Hz, which agrees with the measured linewidth as shown in Figure 8. Next, we will further optimize the temperature and magnetic stabilities using a double-layer vapor cell and a multi-layer magnetic shielding, respectively, to narrow the laser linewidth.

In this work, the only beat-note linewidth is given to quantify the instantaneous stability of the 1,470 nm laser. However, the better way to evaluate the frequency stability of a clock is the Allan deviation. Since there still exists the technical noises, especially the temperature drift of the cesium atoms in long timescales, affecting the long-term stability of the 1,470 nm laser, we used the beat-note linewidth between two 1,470 nm Zeeman-sublevel transitions to represent the instantaneous stability. We leave the optimization of the long-term stability for future investigations.

4 Discussion

In this work, we realized the AOC lasing of cesium $7S_{1/2}$-$6P_{3/2}$ transition under a weak magnetic field. The beat-note spectrum is observed between different Zeeman- sublevel transitions. The central frequency of the power spectrum of the beat-note signal versus the cavity-mode frequency, vapor temperature, pumping power under a magnetic field of 0.5 G, respectively, is investigated. Since the Zeeman sublevel transition output from one cavity, the common-mode noises caused by the fluctuation of cavity length, vapor temperature, and pumping power are greatly suppressed. Therefore, the Lorentz fitting linewidth of the beat-note spectrum between Zeeman sublevels is narrower than that between two 1,470 nm lasers' output from two systems. Further studies about the influence of residual noises on the linewidth broadening will be carried out. Such an AOC laser, whose frequency mainly depends on the atomic transition, can be applied as a stable light source, for example, in passive optical clocks.

Data availability statement

The raw data supporting the conclusions of this article will be made available by the authors, without undue reservation.

Author contributions

JC conceived the idea of the four-level active optical clock. TS performed the experiments and carried out the theoretical calculations. TS wrote the manuscript. JM and JZ provided revisions. All authors contributed equally to the discussions of the results.

Funding

This research was funded by the National Natural Science Foundation of China (NSFC) (91436210), Innovation Program for Quantum Science and Technology (2021ZD0303200), China Postdoctoral Science Foundation (BX2021020), and Wenzhou Major Science and Technology Innovation Key Project (ZG2020046).

Acknowledgments

We give our best wishes on the occasion of Yiqiu Wang's 90th birthday. The authors would like to thank Wang for many useful discussions about the realization of active optical frequency standard. In particular, Jingbiao Chen sincerely thanks Wang for his support for the idea of active optical clock put forward as early as 2005. In order to encourage young researchers to explore innovative ideas in depth, Wang specially wrote an article to support the idea of active optical clock. His attitude to scientific investigation is the primordial force that propels us forward.

Conflict of interest

The authors declare that the research was conducted in the absence of any commercial or financial relationships that could be construed as a potential conflict of interest.

Publisher's note

References

1. Oelker E, Hutson RB, Kennedy CJ, Sonderhouse L, Bothwell T, Goban A, et al. Demonstration of 4.8×10^{-17} stability at 1 s for two independent optical clocks. *Nat Photon* (2019) 13:714–9. doi:10.1038/s41566-019-0493-4

2. Brewer SM, Chen J-S, Hankin AM, Clements ER, Chou CW, Wineland DJ, et al. $^{27}Al^{+}$ quantum-logic clock with a systematic uncertainty below 10^{-18}. *Phys Rev Lett* (2019) 123:033201. doi:10.1103/PhysRevLett.123.033201

3. Boulder Atomic Clock Optical Network Collaboration. Frequency ratio measurements at 18-digit accuracy using an optical clock network. *Nature* (2021) 591:564–9. doi:10.1038/s41586-021-03253-4

4. McGrew WF, Zhang X, Fasano RJ, Schäffer SA, Beloy K, Brown RC. Atomic clock performance enabling geodesy below the centimetre level. *Nature* (2018) 564:87–90. doi:10.1038/s41586-018-0738-2

5. Godun RM, Nisbet-Jones PBR, Jones JM, King SA, Johnson LAM, Margolis HS, et al. Frequency ratio of two optical clock transitions in $^{171}Yb^{+}$ and constraints on the time variation of fundamental constants. *Phys Rev Lett* (2014) 113:210801. doi:10.1103/PhysRevLett.113.210801

6. Kolkowitz S, Pikovski I, Langellier N, Lukin MD, Walsworth RL, Ye J. Gravitational wave detection with optical lattice atomic clocks. *Phys Rev D* (2016) 94:124043. doi:10.1103/PhysRevD.94.124043

7. Takamoto M, Ushijima I, Ohmae N, Yahagi T, Kokado K, Shinkai H, et al. Test of general relativity by a pair of transportable optical lattice clocks. *Nat Photon* (2020) 14:411–5. doi:10.1038/s41566-020-0619-8

8. Kessler T, Hagemann C, Grebing C, Legero T, Sterr U, Riehle F, et al. A sub-40-mhz-linewidth laser based on a silicon single-crystal optical cavity. *Nat Photon* (2012) 6:687–92. doi:10.1038/NPHOTON.2012.217

9. Matei DG, Legero T, Häfner S, Grebing C, Weyrich R, Zhang W, et al. 1.5μm lasers with sub-10 mhz linewidth. *Phys Rev Lett* (2017) 118:263202. doi:10.1103/PhysRevLett.118.263202

10. Cook S, Rosenband T, Leibrandt DR. Laser-frequency stabilization based on steady-state spectral-hole burning in Eu^{3+}:Y_2SiO_5. *Phys Rev Lett* (2015) 114:253902. doi:10.1103/PhysRevLett.114.253902

11. Oswald R, Nevsky AY, Schiller S. Burning and reading ensembles of spectral holes by optical frequency combs: Demonstration in rare-earth-doped solids and application to laser frequency stabilization. *Phys Rev A (Coll Park)* (2021) 104:063111. doi:10.1103/PhysRevA.104.063111

12. Chen J. Active optical clock. *Sci Bull (Beijing)* (2009) 54:348–52. doi:10.1007/s11434-009-0073-y

13. Wang Y. Optical clocks based on stimulated emission radiation. *Sci Bull (Beijing)* (2009) 54:347. doi:10.1007/s11434-009-0064-z

14. Meiser D, Ye J, Carlson DR, Holland MJ. Prospects for a millihertz-linewidth laser. *Phys Rev Lett* (2009) 102:163601. doi:10.1103/PhysRevLett.102.163601

15. Norcia MA, Cline JRK, Muniz JA, Robinson JM, Hutson RB, Goban A, et al. Frequency measurements of superradiance from the strontium clock transition. *Phys Rev X* (2018) 8:021036. doi:10.1103/PhysRevX.8.021036

16. Laske T, Winter H, Hemmerich A. Pulse delay time statistics in a superradiant laser with calcium atoms. *Phys Rev Lett* (2019) 123:103601. doi:10.1103/PhysRevLett.123.103601

17. Schäffer SA, Tang M, Henriksen MR, Jørgensen AA, Christensen BTR, Thomsen JW. Lasing on a narrow transition in a cold thermal strontium ensemble. *Phys Rev A (Coll Park)* (2020) 101:013819. doi:10.1103/PhysRevA.101.013819

18. Liu H, Jäger SB, Yu X, Touzard S, Shankar A, Holland MJ, et al. Rugged mhz-linewidth superradiant laser driven by a hot atomic beam. *Phys Rev Lett* (2020) 125:253602. doi:10.1103/PhysRevLett.125.253602

19. Kazakov GA, Schumm T. Active optical frequency standard using sequential coupling of atomic ensembles. *Phys Rev A (Coll Park)* (2013) 87:013821. doi:10.1103/PhysRevA.87.013821

20. Shi T, Pan D, Chen J. Realization of phase locking in good-bad-cavity active optical clock. *Opt Express* (2019) 27:22040–52. doi:10.1364/OE.27.022040

21. Goldenberg HM, Kleppner D, Ramsey NF. Atomic hydrogen maser. *Phys Rev Lett* (1960) 5:361–2. doi:10.1103/PhysRevLett.5.361

22. Yu D, Chen J. Laser theory with finite atom-field interacting time. *Phys Rev A (Coll Park)* (2008) 78:013846. doi:10.1103/PhysRevA.78.013846

23. Yu D, Chen J. Four-level superradiant laser with full atomic cooperativity. *Phys Rev A (Coll Park)* (2010) 81:053809. doi:10.1103/PhysRevA.81.053809

24. Vasilyev AA, Savukov IM, Safronova MS, Berry HG. Measurement of the 6*s* – 7*p* transition probabilities in atomic cesium and a revised value for the weak charge Q_W. *Phys Rev A (Coll Park)* (2002) 66:020101. doi:10.1103/PhysRevA.66.020101

25. Shi T, Miao J, Pan D, Chen J. Optimization of pumping light for Cs four-level active optical clock. In: Joint conference of the IEEE international frequency control symposium (IEEE IFCS) and IEEE international symposium on applications of ferroelectrics. 19-23 July 2020, Keystone, CO, USA, IEEE (2020). 10.1109/IFCS-ISAF41089.2020.9234825.

26. Xu Z, Pan D, Zhuang W, Chen J-B. Experimental scheme of 633 nm and 1359 nm good-bad cavity dual-wavelength active optical frequency standard. *Chin Phys Lett* (2015) 32:083201. doi:10.1088/0256-307x/32/8/083201

27. Pan D, Xue X, Chen J. Detailed problems in cesium active optical clock. In: IEEE international frequency control symposium (IFCS), 09-12 May 2016, New Orleans, LA, USA, (2016).

28. Heavens OS. Radiative transition probabilities of the lower excited states of the alkali metals. *J Opt Soc Am* (1961) 51:1058–61. doi:10.1364/JOSA.51.001058

29. Yin B, Shay TM. Theoretical model for a faraday anomalous dispersion optical filter. *Opt Lett* (1991) 16:1617–9. doi:10.1364/OL.16.001617

30. Dressler ET, Laux AE, Billmers RI. Theory and experiment for the anomalous faraday effect in potassium. *J Opt Soc Am B* (1996) 13:1849–58. doi:10.1364/JOSAB.13.001849

31. Gilbert SL, Watts RN, Wieman CE. Hyperfine-structure measurement of the 7*s* state of cesium. *Phys Rev A (Coll Park)* (1983) 27:581–2. doi:10.1103/PhysRevA.27.581

32. Steck DA. *Cesium D line data* (2019). *available online at* revision 2.2.1 http://steck.us/alkalidata *Novermber* 21, *2019*).

33. Bohnet JG, Chen Z, Weiner JM, Meiser D, Holland MJ, Thompson JK. A steady-state superradiant laser with less than one intracavity photon. *Nature* (2012) 484:78–81. doi:10.1038/nature10920

34. Kuppens SJM, van Exter MP, Woerdman JP. Quantum-limited linewidth of a bad-cavity laser. *Phys Rev Lett* (1994) 72:3815–8. doi:10.1103/PhysRevLett.72.3815

35. Pan D, Shi T, Chen J. Dual-wavelength good–bad-cavity laser system for cavity-stabilized active optical clock. *IEEE Trans Ultrason Ferroelectr Freq Control* (2018) 65:1958–64. doi:10.1109/TUFFC.2018.2854738

frontiers | Frontiers in Physics

TYPE Correction
PUBLISHED 15 September 2022
DOI 10.3389/fphy.2022.1022064

Corrigendum: Active optical clock lasing on the Cs $7S_{1/2}$-$6P_{3/2}$ transition under a weak magnetic field

Tiantian Shi[1]*, Jianxiang Miao[1], Jia Zhang[1] and Jingbiao Chen[1,2]

[1]State Key Laboratory of Advanced Optical Communication Systems and Networks, Institute of Quantum Electronics, School of Electronics, Peking University, Beijing, China, [2]Hefei National Laboratory, Hefei, China

KEYWORDS

bad-cavity limit, suppressed cavity-pulling effect, quantum-limited linewidth, zeeman effect, beat-note spectrum, active optical frequency standard

EDITED AND REVIEWED BY
Andrea Bertoldi,
ParisTech Institut d'Optique Graduate School, France

*CORRESPONDENCE
Tiantian Shi,
tts@pku.edu.cn

SPECIALTY SECTION
This article was submitted to Atomic and Molecular Physics,
a section of the journal
Frontiers in Physics

RECEIVED 18 August 2022
ACCEPTED 26 August 2022
PUBLISHED 15 September 2022

CITATION
Shi T, Miao J, Zhang J and Chen J (2022), Corrigendum: Active optical clock lasing on the Cs $7S_{1/2}$-$6P_{3/2}$ transition under a weak magnetic field.
Front. Phys. 10:1022064.
doi: 10.3389/fphy.2022.1022064

A Corrigendum on
Active-optical-clock lasing on the Cs 7S $_{1/2}$ -6P $_{3/2}$ transition under weak magnetic field

by Shi T, Miao J, Zhang J and Chen J (2022). Front. Phys. 10:967255. doi: 10.3389/fphy.2022.967255

In the original article, there was a mistake in the **Abstract**. Line 4 previously referred to "red cavity fluctuations", which has now been corrected to "cavity fluctuations". The complete sentence now reads "sensitivity of an AOC laser to cavity fluctuations is greatly reduced".

The authors apologize for this error and state that this does not change the scientific conclusions of the article in any way. The original article has been updated.

Publisher's note

Frontiers in Physics

TYPE Review
PUBLISHED 14 September 2022
DOI 10.3389/fphy.2022.995361

EDITED BY
Jingbiao Chen,
Peking University, China

REVIEWED BY
Yang Shiyu,
Lanzhou Instute of Physics, China
Xiumei Wang,
PKU-HKUST Shenzhen-Hong Kong
Institution, China

*CORRESPONDENCE
Jiayu Dai,
daijy@shao.ac.cn

SPECIALTY SECTION
This article was submitted to Atomic and Molecular Physics,
a section of the journal
Frontiers in Physics

RECEIVED 15 July 2022
ACCEPTED 29 July 2022
PUBLISHED 14 September 2022

CITATION
Dai J, Liu T, Cai Y, Chen Z and Li Q (2022), Review of the development of the hydrogen maser technique and a brief introduction to its space applications.
Front. Phys. 10:995361.
doi: 10.3389/fphy.2022.995361

Review of the development of the hydrogen maser technique and a brief introduction to its space applications

Jiayu Dai[1]*, Tiexin Liu[1], Yong Cai[1], Zhichun Chen[1] , Qi Li[1,2]

[1]Laboratory of Time & Frequency Technology Research, Shanghai Astronomical Observatory, Chinese Academy of Sciences, Shanghai, China, [2]School of Materials Science and Engineering, Shanghai University, Shanghai, China

Since 1960, when the first hydrogen frequency standard, the microwave amplification by stimulated emission of radiation (maser), was developed in the laboratory of Norman Ramsey at Harvard University, the performance of its frequency stability and technique development have been closely related to scientific research. A variety of H-maser designs have been developed for the demands of space science applications, including the deep space network (DSN) and the gravity probe (GP) experiment. H-maser is one of three well-developed microwave atomic frequency standards and is widely used worldwide in both ground and on-board-based settings. Along with upgrades to the frequency stability performance of the H-maser, improved knowledge of the world has also been reported.

KEYWORDS

hydrogen maser, time and frequency standard, atomic frequency standard, space science applications, astronomy

1 Introduction

The hydrogen microwave amplification by stimulated emission of radiation (H-maser) is an atomic frequency standard widely used in ground and on-board-based settings. Rather than focusing only on comparing the H-maser to the other two well-developed atomic frequency standards; namely, the cesium beam atomic frequency and rubidium frequency standards, this review discusses the frequency accuracy and stability performance, the volume and mass weight for particular applications, and the power consumption of the H-maser. We also review some of its fields of application.

The H-maser is larger in volume than the other two frequency standards. The frequency accuracy of the H-maser is approximately 1×10^{-12} [1], which is not sufficient for a primary frequency standard compared to the 1×10^{-13} accuracy of the Cesium beam standard. The stability of the frequency output of the H-maser is typically a few parts in 10^{15} for an average time interval, τ, of the order of 10^3–10^5 s. The accuracy and stability performance of the H-maser are mainly limited by factors such as the relaxation time, thermal noise, wall shift, second-order Doppler shift, and second order Zeeman effect, depending on the particular design. Comparisons of the frequency stability performance

TABLE 1 Stability performance of the MHM-2020 active H-maser.

Average time, τ	ADVE
1 s	$\leq 1.5 \times 10^{-13}$
10 s	$\leq 2 \times 10^{-14}$
100 s	$\leq 5 \times 10^{-15}$
1,000 s	$\leq 2 \times 10^{-15}$
10,000 s	$\leq 1.5 \times 10^{-15}$

TABLE 2 Stability performance of the 5071A cesium clock primary frequency standard.

Average time, τ	ADVE
0.01 s	$\leq 7.5 \times 10^{-11}$
0.1 s	$\leq 1.2 \times 10^{-11}$
1 s	$\leq 5.0 \times 10^{-12}$
10 s	$\leq 3.5 \times 10^{-12}$
100 s	$\leq 8.5 \times 10^{-13}$
1,000 s	$\leq 2.7 \times 10^{-13}$
10,000 s	$\leq 8.5 \times 10^{-14}$
100,000 s	$\leq 2.7 \times 10^{-14}$
5 days	$\leq 1.0 \times 10^{-14}$
30 days	$\leq 1.0 \times 10^{-14}$

TABLE 3 Stability performance of the FS725—benchtop rubidium frequency standard.

Average time, τ (s)	AVAR
1	$< 2 \times 10^{-11}$
10	$< 1 \times 10^{-11}$
100	$< 2 \times 10^{-12}$

of the H-maser to those of the Cesium beam tube and Rubidium frequency standards are reported in Refs. [2–4]. Tables 1–3 demonstrate the best performance of the H-maser for a τ value of approximately 10^3.

The H-maser dates back to the 1960s [1] or even earlier. The H-maser experiments originated in an effort to develop a device that proved four features [5]: 1) a narrow resonance line; 2) a reduced broadening of the line due to some effects; 3) a reduced first-order Doppler shift; and 4)a favorable signal-to-noise ratio. H-maser-related studies performed world-wide demonstrated its applications in the fields of time-keeping, the deep space network (DSN), and the very long base line interferometry (VLBI) network for radio astronomy and geophysics, as well as the global navigation satellite system (GNSS) and others. Improvements in the stability performance and reduced mass and volume make the H-maser competitive in modern scientific research applications.

A typical stability performance of 10^{-15} to 10^{-16} per day has been reached for the traditional design and a better than 1×10^{-16} has been demonstrated in the laboratory [6] (Figure 1). The passive H-maser has also reached a one-day average frequency stability of a few parts in 10^{15}.

To help us to understand how the H-maser has been developed and upgraded along with the progress in its scientific applications, Section 2 provides a brief description of the physical principles of the H-maser and pertinent technique developments. Section 3 describes its applications in scientific space experiments and astronomical research. Finally, Section 4 briefly discusses the future of the H-maser.

2 Review of the H-maser

Updates to the H-maser have recently slowed, perhaps for the following reasons.

First, the theory of the H-maser had already been well studied; thus, technique development seems to have reached a ceiling. Even the most recent update of the best stability performance in Russia was mainly contributed by a single-state-selected beam design that had been proposed long before. Secondly, it takes time to develop new theories for improved performance and technology upgrades, including material science research and industry manufacturing. Finally, recent efforts have focused on reducing its volume and mass, as well as improving its robustness for on-board space applications. These may explain why the H-maser is described as a well-developed product.

2.1 Principles and design

Like other frequency sources, the frequency signals of the H-maser occur due to the periodic motion of H atoms. The principles can be roughly summarized as follows: first, the H-maser obeys the theory of conservation of energy, in which the interactions between atoms and electromagnetic waves are expressed by Formula 1. Second, a resonant oscillation leads to the amplification of the useful atomic signal.

$$\Delta E = E_m - E_n = h\nu_{mn} \tag{1}$$

Following these principles, the H-maser is mainly composed of a physical unit, which provides a high-quality reference signal in form of an electromagnetic emission through hyperfine transitions of ground atomic hydrogen, as well as an electrical unit that includes a quartz crystal oscillator that is locked to the physical output to provide the stable frequency signal outputs of

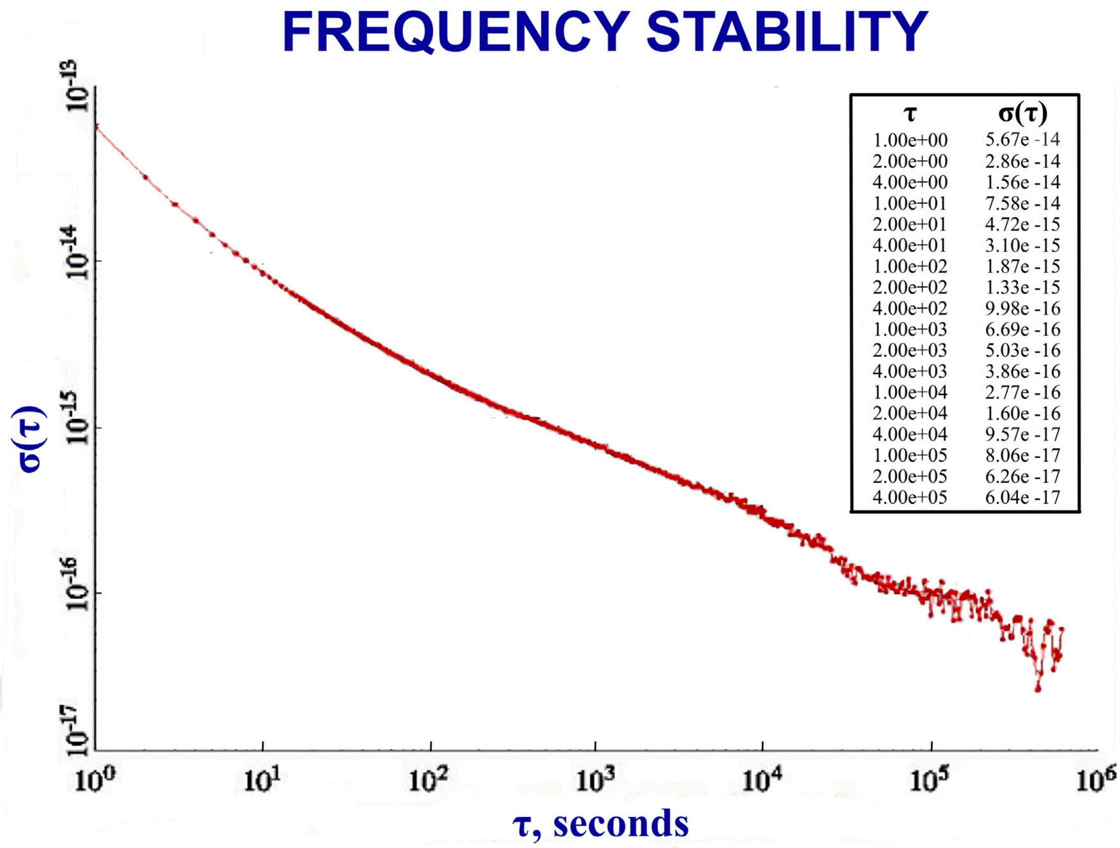

τ	σ(τ)
1.00e+00	5.67e -14
2.00e+00	2.86e -14
4.00e+00	1.56e -14
1.00e+01	7.58e -14
2.00e+01	4.72e -15
4.00e+01	3.10e -15
1.00e+02	1.87e -15
2.00e+02	1.33e -15
4.00e+02	9.98e -16
1.00e+03	6.69e -16
2.00e+03	5.03e -16
4.00e+03	3.86e -16
1.00e+04	2.77e -16
2.00e+04	1.60e -16
4.00e+04	9.57e -17
1.00e+05	8.06e -17
2.00e+05	6.26e -17
4.00e+05	6.04e -17

FIGURE 1
Stability performance of a single-state selection system-designed H-maser.

the H-maser, as shown in Figure 2A [7]. The normal optional standard frequency outputs of the H-maser are 5, 10, 20,. . ., 100 MHz, and 1 pps. While any possible transitional radiation can theoretically be used as a reference signal to lock the quartz crystal oscillator in the electrical unit, since the transitional frequencies are sensitive to environmental effects, the reference signal must be the one between two least-sensitive energy levels. For the H-maser a useful transition is that of the ground hydrogen ($n = 1$) from state ($F = 1$, $m_F = 0$) to a lower state ($F = 0$, $m_F = 0$), as shown in Figure 2B [1]. However, although both spontaneous transitions and transitions induced by perturbations can happen in principle in the physical unit, and the corresponding electromagnetic radiation will be emitted, the signal quality of the spontaneous transition is not sufficient for use in the electrical unit. Due to the low number of such transitions, they likely disappear in the background noise of the environment. To make the signal-to-noise ratio high enough for the electrical unit, large numbers of simultaneous transitions are required. Since the transitional signal magnitude is proportional to the population difference of the energy levels, the solution is induced transitions. In other words, by gathering ($F = 1$, $m_F = 0$) atoms in a container and increasing their fractional population, a sufficiently large number of transitions from ($F = 1$, $m_F = 0$) to ($F = 0$, $m_F = 0$) can be simultaneously induced by a stimulating signal, with a corresponding radiation emission of around 1.420405751 GHz.

Furthermore, to provide self-sustained oscillation possible, for example, in an active H-maser, the energy delivered by the atomic transitional radiation should be at least high enough to compensate for the loss of the practical resonant structure design. This requires numerous atoms at the energy level of ($F = 1$, $m_F = 0$) as well as a large population difference between the two levels of ($F = 1$, $m_F = 0$) and ($F = 0$, $m_F = 0$). This can be achieved through so-called population inversion. Secondly, the population difference between the two energy levels should be even larger to output a sufficiently large atomic transitional signal to contribute to the frequency stability performance, as shown in Eqs 2, 3.

More detailed principles of active H-maser systems have been published previously [1, 5, 8, 9]. The time domain frequency stability is given as the Allan Deviation, as shown in Eqs 2, 3.

When, $0.1\text{ s} < \tau < 10\text{ s}$:

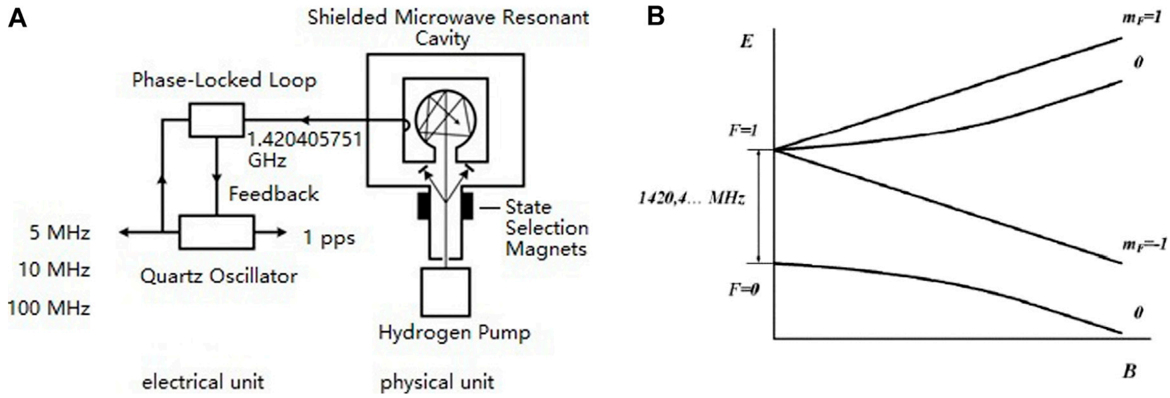

FIGURE 2
(A) Schematic diagram of the standard active H-maser; **(B)** energy requirements for the hyperfine ground S-state hydrogen on the magnetic field.

$$\sigma_y(\tau) = \frac{\beta kT}{v_0^2 P_a \tau}\left(1 + F\frac{P_a}{P_r}\right) \tag{2}$$

and when, $\tau > 10$ s:

$$\sigma_y(\tau) = \frac{1}{Q_a\sqrt{\tau}}\sqrt{\frac{kT}{2P_a}} \tag{3}$$

where β is a constant, k is the Boltzmann constant, T is the temperature in Kelvin, P_r is the power received by the input amplifier, F is the amplifier noise factor, P_a is the power delivered by atoms, and $Q_a$is the quality factor of the atomic resonance.

The stability performance of H-maser output mainly depends on the circuit quality for an average time interval of $0.1\text{ s} < \tau < 10\text{ s}$. The long-term stability performance is influenced by factors such as the second-order Doppler effect, collisional spin exchange, etc. Therefore, the electrical and physical units play roles in the improvements in H-maser performance.

The flux of hydrogen atoms is also critical based on the relationship between the power, ΔP, radiated by H atoms initially in the state of ($F = 1$, $m_F = 0$) and the atomic hydrogen beam, I, given by Eqs 4, 5 [5, 10]. To provide oscillation in the maser, the effective H atomic beam flux should be greater than the minimum flux, I_{th}, given in Formula 6.

$$\Delta P = \frac{1}{2} I h v \frac{\theta^2}{1 + \theta^2 + \delta^2} \tag{4}$$

$$\theta^2 = \frac{\langle x^2 \rangle}{\gamma^2} = \frac{W}{W_c} \tag{5}$$

$$I_{th} = 4\pi \frac{W_c}{Qh} \tag{6}$$

where h is the Planck constant, W is the energy stored in the cavity, and Q is the quality factor of the cavity.

I represents the flux of atoms ($F = 1$, $m_F = 0$). In the evaluation of the fractional population of atoms at this level, the original four hyperfine states are considered to be equally distributed over atoms. This approximation is made only when $e^{(-\Delta E/kT)} \rightarrow 1$. For room-temperature H-masers, the energy separations are three orders smaller than the kT when T = 300 K. Therefore, for simplicity, $\Delta E/_{kT} \rightarrow 0$, although they are not rigorously equally distributed. However, this is not correct for low-temperature H-maser.

The mechanism of passive H-maser is similar to that of active H-maser, except that the physical unit oscillation cannot be self-sustained due to the increased loss when reducing the volume of the microwave resonant cavity. This loss requires compensation by an input from the external electrical circuit to maintain a continuous oscillation. Meanwhile, an extra perturbation is also input. Hence, a sacrifice of the frequency stability is inevitable when reducing the mass and volume of the physical unit for satellite on-board applications. The frequency stability performance [8], also given in form of time domain Allan Deviation, is shown in Formula 7:

$$\sigma_y(\tau) = \frac{A}{Q_a\sqrt{\tau}}\sqrt{\frac{kT}{2P_a}} \tag{7}$$

where A is a constant that depends on the cavity structure.

2.2 Development of H-maser techniques

We focus on reviewing the technique developments only for the physical H-maser units, since the transitional signal contributes to both short and long-term stability. Moreover, the quality of the transitional signal is so sensitive to the environment that the practical physical package must be

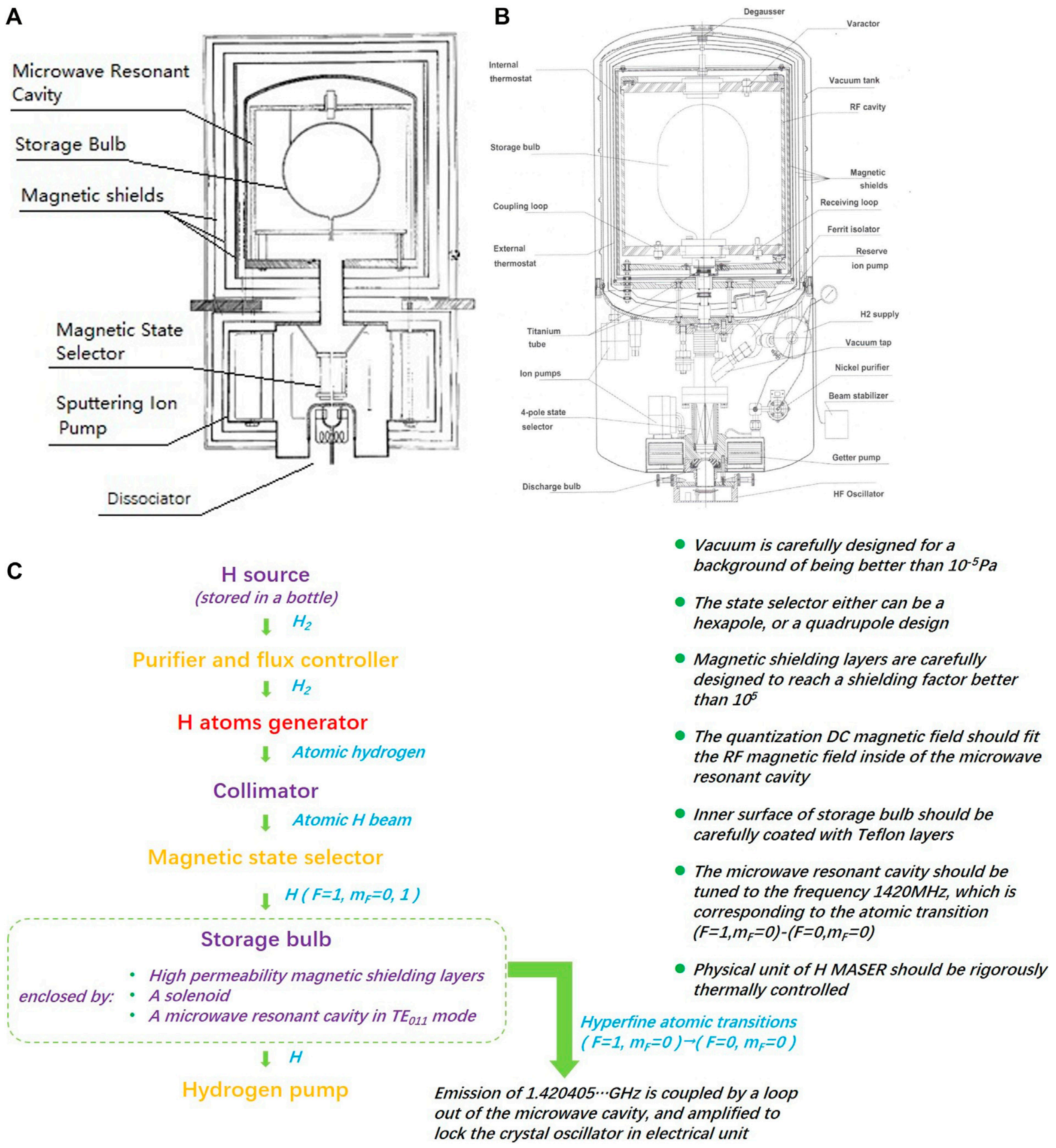

FIGURE 3
Schematic diagram of the standard active H-maser. **(A)** An H-maser unit for a satellite experiment in the 1960s; **(B)** a VCH 1003M unit; **(C)** summary of the standard H-maser unit.

carefully designed to ensure the precision and stability of the maser output frequency. The practical active H-maser of the 1960s and a modern design are shown in Figures 3A,B [11, 12]. The standard active H-maser physical unit design is roughly summarized in Figure 3C.

2.2.1 Hydrogen source

A large amount of pure hydrogen is required to provide a sustained oscillation and ensure a sufficient source of hydrogen for the entire H-maser working period. First, the hydrogen source was designed as a bottle with a high H_2 gas pressure.

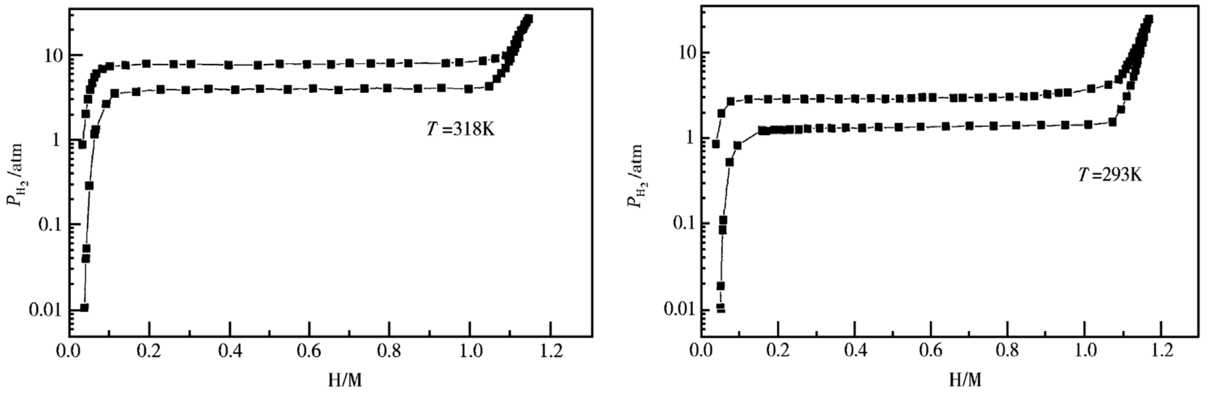

FIGURE 4
Pressure of output of the hydrogen source of a design using a $LaNi_5$ alloy.

However, this was soon replaced by a design that utilized a reversal chemical reaction of H_2 with alloys such as the rare Earth elements, $LaNi_5$ (Formula 8). The replacement extended the working lifetime of the H-maser not only by increasing the storage capacity for the same bottle volume but also by reducing hydrogen leakage. Since hydrogen atoms are small in dimension, they can penetrate through the bottle wall, which is made of steel. The speed of penetration is proportional to the pressure difference. The upgraded design reduced the pressure and, hence, the pressure difference between the two sides of the wall. In addition, by adjusting the components of the alloy compounds, the hydrogen source can output H_2 with an approximately constant pressure (Figure 4 [13]). The output pressure of H_2 can be adjusted by varying the container temperature. Thus, it became easier to regulate the H_2 flux compared to the previous design.

$$LaNi_5 + \mathbf{3H_2} \xrightleftharpoons[\text{slightly heated}]{(2-3)\times10^5\,\text{Pa}} LaNi_5\mathbf{H_6} \tag{8}$$

The hydrogen then enters a component called the purifier through a connection via a thin stainless-steel tube. The purifier was once made from an alloy pellet comprising 70% palladium and 30% silver [10] and acted to provide and control the flux of purified hydrogen by a heating electrical circuit in the atomic oscillator. This purifier has been replaced by a design made from a thin nickel tube, which performs the same function but shows a more stable performance [14].

2.2.2 Preparation of H atoms

To obtain hydrogen atoms, the purified hydrogen flow leads into a dissociator designed to discharge the hydrogen molecules. An RF dissociator design is the best choice for the H-maser [10, 15] due to the simplicity in building and operating, as well as the easy ability to focus the atoms. The molecular hydrogen is then dissociated by the collisions with energetic electrons to produce atoms and more electrons and ions. Those atoms pass through a collimator made of single or multiple channels (Figure 5 [16]) and formed into an atomic beam. The atomic hydrogen beam then passes through a fractional population inversion component called the magnetic state selector, which utilizes a gradient magnetic field to deflect undesired H atoms of the level ($F = 1, m_F = -1$, and $F = 0, m_F = 0$). The flux of atoms entering the storage bulb is of the order of 10^{12}–10^{13}/sec [1]. However, the classical design could not separate undesired ($F = 1, m_F = 1$) level atoms from the ($F = 1, m_F = 0$) and effectively deflect them from the path of the useful atomic beam, as the effective magnetic moment of ($F = 1, m_F = 1$) had the same sign as that of the

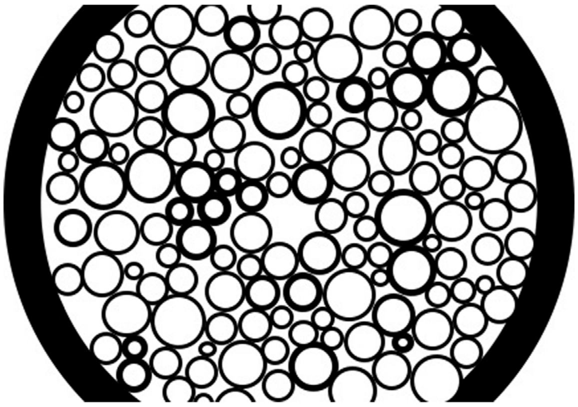

FIGURE 5
Schematic of a multichannel collimator.

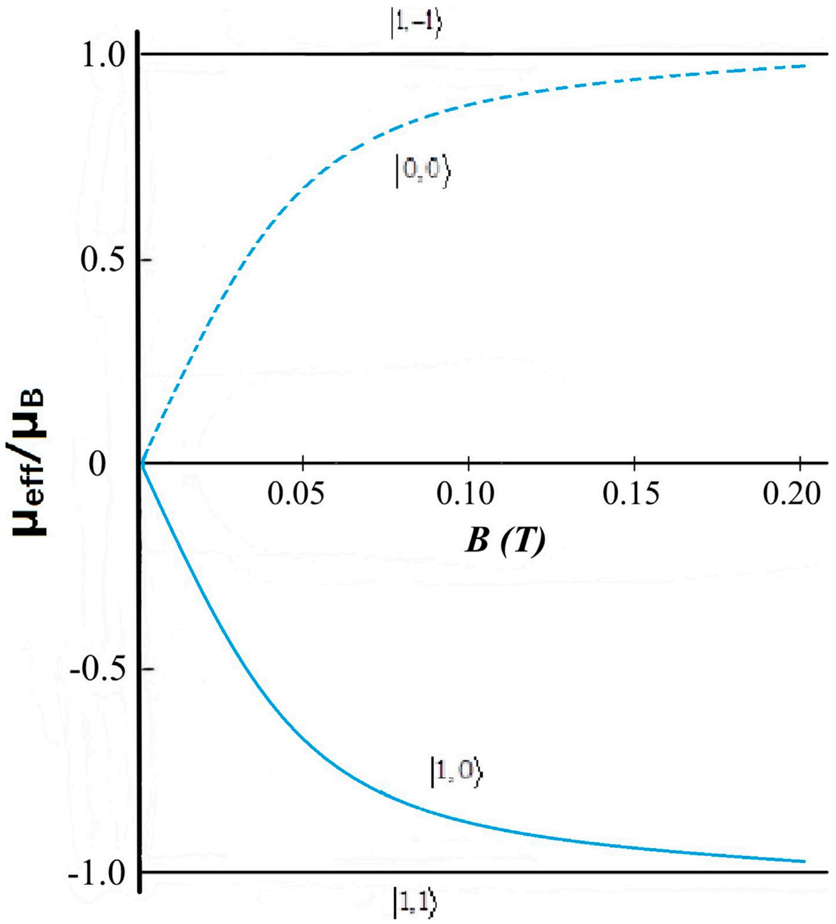

FIGURE 6
Variation of the magnetic moment with the magnetic field.

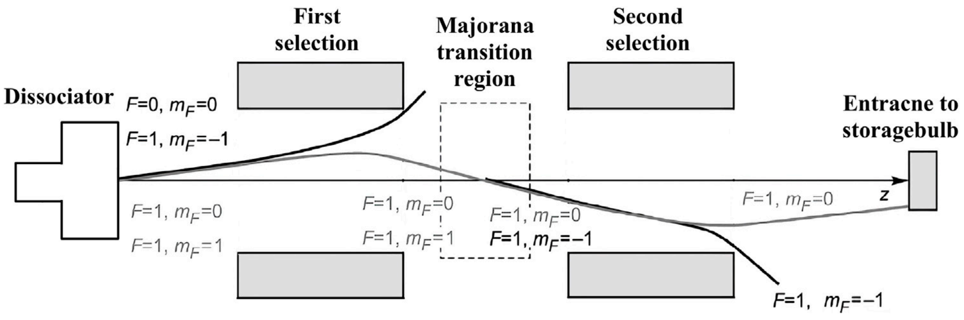

FIGURE 7
Schematic diagram of a single-state ($F = 1$, $m_F = 0$) selector for the H-maser.

($F = 1$, $m_F = 0$); thus, they underwent a deflecting force in the same direction (Figure 6). To improve the quality of the atomic transitional signal to improve the short- and long-term frequency stability performances, a single-state selection system design was proposed based on the adiabatic fast passage theory. This method was reported to remove 90%

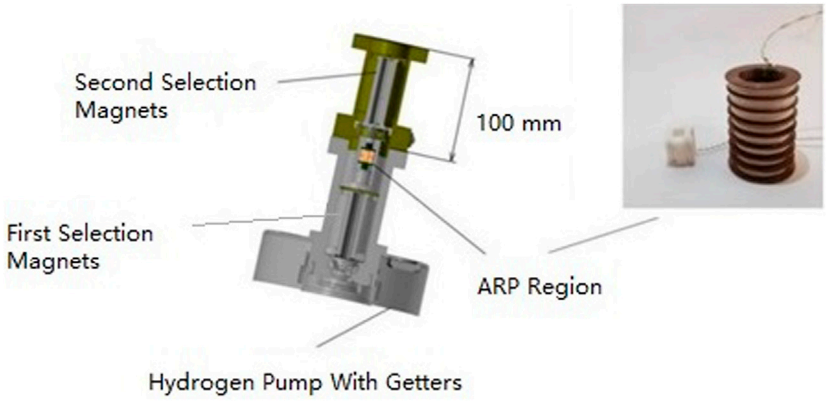

FIGURE 8
Single-state ($F = 1$, $m_F = 0$) selector using the adiabatic rapid passage (ARP) technique.

of undesired ($F = 1$, $m_F = 1$) atoms [17]. The realization of this technique in the laboratory is shown in Figure 7 [18], and Figure 8 [6]. Although the design had been proposed long ago, the technique was developed for use on commercial products for the first time. This technique contributes to the stability performance by reducing the spin exchange.

The prepared H atom ($F = 1$, $m_F = 0$) then goes into a storage bulb to undergo approximately 10^4 collisions with the wall of the bulb [1] during an average storage time of 1 s. To reduce the atomic energy perturbation, the inner surface of the bulb should carefully be coated. Long-chain paraffin and Dri-Film surfaces were attempted before Teflon was finally confirmed to be the best substance owing to its diminished chemical reaction and reduced wall shift [10].

2.2.3 Conditions for a resonant oscillation

As stated previously, the H-maser is set to a resonant oscillation. A microwave resonant cavity was designed for this purpose, based on the TE_{011} mode for the standard-sized H-maser. The electromagnetic field should have a magnetic component distribution that is symmetrically axial, with a central resonant frequency tuned to 1.420405 GHz, which is very close to the ($F = 1$, $m_F = 0$)–($F = 0$, $m_F = 0$) atomic transitions. The microwave cavity is normally made of fused silica or quartz cylinder, with its inner surface coated with silver. It is thermally regulated with a temperature variance of no more than 0.01°C, as the resonant frequency changes with temperature. The cavity can also be made of other materials such as aluminum, titanium, etc. Whatever the material, the central resonant frequency should be rigorously stabilized to a value close to the atomic transitional frequency. The quality factor, Q, should also be high enough for the resonant oscillation. A standard fused quartz cylindrical normally has unloaded and loaded Q factor values of 60,000 and around 35,000–45,000, respectively [1, 8]. The temperature coefficient is around 1 kHz/°C. Metal microwave cavities reach a higher Q factor but also a higher temperature coefficient that is often of a higher order. A higher Q factor can contribute to the coupled power; however, a higher temperature coefficient leads to difficulty in the thermal regulation of servo circuits for the cavity pulling effect. The signal of the physical unit is detected by a loop mounted on one end plate of the microwave cavity, where the magnetic field has a maximum value. The microwave cavity can be coarsely tuned by mechanical adjustment, temperature-adjusted for intermediary tuning, and finely tuned by varying the electric current of the varactor circuit.

To provide numerous atomic transitions, an approximately uniform quantization magnetic field of the order of 10^{-7} T [1] is generated by a solenoid designed to sit outside of the microwave resonant cavity and inside of the ambient magnetic field shielding layers made from a high-permeability permalloy material.

Finally, the vacuum design is generally implemented by application of the VacIon pump, with which a pressure of 10^{-5} mmHg can be maintained for a flux average of 10^{17} atoms flowing out of the collimator. Currently, the getters, as shown in Figure 8, are widely used for their ultra-high vacuum design and working stability.

2.2.4 Small H-masers

To realize and generalize the satellite on-board applications of H-masers, studies have focused on reducing the volume and mass of standard-sized H-masers. Since the volume is mainly limited by the size of the microwave resonant cavity, designs such

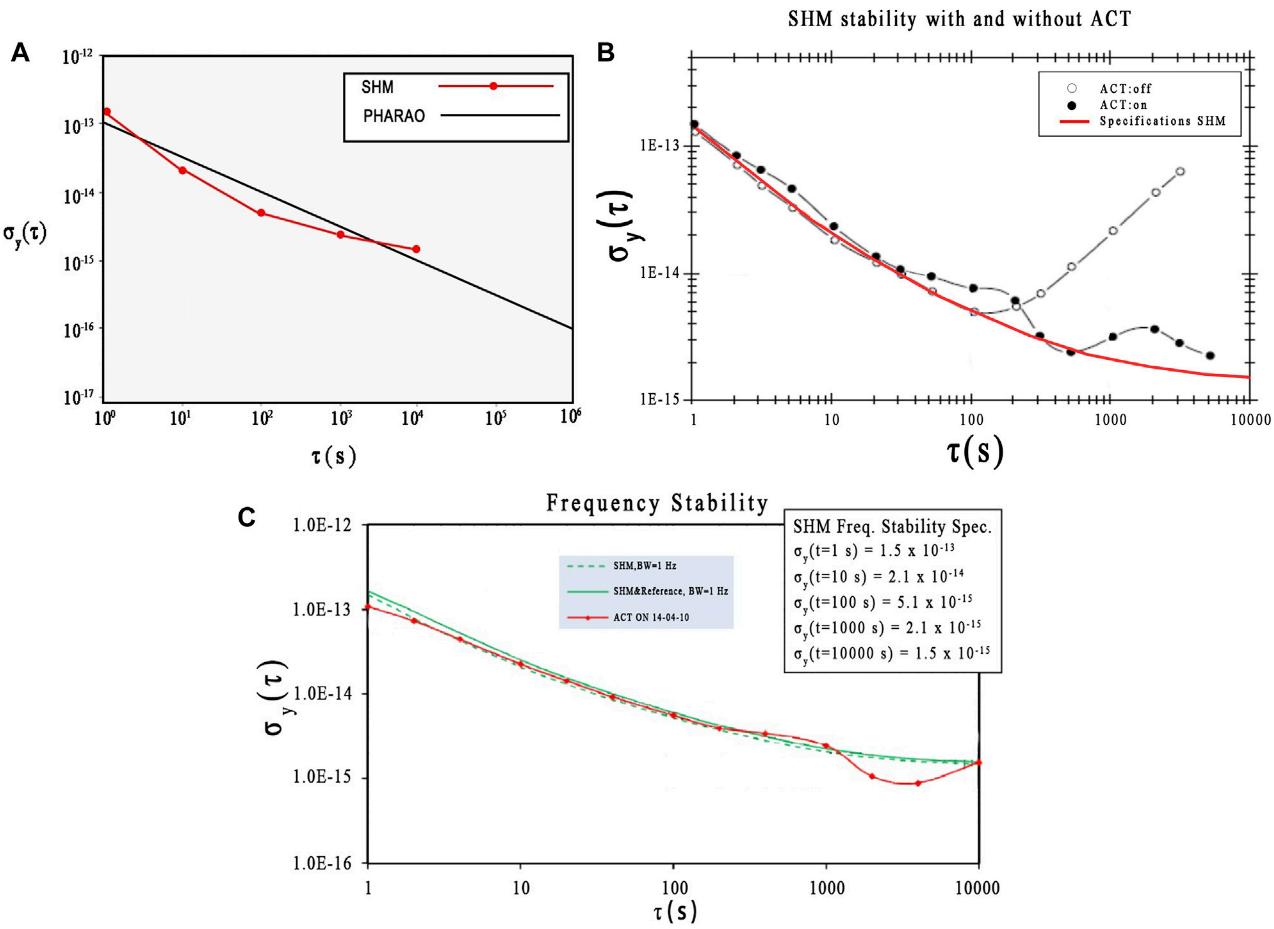

FIGURE 9
Development of the small active H-MASER (SHM). **(A)** is the stability performance of 35 kg SHM for ACES. **(B)** is comparison of the stability with the ACT on and off. **(C)** is the stabilty performance of a 40 kg SHM by SpectraTime.

as the small size TE_{111} mode microwave resonant cavity, Q-enhanced microwave cavity, and sapphire microwave resonant cavity, etc., were made for the small active H-maser.

The passive H-maser [19] has a dramatically reduced volume and mass weight by sacrificing the frequency stability performance. The physical unit techniques of passive H-maser are mostly like those of the standard-size active H-maser.

The H-maser techniques were developed to meet the demands of space experiments, including better stability performance, robustness, and environmental suitability. For on-board applications, the requirements include a smaller, lighter, and lower power consumption design. A traditional standard-sized active H-maser device is >200 kg. Improvements have led to lighter masers that are more favorable for space missions. For example, a small active H-maser (SHM) for the Atomic Clock Ensemble in Space (ACES) mission weighed only 35 kg using a sapphire microwave cavity, in the Neuchâtel observatory [20] in 2003. The frequency stability performance was 1.5 × 10^{-15}/10,000 s (Figures 9A,B).

The ACES utilized an SHM for its medium stability performance, together with the long-term stability performance of a cold cesium atomic clock to provide excellent stability performance [21]. The SHM by SpectraTime, weighing 40 kg, reached a stability performance of 2.1 × 10^{-15} (Figure 9C).

The 60 kg on-board standard active H-maser design of the sitall microwave cavity [22] from Vremya-CH of Russia was planned to be applied to the international space VLBI network (RadioAstron) for researching dark matter, redshift, etc. Its frequency stability successfully reached 2.5 × 10^{-15}/1,000 s (Figures 10A,B). One was launched in 2011 [23].

The Millimetron mission of the International Space Observatory proposed an updated stability performance of the

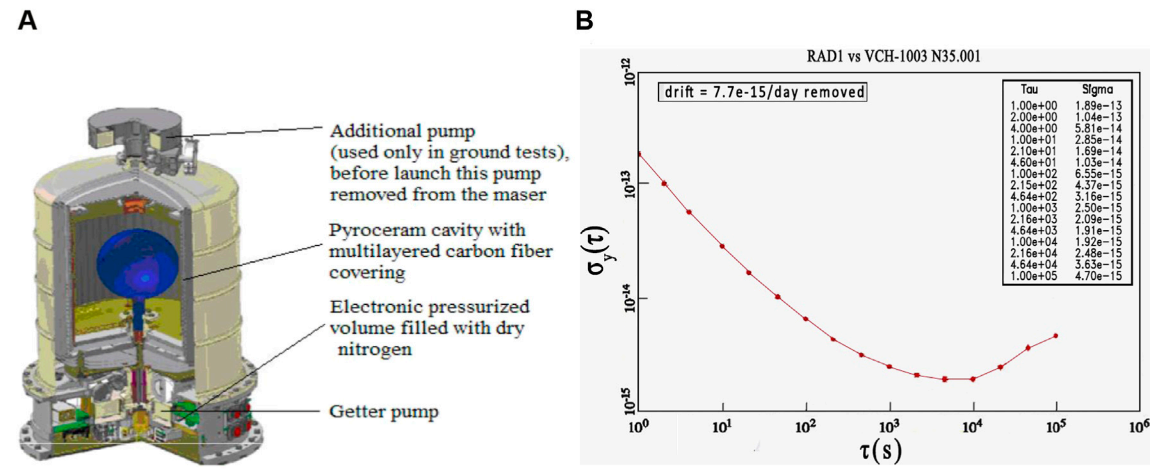

Tau	Sigma
1.00e+00	1.89e−13
2.00e+00	1.04e−13
4.00e+00	5.81e−14
1.00e+01	2.85e−14
2.10e+01	1.69e−14
4.60e+01	1.03e−14
1.00e+02	6.55e−15
2.15e+02	4.37e−15
4.64e+02	3.16e−15
1.00e+03	2.50e−15
2.16e+03	2.09e−15
4.64e+03	1.91e−15
1.00e+04	1.92e−15
2.16e+04	2.48e−15
4.64e+04	3.63e−15
1.00e+05	4.70e−15

FIGURE 10
The 60 kg on-board standard active H-MASER. **(A)** the practical design. **(B)** the stability performance.

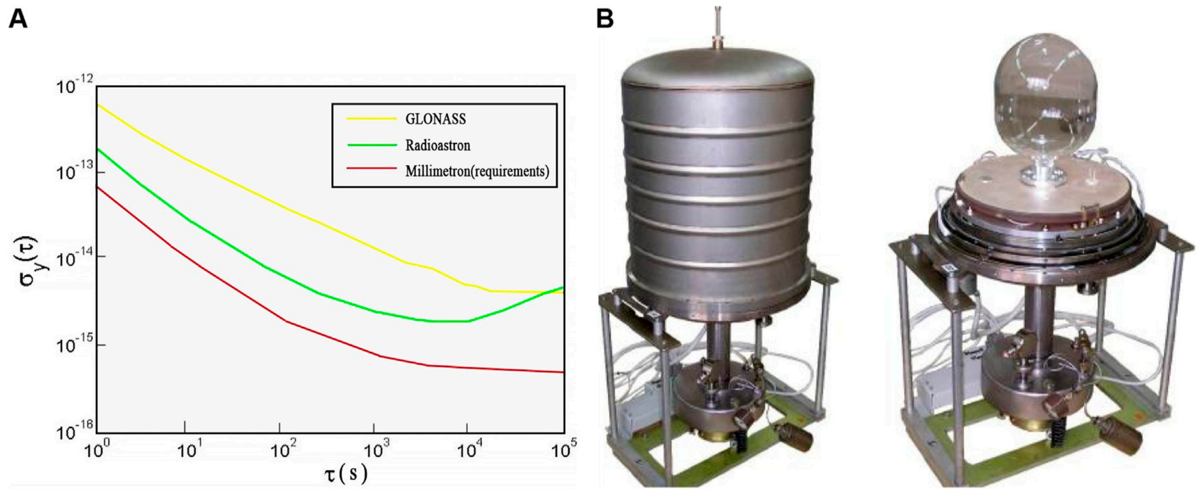

FIGURE 11
Single-state atomic beam selection standard active maser **(A)** the Millimetron requirements. **(B)** Practical design.

frequency source [22] (Figure 11A). Vremya-CH adopted a single-state atomic beam selection standard active H-maser design to meet this (Figure 11B). The microwave resonant cavity was made of titanium, likely to address the need for both toughness and high Q factor.

The advantage of passive H-maser is its small size for on-board applications. This review will not focus on this technology as the physical unit is similar in structure to that of active H-masers. The difference lies in the following. First, its smaller metallic cylindrical cavity, also in the TE_{011} mode, is made of aluminum to provide a loaded quality factor, Q_{loaded}, of no less than 5,000. Electrodes inside the cavity are designed to regulate the electromagnetic field distribution to ensure that the magnetic field is in the same direction in the enclosed space. The atomic storage bulb was also designed in the shape of a long tube according to electromagnetic field distribution. A typical design adopts three or four magnetic shielding layers to reduce the influence of ambient magnetic fields. The selector preferentially uses a quadrupole design to minimize the volume. Since it is smaller than the standard active maser, cavity thermal control is easier to accomplish. Moreover, the

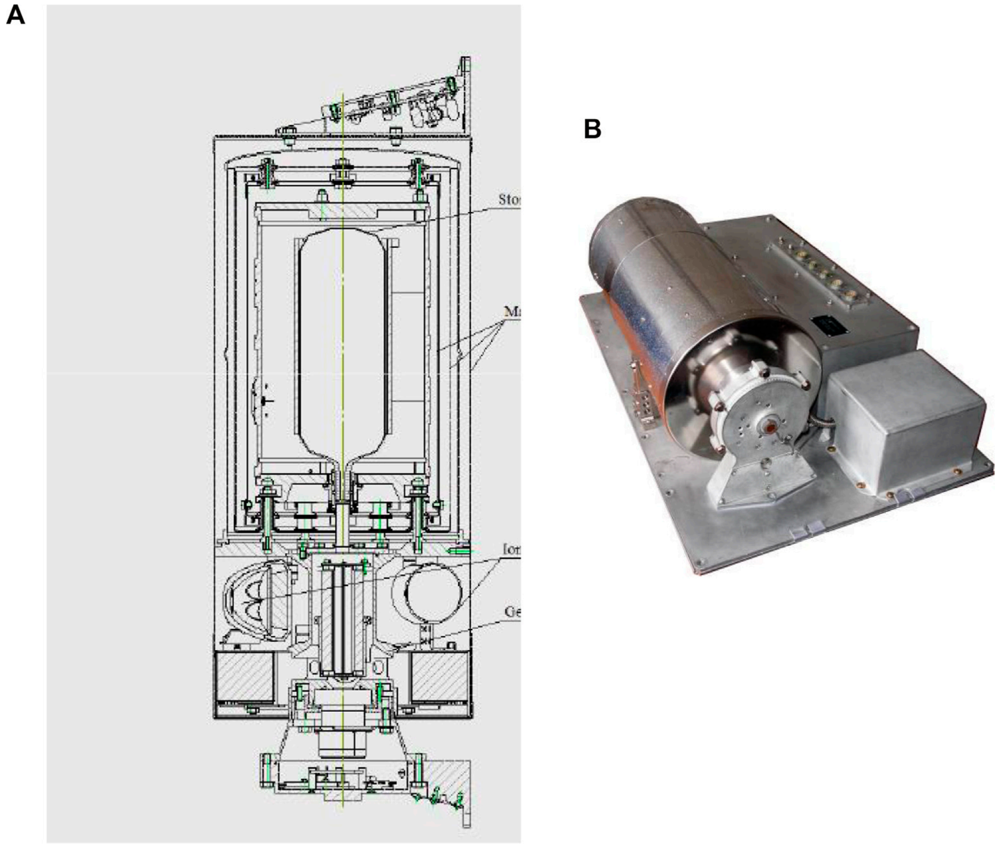

FIGURE 12
Passive H-masers. **(A)** Flight model unit designed by Vremya–CH. **(B)** Flight model passive H-maser fromVremya–CH.

mass of the hydrogen source can be optimized since the consumption is smaller. The design of the on-board passive H-maser by Vremya-CH is shown in Figure 12A [22] as an example of a satellite-based passive H-maser.

Although the stability performance is not good as that of the standard-size active H-maser, passive H-maser has been developed and widely used for GNSS. The on-board Passive H-MASER of Vremya-CH [22], shown in Figure 12B, for the GLONASS-κ had reached a stability performance of 10^{-15}/10,000 s. A Space Mini Passive Hydrogen MASER (mPHM), was carried out in the frame of the ESA European GNSS Evolutions Programme. The design possibly has reduced the mass to only 12 kg, published in 2011 [24].

In China, the stability performance of the ground-based active H-maser has reached a few parts in 10^{15} for an average interval on the order of 10^4 s, while the passive H-maser has reached a few parts in 10^{14} for 10^4 s. Meanwhile, the Beijing Institute of Radio Metrology and Measurement (BIRMM) is working on a 40 kg on-board active H-maser for the China Space Station. The Shanghai Astronomical Observatory (SHAO) has recently participated in this research and is now working on principle model research based on the standard ground-based H-maser.

3 Applications in space scientific research

3.1 The theory of relativity

H-masers can provide standard frequency signals for space experiments, in which their accuracy and stability play important roles. For example, in 1976, the H-maser was used in the famous gravitational redshift test, gravity probe A (GP-A) [25], in which the H-maser was nearly vertically shot into space at an altitude of 10,000 km on board a 100 kg spacecraft.

The experiment was carried out by NASA jointly with the Smithsonian Astrophysical Observatory (SAO). The gravitational redshift was measured by the CW microwave signal frequency comparing technique and a three-way linked Doppler canceling system. The microwave signals were respectively provided by the ground and on-board H-masers.

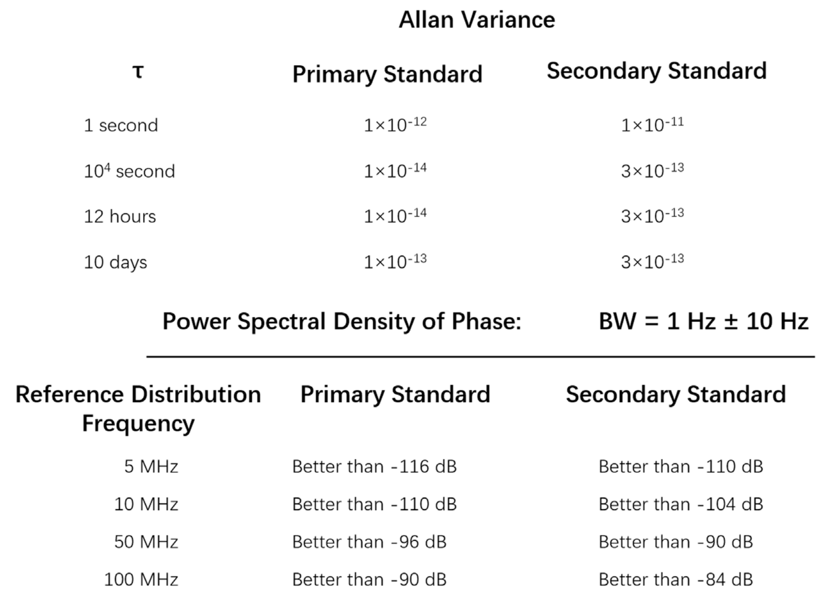

Allan Variance

τ	Primary Standard	Secondary Standard
1 second	1×10^{-12}	1×10^{-11}
10^4 second	1×10^{-14}	3×10^{-13}
12 hours	1×10^{-14}	3×10^{-13}
10 days	1×10^{-13}	3×10^{-13}

Power Spectral Density of Phase: BW = 1 Hz ± 10 Hz

Reference Distribution Frequency	Primary Standard	Secondary Standard
5 MHz	Better than -116 dB	Better than -110 dB
10 MHz	Better than -110 dB	Better than -104 dB
50 MHz	Better than -96 dB	Better than -90 dB
100 MHz	Better than -90 dB	Better than -84 dB

FIGURE 13
Frequency standard requirements, 1981–1986.

The relative frequency variance was determined according to the theory of relativity. The data fit Einstein's theory within the order of 10^{-6}. The precision of the experimental data was due to the (τ = 100 s) frequency stability performance of the H-masers.

3.2 The DSN and spacecraft tracking

H-masers have also been applied to the DSN for stable time and frequency reference signals [26]. Figure 13 shows the requirements proposed by the frequency and time subsystems of DSN applications, from 1981 to 1986. To synchronize the stations distributed in Spain, the United States, and Australia, a low H-maser frequency drift is desired.

In 1968, the H-maser was first put into use for the DSN; since that time, studies have been performed to assess the performance and the possibility of improvements in frequency stability. Figure 14A shows the stability performance measurement of an H-maser with environmental temperatures varying within 0.05°C. The curve starts to go up when τ is approximately 10^3 s. As environment effects and maser aging were attributed to these observations, relevant improvements have been proposed.

Meanwhile, the spacecraft tracking and detecting technique has been used for analyses of planet atmospheres, navigation, distance ranging, and gravitation detection. Observations including the phase, retardation, and amplitude of the transmitted signals can be acquired from the radio waves either sent from the spacecraft and received by a ground station or sent by a station on the ground, transponded by a spacecraft, and received by another ground station. One-, two-, and three-way modes have been established for deep space tracking. Synchronization between stations and antennas is important for the accuracy of tracking and precision of experiments. The H-maser frequency stability performance for deep space tracking in 1991, shown in Figure 14B [27], reached 10^{-16} for $\tau = 10^3$ s. The proposed requirement for the H-maser in the Cassini gravity wave experiment in 1998 was even lower part in 10^{16}.

3.3 The VLBI network

The H-maser is widely used in the very long baseline interferometry network. In the early Orbiting VLBI mission of RadioAstron, the CRONOS experiment [28] was postponed and eventually aborted due to funding challenges [29] but was proposed for space radio telescope receiving, space VLBI observation, Global Satellite Navigation, and gravitational wave detection. An active H-maser system was planned for both ground stations and spacecraft. A sapphire-design microwave cavity small H-maser (SHM), for on-board spacecraft use was developed in 1999 and weighs only 50 kg [30].

Given the technical advantages and high-resolution observations in the VLBI, this system has been used for research on black holes. In the international Earth Horizon Telescope (EHT) project, a huge telescope with a size equivalent to that of the Earth is approximated by relevant worldwide distributed individual telescopes. The quality of the

10.3389/fphy.2022.995361

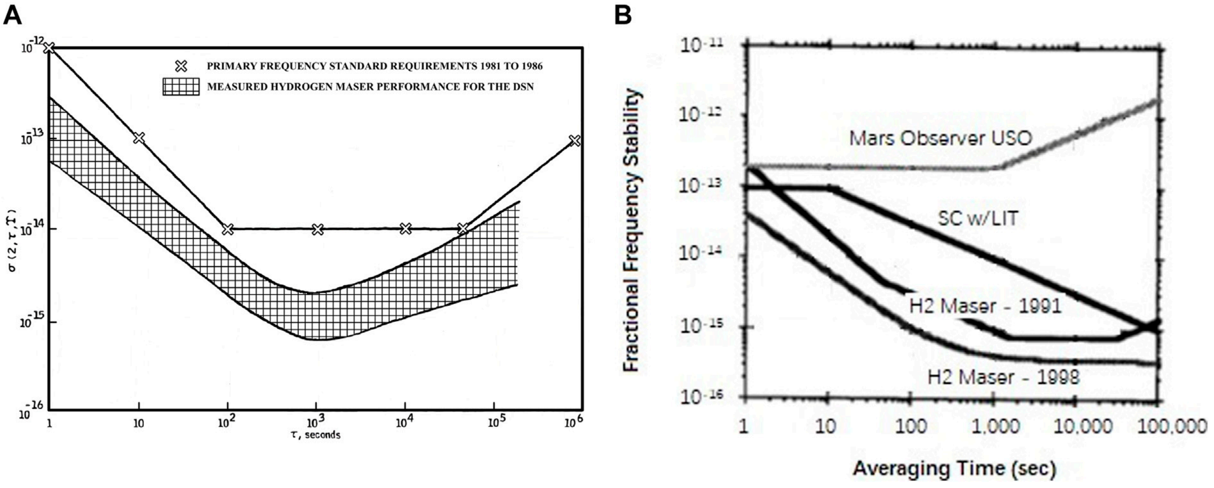

FIGURE 14
Frequency stability performace of the H-Masers for the deep space network (DSN) **(A)** measured stability with the envirionmental temperature varying no more than 0.05°C. **(B)** stability performance for deep tracking in 1990s.

black hole imaging depends on the resolution of the observations, as well as the precise synchronization between individual telescopes, to which the high stability performance of active H-maser units has contributed.

The H-maser has also contributed to the international Square Kilometre Array Telescope (SKA), which is researching on the origin of the universe, space magnetic field distribution, etc., and to the Millimetron projects for even higher sensitivity, millimeter and submillimeter resolution, and infrared observation.

3.4 The GNSS

H-masers are currently widely used in the Global Navigation Satellite System, including GPS in the United States, GLONASS in Russia, GALILEO in Europe, and BDS in China. Besides the high-quality ground-based active H-maser for the ground station, high-quality satellite-based passive H-maser also plays role in the system and promotes the precision of information on the position, time, and speed in space. A typical design adopts one or two on-board passive H-maser systems as the satellite standard frequency source.

4 Discussion

4.1 Summary of recent technique developments

The H-maser is currently widely used worldwide. The research institutions and their latest updates are the following.

The active H-maser MHM-2020 from the Microsemi company in the United States has reached a stability performance of 2.0×10^{-15} (τ = 1,000 s). The VCH-1003M from Vremya-CH in Russia also features a stability of 2.0×10^{-15} for its commercial product. However, the single-state selection beam system design has reached a stability of 6.69×10^{-16} (τ = 1,000 s) and better than 1×10^{-16} (τ = 100,000 s). The iMaser 3000 from T4 Science in Switzerland has reported a stability of 8.71×10^{-16} (τ = 1,000 s). In China, the BIRMM and SHAO have reported H-maser stability values of approximately 5×10^{-15} (τ = 1,000 s).

Among passive H-maser devices, the VCH-1008 from Vremya-CH has reached a stability of 4×10^{-15} (τ = 1 day). The pH Maser 1008 from T4 Science has a stability of 4×10^{-15} (τ = 1 day) too. The passive H-MASER of BIRMM and SHAO have reached the order of 10^{-15} (τ = 1 day).

Concerning the requirements for small size and low mass in the context of space experiments, recent studies have focused on smaller microwave resonant cavities. A smaller cavity constructed of a material with a higher dielectric constant; for example, sapphire has been designed for on-board applications. Metallic cavities of aluminum or titanium have also been developed to improve the robustness and quality factor of the H-maser device. However, their temperature coefficients are higher than those for standard fused quartz cavities, which may negatively affect the stability performance of the H-maser.

Second, pump development has improved the background vacuum of the H-maser. These advances have solved the requirements for lower mass and better vacuum performance and are currently widely used in on-board applications.

Third, the single-state selection beam system has recently improved the stability of the H-maser to better than $1 \times 10^{-16}/10^5$ s, although the realization of this technique is complicated.

4.2 Improvements

H-masers still have space for improvement. Future technique developments will aim to improve the stability performance and miniaturization for space science research.

First, as the stability performance is sensitive to the thermal noise of the microwave cavity and the first-stage receiver, cooling may be one direction for improvement. Atomic oscillation signals were observed by Vessot et al. at the Smithsonian Observatory in studies using a cold h-maser [31]. The estimated average stability performance was 10^{-18} for 10^3s. This solution may warrant efforts toward manufacturing.

Secondly, among room-temperature standard H-masers, the frequency shift mainly occurs due to the second-order Zeeman frequency shift $\Delta\omega_z$, wall shift $\Delta\omega_W$, spin exchange shift $\Delta\omega_e$, and shift induced by the atomic motion in a non-homogeneous magnetic field $\Delta\omega_m$, in terms of the H-maser principles [1, 2], as expressed in Formula 9:

$$\boldsymbol{\omega_0 = \omega_H + \Delta\omega_z + \Delta\omega_W + \Delta\omega_e + \Delta\omega_m} \tag{9}$$

Thus, the performance of the magnetic shielding layers, as well as the wall coating and vacuum techniques, can be improved to reduce the relevant frequency shifts.

Improvements can also result from material science research. For example, the development of ambient magnetic field shielding techniques involves improved permeability, which may include research on the alloy constitution and heat-treating techniques. These advances should contribute to the stability performance of the H-maser by increasing the magnetic shielding efficiency. Another potential example is research on the wall shift, which requires a deeper understanding of the interaction between hydrogen atoms and the coated Teflon layers.

Finally, the failure modes of H-masers have been studied [32]. The dissociator of the maser is used to generate ground atomic hydrogen; although it was developed long ago, we still have not fully solved the problem of efficiently generating atoms due to the complexity of the reaction inside the plasma [33]. Simulations may be useful for addressing this challenge. Another question is the aging speed of the discharging bulb. The ions in plasma continuously collide with the wall of the bulb. Bulb aging is closely related to surface damage caused by impacts and the high temperature in plasma. The surface damage may increase the probability of recombination, which may decrease the discharging efficiency and is critical for long-term H-maser performance.

Author contributions

JD contributed predominantly to this work. All authors participated in the writing of the manuscript.

Acknowledgments

I acknowledge the contributions of Professor Yiqiu Wang to this study. Professor Yiqiu Wang has often visited our institute and has provided many forms of help. He kindly prepared a series of seminars and lectured with passion as a qualified and patient scientist. We have discussed research regarding the H plasma of the H-maser and confirmed the value of this work. He introduced me to another Professor experienced in plasma and optics when he discovered that I was applying for the NSFC and seeking a collaboration. He was invited to join my seminar talk in the summer of 2019 and provided instruction not only on issues related to the hydrogen maser but also on atomic physics. Moreover, I learned the spirit of Beijing University from him and I am also learning from him how to teach my students. He is a real educator.

Conflict of interest

The authors declare that the research was conducted in the absence of any commercial or financial relationships that could be construed as a potential conflict of interest.

Publisher's note

References

1. Vanier J, Claude A. *The quantum physics of atomic frequency standards*. Bristol and Philadelphia: Adam Hilger (2022).

2. Active Hydrogen Maser. Product directory clocks frequency references 3833 active hydrogen maser (2020). Available from: https://www.microsemi.com/product-directory/clocks-frequency-references/3833-active-hydrogen-maser Accessed July 7, 2022.

3. Frequency Standards and Frequency References. Product directory cesium frequency references (2022). Available from: https://www.microsemi.com/

product-directory/cesium-frequency-references/4115-5071a-cesium-primary-frequency-standard#resources Accessed July 9, 2022.

4. Standard Research Systems. Rubidium frequency std (2022). Available from: https://www.thinksrs.com/products/fs725.html Accessed July 15, 2022.

5. Kleppner D, Goldenberg H, Ramsey NF. Theory of the hydrogen maser. *Phys Rev* (1962) 126:603–15. doi:10.1103/physrev.126.603

6. Polyakov V, Timofeev Y, Demidov N. *Frequency stability improvement of an active hydrogen maser with a single-state selection system, page 127, 2021 China Time & Frequency Symposium*. Gansu, China: Dunhuang (2021). p. 13.

7. Time Realization And Distribution. Time and frequency from A to Z, H (2022). Available from: https://www.nist.gov/pml/time-and-frequency-division/popular-links/time-frequency-z/time-and-frequency-z-h#hydrogenmaser Accessed July 7, 2022.

8. Demidov NA. The development and futrue of hydrogen maser clock technology. *J Astronomical Metrology Meas* (2007) 6. doi:10.3969/j.issn.1000-7202.2007.z1.002

9. Ramsey NF. The atomic hydrogen maser. *Metrologia* (1965) Vol. 1:5–15. doi:10.1088/0026-1394/1/1/004

10. Kleppner D, Berg HC, Crampton SB, Ramsey NF, Vessot RFC, Peters HE, et al. Hydrogen-Maser principles and techniques. *Phys Rev* (1965) 138:A972–83. doi:10.1103/physrev.138.a972

11. Vessot R, Levine M, Mueller L, Baker M. *The design of an atomic hydrogen maser system for satellite experiments, 21st annual symposium on frequency control*. Fort Monmouth,NJ,USA (1967). p. 24.

12. Active Hydrogen Maser VCH-1003M. *Active hydrogen MASER VCH-1003M operations manual, 411141.032 OM*. Nizhny Novgorod: VREMYA-CH" JS Company (2006).

13. Dai J, Lin C. Hydrogen absorbing alloys application in hydrogen MASER. *Ann Shanghai Astronomical observatory, CAS, No.* (2007) 28:160.

14. Qi L, Hou X, Dai J, Chen Z, Liu T, Yang H. Research on a material for hydrogen purifying and flux controlling with application to space active hydrogen-masers. *AIP Adv* (2022) 12:035207. doi:10.1063/5.0084176

15. Maleki L. A study of the processes in the RF hydrogen gas dissociator. *TDA Prog Rep* (1980):42.

16. Vessot RFC, Peters HE. *Design and performance of an atomic hydrogen maser*, 183. Ire Transactions On Instrumentation. doi:10.1109/IRE-I.1962.5006627 (1962).

17. Mattison EM, Vessot RFC. Single state selection system for hydrogen masers. In: Proceedings of the Nineteenth Annual Precise Time and Time Interval (PTTI) Applications and Planning Meeting. Redondo Beach, CA (1987). p. 1.

18. Belyaev AA, Demidov NA, Polyakov VA, Timofeev YV. Estimation of the possible reduction of the limit frequency instability of A hydrogen generator using an atom beam in one quantum state. *Meas Tech* (2018) 61:779–83. doi:10.1007/s11018-018-1501-7

19. Howe DA, Walls FL, Bell HE, hellwig H, Small A. *Passively operated hydrogen maser, 33rd annual symposium on frequency control*. Atlantic City, NJ, USA (1979).

20. Jornod A, Goujon D, Gritti D, Bernier LG. The 35kg space active hydrogen maser (SHM-35) for ACES. In: Proceedings of the 2003 IEEE International Frequency Control Symposium and PDA Exhibition Jointly with the 17th European Frequency and Time Forum (2003).

21. Goujon D, Rochat P, Mosset P, Boving D, Perri A, Rochat J, et al. *Development of the space active hydrogen maser for the ACES mission, EFTF-2010 24th European frequency and time forum*.

22. Belyaev AA, Demidov NA, Medvedev SY, Pavienko YK, Sakharov BA, Vorontsov VG. Russian hydrogen masers for ground and space applications, 2019 URSI Asia-pacific radio science conference (AP-RASC), March 2019. doi:10.23919/URSIAP-RASC.2019.8738340 (2015).

23. Belyaev AA, Demidov NA, Gorelov SD, Polyakov VA, Sakharov BA, SkrylTimofeev ASYV. *On-board active hydrogen maser for Millimetron project, China satellite navigation conference*. China: Harbin (2018).

24. Belloni M, Gioia M, Mosset P, Waller P, Busca G. Space Mini passive hydrogen maser- A compact passive hydrogen maser for space applications. In: IEEE 2011 Joint Conference of the IEEE International Frequency Contral and the European Frequcny and Time Forum (FCS). San Francisco, CA, USA (5201). doi:10.1109/FCS.2011.5977320

25. Vessot RFC, Levine MW, Mattison EM, Blomberg EL, Hoffman TE, Nystron GU, et al. Test of relativistic gravitation with a space-borne hydrogen maser. *Phys Rev Lett* (1980) 45:2081–4. doi:10.1103/physrevlett.45.2081

26. Kuhnle PF, Sydnor RL. Present and future frequency and timing capabilities of the deep space network. *J Phys Colloques* (1981) 42:C8-373–81c8381. doi:10.1051/jphyscol:1981844

27. Border JS, Robert Kursinski E. *Deep space tracking and frequency standards*, Los Angeles, CA: Forty-Fifth Annyal Symposium On Frequency Control, IEEE. doi:10.1109/FREQ.1991.145957 (1991).

28. Busca G, Bernier LG, Schweda H, Kardashev N, Andreianov V, Toxburgh IW, et al. The cronos hydrogen maser clock redshift experiment on Radioastron. *Adv Space Res* (2003) 32(7):1421–8. doi:10.1016/s0273-1177(03)90356-5

29. Schweda H, Zivanov S, Perruchoud G, Weber C, Thieme B, Baister G. Performance demonstration of the on-board active hydrogen maser for the ACES space mission of ESA. In: 2007 IEEE International Frequency Control Symposium Joint with the 21st European Frequency and Time Forum.

30. Bernier LG, Jornod A, Schweda H, Gentsch R, Busca G. *The SHM hydrogen atomic clock for space applications: Development and test of the PEM physics package, 29th annual precise time and time interval*. California: PTTI Meeting (1997). p. 61–8.

31. Vessot RFC, Mattison EM, Imbier E. Cold hydrogen maser research at SAO and related developments. In: IEEE 37th Annual Symposium on Frequency Control (1982).

32. Popa AE, Wang HTM, Bridge WB, Chester AN, Etter JE, Walsh BL. A study to identify hydrogen maser failure modes. In: Hughes Research Laboratories, 30th Annual Symposium on Frequency Control (1976).

33. van Schreven E, Belloni M. *Hydrogen plasma simulation for atomic clock lifetime assessment*. York, United Kingdom: IEEE 2016 European Frequency and Time Forum (EFTF). doi:10.1109/eftf.2016.7477811 (2016).

frontiers | Frontiers in Physics

TYPE Review
PUBLISHED 15 September 2022
DOI 10.3389/fphy.2022.1012446

OPEN ACCESS

EDITED BY
Joan Marler,
Clemson University, United States

REVIEWED BY
Yin Cai,
Xi'an Jiaotong University, China
Youbin Yu,
Zhejiang Sci-Tech University, China

*CORRESPONDENCE
Xuzong Chen,
xuzongchen@pku.edu.cn

SPECIALTY SECTION
This article was submitted to Atomic and Molecular Physics,
a section of the journal
Frontiers in Physics

RECEIVED 05 August 2022
ACCEPTED 31 August 2022
PUBLISHED 15 September 2022

CITATION
Chen X, Zhou X, Ye A, Wang Y and Chen J (2022), The scientific career and contributions of Prof. Wang Yiqiu. *Front. Phys.* 10:1012446.
doi: 10.3389/fphy.2022.1012446

The scientific career and contributions of Prof. Wang Yiqiu

Xuzong Chen[1]*, Xiaoji Zhou[1], Anpei Ye[2], Yanhui Wang[1] and Jingbiao Chen[1]

[1]State Key Laboratory of Advanced Optical Communication, System and Network, School of Electronics, Peking University, Beijing, China, [2]Key Laboratory for the Physics and Chemistry of Nanodevices, School of Electronics, Peking University, Beijing, China

This review aimed to recount the scientific career and contributions of Prof. Wang Yiqiu, as well as his contribution to the research on quantum precision measurement and cold atom physics, as a tribute to his upcoming 90th birthday. Having contributed greatly to fields of research such as nuclear magnetic resonance, microwave atomic clocks, laser cooling of atoms, Bose–Einstein condensate, optical tweezers, and optical atomic clocks, the venerable Prof. Wang is a prominent figure in these research fields in China and has played a pivotal role in China's development of these subjects.

KEYWORDS
quantum precision measurement, cold atom physics, nuclear magnetic resonance, Bose–Einstein condensate, optical tweezers, atomic clock, optical clock

Introduction

Prof. Wang Yiqiu, born on September 1932, has been a prominent figure in China's research on quantum precision measurement and cold atom physics. Early on in his career, he studied nuclear magnetic resonance as a graduate student at Leningrad University and independently made several important discoveries. After his return from the Soviet Union, he turned his expertise toward China's development of microwave atomic clock, establishing China's first cesium beam atomic clock, as well as systematically explaining the Majorana shift in cesium beam atomic clocks. During his research on atomic clocks, his experience with laser frequency stabilization allowed him to pioneer China's earliest studies on the laser cooling of atoms, Bose–Einstein condensates and optical tweezers. In addition, Prof. Wang provided valuable insights and inspiration for the research of optical atomic clocks. This article aimed to recount Prof. Wang's scientific career and contributions, in honor of his academic legacy, as well as in celebration to his upcoming 90th birthday.

Nuclear magnetic resonance

In 1957, Wang Yiqiu entered the Physics Department of Moscow State University to study radio and microwave spectroscopy. In 1958, he transferred to Leningrad University and became a graduate student in the Prof. Scripov's group of radio-frequency spectroscopy. Prof. Scripov was a young and innovative scientist. He first invented the Fourier transform with nuclear magnetic resonance free induction signal to solve the problem of the high-resolution spectrum. He also invented a radio-frequency quantum oscillator (perhaps it could be called "Raser"), which can accurately measure the strength of the earth's magnetic field. In the first year, he suggested that Wang Yiqiu prepared some experimental instruments while passing all radio science course examinations. The most important thing was to build a high uniformity electromagnet with a stable magnetic field. With the help of laboratory experience, Wang Yiqiu made an electromagnet with a magnetic field controlled at about 4000 G (0.4 T) and an electronic circuit with higher sensitivity at the end of 1959. This device can be used to measure NMR signals of liquids and solids. Prof. Scripov suggested that Wang Yiqiu measured the chemical shifts of fluorine NMR signals in some fluoride solutions, especially to determine the chemical shifts of HF molecules. This is of certain significance because there were differences in this value in the scientific literature of the Soviet Union at that time, which is related to the explanation of the properties of chemical bonds in HF molecules. By systematically measuring the concentration effect of aqueous solution of KHF_2–H_2O, Wang definitively determined the chemical shift value of the HF molecule and the discrepancy was eliminated. Prof. Scripov sent the research study to the most authoritative scientific journal in the Soviet Union, ДАН *CCCP* (report of Soviet Academy of Sciences) [1].

Thereafter Wang Yiqiu measured the chemical shifts of fluorine NMR signals in aqueous solution systems of some fluorides. The results were published in a journal of structural chemistry [2]. However, Prof. Scripov suggested that he did a more difficult task. That was to find the anisotropy in the chemical shift of NMR signals in solids. The subject he proposed was graphite. Apparently, its layer structure indicates that the chemical bond of the carbon atoms within the same layer should be different than that between layers, so the anisotropy would appear in the chemical shifts of the 13C isotope NMR signals if the experiments were conducted when the graphite layers were parallel to the magnet field or perpendicular to that. This is because the natural abundance of the ^{13}C isotope is only about 1.1% (usual ^{12}C isotope nuclei have no magnet moment and no NMR signals). Furthermore, the NMR frequency of the ^{13}C isotope in the same magnetic field is about 1/4 compared with the ^{19}F (its abundance is 100%), according to the general rule, the intensity of the NMR signals is proportional to the cubic of frequency, in this regards; the sensitivity of the ^{19}F signals is more than 5000 times to that of ^{13}C. So, Wang Yiqiu suspected that he could detect the ^{13}C NMR signal. Nevertheless, he had improved the sensitivity of his homemade NMR spectrograph and finally detected the fluorine signals in LiF solid powder with a good signal-to-noise ratio. However, for detecting the ^{13}C signal in the graphite, Wang Yiqiu had estimated that the sensitivity of his instruments would need to be raised at least more than one order of magnitude. It was impossible at that time in his laboratory.

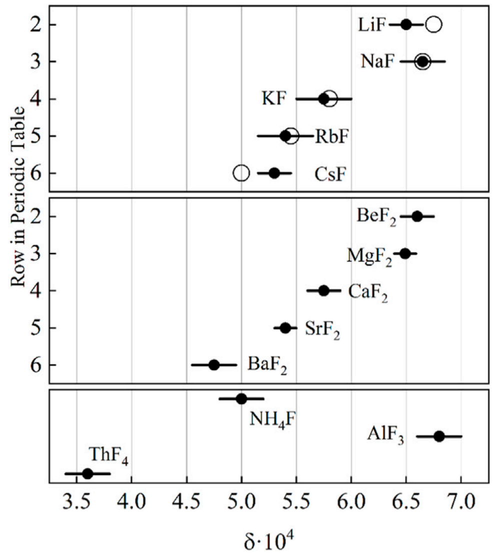

FIGURE 1
Chemical shift of the ^{19}F NMR signal in different fluoride crystals, the black dots with the error bar are the experimental results, the circle is theoretical value calculated from [11].

Ironically, while Wang Yiqiu had been bothered by improving the sensitivity of his apparatus to measure the anisotropy of the ^{13}C NMR signals, he found a study by Lauterbur in "Physical Review Letters," who had discovered the anisotropy of the ^{13}C NMR signals in $CaCO_3$ crystal [3] (In 2003, he got the Nobel Prize in Physiology and Medicine for his invention of NMR imaging technology). So, searching for this phenomenon had lost any significant physical meaning. However, when Wang Yiqiu tested the signals in LiF crystalline powder, he also got the ^{19}F signal for NH_4F crystalline powder. Fortunately, he found that the data of the chemical shifts of the ^{19}F signals for these two crystals were different on a big scale. Then Wang Yiqiu tried to get all the alkaline and alkaline-earth fluoride crystals, and carefully measured the values of the chemical shift for each of them. He conducted the measurement from midnight to 3 or 4 o'clock morning for the lowest noise. It was clear that the value of the chemical shift for every fluoride depends on the atomic number of the neighboring metal, with exception for some light metals. The overall results are shown in Figure 1 [4]. One can see that, in general, the chemical shift decreases with the atomic number of the alkali or alkali-earth metal increases with exception for LiF. This systematic rule of the chemical shifts for the 19F NMR spectra of the alkaline and alkali-earth fluoride crystals brought great attention to Prof. Scripov, and he asked Wang Yiqiu to write an article soon. It was published also in "ДАН CCCP" [5], but Prof. Scripov refused to be an author. He said, all ideas and

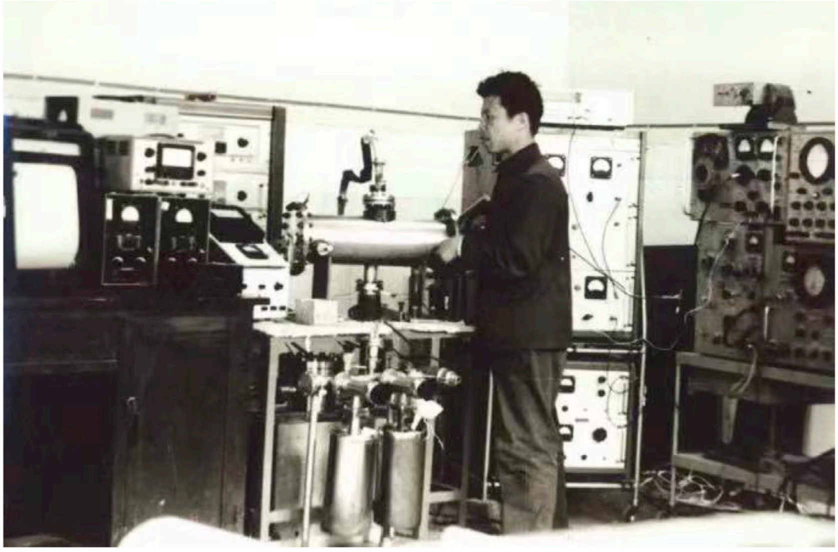

FIGURE 2
Prof. Wang Yiqiu worked on a cesium tube atomic clock prototype in 1978.

explanations belonged to Wang, and he should just mention Prof. Scripov in the acknowledgment. The work was of interest to other groups [6–9], and there were still some research groups citing this work after 10 years.

For explaining the experimental facts, Wang Yiqiu had read a lot of literature as well as some famous books, such as "Nature of the Chemical Bond" (Pauling),"Dynamic Theory of Crystal Lattice" (Born M. and Huang Kun), and especially the "Structure of Matter" (Xu Guangxian, in Chinese). According to the Ramsey theory [10] of the chemical shifts, they originated from the different shielding effects of the electrons around the nucleus to the outside magnetic field. They consist of two parts, the first part is the effect of the electrons of the inner spherical closed shells, which gives rise to the diamagnetic effect; and the other part is contributed by outer valence electrons, which may give rise to a total magnetic moment, and it will not shield, but strengthen the magnetic field outside. This is a paramagnetic effect and produces a negative value for the shielding factor. Wang Yiqiu recognized that in these ionic crystals there exists also some partial covalent bond, and the chemical shifts might be related to the deformation of this outer shell valence electron wave function of the fluorine ion F- in different fluoride crystals during their combination with metal atoms to form a crystal. In the literature, Wang Yiqiu found several studies that dealt with the bond characteristic of the different crystals. However, most of them could not explain the experimental results. Finally, he found a study by [11], which proposed that the overlap of the wave functions of the electrons of the fluorine and the neighboring metal in the free ion state may approximately give rise to the chemical shift for these ionic crystals. They give a formula, which is related to the overlap integrals of the two-electron wave functions and the mean distance between two atoms. For the latter, Wang Yiqiu could use the data from the book of Born and Huang Kun, but the overlap integrals should be calculated from the known wave functions of the outer electrons for both fluorine and alkali and alkali-earth metal ions, at least, for the outer shell electron. Furthermore, Wang Yiqiu had no idea how to calculate these overlap integrals and did not know the wave functions of the electrons with different quantum numbers for all these atoms. Prof. Scripov introduced Wang Yiqiu to the director of the theoretical physics division of the Institute, Professor Petrashin. Fortunately, he was delighted to help Wang Yiqiu to perform this work. He nominated a clever student of the last undergraduate year to help Wang Yiqiu in the calculation. They had all the data of the Hartree or Hartree–Fock wave functions for the fluorine and alkali atoms, but no such data for alkali-earth atoms. At that time the electronic computer was not popular. But the work load was huge. So they performed this calculation in a machinery calculation factory for more than 1 month. Then they used the formula of [11] to get the results in Figure 1 (circle for each alkali fluoride crystal). Though the theory was not so accurate, the theoretical data agree with the experiment rather well. The discrepancy for the LiF crystal can be easily explained by the fact that in comparison with other ions the volume of the Li+ ion is too small, so the repelling force between neighboring F-ions will distort the wave functions and result in a smaller chemical shift. With these results, Wang Yiqiu earned the Degree of the Candidate of the Physics-Mathematical Sciences in 1961. Afterward, the theoretical division worked out some new data of

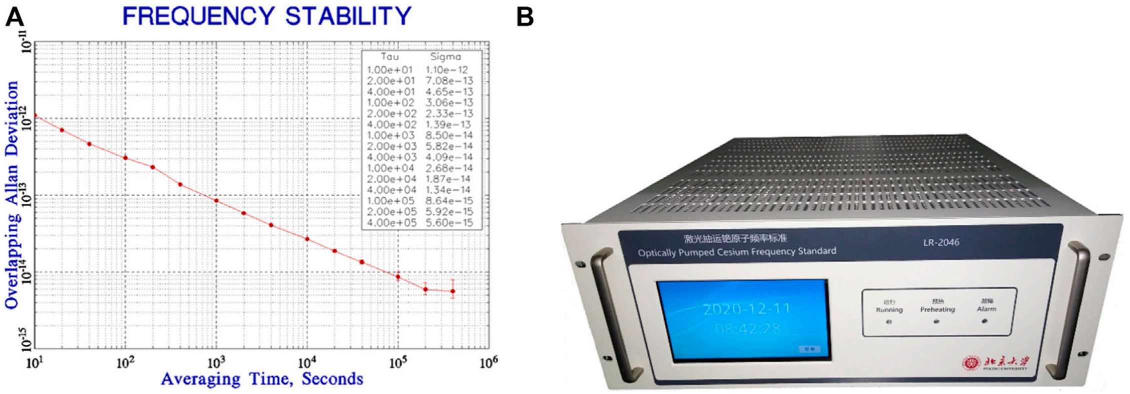

FIGURE 3
(A) Frequency stability curve for the optically pumped cesium clock. **(B)** Portable optical pumped cesium clock.

the electron wave functions modified by the crystalline field, they calculated again for these overlap integrals, and produced even better results considering some electron wave functions for the next nearest neighboring ions. They were published after Wang Yiqiu returned to China [12]. These results were interesting also because from them people could estimate the chemical shift figure for the nude (without electron shielding) fluorine nucleus [6–9, 13–20] and thus got approximately the value of the nuclear magnetic moment of fluorine. It has some meaning in nuclear physics, so far, the only one which we know the accurate value of its nuclear magnetic moment is hydrogen . Vice-president of Peking University, a famous theoretical physicist, Professor Wang Zhuxi suggested Wang Yiqiu to write a study concerning his thesis and to publish in "Acta Physica Sinica," and meanwhile translate it in Russian to publish in the "Science China" also. The former had come out in 1984 [11]. The latter had passed the evaluation by editors of this journal but failed because of the mistake of Peking University administration. Fortunately, this study has been translated into English in the United States and published in a journal of "Chinese Physics." Wang Yiqiu's work on the alkali fluoride crystals has been repeated in the United States more than 10 years later, and the results and conclusion were very similar [8].

When Wang Yiqiu came back to Peking University, he belonged to the newly established Department of Radio-Electronics in the Division of the Radio-Frequency Spectroscopy. At that time, they had a group of NMR, possessing a commercial 40 MHz high-resolution NMR spectrograph with a permanent magnet and a homemade spectrograph with less sensitivity. It was impossible to perform the work that Wang Yiqiu supposed. It was the temperature or pressure effects of the chemical shifts in alkali fluorides because of the lack of both an appropriate NMR spectrograph and the useful set-up for change of the temperature or pressure on a large scale. With the great help of Professor Xu Guangxi of the Chemistry Department and Professor Qian Renyuan of the Chemistry Institute of Academy of Science, they organized a systematic seminar on NMR application in chemistry, utilizing the 40 MHz spectrograph as a practical tool. After more than 1 year, the department moved to the new campus in Changping, the liaison with chemistry was cut off totally by long distance. Also, the name of the division was changed to "Radio-Frequency Spectroscopy and Quantum Electronics." His research task turned to magnetic optical double resonance, and his research direction began to change. However, in Changping, Wang Yiqiu with his two advanced students spent 2 years to made a radio-frequency quantum generator by using the Overhauser effect in the aqueous solution of $K_2(SO_3)_2NO$ in a weak magnetic field, and observed the building up process of stimulated emission in details [21]. It could simulate the laser establishing process and develop a magnetometer. The research method of nuclear magnetic resonance—the interaction between the electromagnetic field and matter affects his subsequent research: atomic clock, laser cooling, and Bose–Einstein condensation.

Microwave atomic clocks

In the recent decades, microwave atomic clocks have seen tremendous progress in the development of various aspects of their performance [22, 23]. Prof. Wang Yiqiu is a pioneering figure in the research on quantum frequency standards in China [24]. In 1961, Wang Yiqiu returned from the Soviet Union and was appointed director of the section of Spectrum and Quantum Electronics. In 1963, Wang Yiqiu began to lead the research on the atomic clock based on optically pumped cesium vapor cells. At the end of 1965, the optically pumped cesium vapor cell atomic clock was successfully developed, and the stability of the three prototypes was from 1×10^{-10} to 5×10^{-11}. In 1966, this research was interrupted because of the Cultural Revolution. In 1972, Wang Yiqiu and his colleague began to work on optically pumped vapor cell atomic clock again, but instead of cesium, this time they used rubidium isotopes, and worked in cooperation with the Beijing Dahua Electronic Instrument Factory. In the beginning of 1976, their design passed the appraisal of the Ministry of Electronics for mass production, and in 1978, they had produced more than 200 sets of Rb frequency standards; the physical parts were completed in the Hanzhong Peking University Branch. This work has been awarded with a National Science Conference Prize. After 1976 Wang Yiqiu has led the development of magnetic-state-selected cesium beam atomic clocks. Figure 2 shows a photo of Prof. Wang working on a cesium tube atomic clock. In 1981, Wang first reported observations on Majorana transitions in cesium beam atomic clocks [25]. Majorana transitions are indicated by a subsequent peak in the intensity distribution of the deflected beam and asymmetry in hyperfine σ transitions resonance which reverses with the C-field. Wang also made further detailed analyses of Majorana transitions in a follow-up study [26], drawing the conclusion that Majorana transitions are mostly excited by the inhomogeneity of the C-field, which is the magnetic field used in the drift phase of cesium beam microwave clocks for separating hyperfine levels. The discovery of Majorana transitions shed new light on the underlying physical principles of the cesium beam atomic clock and provides new insight into the evaluation and elimination of frequency shifts in atomic clocks [27, 28]. It was found that Majorana transitions exist not only in cesium beam atomic clocks with magnetic state selection, but also affect the transition frequency in optically pumped cesium beam clocks [27] and atomic fountain clocks [28]. Prof. Wang also proposed an experimental scheme for realizing a continuous atomic fountain clock [29, 30], and the concept is being developed in JILA.

In 1980, Prof. Wang Yiqiu also began to lead the development of optically pumped cesium beam atomic clocks, deducing a formula of the clock signal for different pumping and detecting schemes [31]. Then they built up the first prototype optically pumped cesium beam atomic clock in China [32, 33]. In the 1990s, after receiving his doctorate from the United States, Yang Donghai returned to Peking University to join Professor Wang's optically pumped cesium atomic clock research group [34–36]. Together with Yang, Prof. Wang proposed and realized an optically pumped cesium beam atomic clock with a sharp angle incidence probe laser [37–40]. This novel design utilizes the Doppler shift and broadening from the atomic beam to drastically reduce the effect of laser frequency noise on the signal-to-noise-ratio and is widely used in compact atomic beam frequency standards [41–43]. Since the effect of laser frequency noise on the clock's SNR is reduced, a similar level of clock performance can be achieved without sophisticated laser frequency stabilization schemes, thereby greatly reducing the size and complexity of the system. They obtained the long-term stability data for this kind of frequency standard first [40]. For their outstanding work, Prof. Wang and Prof. Yang received the Rao Yutai Award from the Chinese Physics Society in 1993. In his research on compact cesium beam atomic clocks, Wang also contributed greatly to the development of compact frequency-stabilized diode laser systems that are utilized as pumping and probing lasers in the atomic clocks, reducing the size of the physical package to below $10 \times 10 \times 5\ \mathrm{cm}^3$ while maintaining a high level of frequency stability [44, 45]. From 1995 to 2005, with the help of Prof. Wang Yiqiu, Prof. Yang Donghai and associate professor Wang Fenzhi were granted some national projects to develop a compact optically pumped cesium clock. Doctoral students, Chen Jingbiao and Zhang Junhai are the key members in the team to build a compact optically pumped cesium atomic clock [36].

Wang's pioneering work on quantum precision measurement, atomic clocks, in particular, has greatly inspired China's development of commercial atomic clocks, with various institutes such as Peking University [46, 47], Chengdu Spaceon Electronics Co., Ltd. [48], and Lanzhou Institute of Physics [49, 50] all working toward commercial clocks with high performance at a relatively low cost.

Recent works on experimental cesium atomic clocks have also benefitted greatly from helpful discussions with and suggestions from Prof. Wang. Among these works are optically pumped cesium-beam atomic frequency standards by Peking University [51] and collaboration between Peking University and Chengdu Spaceon Electronics Co., Ltd. [52], reaching $3e{-}12/\sqrt{\tau}$ and $2e{-}12/\sqrt{\tau}$ frequency stability, respectively. Wang's work also inspired research on optically pumped cesium beam atomic clocks with multi-pole magnets for magnetic focusing of the atomic beam [53, 54].

In order to further improve the technique of the optically pumped cesium atomic clock and meet the needs of the country, under the instruction and help of Prof. Wang Yiqiu and Prof. Yang Donghai, Prof. Chen Xuzong together with his PhD students, Qi Xianghui (now is an associate professor) and Wang Qing (now is a lecturer) inherited research on the optically pumped cesium atomic clock from 2008, Chen's team was granted four terms of national projects to study the high-performance optically pumped cesium clocks since 2008. The goal is to achieve the stability of the 5071A high-quality cesium atomic clock. During the research, first, the theoretical analysis of the interaction between atomic beam and light and microwave is carried out [55], and the main factors affecting the high stability of atomic clock are found. It has improved the stability of laser frequency stabilization, reduced the noise of laser frequency stabilization [56, 57], and improved the frequency stability and power stability of microwave. After more than 10 years of efforts, the stability of miniaturized optically pumped cesium atomic clock has been improved to $3 \times 10^{-12}/\sqrt{\tau}$, which is three times that of the 5071A high-quality clock

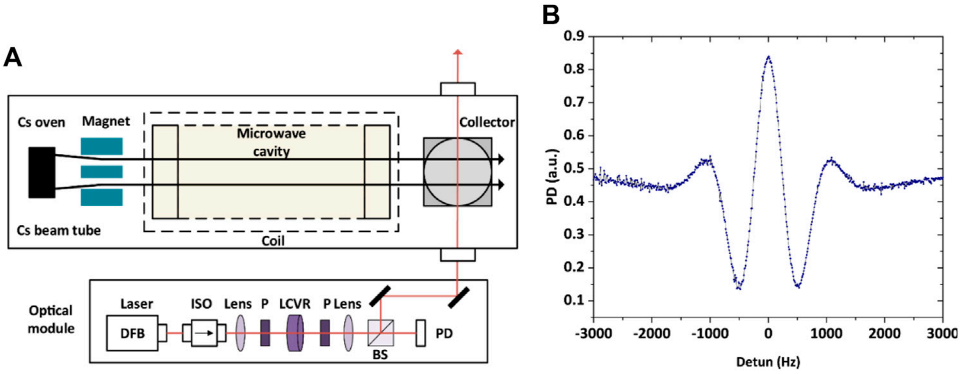

FIGURE 4
(A) Configuration of OMCC. ISO, isolator; P, polarizer; lens, convex lens; BS, beam splitter; PD, photodiode; LCVR, liquid crystal variable retarder. **(B)** Ramsey fringe.

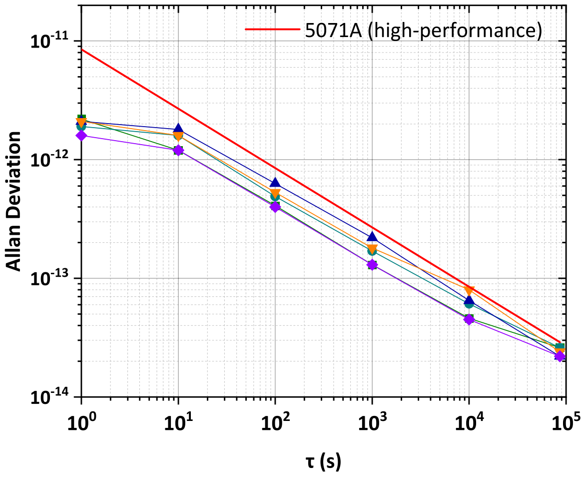

FIGURE 5
Frequency stability test result of five OMCC in comparison with the high-performance version of 5071A.

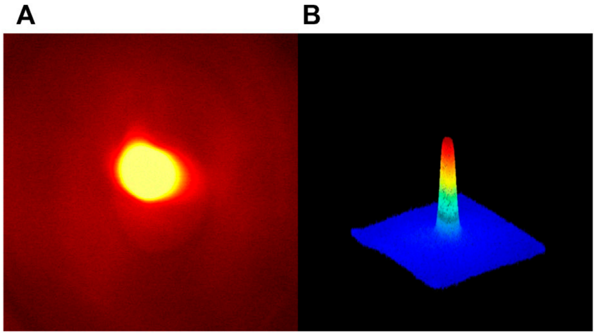

FIGURE 6
(A) First cesium magnetic optical trap in China. **(B)** Cold atoms with 100 μK and number of 1E+9 at Peking University in 1996.

[58], and the 5-day stability is better than 7×10^{-15} [59, 60]. Figures 3A,B show the frequency stability and photo of the portable optically pumped cesium clock developed by Peking University.

Meanwhile, another new structure of the compact cesium beam clock is also under development by an associate professor, Dr. Wang Yanhui, collaborating with his formal supervisor, Prof. Dong Taiqian and associate professor Liu Shuqing at Peking University. The optically detected the magnetic-state-selected cesium beam clock (OMCC) combines both the advantages of the magnetic-state-selected schemes and the optically detection schemes [61]. It avoids the technical issues concerning the lifetime of the electron multiplier and has narrower velocity distribution, resulting in a narrower Ramsey linewidth. The schematic and Ramsey fringe of the OMCC is shown in Figure 4.

The fluorescent spectroscopy is adopted to stabilize the laser frequency. Laser frequency is kept resonant with the atomic beam, and the mis-locking problem is avoided.

The frequency stability test result of five OMCCs at the National Institute of Metrology in China is plotted in Figure 5. The frequency reference is an active hydrogen maser and the measurement time is over 15 days. The result shows promising frequency stability and good consistency of OMCCs.

Laser cooling

In order to improve the accuracy of atomic clocks, it is necessary to reduce the temperature of free atoms. In the 1980s, scientists proposed many methods to cool neutral atoms, among

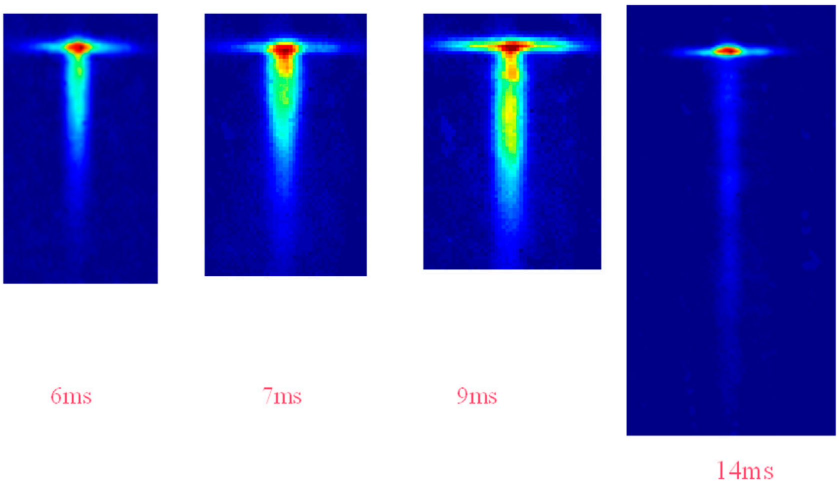

FIGURE 7
Atom laser at Peking University with different duration.

which Steven Chu, Claude Cohen-Tannoudji, and Bill Philips, three outstanding scientists, won the 1997 Nobel Prize in physics. In the 1980s, the research on laser cooling in the world developed rapidly in the world, but the research in China was relatively lagging behind. In 1994, the Chinese Nature Science Foundation (NSFC) began to support the research on laser cooling. Professor Wang Yiqiu was granted funding by the major project of NSFC. The project is: research on the new cesium atomic frequency standard based on the atomic fountain clock. Peking University has set up a laser cooling research group headed by Professor Wang Yiqiu.

There are many technical problems to be solved in the construction of the magneto-optical trap. In addition to vacuum technique and frequency stabilization technique, there are also many techniques such as laser amplification, laser frequency shift, magneto-optical trap laser alignment, and fluorescence detection . These techniques were new challenges for the team. Under the guidance of Prof. Wang, the team successfully solved these techniques problems [62–64].

In the process of building a magneto-optical trap, in addition to frequency stabilization laser, semiconductor laser amplification is also very important. Since the power of the purchased laser diode is about 50 mW, the power is not enough to cool atoms, so it needs to be amplified. But there was no power-amplified diode at that time. The team developed the "large frequency difference injection locking" technique which was used for a high power diode with multiple modes. With this technique, 852 nm wavelength laser injection locking can be realized by changing the laser current or fine-tuning the laser diode temperature at room temperature. In this way, the stable laser output with narrow laser line-width, long-term stable frequency, and power greater than 300 mW is achieved, which meets the light source conditions required by the magneto-optical trap [65, 66].

After the laser and optical system were ready, the research team began to implement the magneto-optical trap experiment. At that time, as deputy president of Peking University, Prof. Wang was very busy during the day, but he came to the laboratory every night . The experiment was mainly conducted by post-doctor, Dr. Chen Xuzong, and doctoral students: Li Yimin and Gan Jianhua. Professor Wang Yiqiu directed the laboratory. After 3 days of continuous experiments, cold atoms were finally obtained by using the magneto-optical trap at 10:30 p.m. on April 16, 1996, which was also the first cesium magneto-optical trap in China (Newspaper Wen Wei Bo and others reported this news) [67]. The photo and atomic distribution are shown in Figure 6.

Later, Professor Wang Yiqiu continued to guide doctoral students Fu Junxian and Dr. Li Yimin to carry out optical molasses experiments, and Hou Jidong, Wang Xiaohui and Chen Shuai to carry out atomic fountain experiments. The first optical molasses in China was obtained in 1997 [68, 69], and the first atomic fountain experiment in China was demonstrated in 2000 [70–72]. After 2000, Prof. Wang Yiqiu's cold atom group began to turn its research direction to Bose–Einstein condensation. In order to build the atomic fountain microwave atomic clock in China more quickly, Prof. Wang Yiqiu went to the Chinese National Institute of Metrology (NIM) very enthusiastically to help the research group that is building the atomic fountain microwave atomic clock there and introduced the NIM research group about how Peking University realized the magneto-optical trap and optical molasses. It accelerates NIM to build up the first atomic fountain microwave atomic clock in China .

FIGURE 8
Books written or translated by Prof. Wang Yiqiu. From left to right: "The Principles of Quantum Frequency Standards," "Laser Cooling and Trapping of Atoms," "Atomic Physics: Volume 1" (originally in French), "Atomic Physics: Volume 2" (originally in French), and "Advances in Atomic Physics: an Overview" (originally in French).

To reduce the atoms to an ultra-low temperature has always been a goal pursued by scientists engaged in atomic cooling research. Due to the influence of the earth's gravity, when the potential barrier of any potential well that traps atoms is reduced to a certain extent, a leak appears at the bottom of the potential well, which stops evaporative cooling. The space microgravity environment provides a new opportunity to further reduce the atomic temperature. In 2011, China began to develop the space station. It plans to launch the space station and the scientific experiment module from 2021 to 2022, and 14 scientific experimental racks will be launched with the module, including the cold atomic physics rack (CAPR). The development of the space ultra-cold atomic physics rack was jointly undertaken by Peking University and Shanghai Institute of Optics and Fine Mechanics, Chinese Academy of Sciences. Professor Chen Xuzong, who was originally a member of Prof. Wang Yiqiu's team, was appointed as the chief scientist for CAPR. In 2015, Dr. Xiong Wei joined the project for CAPR project as a deputy chief designer.

CAPR is a very advanced scientific experimental platform for ultra-cold atom physics. At present, only the United States and China are carrying out research in this field. The CAPR will take advantage of the microgravity environment to create a new extreme cold atomic sample, develop the lowest temperature record in the universe (10^{-12} K, that is, pK level ultra-low temperature), and build an open experimental system of Bose and Fermi quantum degenerate working substances with ultra-low temperature, large scale, high quality, and suitable for long-term precise measurement. The platform will enable the regulation of cold atoms to reach a new parameter region, so that a series of ultra-cold atom physics experiments under extreme conditions can be carried out, including simulation of strongly correlated multi-body quantum systems, exploration of novel quantum states, acoustic black hole simulation and Hawking radiation observation, and verification of basic physical laws. Relevant work will bring breakthroughs to the fields of quantum physics and precision physical measurement, and improve the level of new aerospace technology in China, including the ultra-old atomic vacuum system, ultra-high stability laser system, precision integrated optical system, and related precision intelligent control system suitable for thr space environment.

Peking University has put forward a new scheme of deep cooling under microgravity conditions, which uses an all-optical trap for two-stage cooling [14–17]. The basic idea was to use two cross laser beams with different beam diameters and different powers to carry out evaporative cooling and diffusion cooling, respectively, under special timing control, so as to obtain a quantum gas with a temperature of 100 pK in a short time (such as 10 s). The aforementioned scheme has been verified by ground experiments [18]. In order to obtain a very low limit temperature, it is necessary to reduce the influence caused by the vibration of the space station itself during the experiment on the space station. Therefore, Peking University theoretically studied the influence of the vibration spectrum of the space station on the atomic cooling limit [19], and proposed a solution on this basis. Based on two-stage cooling, further cooling of the mean-field energy and reducing the relative temperature, the new proposals are also given by the PKU group [20]. In 2020, Peking University was invited to publish a review stydy [35] in an internationally renowned magazine, introducing how to break the limit of ground gravity, obtain a temperature of pK under microgravity conditions, and conduct challenging experiments, it also introduced the important applications in future fundamental research [73] based on 100 pK ultra-cold atoms.

In 2021, the ultra-cold atomic physics experiment platform project progressed smoothly, and Peking University and Shanghai Institute of Optics and Precision Machinery, Chinese Academy of Sciences, have made many phased achievements, respectively. The functions of the prototype and the normal prototype of CAPR have been verified on the ground, meeting the requirements of the experiment after the launch at the end of 2022.

In order to further use this platform to carry out a series of scientific experiments, in 2021, the Chinese Ministry of Science and Technology organized a national key research and development program: "Research on the strange physical properties of extremely low-temperature atoms in the space microgravity environment," with Professor Zhou Xiaoji. The experiment of "superfluid to the model phase transition of one-dimensional to three-dimensional hexagonal optical lattice" [74] proposed by Professor Zhou Xiaoji, will become the first quantum simulation experiment in the series of experiments based on CAPR.

Bose–Einstein condensate

In 1925, Satyendra Nath Bose and Albert Einstein predicted that the Bose gas would behave as an extraordinary phenomenon near absolute zero temperature [75, 76]. Under this condition, the vast majority of atoms occupy the quantum ground state, producing a macroscopic wave function called Bose–Einstein condensate (BEC) [76]. In recent years, with the development of laser cooling technologies, people have had the opportunity to cool atoms to very low temperatures. In 1995, Eric Cornell and Carl Wieman at the University of Colorado at Boulder NIST-JILA laboratory, and Wolfgang Ketterle at Massachusetts Institute of Technology prepared and observed BEC in the rubidium atomic system and sodium atomic system, respectively [77, 78]. For this, Cornell, Wieman, and Ketterle won the 2001 Nobel Prize in physics. Professor Wang Yiqiu of Peking University is also one of the first scientists in China to start the research on Bose–Einstein condensates and prepared China's second Bose–Einstein condensates in 2004 [79, 80]. Prof. Wang Yiqiu was interested in building up an atom laser, which is a coherent atomic beam coupled out from the BEC trap. The pulsed and quasi-continuous atom laser was realized in 2005 [81], as shown in Figure 7. In 2000, under the instruction of Prof. Wang Yiqiu, doctoral student Zhou Xiaoji proposed a scheme for realizing the long-term continuous output of an atom laser. In this scheme, the cold atoms in several subsidiary Bose–Einstein condensates (BECs) would be coupled one by one, in turn, into one main BEC, which served for the continuous output of a coherent atomic beam [82, 83]. This kind of scheme was realized in the Ketterle group at MIT by using the sophisticated technique of optical tweezers [84]. In 2001, Prof. Wang Yiqiu and Prof. Chen Xuzong led the group to build up the setup for BEC, the key members were associate professor Zhou Xiaoji, doctoral students: Chen Shuai, Yang Fan, and Xia Lin. They used RF evaporative cooling technology to obtain a ^{87}Rb Bose–Einstein condensate in a QUIC trap, and used Majorana technology to obtain a multi-component BEC. In 2004, the team published first studies on BEC experiments in international journals [85, 86], and obtained the first atom laser in China in 2005 [81, 87]. [88] studied intensity fluctuations of the pulsed atom laser. They found that the atomic loss of the condensate due to atom laser output leads to fluctuations of the laser pulses [88].

Up to now, in Wang's laboratory, there are two groups led by Prof. Chen Xuzong and Prof. Zhou Xiaoji, respectively, and they have successfully prepared BECs on four platforms. In these systems, they have performed a lot of research, such as the atom laser, multi-component BEC, superradiance, and quantum simulation, one-dimensional gas and Bose–Fermi mixing. In 2008, [89] realized the superradiant Rayleigh scattering in an elongated Bose–Einstein condensate, where the pump laser pulse travels along the long axis. After that, the team conducted more in-depth research on superradiance. For example, they studied sequential scattering in superradiance from a Bose–Einstein condensate pumped by a two-frequency laser beam, which revealed that the frequency overlap between the end-fire modes related to different side modes plays an essential role in the dynamics of sequential superradiant scattering [90]. [91, 92] studied the high-order momentum modes and mode competition in the superradiant scattering of matter waves. [93] studied superradiant scattering from a Bose–Einstein condensate using a pump laser incident at a variable angle and showed the presence of asymmetrically populated scattering modes.

In 2002, [94] used the optical lattice to confine the BECs for the first time and observed the phase transition from a superfluid to a Mott insulator. Since then, BECs in optical lattices have gradually become a powerful tool for quantum simulation, quantum calculation, and precision measurement. Wang's laboratory has conducted a lot of research on ultra-cold atoms in optical lattices. In 2010, Prof. Zhou Xiaoji, developed a shortcut method to quickly manipulate Bloch states of optical lattices with high fidelity [95]. The shortcut is composed of lattice pulse sequences imposed on the system before the lattice is switched on. The time duration and interval in each step are optimized in order to reach the target state with high fidelity and robustness. This process usually takes tens of seconds, which is much shorter than the traditional adiabatic loading process [95]. The idea of the shortcut to controlling Bloch states of optical lattices was first proposed in 2011 [96, 97]. At first, Liu Xinxing used a single light pulse, with conditions where the scattering of photons can be resonantly amplified by an atomic density grating, to explore multiband excitations of interacting Bose gases in a one-dimensional optical lattice [97]. Then they presented a scheme for nonadiabatically loading a Bose–Einstein condensate into the ground state of a one-dimensional optical lattice within a few tens of microseconds, which is much shorter than the traditional adiabatic loading time scale. This scheme is based on sequences of pulsed perturbations

[96]. At the same time, Xiong Wei analyzed the effects of sequences of standing-wave pulses on a Bose–Einstein condensate in experiments and manipulated the momentum state of condensates by these sequences [98]. In 2013, Zhai Yueyang extended this method to load the atoms to the third band (D band) of the one-dimensional optical lattice and studied the collisional decay of atomic condensates in the D band [99]. Next, Wang Zhongkai successfully loaded atoms into the higher Bloch band, the G band. They were able to control the Bragg reflections at the Brillouin-zone edge up to the third order and observed quantum dynamical oscillations of ultra-cold atoms in the F and D bands of an optical lattice [100]. For the Bloch states at zero quasi-momentum in the ground band (S band), D band, and G band with even parity, the shortcut method is effective. However, this method cannot prepare atoms into odd parity states [95], such as the Bloch states in the second band (P band). In 2015, Hu Dong improved the method by using a shift pulse to load atoms into the P band and studied the long-time nonlinear dynamical evolution and quantum equilibration for P-band ultra-cold atoms in the optical lattice [101, 102]. In recent years, Chen and Zhou's group have extended this shortcut method to two-dimensional and three-dimensional optical lattices, such as the square lattice and the triangular lattice [95, 103]. So far, this method can realize the preparation and manipulation of any Bloch state in any dimensional optical lattice. In 2016, Chen' group achieved first 3D optical lattice in China and implemented quantum collapse and revival dynamics in 3D optical lattice [104, 105], they used the 3D lattice to form the one-dimensional gas and conducted serial experiments to study how an integrable system approaches thermal equilibrium [106, 107]. This is an interesting problem that has been puzzling everyone since D. Weiss' famous Newton pendulum experiment was performed in 2006 [108].

Based on the method of manipulating BECs in optical lattices, the team carried out considerable research on quantum simulation, quantum precision measurement, and quantum computation. For example, [109] constructed a momentum filter for BECs based on a designed Talbot–Lau interferometer, which was an effective method for rapidly purifying the momentum width of atomic gas and has great potential for achieving ultra-low temperatures. [102] investigated the multiphoton process between different Bloch states in an amplitude-modulated optical lattice and realized a large-momentum-transfer beam splitter. [110] produced narrower momentum patterns by designing the shortcut pulses on a superposed state, and these narrower momentum modes were helpful in precision measurement and quantum control. [111] improved the band-mapping method to investigate the quantum phase transition from superfluid to Mott insulators and observed the critical behaviors of quantum phase transitions in both the dynamical steady-state-relaxation and the phase-oscillation regions. Based on various observables, two different values for the same quantum critical parameter were observed. This result was beyond a universal-scaling-law description of quantum phase transitions known as the Kibble–Zurek mechanism and suggests that multiple quantum critical mechanisms were completed in many-body quantum phase transition experiments in inhomogeneous systems [111]. BEC in optical lattice can also be used to simulate and prepare novel quantum states. For example, in 2018, [112] loaded the BECs into the P band at zero quasi-momentum of a one-dimensional optical lattice, which can be viewed as a series of "pancake"-shaped atomic samples. For this far-out-of-equilibrium system, they found an intermediate time window where the atomic ensemble exhibited superfluid phase coherence in the pancake directions but no coherence in the lattice direction, which implied a dynamical sliding phase superfluid. This experiment opened up a novel venue to search for exotic dynamical phases [112]. In 2021, [113] constructed a staggering hexagonal optical lattice and transferred BECs from the ground band into the second band. They observed a three-state quantum nematic order, dubbed "Potts-nematicity," in a system described by an sp2-orbital hybridized model. This discovery paves the way to investigate quantum vestigial orders in multiorbital atomic superfluids [113]. The BECs in an optical lattice can also be used in quantum computation. For example, [114] proposed and realized an atom-orbital qubit by manipulating s and d orbitals of BECs in an optical lattice. They also achieved noise-resilient single-qubit gates by performing holonomic quantum control. This work was the first time for qubit based on the atom-orbitals in optical lattices and opened up broad opportunities for atom-orbital-based quantum information processing of vital importance to programmable quantum simulations of multiorbital physics in molecules and quantum materials [114].

Recently, BECs have also been used for precise measurements. Zhou's group has constructed a compact BEC gravimeter based on the Ramsey–Bordé approach by two pairs of/2 Raman pulses to get a small volume [115]. Between the two pairs of/2 Raman pulses, the Bloch oscillation caused by the accelerated optical lattice was carried out. This BEC gravimeter is expected to reach sub-μGal with atoms falling a distance of 2 cm [115]. In addition, Zhou's group is also building a BEC gyroscope based on the momentum states of the optical lattice. Under the same loop area, its theoretical sensitivity is much higher than that of the traditional gyroscope.

Optical tweezers

In 1986, A. Ashikin proposed the optical tweezers concept, that is, a single focused laser beam forms a three-dimensional optical well to trap a single biological particle such as single bacteria and viruses. The optical tweezers concept has many useful applications, and A. Ashikin was awarded the Noble prize for its invention in 2018. In the 1990s, as the leader of the laser trapping atom project, Professor Wang Yiqiu paid keen attention to laser tweezers technology and its potential application in biomedicine. He strongly advocated and supported the development of optical tweezers technology and application in his laboratory [116] and personally guided a graduate student Sun Wei to build a simple optical tweezers system using a wavelength of 852 nm semiconductor laser and successfully trapped a single cell. In 2000, Ye Anpei, a Professor of the same institute, inherited the research of optical tweezers and continued carrying out comprehensive studies on laser tweezers technology and its application. Ye's work was greatly supported by the foundation of the Peking University Frontier Cross Fund project. Soon after, Prof. Ye established the Nanobiophotonics Group and focused on developing biomedical photonic techniques and applications in biological single molecule and single-cell detection. First, Ye made a great effort to develop the optical tweezers technology and set up a multi-function optical platform which included automatic dual-optical tweezers constructed using a 1064 nm CW solid laser and an inverted optical microscope. Soon, a high-precision four-quadrant photodetector (QPD) was successfully developed in the group, thus they achieved accurate position measurement with nanometer precision. Meanwhile, [117] calibrated the stiffness of optical tweezers based on an acousto-optic deflector and field programmable gate array, and therefore laid the foundation for quantitative measuring weak force of a single molecule. [118] built the first dynamic holographic optical tweezers (HOT) based on a commercial twisted-nematic liquid crystal display (TN-LCD) which was from a waste video projector, and therefore first provided easier and lower-cost access to the set-up of a HOT system which can manipulate multiple particles simultaneously. Ten years later, Prof. Ye's group coupled optical tweezers and optical scissors together to construct a laser micro-manipulating workstation using Labview automatic control software that automatically controls each part of the entire platform with a computer, while the laser tweezers' spatial resolution reached the sub-nanometer level. Furthermore, they coupled confocal micro-Raman spectroscopy to laser tweezers so that they formed a so-called laser tweezers-Raman spectral (LTRS) system. Therefore, Ye's group can both trap single suspension living cells *in vitro* and meanwhile identify the type or state of the cell.

At the same time as technology development, Prof. Ye placed emphasis on its application in biomedical fields. Intermolecular interactions dominate the behavior of signal transduction in various physiological and pathological cellular processes. However, assessing these interactions remains a challenging task. Ye's laboratory developed a single-molecule force spectroscopic method and analyzed cellular signal transduction with single-molecule force spectroscopy on a piconewton-scale, thus established single-molecule force spectroscopy as an effective platform for evaluating the piconewton-level interaction of signaling molecules and predicting the behavior outcome of signal transduction. For example, [119] investigated the activation of living monocytic U937 cells induced by interleukin-6 (IL-6) at the single cell level. [120] measured low affinity between IL-6 and IL-6R on living cells at a single molecular level, the affinity was 42.1 ± 11.7 pN at the loading rate of 3100 pN nm/s. Using the single-molecule force spectroscopy of RAS–RAF interaction *in vitro*, [121] illustrated the interaction conformation of RAF protein and its upstream G-protein (RAS) at a single-molecule level, they demonstrated that RAS has different numbers of binding domains between wild-type and mutant-type RAF. [122] measured single-molecule force *via* optical tweezers and revealed different kinetic features of two BRaf mutants responsible for cardio-facialcutaneous (CFC) syndrome. [123] investigated the specific single-interaction between apoA-I molecules and ABCA1 on living cells. [124] regulated cell migration in a myosin light chain kinase, a phosphorylation-independent mechanism regulatory light chain phosphorylation-independent mechanism. In addition, [125] investigated the mechanical property changes of red blood cells with the stored time and experimentally demonstrated that the deformability of red blood cells was impaired with the stored time.

The ability to discriminate between single cells in a label-free and noninvasive fashion is important for the classification of cells, especially to identify similar morphological cells from different origins. Ye's group investigated single living cells and individual floating-particle using the homemade LTSR system, identified different types of single cells in aqueous media, and discriminated them among the same types of cells from different donors using a novel LTRS technique. [126] developed a novel anti-cancer drug sensitivity testing (DST) approach based on *in vitro* single-cell Raman spectrum intensity (RSI), which provided a powerful tool for simple and rapid detection of the sensitivity of tumor cells to anti-cancer drugs and the heterogeneity of their responses to these drugs. Also, [127] investigated drug resistance and heterogeneous characteristics of human gastric carcinoma cells (BGC823) under the treatment of paclitaxel (PTX) meanwhile, indicated that single-cell RS may be useful in systematically and dynamically characterizing the drug response of cancer cells at the single-cell level. [128] investigated chondrocyte dedifferentiation during *in vitro* proliferation. [129] reported laser-trapped metallic nanoparticles (NPs) as a novel approach for enhancing Raman spectroscopy in aqueous media. Recently, [130] combined LTRS and a specifically designed sample pool to achieve nondestructive identification and accurate isolation of single cells, which paves the pathway for multimodel analysis of a single cell. Furthermore, [131] reported a single-cell multimodal analytical approach by integrating Raman optical tweezers and RNA sequencing. Very recently, [132] realized fast label-free recognition of NRBCs by deep learning visual object detection and single-cell Raman spectroscopy, in order to rapidly and automatically analyze the single-cell Raman spectra based on AI techniques, Ye's group meanwhile developed applied software, which can quickly and accurately identify the Raman spectroscope of a single cell, especially in single bacteria. For instance, [133] explored one-dimension convolutional neural networks (1CNNs) and applied them to identify marine microbes with single-cell Raman spectroscopy. [134] furtherly developed the CNN model using the residual network (ResNet) model and succeeded in rapidly and accurately identifying 15-species pathogenic bacteria with the accuracy of 94.53% at the single-cell level.

Moreover, Ye's group recently developed an aerosol optical tweezers Raman spectroscopy technique and used it to levitate individual atmospheric aerosol droplets. For example, [135] realized single aerosol droplet capture for a long time without contact and simulated the hygroscopic-volatilization thermodynamic evolution process of aerosol droplets in the actual atmosphere *via* changing the ambient relative humidity around aerosol particles. By measuring the cavity resonance Raman signal of the single droplet particle and combining it with the appropriate physical models, [135] accurately measured the particle size, refractive index, diffusion coefficient, volatile flux, and other important physicochemical parameters of sodium chloride, sucrose, and citric acid in the hygroscopic-volatile process. Moreover, the effects of relative humidity on the hygroscopic-volatilization process for organic and inorganic aerosols as well as the possible phase transitions such as glassy and gel transitions are investigated. This work provides an important reference for understanding the hygroscopic-volatilization process of actual atmospheric aerosol. Also, [136] measured the viscosity of single suspended aerosol droplets under different RH conditions. They trapped and levitated a pair of quasi atmospheric aerosol droplets composed of organic and inorganic chemical substances by dual laser beams, respectively, and then collided and coalesced them. By recording the backscattering light signals and bright-field images of the dynamic coalescence process to infer the morphological relaxation time and the diameter of the composited droplet, and therefore measured the viscosity of the droplet. Furthermore, to give a deep insight into the relationship between viscosity and the mass transfer process, they researched the hygroscopicity of droplets with a solute of organic/inorganic mixtures. This work provided a robust approach for investigating the viscosity and hygroscopicity of actual individual liquid PM10 aerosols. Very recently, [136] investigated the pH-dependent liquid–liquid phase separation (LLPS) of a single artificial aerosol particle by self-developed optical tweezer-Raman spectroscopy (OTRS). This study provides the first comprehensive account of the pH-dependent LLPS in a single levitated microdroplet and brings a possible implication on phase separation in actual atmospheric aerosol particles.

Optical atomic clocks

In order to detect atomic transition spectral lines with a linewidth on the order of mHz, the linewidth of the local oscillator laser must be narrow enough. Generally, Pound–Drever–Hall frequency stabilization technology [137] is used to lock the frequency of the local oscillator laser to an ultra-stable optical resonator to obtain a highly coherent ultra-narrow-linewidth laser, but it is still limited by the thermal noise of the cavity length. In order to essentially solve the cavity length thermal noise problem of the resonator and with the support of Prof. Wang Yiqiu, the innovative concept of the active optical clock was proposed by Prof. Chen Jingbiao, who was formerly a doctoral student of Prof. Yang Donghai. In 2005, the concept of the active optical clock was formally proposed [138–140]. Active optical clock forms of polyatomic coherent stimulated radiation between atomic transition energy levels in the optical resonator. The stimulated radiation of the quantum reference system can be directly used as the clock laser signal, which can break through the limit of the Schawlow–Townes quantum linewidth [79]. In April 2013, the stimulated emission output of the active optical clock transition in the deep bad cavity regime (cavity mode linewidth-gain linewidth proportional coefficient $a \gg 1$) was experimentally realized for the first time [141]. In the experiment, using a 455 nm laser as the pumping laser, atomic population inversion was realized on the 1469.9 nm clock transition line of the Cs atom four-level active optical clock. The research team further experimentally measured the cavity-pulling coefficient of the four-level active optical clock up to 40, and the output laser linewidth was 590 Hz [142]. In the four-level active optical clock scheme, the frequency standard used as a quantum reference and the gain medium for stimulated emission are all from the same atomic system. Since it is difficult to experimentally achieve stimulated emission output using both long-lived atomic energy levels and bad cavity structures, this requirement greatly limits the quantum systems that can be used for the active optical frequency standard. In principle, the Faraday active optical clock separates the gain medium from the frequency reference. The semiconductor laser provides a larger gain, and the ultra-narrow bandwidth Faraday atomic filter provides the frequency reference to realize the optical frequency standard signal. The output laser linewidth obtained experimentally is 281 Hz, which is 19000 times narrower than the natural linewidth of the 852 nm transition of the Cs atom [143]. In order to eliminate the influence of the residual cavity-pulling effect on the active optical frequency standard, the dual-wavelength good-bad-cavity scheme was carried out [144]. In the experiment, two sets of dual-wavelength good-bad-cavity systems were built, and the phase locking of the good cavity laser was used to reduce the influence of the asynchronous cavity-length variation between two dual-wavelength laser systems on the linewidth broadening of the 1470 nm clock laser. The linewidth of the realized 1470 nm active optical clock signal reached the level of Hz. In theory, [145] demonstrated the state-of-the-art technique of an active clock to provide a continuous superradiant lasing signal using an ensemble of trapped Cs atoms in an optical lattice, which can achieve a fractional uncertainty in the clock frequency of about 10^{-15} and a linewidth of a few mHz.

After the active optical clock scheme was proposed, it attracted the attention of international counterparts. Several research groups have carried out experimental verifications of it and conducted research on active optical clock schemes based on different atomic systems. The Niels-Bohr Institute (University of Copenhagen, Denmark) used the ^{88}Sr atom trapped in the magneto-optical trap working in the bad cavity region as the quantum reference and realized a pulsed superradiant light [146]. The JILA research group realized a superradiant light emitted from the ultra-narrow, 1-mHz-linewidth optical clock transition in an ensemble of cold ^{87}Sr atoms. They observed a fractional Allan deviation of 6.7×10^{-16} at 1 s of averaging, established absolute accuracy at the 2 Hz (4×10^{-15} fractional frequency) level, and demonstrated insensitivity to key environmental perturbations [147]. Using the two-level scheme, the University of Hamburg observed a superradiant emission of hyperbolic secant-shaped pulses into the cavity with an intensity proportional to the square of the atom number based on the 657 nm transition of cold Ca atoms [148]. [149] investigated the full model for the collective decay process and aimed at direct implications for the laser linewidth of a magic wavelength lattice laser in the superradiant regime. Using the Raman transition of the cold ^{87}Sr atom in bad cavity, JILA obtained a superradiant laser, in which FWHM of the Gaussian fitting was 350 Hz and the FWHM of the Lorentzian fitting was 4.5 Hz [150]. Based on the narrow quantum transition line of the ^{87}Sr atom, the active optical frequency standard of the order of mHz can be realized theoretically [151]. In terms of theoretical research, the Department of Physics and Astronomy of Aarhus University in Denmark analyzed the ^{87}Sr atoms trapped in the one-dimensional optical lattice in the bad cavity region. Under the action of a magnetic field, this system can output superradiant pulsed light with a linewidth of less than 2 Hz [152]. [153] studied two-frequency-detuned active atomic clocks which are coupled in a cascaded setup and demonstrated that synchronization still occurs in cascaded setups but exhibits distinctly different phase diagrams. Georgy A. [154] investigated the spectral properties and the stability of active clocks, including homogeneous and inhomogeneous broadening effects. By using realistic numbers for an active clock with ^{87}Sr, it is possible to realize an optimized stability of $\sigma_y(\tau) \approx 4 \times 10^{-18}/\sqrt{\tau}$ [154]. The active optical clock is gaining more international attention. Specifically, at the 2015 IEEE International Frequency Control Symposium, the active optical clock was listed as one of the three most talked about emerging technologies in this field.

In addition to the active optical clock, many of Professor Wang Yiqiu's ideas, such as Cs beam tube optical frequency standards and Ca atom compact optical clocks, have been realized. For the cesium beam tube optical frequency standard, [155] reported a compact optical clock scheme based on Cs atomic beam. Under the condition of a 1.4 MHz narrow-linewidth laser spectrum and 100,000 signal-to-noise ratio (SNR), the limited stability of the compact Cs optical clock is expected to be 2.2×10^{-14} at 1 s. The performance of this Cs optical clock is superior to that of the hydrogen atomic clock. For the Ca atom compact optical clock, [156] implemented a miniaturized Ca beam optical frequency standard whose fractional instability reached 1.8×10^{-15} after 1600 s of averaging. It was the first time to realize the optical frequency standard using a fully-sealed vacuum tube. For the Cs atom compact optical clock, using the modulation transfer spectrum stabilization technique with a high signal-to-noise ratio, the clock laser was directly locked on the transition spectrum line of the Cs atom, and a compact high-performance Cs atomic optical frequency standard with a frequency stability of $1.4 \times 10^{-14}/\sqrt{\tau}$ was developed [157]. Then, the 1470 nm active optical frequency standard was realized by using this small optical frequency standard as the pumping laser, which can go beyond the limits of the Schawlow–Townes formula and has the advantage of the suppressed cavity-pulling effect.

Other contributions by Prof. Wang

"The Principles of Quantum Frequency Standards," the first book on the principle of frequency standard in the world, was written by Wang Yiqiu in 1986 [24]. This book mainly describes the physical principles of quantum frequency standards and includes new achievements at home and abroad, which promotes the research work on the quantum frequency standard and the development of quantum metrology. In the field of laser cooling and trapping of atoms, there was a fundamental and comprehensive book of "Laser Cooling and Trapping of Atoms" also written by Wang Yiqiu (published at the beginning of the new century by Peking University Press). In addition to the aforementioned two important monographs, Wang Yiqiu translated the first and second volumes of the French original book "Atomic Physics," providing an excellent textbook for teachers and students of atomic and molecular physics, optics, quantum electronics, and other majors. Furthermore, under the personal attention of Prof. C. Cohem-Tannoudji, Prof Wang Yiqiu organized the translation of Cohem-Tannoudji's famous book (with Guéry-Odelin) of "Advances in Atomic Physics, an Overview" in Chinese and made the compilation and revision by himself. Figure 8 shows several books written or translated by Prof. Wang Yiqiu.

Conclusion

This review gives an account of the scientific career and contributions of Prof. Wang Yiqiu, who is a prominent figure in China's research on quantum precision measurement and cold atom physics. During his long scientific career, Prof. Wang has contributed greatly to the fields of research such as nuclear magnetic resonance, microwave atomic clocks, laser cooling of atoms, Bose–Einstein condensate, optical tweezers, and optical atomic clocks. We list the major scientific achievement by Prof. Wang, as well as advances in the relevant research fields inspired by Prof. Wang's work, roughly in a chronological order.

Author contributions

XC wrote the sections "Nuclear Magnetic Resonance" and "Laser cooling," and participated in the writing of the section "Microwave Atomic Clocks;" XZ wrote the section "Bose–Einstein Condensate;" AY wrote the section "Optical Tweezers;" YW participated in the writing of the section "Microwave Atomic Clocks;" JC wrote the abstract, introduction, conclusion, the sections "Optical Atomic Clocks" and "other contributions by Prof. Wang," and participated in the writing of the section "Microwave Atomic Clocks."

Funding

The work was supported by the National Natural Science Foundation of China (Grants Nos. 11920101004, 11334001, 61727819, 61475007), and the National Key Research and Development Program of China (Grant No. 2021YFA1400900, 2021YFA0718300).

Conflict of interest

The authors declare that the research was conducted in the absence of any commercial or financial relationships that could be construed as a potential conflict of interest.

Publisher's note

References

1. СкриЦов ФИ, Дан СССР. Skripov F I. *Soviet Phys Doklady* (1961) 6:27. doi:10.1063/1.3057553

2. И-цю В, (王义遒), Ж. Струк. Чим.(J. Struc. Chem.), 2(1961), 58.

3. Lauterbur PC. Anisotropy of theC13Chemical shift in calcite. *Phys Rev Lett* (1958) 1:343–4. doi:10.1103/physrevlett.1.343

4. Scripov FI, Wang Y, 20. USA (1964). p. 41. (in Chinese); also in "Chinese Physics" in.*Acta Physica Sinica*

5. И-цю В, 王义遒Yi-Ch'iu W. Дан СССР. *Soviet Phys Doklady*. (1961) 1366: 31739.

6. Deverell C, Schaumburg K, Bernstein HJ. ^{19}F nuclear magnetic resonance chemical shift of alkali fluorides in light- and heavy-water solutions. *J Chem Phys* (1968) 49(3):1276–83. doi:10.1063/1.1670220

7. Vaughan RW, Elleman DD, Rhim WK, Stacey LM. 19F chemical shift tensor in group II difluorides. *J Chem Phys* (1972) 57(12):5383–90. doi:10.1063/1.1678236

8. Sears REJ. Fluorine chemical shifts in the alkali fluorides. *J Chem Phys* (1974) 61(10):4368–9. doi:10.1063/1.1681750

9. Burum DP, Elleman DD, Rhim WK. A multiple pulse zero crossing NMR technique, and its application to 19F chemical shift measurements in solids. *J Chem Phys* (1978) 68(3):1164–9. doi:10.1063/1.435806

10. Ramsey NF. Magnetic shielding of nuclei in molecules. *Phys Rev* (1950) 78: 699–703. doi:10.1103/physrev.78.699

11. Kondo J, Yamashita J. Nuclear quadrupolar relaxation in ionic crystals. *J Phys Chem Sol* (1959) 10:245–53. doi:10.1016/0022-3697(59)90001-0

12. И-цю В, Володичева МИ. ФТТ *(Solid State Physics)* (1962) 4:642.(王义遒)

13. Deverell C. Chapter 4 Nuclear magnetic resonance studies of electrolyte solutions. *Prog Nucl Magn Reson Spectrosc* (1969) 4:235–334. doi:10.1016/0079-6565(69)80005-1

14. Author Anonymous. *Proposal for atomic cooling approach in space and a cold atom experimental system in Chinese space station*. Noordwijk, Netherlands: Chen X,book of abstract (2013). p. 22–3. page 11, STE-QUEST Workshop.

15. Lu W, Peng Z, Xu-Zong C, Zhao-Yuan M. Generating a picokelvin ultracold atomic ensemble in microgravity. *J Phys B: Mol Opt Phys* (2013) 46:195302. doi:10.1088/0953-4075/46/19/195302

16. Hepeng Y, Tian L, Chen L, Yin Z, Zhaoyuan M, Xuzong C. Comparison of different techniques in optical trap for generating picokelvin 3D atom cloud in microgravity. *Opt Commun* (2016) 359:123. doi:10.1016/j.optcom.2015.09.065

17. Luan T, Yao H, Wang L, Li C, Yang S, Chen X, et al. Two-stage crossed beam cooling with 6Li and 133Cs atoms in microgravity. *Opt Express* (2015) 23:11378. doi:10.1364/OE.23.011378

18. Tian L, Yufan L, Zhang X, Chen X, Xuesong Z, Xuzong C. Realization of two-stage crossed beam cooling and the comparison with Delta-kick cooling in experiment. *Rev Scientific Instr* (2018) 89:123110. doi:10.1063/1.5046815

19. Bo F, Luheng Z, Yin Z, Jingxin S, Wei X, Jinqiang C, et al. Numerical study of evaporative cooling in the space station. *J Phys. B: Mol. Opt. Phys.* (2021) 54:015302. doi:10.1088/1361-6455/abc72d

20. Xuzong C, Bo F. The emergence of picokelvin physics. *Rep Prog Phys* (2020) 83:076401. doi:10.1088/1361-6633/ab8ab6

21. Wang X, Zhang C, Wang Y. *Proc. Of the national conf. Of optical and radio frequency spectroscopy*. ShanghaiBeijiing: Chinese Physical Society (1965).

22. Ramsey NF. History of atomic clocks. *J Res Natl Bur Stand (1977)* (1983) 88: 301–20. doi:10.6028/jres.088.015

23. Ramsey NF. Experiments with separated oscillatory fields and hydrogen masers. *Science* (1990) 248:1612–9. doi:10.1126/science.248.4963.1612

24. Wang Y, Wang Q, Fu J, Dong T. *Principles of quantum frequency standards*. Beijing: Science Press (1986).

25. Yi-qiu W. Majorana transitions in cesium beam tube. *Acta Metrologica Sinica* (1981) 2:42–8.

26. Yi-qiu W. The causes of Majorana transitions in one type of small cesium beam tube. *Acta Metrologica Sinica* (1983) 4:86–95.

27. Bauch A, Schröder R. Frequency shifts in a cesium atomic clock due to Majorana transitions. *Ann Phys* (1993) 2:421–49. doi:10.1002/andp.19935050502

28. Wynands R, Schroder R, Weyers S. Majorana transitions in an atomic fountain clock. *IEEE Trans Instrum Meas* (2007) 56(2):660–3. doi:10.1109/tim.2007.891116

29. Wang Y. A proposal for a laser deceleration atomic standard. *Chin J Magn Reson* (1988) 5(1):1. in Chinese.

30. Wang Y, Li Y, Gan J, Chen X, Yang D. Some considerations on the cesium atomic fountain standard. *Proc Intern Freq Stand Metrology, Woods Hole* (1995) 74–80.

31. Xin-xin W, Yue-ting X, Kun-yu T, Shu-tong Y, Lin-zhen X, Yi-qiu W. Main aspects in the design of optically pumped cesium beam tube. *Acta Metrologica Sinica* (1985) 6:15–23.

32. Wang DP, Xie LZ, Wang YQ, Guo SJ. GaAlAs laser diode pumped cesium beam frequency standard. *Chin Phys Lett* (1988) 5(3):97. doi:10.1088/0256-307X/5/3/001

33. Wang YQ, Xie LZ, Wang DP, Yao ST. Preliminary results and some considerations on the optically pumped Cs beam frequency standard. *Proc 4th Symp Frequency Stand Metrology* (1988) 126–31. doi:10.1007/978-3-642-74501-0_23

34. Yang DH, Wang YQ. Detection by cycling transition in an optically pumped cesium beam frequency standard. *Opt Commun* (1990) 73:285–8. doi:10.1016/0030-4018(89)90218-6

35. Yang DH, Wang YQ. Preliminary results of an optically pumped cesium beam frequency standard at Peking University. *IEEE Trans Instrum Meas* (1991) 40(6): 1000–2. doi:10.1109/19.119781

36. Zhang J, Chen J, Wang F, Yang D, Wang Y. Influence of a static magnetic field on the detected atomic velocity distribution in an optically pumped cesium beam frequency standard. *IEEE Trans Ultrason Ferroelectr Freq Control* (2003) 50(9):1210–3. doi:10.1109/tuffc.2003.12353339

37. Yang D-H, Wang Y-Q. A novel design of optically pumped cesium beam frequency standards. In: Proceedings of the Conference on Precision Electromagnetic Measurements; 11-14 June 199; Ottawa, ON, Canada (1990). p. 244–5.

38. Yang DH, Wang YQ. The effective velocity distribution of atoms and the improvement of the accuracy for an optically pumped cesium beam frequency standard with sharp angle incidence of probing laser beam. *Opt Commun* (1991) 85: 319–25. doi:10.1016/0030-4018(91)90484-u

39. Dong-Hai Y, En-Xian L, Le-Ming C, Bing-Ying H, Yi-Qiu W, Wang YQ. Experiment on optically pumped cesium beam frequency standard with sharp angle incidence probing laser beam. *Opt Commun* (1991) 84:275–8. doi:10.1016/0030-4018(91)90086-s

40. Dong-Hai Y, Yi-Qiu W. Long-term operation and frequency stability of an optically pumped cesium beam frequency standard with sharp-angle incidence of probing laser beam. *Jpn J Appl Phys (2008)* (1994) 33:1674–5. doi:10.1143/jjap.33.1674

41. de Clercq E, Rovera GD, Bouzid S, Clairon A. The LPTF optically pumped primary frequency standard. *IEEE Trans Instrum Meas* (1993) 42:457–61. doi:10.1109/19.278604

42. Lee HS, Yang SH, Kim JO, Kim YB, Baek KJ, Oh CH, et al. Frequency stability of an optically pumped caesium-beam frequency standard at the KRISS. *Metrologia* (1998) 35:25–31. doi:10.1088/0026-1394/35/1/5

43. McFerran JJ, Luiten AN. Fractional frequency instability in the 10ˆ−14 range with a thermal beam optical frequency reference. *J Opt Soc Am B* (2010) 27:277–85. doi:10.1364/josab.27.000277

44. Wang F, Yang D, Wang Y. A portable diode laser frequency locking system for optically pumped cesium beam frequency standard. *Acta Metrologica Sinica* (1994) 15:155–8.

45. Yang DH, Wang FZ, Wang YQ. A compact diode laser system for small optically pumped cesium beam frequency standard. In: Proceedings of the 50th IEEE International Frequency Control Symposium; 05-07 June 1996; Honolulu, HI, USA (1996).

46. Liu C, Zhou S, Wang Y, Hou S. Rubidium-beam microwave clock pumped by distributed feedback diode lasers. *Chin Phys B* (2017) 26:113201. doi:10.1088/1674-1056/26/11/113201

47. Liu C, Wang S, Chen Z, Wang Y, Hou S. Optical detection in magnetic state-selection Cs beam tubes for transportable Cs beam clocks. *Meas Sci Technol* (2019) 30:075004. doi:10.1088/1361-6501/ab11af

48. Xing-wen Z, Qiang W, Dong-xu L, Yu-ao L, Lin Y. Progress on optically pumped cesium beam frequency standard. *J Time Frequency* (2021) 45:1–8.

49. Chen J, Ma P, Wang J, Guo L, Tu JH, Yang W. Test of magnetic-selected cesium atomic clock LIP Cs3000C. *J Time Frequency* (2018) 41(3):1674–0637.

50. Chen J, Ma P, Wang J, Guo L, Liu ZD, Yang J, et al. Progress in commercialization of compact magnetically selected cesium atomic clocks. *J Astronautic Metrology Meas* (2020) 40:12–6.

51. Xie W, Wang Q, He X, Chen N, Xiong Z, Fang S, et al. Frequency instability of a miniature optically pumped cesium-beam atomic frequency standard. *Rev Scientific Instr* (2020) 9:074705. doi:10.1063/5.0001749

52. Shang H, Zhang T, Miao J, Shi T, Pan D, Zhao X, et al. Laser with 10−13 short-term instability for compact optically pumped cesium beam atomic clock. *Opt Express* (2020) 28:6868. doi:10.1364/oe.381147

53. Liu T, Pan D, Chen J. Optical pumped cesium atomic clock with multipole magnet. In: Proceedings of the 2020 Joint Conference of the IEEE International Frequency Control Symposium and International Symposium on Applications of Ferroelectrics (IFCS-ISAF); 19-23 July 2020; Keystone, CO, USA (2020). p. 1–4.

54. Yan Y, Chen H, Feng J, Pan D, Liu T, Chen J. Enhancing the signal-to-noise ratio in optically pumped cesium beam tubes using a hexapole magnetic system. In: Proceedings of the 2021 Joint Conference of the European Frequency and Time Forum and IEEE International Frequency Control Symposium (EFTF/IFCS); 07-17 July 2021; Gainesville, FL, USA (2021). p. 1–7.

55. Chen X, Wang Q, Yu J, Zhao W, Zhang Y, Qi X, et al. Theoretical analysis on optical pumped cesium atomic clock. *Acta Metrology Sinica* (2015) 36:108.

56. Wang Q, Qi X, Liu S, Yu J, Chen X. Laser frequency stabilization using a dispersive line shape induced by Doppler Effect. *Opt Express* (2015) 23:2982. doi:10.1364/oe.23.002982

57. Xie WB, Wang Q, He X, Xiong ZZ, Chen N, Fang SW, et al. A linewidth locking method to control the microwave power in optically pumped cesium-beam clocks. *Rev Sci Instrum* (2020) 91:094708. doi:10.1063/1.5144478

58. Xie WB, Wang Q, He X, Chen N, Xiong ZZ, Fang SW, et al. Frequency instability of a miniature optically pumped cesium-beam atomic frequency standard. *Rev Sci Instrum* (2020) 91:074705. doi:10.1063/5.0001749

59. He X, Fang S, Yuan Z, Xie W, Chen N, Xiong Z, et al. Compact optically pumped cesium beam atomic clock with a 5-day frequency stability of 7×10−15. *Appl Opt* (2021) 60:10761–5. Editors' Pick. doi:10.1364/ao.443812

60. He X, Wang Q, Yuan Z, Qi X, Chen X. Observation of a hole in the laser-induced cesium beam spectrum. *IEEE Access* (2021) 9, 49974–9. doi:10.1109/access.2021.3069031

61. Liu C, Wang S, Chen Z, Wang Y, Hou S. *Optical detection in magnetic state-selection Cs beam tubes for transportable Cs beam clocks*[J]. Measurement Science and Technology, United Kingdom, 2019.

62. Yimin L, Xuzong C, Jianhua G, Wangxi J, Jingshan H, Donghai Y, et al. Intensity dependence of Cs D2-line saturation spectra. *Chin Phys.Lett* (1996) 13(6): 424. doi:10.1088/0256-307X/13/6/007

63. Gan J, Chen X, Liyimin JW, Hua J, Yao J, Yang D, et al. The dependence of Cs saturated absorption spectra on the intensity of pumping light, *Acta Physica Sinica* (1996) 45(10), 1622–8.

64. Chen X, Yao J, Li Y, Yang D, Wang Y. A narrow linewidth diode laser for high resolution spectroscopy and its properties. *Acta Optica Sinica* (1996) 10.

65. Wang X, Chen X, Hou J, Yang D, Wang Y. Side-mode injection locking characteristics of 150 mW AlGaAs semiconductor lasers. *Opt Commun* (2000) 178: 165–73. doi:10.1016/s0030-4018(00)00617-9

66. Wang X, Chen X, Hou J, Yang D, Wang Y. Theoretic and experimental study on large-frequency-difference side-mode infection locking of high power semiconductor lasers of laser cooling. *Acta Physica Sinica* (2000) 49:85–93.

67. Gan J, Li Y, Chen X, Liu H, Yang D, Wang Y. Magneto-optical trap for Cs atoms. *Chin.Phys.Lett.* (1996) 13(11):821. doi:10.1088/0256-307X/13/11/006

68. Fu J, Li Y, Chen X, Yang D, Wang Y. Experimental study on the properties of magneto optical trap and the collective behaviors of cold atoms. *Acta Sinica Puantum Optica* (1998) 03.

69. Hou J, Wang X, Chen X, Yang D, Wang Y. Obtaining ultra-cold atoms by optical molasses directly from vapor. *Acta Scientiarum Naturalium Universitatis Pekinensis* (2001) 37(5):716–20.

70. Wang X, Hou J, Chen X, Yang D, Wang Y. Design and setting up of a practical optical system for cesium atomic fountain. *Acta Optica Sinica* (2000) 11.

71. Fu J, Li Y, Chen X, Yang D, Wang Y. A new method for measuring density and temperature of cold atoms in magneto-optical trap. *Acta Optica Sinica* (2001) 414–6.

72. Fu J, Chen S, Chen X, Yang D, Wang Y. Realization of an atomic fountain using a novel launching method. *Chin Phys Lett* (2001) 18:1457–9. doi:10.1088/0256-307x/18/11/310

73. Tino1 GM, Angelo Bassi A, Bianco G, Bongs K, Bouyer P, Cacciapuoti L, et al. SAGE, A proposal for a space atomic gravity explorer. *Eur Phys J* (2019) D73:22. doi:10.1140/epjd/e2019-100324-6

74. Jin S, Guo X, Peng P, Chen X, Li X, Zhou X. Finite temperature phase transition in a cross-dimensional triangular lattice. *New Jou Phys* (2019) 21:073015. doi:10.48550/arXiv.1805.08790

75. Bose SN. Plancks Gesetz und Lichtquantenhypothese. *Z Physik* (1924) 26: 178–81. doi:10.1007/bf01327326

76. Einstein A. Quantentheorie des einatomigen idealen Gases. *Sitzungsber Kgl Preuss Akad Wiss* (1924) XXII:261. doi:10.1002/3527608958.ch27

77. Anderson MH, Ensher JR, Matthews MR, Wieman CE, Cornell EA. Observation of bose-einstein condensation in a dilute atomic vapor. *Science* (1995) 269:198–201. doi:10.1126/science.269.5221.198

78. Davis KB, Mewes MO, Andrews MR, van Druten NJ, Durfee DS, Kurn DM, et al. Bose-einstein condensation in a gas of sodium atoms. *Phys Rev Lett* (1995) 75: 3969–73. doi:10.1103/physrevlett.75.3969

79. Shuai C, Xiao-Ji Z, Fan Y, Lin X, Yi-Qiu W, Xu-Zong C. Optimization of the loading process of the QUIC magnetic trap for the experiment of bose–einstein condensation. *Chin Phys Lett* (2004) 21:2227–30. doi:10.1088/0256-307x/21/11/042

80. Shuai C, Xiao-Ji Z, Fan Y, Lin X, Ya-Ya S, Yi-Qiu W, et al. Analysis of runaway evaporation and bose–einstein condensation by time-of-flight absorption imaging. *Chin Phys Lett* (2004) 21:2105–8. doi:10.1088/0256-307x/21/11/009

81. Fan Y, Lin X, Xiao-Ji Z, Xiu-Quan M, Xu-Zong C. Strong outcoupling from spin-2 87Rb Bose{Einstein condensates. *Chin Phys Lett* (2005) 22:1596.

82. Yiqiu W, Xiaoji Z, Donghai Y. Realization of the long-term continuous output for an atom laser: A proposal. In: Z Xu, S Xie, S-Y Zhu, MO Scully, editors. *Frontiers of laser physics and quantum optics*. Berlin, Heidelberg: Springer Berlin Heidelberg (2000). p. 473–6.

83. Xiao-Ji Z, Yi-Qiu W, Dong-Hai Y. A scheme for realizing the continuous wave atom laser. *Chin Phys Lett* (2000) 17:784–6. doi:10.1088/0256-307x/17/11/002

84. Chikkatur AP, Shin Y, Leanhardt AE, Kielpinski D, Tsikata E, Gustavson TL, et al. A continuous source of bose-einstein condensed atoms. *Science* (2002) 296: 2193–5. doi:10.1126/science.296.5576.2193

85. Ma X, Xia L, Yang F, Zhou X, Wang Y, Guo H, et al. Population oscillation of the multicomponent spinor Bose-Einstein condensate induced by nonadiabatic transitions. *Phys Rev A (Coll Park)* (2006) 73:013624. doi:10.1103/physreva.73.013624

86. Xia L, Xu X, Guo R, Yang F, Xiong W, Li J, et al. Manipulation of the quantum state by the Majorana transition in spinor Bose-Einstein condensates. *Phys Rev A (Coll Park)* (2008) 77:043622. doi:10.1103/physreva.77.043622

87. Lin X, Wei X, Fan Y, Lin Y, Xiao-Ji Z, Xu-Zong C. High field seeking state atom laser and properties of flux. *Chin Phys Lett* (2008) 25(7):2374. doi:10.1088/0256-307x/25/7/012

88. Xia L, Yang F, Zhou X, Chen X. Intensity fluctuations of the 87Rb pulsed atom laser. *Phys Lett A* (2009) 373:1429–33. doi:10.1016/j.physleta.2009.02.042

89. Li J, Zhou X, Yang F, Chen X. Superradiant Rayleigh scattering from a Bose–Einstein condensate with the incident laser along the long axis. *Phys Lett A* (2008) 372:4750–3. doi:10.1016/j.physleta.2008.04.049

90. Yang F, Zhou X, Li J, Chen Y, Xia L, Chen X. Resonant sequential scattering in two-frequency-pumping superradiance from a Bose-Einstein condensate. *Phys Rev A (Coll Park)* (2008) 78:043611. doi:10.1103/physreva.78.043611

91. Zhou X, Fu J, Chen X. High-order momentum modes by resonant superradiant scattering. *Phys Rev A (Coll Park)* (2009) 80:063608. doi:10.1103/physreva.80.063608

92. Vogt T, Lu B, Liu X, Xu X, Zhou X, Chen X. Mode competition in superradiant scattering of matter waves. *Phys Rev A (Coll Park)* (2011) 83:053603. doi:10.1103/physreva.83.053603

93. Lu B, Zhou X, Vogt T, Fang Z, Chen X. Laser driving of superradiant scattering from a Bose-Einstein condensate at variable incidence angle. *Phys Rev A (Coll Park)* (2011) 83:033620. doi:10.1103/physreva.83.033620

94. Greiner M, Mandel O, Esslinger T, Hänsch TW, Bloch I. Quantum phase transition from a superfluid to a Mott insulator in a gas of ultracold atoms. *Nature* (2002) 415:39–44. doi:10.1038/415039a

95. Zhou X, Jin S, Schmiedmayer J. Shortcut loading a Bose-Einstein condensate into an optical lattice. *New J Phys* (2018) 20:055005. doi:10.1088/1367-2630/aac11b

96. Liu X, Zhou X, Xiong W, Vogt T, Chen X. Rapid nonadiabatic loading in an optical lattice. *Phys Rev A (Coll Park)* (2011) 83:063402. doi:10.1103/physreva.83.063402

97. Liu X, Zhou X, Zhang W, Vogt T, Lu B, Yue X, et al. Exploring multiband excitations of interacting Bose gases in a one-dimensional optical lattice by coherent scattering. *Phys Rev A (Coll Park)* (2011) 83:063604. doi:10.1103/physreva.83.063604

98. Xiong W, Yue X, Wang Z, Zhou X, Chen X. Manipulating the momentum state of a condensate by sequences of standing-wave pulses. *Phys Rev A (Coll Park)* (2011) 84:043616. doi:10.1103/physreva.84.043616

99. Zhai Y, Yue X, Wu Y, Chen X, Zhang P, Zhou X. Effective preparation and collisional decay of atomic condensates in excited bands of an optical lattice. *Phys Rev A (Coll Park)* (2013) 87:063638. doi:10.1103/physreva.87.063638

100. Wang Z, Yang B, Hu D, Chen X, Xiong H, Wu B, et al. Observation of quantum dynamical oscillations of ultracold atoms in theFandDbands of an optical lattice. *Phys Rev A (Coll Park)* (2016) 94:033624. doi:10.1103/physreva.94.033624

101. Hu D, Niu L, Yang B, Chen X, Wu B, Xiong H, et al. Long-time nonlinear dynamical evolution forP-band ultracold atoms in an optical lattice. *Phys Rev A (Coll Park)* (2015) 92:043614. doi:10.1103/physreva.92.043614

102. Niu L, Hu D, Jin S, Dong X, Chen X, Zhou X. Excitation of atoms in an optical lattice driven by polychromatic amplitude modulation. *Opt Express* (2015) 23:10064–74. doi:10.1364/oe.23.010064

103. Guo X, Yu Z, Peng P, Yin G, Jin S, Chen X, et al. Dominant scattering channel induced by two-body collision of D-band atoms in a triangular optical lattice. *Phys Rev A (Coll Park)* (2021) 104:033326. doi:10.1103/physreva.104.033326

104. Li C, Zhou T, Zhai Y, Yue X, Xiang J, Yang S, et al. Optical Talbot carpet with atomic density gratings obtained by standing-wave manipulation. *Phys Rev A* (2017) 95:033821. doi:10.1103/PhysRevA.95.033821

105. Zhou T, Yang K, Zhu Z, Yu X, Yang S, Xiong W, et al. Observation of atom-number fluctuations in optical lattices via quantum collapse and revival dynamics. *Phys Rev A (Coll Park)* (2019) 99:013602. doi:10.1103/physreva.99.013602

106. Chen L, Zhou T, Mazets I, Hans-Peter S, Frederik M, Zijie Z, et al. Relaxation of bosons in one dimension and the onset of dimensional crossoverSciPost. *Phys* (2020) 9:058. doi:10.21468/SciPostPhys.9.4.058

107. Frederik M, Chen L, Igor M, Hans-Peter S, Tianwei Z, Zijie Z, et al. Extension of the generalized hydrodynamics to the dimensional crossover regime. *Phys Rev Lett* (2021) 126:090602. doi:10.1103/physrevlett.126.090602

108. Kinoshita T, Wenger T, David WS. A quantum Newton's cradle. *Nature* (2006) 440:900–003.

109. Xiong W, Zhou X, Yue X, Zhai Y, Chen X. A momentum filter for atomic gas. *New J Phys* (2013) 15:063025. doi:10.1088/1367-2630/15/6/063025

110. Yang B, Jin S, Dong X, Liu Z, Yin L, Zhou X. Atomic momentum patterns with narrower intervals. *Phys Rev A (Coll Park)* (2016) 94:043607. doi:10.1103/physreva.94.043607

111. Huang Q, Yao R, Liang L, Wang S, Zheng Q, Li D, et al. Observation of many-body quantum phase transitions beyond the kibble-zurek mechanism. *Phys Rev Lett* (2021) 127:200601. doi:10.1103/physrevlett.127.200601

112. Niu L, Jin S, Chen X, Li X, Zhou X. Observation of a dynamical sliding phase superfluid with P-band bosons. *Phys Rev Lett* (2018) 121:265301. doi:10.1103/physrevlett.121.265301

113. Jin S, Zhang W, Guo X, Chen X, Zhou X, Li X. Evidence of potts-nematic superfluidity in a hexagonal sp2 optical lattice. *Phys Rev Lett* (2021) 126:035301. doi:10.1103/physrevlett.126.035301

114. Shui H, Jin S, Li Z, Wei F, Chen X, Li X, et al. Atom-orbital qubit under nonadiabatic holonomic quantum control. *Phys Rev A (Coll Park)* (2021) 104: L060601. doi:10.1103/physreva.104.l060601

115. Dong X, Jin S, Shui H, Peng P, Zhou X. Improve the performance of interferometer with ultra-cold atoms. *Chin Phys B* (2021) 30:014210. doi:10.1088/1674-1056/abcf33

116. Ji W, Wang Y. Recent developments in the application of optical tweezers. *Physics* (1996) 25(12):707–12.

117. Song Q, Wen C, Zhang Y, Wang G, Ye A. Calibration of optical tweezers based on acousto-optic deflector and field programmable gate array. *Chin Opt Lett* (2008) 6(8):600–2. doi:10.3788/col20080608.0600

118. Wang G, Wen C, Ye A. Dynamic holographic optical tweezers using a twisted-nematic liquid crystal display. *J Opt A: Pure Appl Opt* (2006) 8:703–8. doi:10.1088/1464-4258/8/8/013

119. Ye A, Zhang Y. Micro-Raman spectroscopy of optically trapped single cell, 2009 international conference on optical instruments and technology: Optical trapping and microscopic imaging. *Proc SPIE* (2009) 7507:750705–1. doi:10.1117/12.838232

120. Ye A, Yuan F, Wen C, Zhang Y. *Single-molecule force measurement of IL-6 and IL6-receptor interaction in living cells*. Biophys. J. Jan (2008):350a.

121. Shu H, Cheng W, Ye A. Analysis of RAS-RAF interaction domains by single-molecule force spectroscopy measurements. *ACTA BIOPHYSICA SINA* (2011) 27(11):941–7.

122. Wen C, Ye A. single-molecule force measurement via optical tweezers reveals different kinetic features of two BRaf mutants responsible for cardio-facialcutaneous (CFC) syndrome. *Biomed Opt Express* (2013) 4(12):2835–45. doi:10.1364/boe.4.002835

123. Yu J, Tong X, Li C, Huang Y, Ye A. Using optical tweezers to investigate the specific single-interaction between apoA-I molecule and ABCA1 on living cells. *Chin Opt Lett* (2013) 11(9):091701–4. doi:10.3788/col201311.091701

124. Chen C, Tao T, Wen C, He W, Yn Q, Yq G, et al. Myosin light chain kinase (MLCK) regulates cell migration in a myosin regulatory light chain phosphorylation-independent mechanism. *J Biol Chem* (2014) 13:28478–88. doi:10.1074/jbc.m114.567446

125. Li Y, Wen C, Xie H, Ye A, Yin Y. Mechanical property analysis of stored red blood cell using optical tweezers. *Colloids Surf B: Biointerfaces* (2009) 70:169–73. doi:10.1016/j.colsurfb.2008.11.012

126. Zhang Y, Xu J, Yu Y, Shang W, Ye A. Anti-cancer drug sensitivity assay with quantitative heterogeneity testing using single-cell Raman spectroscopy. *Molecules* (2018) 23:2903. doi:10.3390/molecules23112903

127. Zhang Y, Jin L, Xu J, Yu Y, Shen L, Gao J, et al. Dynamic characterization of drug resistance and heterogeneity of the gastric cancer cell BGC823 using single-cell Raman spectroscopy,Dynamic characterization of drug resistance and heterogeneity of the gastric cancer cell BGC823 using single. *-cell Raman spectroscopy,Analyst* (2018) 143:164–74. doi:10.1039/c7an01287j

128. Lu-Di J, Jing-jing X, Yong Z, Yue-Zhou Y, Chang L, Dong-Ping Z, et al. YE an-pei, Raman spectroscopy analysis of chondrocyte dedifferentiation during in vitro proliferaion. *Acta Phys -Chim Sin* (2017) 33(12):2446–53. doi:10.3866/PKU.WHXB201706133

129. Jingjing X, Anpei Y. Laser trapping of Ag nanoparticles to enhance Raman spectroscopy in aqueous media. *OPTICS EXPRESS* (2019) 11(27):15528–39. doi:10.1364/OE.27.015528

130. Fang T, Shang W, Liu C, Xu J, Zhao D, Liu Y, et al. Nondestructive identification and accurate isolation of single cells through a chip with Raman optical Tweezers,Nondestructive identification and accurate isolation of single cells through a chip with Raman optical Tweezers,Anal. *Anal Chem* (2019) 91:9932–9. doi:10.1021/acs.analchem.9b01604

131. Fang T, Shang W, Liu C, Liu Y, Ye A. Single-cell multimodal analytical approach by integrating Raman optical tweezers and RNA Sequencing,Anal. *Chem* (2020) 92:10433–41. doi:10.1021/acs.analchem.0c00912

132. Fang T, Yuan P, Gong C, Jiang Y, Yu Y, Shang W, et al. Fast label-free recognition of NRBCs by deep-learning visual object detection and single-cell Raman spectroscopy. *Analyst* (2022) 147:1961–7. doi:10.1039/d2an00024e

133. Liu Y, Xu J, Tao Y, Fang T, Du W, Ye A. Rapid and accurate identification of marine microbes with single-cell Raman spectroscopy. *Analyst* (2020) 145:3297–305. doi:10.1039/c9an02069a

134. Zhou B, Sun L, Fang T, Li H, Zhang R, Ye A. Rapid and accurate identification of pathogenic bacteria at the single-cell level using laser tweezers Raman spectroscopy and deep learning.J. *J Biophotonics* (2022) 15:e202100312. doi:10.1002/jbio.202100312,

135. Tong Y, Fang T, Liu Y, Zhao D, Ye A. Research on hygroscopicity and volatility of single aerosol droplet. *J Atmos Environ Opt* (2020) 15:486–95.

136. Tong Y, Liu Y, Meng X, Wang J, Zhao D, Wu Z, et al. The relative humidity-dependent viscosity of single quasi aerosol particles and possible implications for atmospheric aerosol chemistry. *Phys Chem Chem Phys* (2022) 24:10514–23. doi:10.1039/D2CP00740A

137. Drever RWP, Hall JL, Kowalski FV, Hough J, Ford GM, Munley AJ, et al. Laser phase and frequency stabilization using an optical resonator. *Appl Phys B* (1983) 31:97–105. doi:10.1007/bf00702605

138. Chen J, Chen X. Optical lattice laser. In: Proceedings of the 2005 IEEE International Frequency Control Symposium and Exposition; 29-31 Aug. 2005; Vancouver, Canada. IEEE (2005).

139. Chen J. Active optical clock. *Sci Bull (Beijing)* (2009) 54:348–52. doi:10.1007/s11434-009-0073-y

140. Wang Y. Optical clocks based on stimulated emission radiation. *Sci Bull (Beijing)* (2009) 54:347. doi:10.1007/s11434-009-0064-z

141. Xu Z, Zhuang W, Wang Y, Wang D, Zhang X, Xue X, et al. Lasing of Cesium four-level active optical clock. In: Proceedings of the 2013 Joint European Frequency and Time Forum & International Frequency Control Symposium (EFTF/IFC); 21-25 July 2013; Prague, Czech Republic (2013). p. 395–8.

142. Pan D, Xu Z, Xue X, Zhuang W, Chen J. Lasing of cesium active optical clock with 459 nm laser pumping. In: Proceedings of the IEEE International Frequency Control Symposium (IFCS); 19-22 May 2014; Taipei, Taiwan (2014). p. 1–4.

143. Zhuang W, Chen J. Active Faraday optical frequency standard. *Opt Lett* (2014) 39:6339–42. doi:10.1364/ol.39.006339

144. Shi T, Pan D, Chen J. Realization of phase locking in good-bad-cavity active optical clock. *Opt Express* (2019) 27:22040–52. doi:10.1364/oe.27.022040

145. Pan D, Arora B, Yu Y, Sahoo BK, Chen J. Optical-lattice-based Cs active clock with a continual superradiant lasing signal. *Phys Rev A (Coll Park)* (2020) 102:041101. doi:10.1103/physreva.102.041101

146. Schäffer SA, Tang M, Henriksen MR, Jorgensen AA, Christensen BTR, Thomsen JW. Lasing on a narrow transition in a cold thermal strontium ensemble. *Phys Rev A (Coll Park)* (2020) 101:013819. doi:10.1103/physreva.101.013819

147. Norcia MA, Cline JRK, Muniz JA, Robinson JM, Hutson RB, Goban A, et al. Frequency measurements of superradiance from the strontium clock transition. *Phys Rev X* (2018) 8:021036. doi:10.1103/physrevx.8.021036

148. Laske T, Winter H, Hemmerich A. Pulse delay time statistics in a superradiant laser with calcium atoms. *Phys Rev Lett* (2019) 123:103601. doi:10.1103/physrevlett.123.103601

149. Maier T, Krämer SS, Ostermann L, Ritsch H. A superradiant clock laser on a magic wavelength optical lattice. *Opt Express* (2014) 22:13269–79. doi:10.1364/oe.22.013269

150. Bohnet JG, Chen Z, Weiner JM, Meiser D, Holland MJ, Thompson JK. A steady-state superradiant laser with less than one intracavity photon. *Nature* (2012) 484:78–81. doi:10.1038/nature10920

151. Meiser D, Ye J, Carlson DR, Holland MJ. Prospects for a millihertz-linewidth laser. *Phys Rev Lett* (2009) 102:163601. doi:10.1103/physrevlett.102.163601

152. Debnath K, Zhang Y, Mølmer K. Lasing in the superradiant crossover regime. *Phys Rev A (Coll Park)* (2018) 98:063837. doi:10.1103/physreva.98.063837

153. Roth A, Hammerer K. Synchronization of active atomic clocks via quantum and classical channels. *Phys Rev A (Coll Park)* (2016) 94:043841. doi:10.1103/physreva.94.043841

154. Kazakov GA, Dubey S, Bychek A, Sterr U, Bober M, Zawada M. Ultimate stability of active optical frequency standards. *At Phys (physics.atom-ph)* [Preprint] (2022). doi:10.48550/arXiv.2205.14130

155. Zhang S, Zhang X, Jiang Z, Pan D, Peng X, Chen H, et al. A compact optical clock scheme based on caesium atomic beam. In: Proceedings of the IEEE International Frequency Control Symposium (IFCS); 09-12 May 2016; New Orleans, LA, USA (2016). p. 1–4.

156. Shang H, Zhang X, Zhang S, Pan D, Chen H, Chen J. Miniaturized calcium beam optical frequency standard using fully-sealed vacuum tube with 10ˆ–15 instability. *Opt Express* (2017) 25:30459–67. doi:10.1364/oe.25.030459

157. Miao J, Shi T, Zhang J, Chen J. *Compact 459 nm Cs cell optical frequency standard with 2.1×10–13/*$\sqrt{\tau}$ *short-term stability*. Beijing China: Physical Review Applied (2022). arXiv:2206.09409.

Frontiers in Physics

TYPE Review
PUBLISHED 15 September 2022
DOI 10.3389/fphy.2022.970030

OPEN ACCESS

EDITED BY
José Paulo Santos,
Universidade NOVA de Lisboa, Portugal

REVIEWED BY
Xinye Xu,
East China Normal University, China
Ma Hongyang,
Qingdao University of Technology,
China

*CORRESPONDENCE
Xianghui Qi,
xhqi@pku.edu.cn
Qing Wang,
qw1988@pku.edu.cn

SPECIALTY SECTION
This article was submitted to Atomic and Molecular Physics,
a section of the journal
Frontiers in Physics

RECEIVED 15 June 2022
ACCEPTED 16 August 2022
PUBLISHED 15 September 2022

CITATION
He X, Yuan Z, Chen J, Fang S, Chen X, Wang Q and Qi X (2022), Improvement of the short- and long-term stability of high performance portable optically pumped cesium beam atomic clock.
Front. Phys. 10:970030.
doi: 10.3389/fphy.2022.970030

Improvement of the short- and long-term stability of high performance portable optically pumped cesium beam atomic clock

Xuan He[1], Zhichao Yuan[1], Jiayuan Chen[1], Shengwei Fang[1], Xuzong Chen[1], Qing Wang[2]* and Xianghui Qi[1]*

[1]Institute of Quantum Electronics, Peking University, Beijing, China, [2]Institute of Fundamental Experiment Education, Peking University, Beijing, China

The research of optically pumped cesium beam atomic clock (OPCB) at Peking University has lasted for decades. At present, the short-term frequency stability is $3 \times 10^{-12}/\sqrt{\tau}$ and the long-term (5-day) frequency stability can reach 7×10^{-15}. The optimization methods of the short-term frequency stability are using laser induced beam spectrum to stabilize the laser frequency, using cyclic transition to detect the atomic state and using a cesium oven with a collimator to generate the cesium atomic beam. The methods of obtaining the good long-term frequency stability are controlling the microwave power based on the atomic transition probability, controlling the C-field intensity based on Zeeman frequency and controlling the laser power using fluorescence. The compact optically pumped cesium beam atomic clock of Peking University is expected to contribute to the field of timing, positioning, navigation and high speed digital communication.

KEYWORDS

cesium clock, optically pumped, stability, laser, frequency

1 Introduction

The portable cesium beam atomic clock occupies an important position in the field of time and frequency [1]. Its excellent medium and long-term frequency stability can not be completely replaced by other atomic clocks. Cesium beam atomic clocks can be divided into two types: magnetic state-selection and optically pumped. Compact magnetic state-selection cesium beam atomic clocks have commercial products and have been widely used, such as 5071A [2] from the Microsemi, OSA3235B [3] from Oscilloquartz and LIP-Cs3000 [4] from China. The frequency stability of the magnetic state-selection cesium beam atomic clocks is approximately $8.5 \times 10^{-12}/\sqrt{\tau}$ in short-term and can reach 1×10^{-14} at several days. Due to the limitation of magnetic state-selection scheme, the frequency stability of magnetic state-selection cesium beam atomic clocks can hardly be further improved.

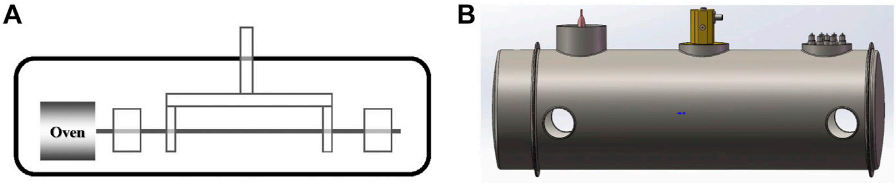

FIGURE 1
Cesium beam tube of the OPCB. **(A)** There is a cesium oven, a microwave cavity and two fluorescent collecting bowls, which are arranged in a straight line in a cesium beam tube. **(B)** A cesium beam tube of the portable OPCB in Peking university.

The portable OPCB adopts the optical pumping technology [5], which can have both high performance and long life compared to magnetic state-selection cesium beam atomic clock. OPCBs are expected to replace the existing magnetic state-selection cesium beam atomic clocks.

Researches on OPCB have been carried out both in China and abroad. GPS3 [6] using commercial laser can reach $3.8 \times 10^{-12}/\sqrt{\tau}$. OSCAR [7] and CS4 [8] have also achieved good short-term frequency stability. The frequency stability of TA1000 from Chengdu Spaceon [9] can reach $8.5 \times 10^{-12}/\sqrt{\tau}$. The research on portable OPCB in Peking University began in 1990s [10]; [11], and now it has been nearly 30 years. The frequency stability at 1 s has gradually improved from the initial 10^{-11} to 10^{-12} [12]. Its long-term frequency stability has gradually improved from 1-day frequency stability of 10^{-13} to 5-day frequency stability of 7×10^{-15}, reaching the forefront of the portable cesium beam atomic clock field [13]. In these years, the principle of the portable OPCB was improved, and the short-term frequency stability and long-term frequency stability were improved respectively [14]; [15].

This paper introduces the improvement of the frequency stability of the portable OPCB in Peking University. It is divided into the following parts: in the Section 2, the principle of portable OPCB is introduced. Section 3 introduced the improvement of short-term and long-term frequency stability of portable OPCB. The last section is a conclusion.

2 Principle

The portable OPCB is a closed-loop feedback system, which can output the transition frequency of cesium atoms. It can be divided into three parts: cesium beam tube, optical part and circuits.

2.1 Cesium beam tube

The cesium beam tube part of the portable OPCB includes a vacuum tube, a cesium oven, a microwave cavity and two fluorescence collecting bowls (Figure 1). The vacuum tube provides an environment for realizing atomic transition. It is a cylindrical tube approximately 40 cm long and approximately 18 cm in diameter. After sealing, its interior is pumped to a vacuum of 10^{-7} Pa. In such a vacuum environment, the cesium atomic beam can hardly collide with stray gas. The cesium oven stores about 5 g cesium atoms. Under the heating effect of the heating wire, the cesium atoms are gasified into gas and ejected from the collimator on the cesium oven due to the saturated steam pressure to form a cesium atomic beam. At 100 °C, the flux of cesium atomic beam can reach 4×10^{13} atom/s. Under this beam flow, the cesium oven can continuously eject cesium atoms for 10 years, meeting the needs of long-term continuous operation and time-keeping. The microwave cavity is a waveguide cavity in the shape of two arms. When the cesium atomic beam passes through the openings of the two arms of the microwave cavity, it interacts with the microwave and realize the Ramsey double resonance [16]. The length of the microwave cavity is 16.7 cm, and the opening of the microwave cavity is about 12 mm^2. The detuning of the microwave cavity can be controlled within 500 kHz. There are two fluorescence collecting bowls in the OPCB, which provides a place for the interaction between light and atoms. When the atomic beam passes through fluorescence collecting bowls, it interacts with a vertical laser beam and generates fluorescence. The fluorescence is reflected in the fluorescent bowl and is collected by photodetectors installed on fluorescent bowls. The fluorescence collection efficiency can reach 25%.

2.2 Optical bench

Compared with magnetic state-selection cesium beam atomic clock, the optical part is added to the portable OPCB. The optical part mainly includes a laser, an isolator, an acousto-optic modulator (AOM), a liquid crystal phase retarder and various optical lenses (Figure 2). The output wavelength of the laser is 852 nm, which corresponds to the transition of the D2 line of cesium atoms. Its maximum output power can reach 100 mW,

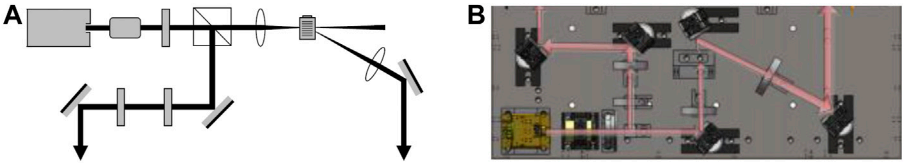

FIGURE 2
Optical bench of the OPCB. **(A)** The pumping laser and the probing laser are generated by one laser. **(B)** A photo of the optical bench.

which is enough to meet the requirements of laser pumping and laser detection. The function of the optical isolator is to prevent the laser beam from being fed back inside to the laser thereby affecting the operation of the laser and resulting in the instability of the laser frequency and power. The function of the AOM is to realize laser frequency shift. The pumping laser uses $|F = 4\rangle - |F' = 4\rangle$ line of cesium atoms, and the detection laser uses $|F = 4\rangle - |F' = 5\rangle$ line of cesium atoms. The frequency interval between them is about 251 MHz. We obtain the two lasers respectively with one laser and the AOM. Power of the pumping laser can be stabilized through the AOM. The liquid crystal phase retarder can control the polarization of the probing laser. With a polarizer, the power can be controlled by the voltage applied to the retarder.

2.3 Circuits

The circuit system of the portable OPCB consists of three parts: microwave source, control-servo part and auxiliary circuits. The auxiliary circuits include power supply circuit, screen display part, frequency output and phase synchronization part, satellite calibration part and other interactive parts. The microwave source realizes the function of frequency multiplication of 10 MHz OCXO crystal oscillator signal to 9192 MHz microwave signal. The maximum output power of the microwave source is 5 dBm, and the obtained phase noise is − 45dBc@1Hz. The phase noise can reach − 120dBc@ 1MHz, and the frequency and power of the final microwave signal can be accurately tuned. The frequency adjustment accuracy can reach 1μHz, and the power adjustment accuracy can reach 0.01 dBm. The control-servo part realizes the precise control of the operating parameters in the OPCB, including maintaining the high-voltage for vacuum, controlling the cesium oven temperature, controlling the C-field current, laser driver, AOM and liquid crystal retarder driver circuits. The high-voltage can be maintained at 3500 V, the fluctuation range of the cesium oven temperature can be stabilized within 0.01°C for a long time, the fluctuation range of the C-field current can be controlled within 100 nA, and the fluctuation range of the laser current can be controlled within 10 μA. The control-servo part also includes OCXO closed-loop locking, active C-field intensity servo, active microwave power servo and active laser powers servo.

3 Improvement of frequency stability

The frequency stability of the OPCB includes two aspects: short-term frequency stability and long-term frequency stability. The short-term frequency stability mainly depends on the signal-to-noise ratio of the obtained Ramsey signal, while the long-term frequency stability mainly depends on the sensitivity of both the controlled system parameters and the associated frequency shift to the environment.

3.1 Short-term frequency stability

The short-term frequency stability of the portable OPCB is inversely proportional to the signal-to-noise ratio. The higher the signal-to-noise ratio of Ramsey signal, the better the short-term frequency stability:

$$\sigma(\tau) = \frac{1}{K}\frac{\Delta\nu}{f_0}\frac{1}{SNR}\sqrt{\frac{T_s}{\tau}}. \tag{1}$$

3.1.1 Atomic beam

Adding a collimator to the cesium oven can improve the intensity of cesium atomic beam. There is a certain divergence angle after cesium atoms ejected from the cesium oven. If a collimator is not installed, the divergence angle of cesium atomic beam is large (Figure 3), and the number of effective cesium atoms that can actually pass through the two microwave cavities to the detection area is small. That means the signal-to-noise ratio of the beam reduced [17]:

$$\left(\frac{S}{N}\right)_{\text{atom}} = \frac{S_{\text{fluo}}}{\sqrt{\varphi_a}} = \frac{1}{2}\sqrt{\frac{\pi I_a}{2}}. \tag{2}$$

The length of the collimator of the cesium oven in our OPCB has been increased to 6mm, and the nozzle area of the collimator is about 12 mm^2 (Figure 3). In this case, the divergence angle of the cesium atomic beam can be controlled to about 40 mrad. The

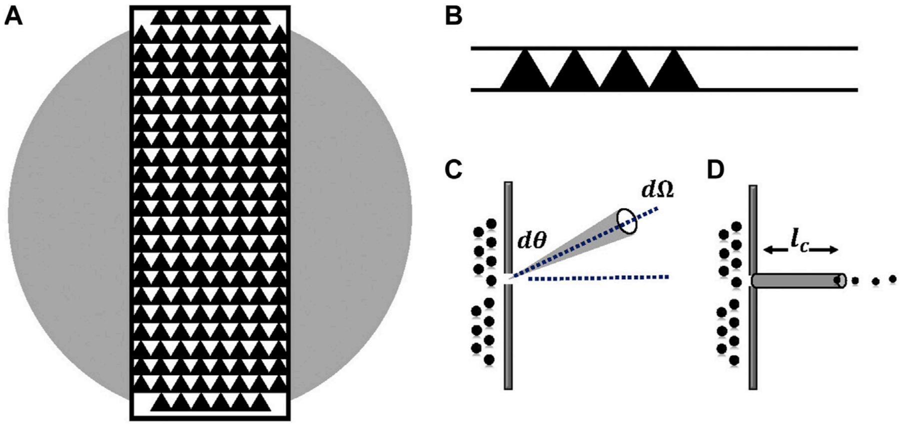

FIGURE 3
Cesium oven collimator of the OPCB. Front view: Cesium oven nozzle is rectangular, consists of many triangular thin tubes (0.003 mm^2), with a total area of 12 mm^2. **(A)** Zoom out **(B)** zoom in. Side view: **(C)** no collimator **(D)** collimator.

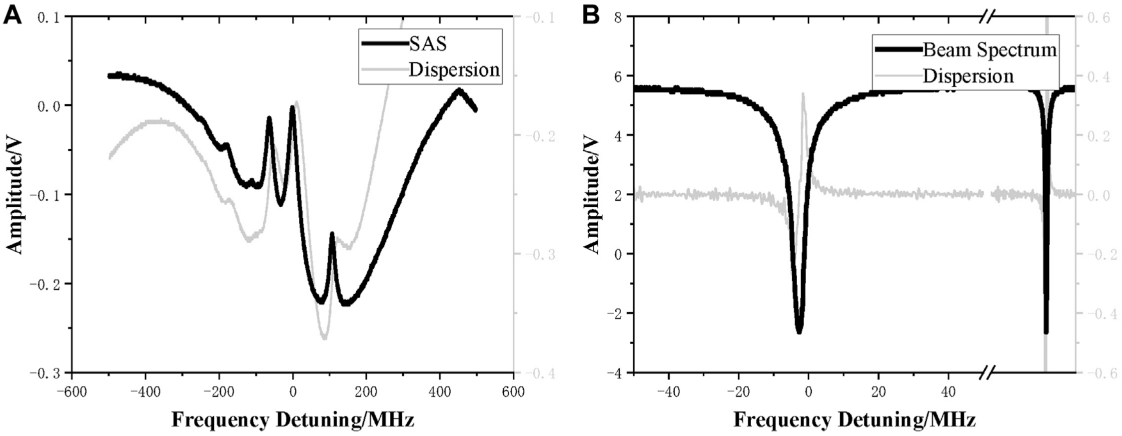

FIGURE 4
Laser stabilization spectroscopy of the OPCB. **(A)** Saturated absorption spectrum. **(B)** Atomic beam spectrum.

actual cesium atomic beam flow from the collimator is 4×10^{13} atoms/s, and the actual effective cesium atomic beam flow in the detection area is:

$$\phi_a = I_{all} \times L_e \times P_e \times T_e \times D_e. \tag{3}$$

It is approximately 10^9 atoms/s. Therefore, it can be concluded that the signal-to-noise ratio of the beam noise in the portable OPCB is approximately 30,000, and the short-term frequency stability that can be supported reaches $1 \times 10^{-12}/\sqrt{\tau}$, meeting the current requirement.

3.1.2 Laser stabilization

Using atomic beam spectrum to stabilize the laser frequency can reduce laser noise [18]. Compared with previous laser frequency stabilization method (saturated absorption spectrum frequency stabilization), beam spectrum frequency stabilization has the following advantages (Figure 4):

First, the intensity of the beam spectrum is greater than that of the saturated absorption spectrum. The frequency stabilization using saturated absorption spectrum needs a cesium cell in the optical path. The number of cesium atoms used in the saturated absorption spectrum in a cell is approximately 10^6 atoms, while the effective number of cesium atoms used in the frequency stabilization by atomic beam spectrum is approximately 10^9 atoms.

Second, the laser frequency obtained by beam spectrum can generate the maximum fluorescence signal. The beam spectrum has no Doppler background and no interference of cross

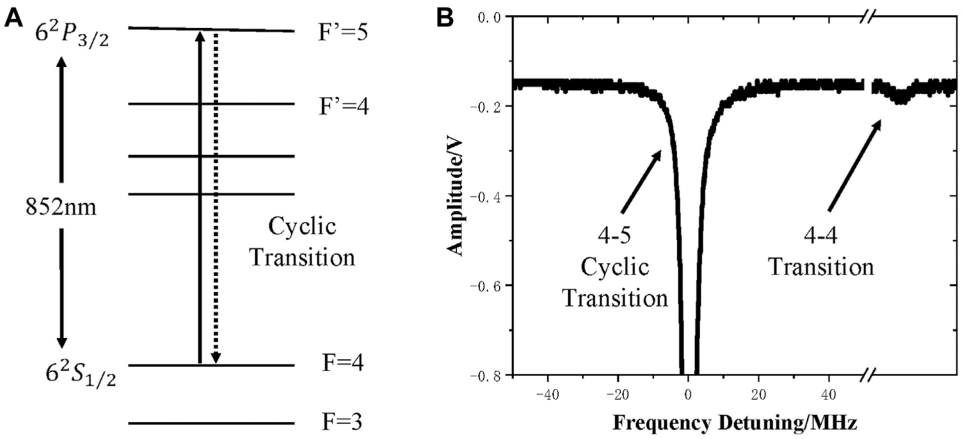

FIGURE 5
Cyclic transition of the OPCB. **(A)** $|F = 4\rangle - |F' = 5\rangle$ line is a cyclic transition. **(B)** $|F = 4\rangle - |F' = 5\rangle$ cyclic transition line is much larger than the $|F = 4\rangle - |F' = 4\rangle$ transition line under the same conditions.

absorption peaks. When using the saturable absorption spectrum, there will be a frequency shift of the transition peak due to the existence of the Doppler background and the larger cross-absorption peaks. At the same time, there will be an frequency error between the cesium atoms and the cesium atomic beam because the probing laser and the cesium atomic beam in detection area may not be completely vertical. Therefore, the laser frequency obtained by saturated absorption spectrum may not generate the maximum fluorescence signal.

Third, cesium cell is highly sensitive to the environment. The atomic beam is in the cesium atomic beam tube and the magnetic shielding layer of the tube effectively shields the influence of the external magnetic field. Meanwhile the cesium atoms in cell are greatly affected by the ambient temperature and there are more collisions between atoms and the cell, but this does not occur in a cesium atomic beam.

Fourth, the long-term reliability of a beam spectrum frequency stabilization is better. Cesium beam atomic clock needs long-term and continuous operation. So, maintaining long-term and reliable frequency stabilization of the laser is important. Compared with the saturated absorption spectrum, the beam spectrum has only three peaks. And it is easy to identify the largest $|F = 4\rangle - |F' = 5\rangle$ line peak, while the saturated absorption spectrum has six peaks with small size difference. In long-term operation of the atomic clock, the laser can be relocked in a short time after laser frequency unlocked using the beam spectrum. When using the saturated absorption spectrum, however, it requires complex spectrum finding and spectral peak identification processes.

3.1.3 Cyclic transition

Using $|F = 4\rangle - |F' = 5\rangle$ line cyclic transition of cesium atoms to detect atomic states can improve the signal-to-noise ratio. $|F = 4\rangle - |F' = 5\rangle$ is a cyclic transition line of the D2 line of cesium atoms (Figure 5). When the cesium atoms excited to the excited state of $|F' = 5\rangle$, it can only return to the ground state of $|F = 4\rangle$ through spontaneous emission due to the transition selection rule. In the process of laser detection, the cesium atoms in the $|F = 4\rangle$ state can be repeatedly excited by $|F = 4\rangle - |F' = 5\rangle$ cyclic transition line and generating a large fluorescence. Compared with the detection using the $|F = 4\rangle - |F' = 4\rangle$ line, the detection efficiency can be increased by 200 times, that means, the signal-to-noise ratio of the atomic clock in this process can be increased.

Through the above three improvements, under the conditions of the commercial DFB laser, the short-term frequency stability of the portable OPCB in our group has reached $3 \times 10^{-12}/\sqrt{\tau}$, which is approximately three times that of the 5071A high-performance, reaching the forefront of the portable cesium beam atomic clock.

3.2 Long-term frequency stability

In a portable OPCB, microwave power, C-field intensity and laser powers are the three most sensitive parameters to the environment. During the long-term operation of the OPCB, they need to be maintained by active servos otherwise the OPCB can not withstand the environmental fluctuations. For the portable OPCB, if the frequency stability needs to be less than 1×10^{-14} at 5 days, under the assumption of a linear drift,

$$y(t) = a + bt, \tag{4}$$

and according to the calculation formula of Allan variance, we have:

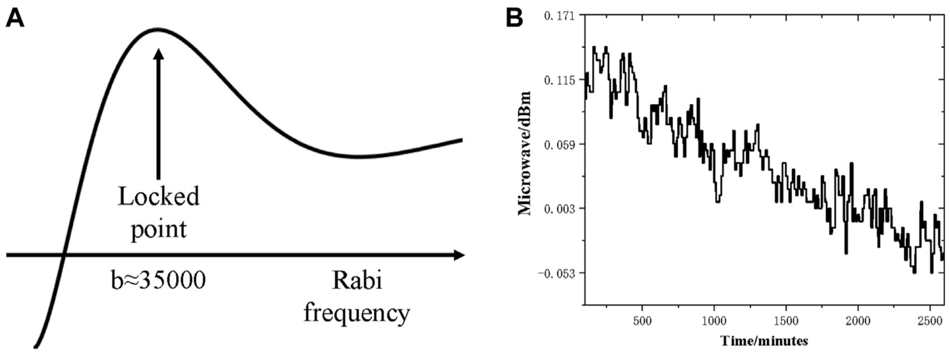

FIGURE 6
Microwave servo of the OPCB. **(A)** Transition probability curve. **(B)** Servo data.

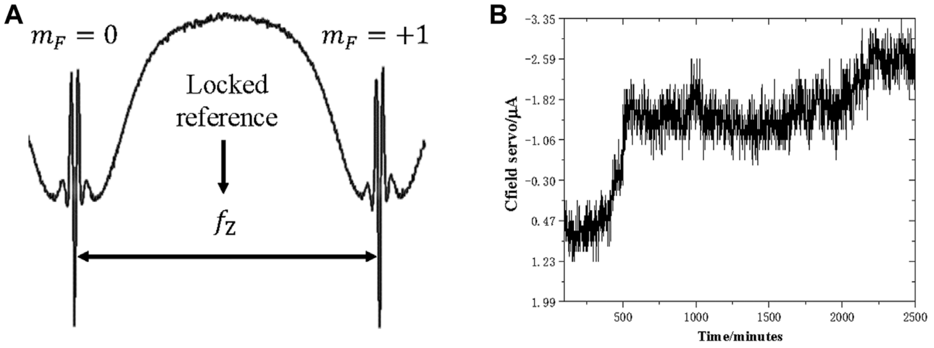

FIGURE 7
C-field servo of the OPCB. **(A)** Zeeman frequency as the locked reference. **(B)** Servo data.

$$\sigma(\tau) = \frac{\sqrt{2}}{2} b\tau. \quad (5)$$

The drift rate of the portable OPCB should be controlled in the range of 2.8 × 10^{-15} /day.

3.2.1 Microwave servo

We use the transition probability curve to servo the microwave power (Figure 6). The reason is that this curve is depended by the physical system and is a stable reference. Compared with the locking method through the detection of microwave power, this method can eliminate the influence of the microwave cavity, the microwave signal wiring and other parts. It directly control the microwave power actually interacting with atoms. In other words, the method decides the Rabi frequency of the interaction. During the operation of the OPCB, the microwave power is served once every 2 min. The microwave power is square wave modulated to obtain the error signal, which is then fed back to the microwave source. In normal operation, the microwave source only has an bad impact on the frequency stability of the OPCB after several thousands seconds averaging time. Therefore, the servo every 2 min can achieve a good long-term maintenance of the microwave power.

3.2.2 C-field servo

The intensity of the C-field directly affects the second-order Zeeman frequency shift in the OPCB and also affects the Rabi pulling frequency shift in the OPCB. During the long-term operation of the portable OPCB, the change of the external magnetic field will lead to the change of the internal magnetic field in the cesium beam tube, resulting in a frequency shift. We lock the C-field intensity according to the Zeeman frequency of the cesium atomic spectral line (Figure 7). The Zeeman frequency refers to the frequency difference between the $m_F = 0$ and $m_F = +1$ Ramsey signals. The magnitude of Zeeman frequency is directly related to the magnetic field intensity in the actual microwave cavity,

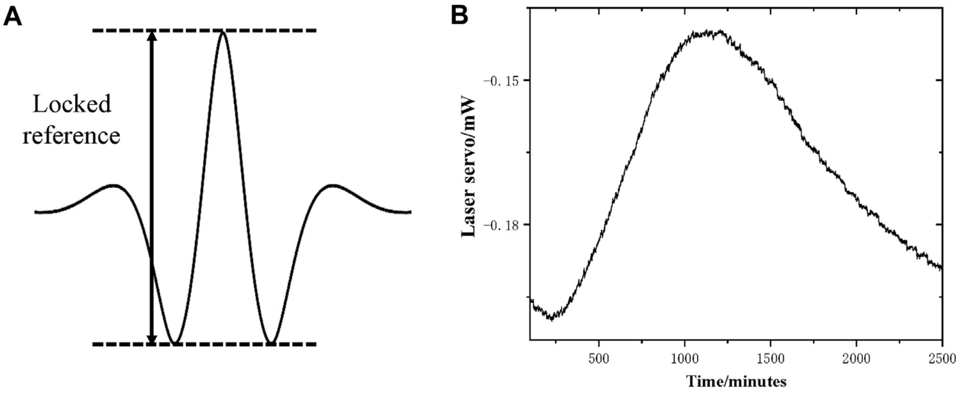

FIGURE 8
Laser power servo of the OPCB. **(A)** Locked reference of the laser power. **(B)** Servo data.

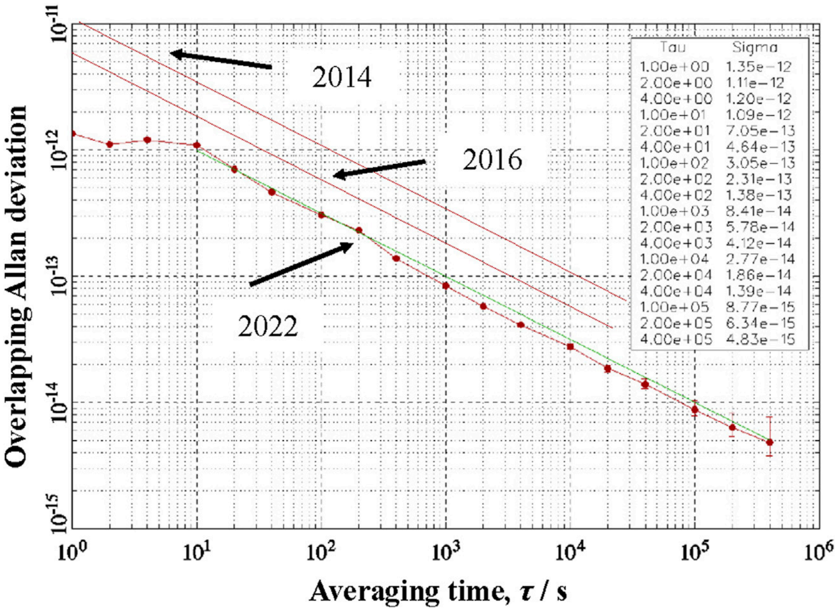

Tau	Sigma
1.00e+00	1.35e−12
2.00e+00	1.11e−12
4.00e+00	1.20e−12
1.00e+01	1.09e−12
2.00e+01	7.05e−13
4.00e+01	4.64e−13
1.00e+02	3.05e−13
2.00e+02	2.31e−13
4.00e+02	1.38e−13
1.00e+03	8.41e−14
2.00e+03	5.78e−14
4.00e+03	4.12e−14
1.00e+04	2.77e−14
2.00e+04	1.86e−14
4.00e+04	1.39e−14
1.00e+05	8.77e−15
2.00e+05	6.34e−15
4.00e+05	4.83e−15

FIGURE 9
Overlapping Allan deviation of the OPCB. In 2014, the short-term stability reached $1 \times 10^{-11}/\sqrt{\tau}$ and in 2016, the short-term stability reached $6 \times 10^{-12}/\sqrt{\tau}$. At present, the short-term stability is $3 \times 10^{-12}/\sqrt{\tau}$ and the 5-day stability can reach 7×10^{-15}. The green line is the fitting curve.

$$f_{Zeeman} \propto B_c. \qquad (6)$$

Since the frequency resolution of the Ramsey resonance line in the OPCB can reach 1×10^{-12}, the locking of C-field intensity can reach 10^{-5}. At this time, the control accuracy of second-order Zeeman effect can be within the range of 10^{-15}. In order to reduce the impact of Rabi pulling on the atomic clock, we control the Zeeman frequency of cesium atomic clock at 60 kHz. In this case, the frequency uncertainty caused by Rabi pulling can be controlled and the impact of the magnetic field on stability is eliminated during long-term operation.

FIGURE 10
Prototype of the OPCB.

3.2.3 Laser power servo

The fluctuation of laser powers will bring about the light shift and the fluctuation of the Ramsey signal, which will affect the normal close-loop of the OPCB. We have measured the frequency shift caused by laser power fluctuation, and found that the frequency shift caused by laser powers are approximately 4×10^{-13} /mw. In the case of 10^{-2} /day drift in laser power, the frequency shift caused by laser power change can reach 4×10^{-15} /day, which exceeds the requirement of the portable OPCB. The laser power drift caused by the aging of the laser and the long-term aging of the optical devices can hardly be overcome, so it is necessary to servo the laser powers actively. We proposed a method of using fluorescence to lock the laser powers (Figure 8). Compared with locking the laser powers in optical path, the method has the following advantages: 1) Directly controlling the intensity of fluorescence inside the cesium beam tube, which is the direct causes of the light shift. 2) Controlling the Ramsey signal of the atomic clock to make the feedback system of the OPCB stable. The control of the laser powers makes the frequency drift caused by the laser powers shift in the order of 10^{-17}, which meets the requirement.

After the above works, the long-term frequency stability of the portable OPCB in our group has been improved. The latest measurement results show that the long-term (5-day) frequency stability of the portable OPCB can exceed 7×10^{-15}.

4 Conclusions and prospects

The frequency stability of the portable OPCB is shown in Figure 9, which respectively shows the research results over the years, from $1 \times 10^{-11}/\sqrt{\tau}$ in 2014 to $3 \times 10^{-12}/\sqrt{\tau}$ now. The measurement time is gradually increasing. Figure 10 is the photo of the OPCB. It is 30 kg and in a 4 U size ($500 \times 440 \times 175$ mm^3). The rate power is 60 W, and the maximum power consumption does not exceed 100 W.

In the future, we will continue the research of the OPCB. One the one hand, we will continue to improve the frequency stability of the OPCB through the following methods: 1) Using a narrower linewidth laser. The frequency noise of the laser is one of the main noise sources in OPCBs [19] at present; 2) Using two lasers to prepare the atomic state [20]. The method can greatly increase the effective atomic beam flow and reduce the beam noise; 3) Using 2D-MOT to realize the cold cesium atomic beam [21]. The method can reduce the linewidth of the Ramsey signal. On the other hand, we will also explore the frequency stability performance of the portable OPCB in complex environments, such as in vehicle, satellite and others.

The portable OPCB is expected to move towards commercial production, make contributions to the time-frequency field in China and even the world, and provide important reference instruments for time-frequency service systems, satellite navigation and positioning systems and high-speed digital communication systems.

Author contributions

XQ, QW, and XC contributed to conception and design of the study. XH, SF, and XQ organized the database. XH performed the statistical analysis. XH, ZY, and JC wrote the first draft of the manuscript. All authors contributed to manuscript revision, read, and approved the submitted version.

Funding

This work is supported by the National Natural Science Foundation of China (Grants Nos.11920101004, 11334001, 61727819, 61475007), and the National Key Research and Development Program of China (Grant Nos. 2021YFA1400900, 2021YFA0718300).

Acknowledgments

The author would like to thank all the predecessors who have made efforts in the research project of portable OPCB, especially Yiqiu Wang, Donghai Yang, Jianwei Zhang and others.

Conflict of interest

The authors declare that the research was conducted in the absence of any commercial or financial relationships that could be construed as a potential conflict of interest.

Publisher’s note

References

1. Vanier J, Audoin C. The classical caesium beam frequency standard: Fifty years later. *Metrologia* (2005) 42:S31–S42. doi:10.1088/0026-1394/42/3/s05

2. Microsemi. *5071a primary frequency standard*. Aliso Viejo, California, United States: Microsemi (2018). Available from: https://www.microsemi.com/product-directory/cesium-frequency-references/4115-5071a-cesium-primary-frequency-standard (Accessed September 6, 2022).

3. Oscilloquartz. *Osa 3235b cesium clock*. Neuchâtel, Switzerland: Oscilloquartz (2022). Available from: https://www.oscilloquartz.com/en/products-and-services/cesium-clocks/osa-3230-series (Accessed September 6, 2022).

4. Chen J, Ma P, Wang J, Guo L, Ma Y, Cui J, et al. Progress in commercialization of compact magnetically selected cesium atomic clocks. *J Astronautic Metrology Meas* (2020) 40:12–6. doi:10.12060/j.issn.1000-7202.2020.03.03

5. Picqué J-L. Hyperfine optical pumping of a cesium atomic beam, and applications. *Metrologia* (1977) 13:115–9. doi:10.1088/0026-1394/13/3/006

6. Lutwak R, Emmons D, Garvey R, Vlitas P. *Optically pumped cesium-beam frequency standard for gps-iii* (2001). p. 15.

7. Lecomte S, Haldimann M, Ruffieux R, Berthoud P, Thomann P. Performance demonstration of a compact, single optical frequency cesium beam clock for space applications. In: 2007 IEEE International Frequency Control Symposium Joint with the 21st European Frequency and Time Forum. Geneva, Switzerland: IEEE (2007). p. 1127–31. doi:10.1109/FREQ.2007.4319254

8. Gurandell S, Hermann V, Barillet R, Cerez P, Theobald G, Audoin C, et al. Operation of a compact cesium beam tube: How to improve the stability towards the 10/sup -12//spl tau//sup -1/2/level. In: Proceedings of the 2002 IEEE International Frequency Control Symposium and PDA Exhibition (Cat. No.02CH37234). New Orleans, LA, USA: IEEE (2002). p. 480–3. doi:10.1109/FREQ.2002.1075931

9. Spaceon C. *Ta1000 optically pumped cesium beam atomic clock* (2022). Available from: http://www.elecspn.com/productdetail-1395.html (Accessed September 6, 2022).

10. Yang DH, Wang YQ. Preliminary results of an optically pumped cesium beam frequency standard at peking University. *IEEE Trans Instrum Meas* (1991) 40: 1000–2. doi:10.1109/19.119781

11. Chen J, Wang F, Wang Y, Yang D. A new design of a diffused laser light optically pumped small cesium beam frequency standard. *IEEE Trans Ultrason Ferroelectr Freq Control* (2000) 47:457–60. doi:10.1109/58.827435

12. Dong-Hai ZJW, Dong-Hai Y. High performance small optically pumped caesium beam frequency standard. *Chin Phys Lett* (2007) 24:1553–5. doi:10.1088/0256-307x/24/6/033

13. He X, Fang S, Yuan Z, Xie W, Chen N, Xiong Z, et al. Compact optically pumped cesium beam atomic clock with a 5-day frequency stability of 7 × 10 − 15. *Appl Opt* (2021) 60:10761–5. doi:10.1364/AO.443812

14. He X, Wang Q, Xie W, Chen N, Xiong Z, Qi X, et al. A high performance and portable optically pumped cesium beam frequency standard. In: 2020 Joint Conference of the IEEE International Frequency Control Symposium and International Symposium on Applications of Ferroelectrics (IFCS-ISAF). Keystone, CO, USA: IEEE (2020). p. 1–4. doi:10.1109/IFCS-ISAF41089.2020.9234812

15. Xie W, Wang Q, He X, Chen N, Xiong Z, Fang S, et al. Frequency instability of a miniature optically pumped cesium-beam atomic frequency standard. *Rev Scientific Instr* (2020) 91:074705. doi:10.1063/5.0001749

16. Ramsey NF. A molecular beam resonance method with separated oscillating fields. *Phys Rev* (1950) 78:695–9. doi:10.1103/PhysRev.78.695

17. Dimarcq N, Giordano V, Cerez P. Statistical properties of laser-induced fluorescence signals. *Appl Phys B* (1994) 59:135–45. doi:10.1007/BF01081164

18. Wang Q, Duan J, Qi X-H, Zhang Y, Chen X. Improvement of laser frequency stabilization for the optical pumping cesium beam standard. *Chin Phys Lett* (2015) 32:054206. doi:10.1088/0256-307x/32/5/054206

19. Dimarcq N, Giordano V, Cerez P, Theobald G. Analysis of the noise sources in an optically pumped cesium beam resonator. *IEEE Trans Instrum Meas* (1993) 42: 115–20. doi:10.1109/19.278532

20. Avila G, Giordano V, Candelier V, de Clercq E, Theobald G, Cerez P. State selection in a cesium beam by laser-diode optical pumping. *Phys Rev A (Coll Park)* (1987) 36:3719–28. doi:10.1103/PhysRevA.36.3719

21. Xie W, Wang Q, He X, Qi X, Chen X. Optically pumped cold cesium beam atomic clock based on two-dimensional magneto-optical trap. In: 2020 Joint Conference of the IEEE International Frequency Control Symposium and International Symposium on Applications of Ferroelectrics (IFCS-ISAF). Keystone, CO, USA: IEEE (2020). p. 1–4. doi:10.1109/IFCS-ISAF41089.2020.9234950

frontiers | Frontiers in Physics

TYPE Original Research
PUBLISHED 15 September 2022
DOI 10.3389/fphy.2022.956452

Development of Rb fountain clock for time keeping

Chen Weiliang*, Fang Fang*, Liu Kun, Zheng Fasong, Dai Shaoyang, Zuo Yani and Li Tianchu

National Institute of Metrology, Beijing, China

Check for updates

OPEN ACCESS

EDITED BY
Emmanouil P. Benis,
University of Ioannina, Greece

REVIEWED BY
Tom Parker,
National Institute of Standards and Technology (NIST), United States
Poonam Arora,
NPLI, India

*CORRESPONDENCE
Chen Weiliang,
chenwl@nim.ac.cn
Fang Fang,
fangf@nim.ac.cn

SPECIALTY SECTION
This article was submitted to Atomic and Molecular Physics,
a section of the journal
Frontiers in Physics

RECEIVED 30 May 2022
ACCEPTED 03 August 2022
PUBLISHED 15 September 2022

CITATION
Weiliang C, Fang F, Kun L, Fasong Z, Shaoyang D, Yani Z and Tianchu L (2022), Development of Rb fountain clock for time keeping.
Front. Phys. 10:956452.
doi: 10.3389/fphy.2022.956452

A new Rb fountain clock was built at the National Institute of Metrology with the aim to realize robustness and excellent long-term instability for time keeping. While some basic designs have been adopted from our Cs fountain clocks, new features have been included for improved performance. A double-metal interrogation microwave cavity with a thermal expansion self-compensating mechanism was used to reduce the clock sensitivity to temperature fluctuations for the first time, to our knowledge. Moreover, a compact optical system was developed to ensure robustness. These features dramatically increased the ambient temperature range. The developed Rb fountain clock achieved a typical fractional frequency instability of $1.49 \times 10^{-13}\,(\tau/\mathrm{s})^{-1/2}$ within 10 days of continuous operation without any intervention, demonstrating the potential for time keeping.

KEYWORDS

fountain clock, time keeping, Rb, double metal cavity, instability

1 Introduction

The quantum era in time and frequency metrology began when the SI unit second was redefined from an astronomical one to the hyper-fine transition frequency of Cs atoms [1]. Nowadays, Cs fountain clocks are employed as the primary frequency standards to realize the definition of the second [2, 3], and they have achieved the Type B uncertainties of a few parts in 10^{16} with instability ranging from a few parts in 10^{15} to several parts in 10^{16} in a day [4–16]. Furthermore, they are playing important roles in generating Coordinated Universal Time (UTC) [17] and providing accurate absolute frequency measurements for different atomic transitions [18]. For a Cs fountain clock, the detection of abundant atoms is highly desirable to increase the signal-to-noise ratio (SNR) for low instability. However, more atoms will result in a larger collisional frequency shift [19]. Thus, a compromise needs to be achieved between these two requirements during the clock operation. The collisional frequency shift of ^{87}Rb is about 50 times lower than that of ^{133}Cs; consequently, an ^{87}Rb fountain clock can operate with a higher atomic density than a ^{133}Cs clock, thereby reducing the frequency uncertainty [20, 21]. Furthermore, the laser sources used for trapping and cooling ^{87}Rb atoms are more stable than those for trapping and cooling Cs atoms, which improves the operation robustness of fountain clocks. Thus, ^{87}Rb fountain clocks have attracted significant interest and have been used as secondary frequency standards and time-keeping clocks [21–25]. For a commercial clock, it is important to

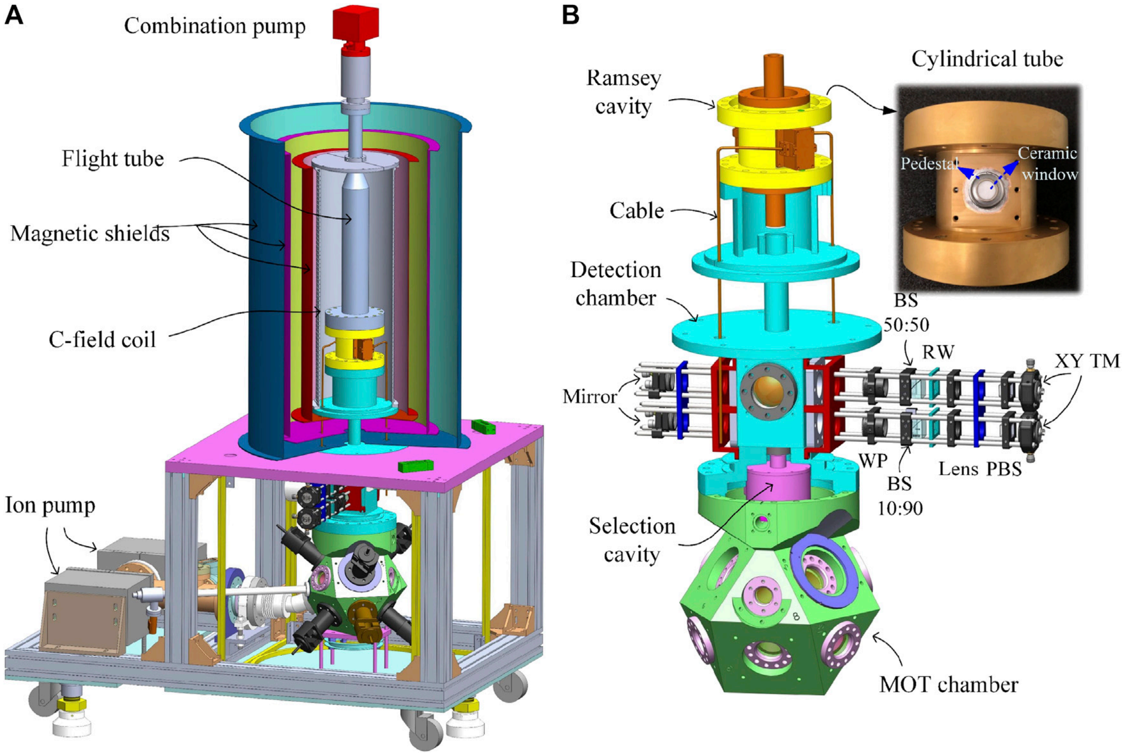

FIGURE 1
(A) Schematic of the Rb fountain clock physical package. **(B)** The cavities and detection system (XY TM: XY translation mount, PBS: polarization beam splitter, RW: rectangular window, BS: non-polarization beam splitter, and WP: waveplate).

release the operating requirements. One of the requirements is ambient temperature. Both Ramsey cavity and optical system are sensitive to it. A Ramsey cavity composed of oxygen-free copper (OFC) is sensitive to ambient temperature variations and its typical thermal coefficient of resonance frequency reaches up to 150 kHz/°C [24], which results in these fountain clocks only operating at the preset temperature with a narrow range.

Herein, a Rb fountain clock for time-keeping that was built at the National Institute of Metrology (NIM) is reported. Notably, it has a low-temperature sensitive Ramsey cavity that is based on a double-metal thermal expansion self-compensating mechanism, which has been used for the first time to reduce the clock temperature sensitivity. This cavity functions as both a microwave resonator and a part of the vacuum chamber, making the clock physical package more compact. Additionally, a compact and robust laser system with a laser frequency auto-locking technology is employed to enable continuous operation for months without intervention.

Section 2 presents a detailed description of the NIM Rb fountain clock apparatus, focusing on the new designs. In Section 3, the deterioration of the clock frequency instability in relation to the Ramsey cavity is analyzed. Finally, the experimental results are presented, and the clock instability is evaluated and analyzed.

2 Rb Fountain clock apparatus

Similar to our Cs fountain clocks, the Rb fountain clock comprises four systems: physical package, optical bench, microwave rack, and control rack. Each system is connected with cables or fibers, and it is transportable and easy to reassemble for operation.

2.1 Physical package

Figure 1 displays the schematic of the physical package of the Rb fountain clock. It comprises four main functional units: the magneto-optical trap (MOT), state-selection unit, interrogation unit, and detection unit. The novel feature of this system is the double-metal Ramsey cavity. This cavity is a typical TE_{011} cylindrical microwave resonator, but the cylindrical tube is composed of titanium (Ti) and the two caps are composed of OFC. Thus, the changes of the cavity resonance frequency to temperature can be self-compensated due to the different thermal expansions of the two metals [26], and the system becomes insensitive to the temperature variations. This cavity design enables the resonance frequency to remain stable during the operation, leading to a highly stable Ramsey pulse amplitude and reduced frequency shift, such as cavity pulling. This design also ensures that the clock operates in a wide operating-temperature range and realizes the tolerance of the clock to ambient temperature changes. Furthermore, the two microwave-coupling holes on the cylindrical tube of the cavity are sealed with a ceramic window, as shown in Figure 1. Thus, the cavity itself can function as both a microwave resonator and a part of the vacuum chamber of the physical package. The Ramsey cavity is directly connected to the detection chamber and the flight tube via indium wires for vacuum seals. The rigid copper microwave coaxial cables are totally out of the vacuum. Compared to a traditional design of atomic fountain clocks with a Ramsey cavity inside the vacuum [9, 15, 16], the physical package in the proposed design is smaller and lighter, has less microwave leakage to the interrogation regime, and is much easier to assemble. Additionally, the resonance frequency of the cavity can be fine-tuned after vacuum baking. A detailed description of our constructed Ramsey cavity can be found in [26]. The Ti tube inner surface is coated with a copper layer and a thin gold layer to maintain a suitable *Q*-factor of about 11,500. Additionally, the sensitivity of its resonance frequency to the temperature variation is measured to be 16.3 kHz/°C, which is about seven times better than that of a traditional OFC cavity with the same size.

Above the flight tube, a complex pump is attached to maintain a pressure of 7×10^{-8} Pa in the flight tube. Two ion pumps are attached at the lower part of the vacuum system, and each of them is shielded with soft iron to maintain a pressure of 3×10^{-7} Pa in the MOT chamber. They are placed in opposite directions to balance the magnetic field produced by them. A tube reservoir connected to the MOT chamber holds an ampule of rubidium at room temperature, providing rubidium vapor. The Rb atoms are cooled and trapped in the MOT chamber, which has a design similar to that of the NIM5 Cs fountain clock [9]. Seven beam expanding and collimating modules (BECMs) are directly mounted on the MOT chamber, providing seven laser beams (diameter 24 mm, $1/e^2$ level): one for repumping atoms and six for cooling atoms. The adjustments of these modules for beam collimation, polarization, and angle are performed offline. A cylindrical state-selection cavity composed of aluminum with a Qfactor of about 3,200 is mounted between the MOT and detection chambers. The detection chamber is mounted above the MOT chamber; it is mainly used for pushing away the residual atoms in the $|F = 2\rangle$ state during the ascending and for detecting atoms in $|F = 1\rangle$ and $|F = 2\rangle$ clock states during the descending.

The detection system of the developed Rb fountain clock has a novel design that differs from that of our Cs fountain clocks. As shown in Figure 1, to shorten the optical path and improve the reliability, the detection system, comprising two 30-mm cage systems in a parallel layout, is directly mounted on the detection chamber using a homemade adapter. The lights for atomic detection and repumping are input from two polarization-maintaining (PM) fibers and are then shaped by the cage systems to yield two rectangular parallel standing wave beams with a spacing of 50 mm in the vertical direction. A fiber is connected to the fiber adapter mounted on the XY translation mount of the upper cage system to transport the detection light, and then, the light is collimated by a lens with a focal length of 100 mm. Thereafter, a 16×8 mm^2 rectangular detection light beam is cut out by a rectangular window (RW) and is incident on to a non-polarization beam splitter (BS) with a splitting ratio of 50T:50R. The transmission light through the BS is used as the detection light that interacts with the $|F = 2\rangle$ state atoms, and the reflection light is incident on to a BS with a splitting ratio of 10T:90R in the lower cage system. The reflection light of BS (10T:90R) is used for the detection of atoms in the $|F = 1\rangle$ state. Both the detection lights are retroreflected by mirrors on the opposite side of the detection chamber, yielding counterpropagating standing waves. A small part of the upper detection light at the bottom is blocked in front of the mirror, yielding the traveling wave for pushing away the $|F = 2\rangle$ atoms. The repumping light transmitted by the fiber is collimated by another lens with the same focal length in the lower cage system, is shaped by RW, and is incident on to the BS (10T:90R). The transmission part, only 10% of the incident repumping light, is retroreflected and used to repump the atoms in the $|F = 1\rangle$ state to the $|F = 2\rangle$ state. Since the two cage systems are quite near the two microwave cavities and along the quantum axis for the atom–microwave interactions, the posts for the cages and the fastening bolts for the optical mounts are composed of titanium and brass, respectively, to avoid unwanted magnetic fields.

Three pairs of Helmholtz coils with a mutually orthogonal layout are used to compensate for the magnetic field around the MOT chamber and the state-selection unit. A pair of anti-Helmholtz coils set along the axis of one pair of light modules is used to afford the MOT magnetic field. A vertical magnetic field of approximately 130 nT is applied in the flight tube using a double wound solenoid coil (called C-field coil) with a length of approximately 1 m surrounded by three layers of μ-metal magnetic shields, with the aim to provide a quantum axis and lift the degeneracy of the Zeeman sublevels. To obtain a uniform magnetic field, two additional coils are wound at both ends of the C-field coil.

2.2 Optical bench

Figure 2 displays the optical schematic of the Rb fountain clock. The master laser is a commercial second harmonic generation fiber laser with an output power of more than 1 W at a wavelength of 780.24 nm. The repump laser is a customized fiber-coupled-output distributed feedback laser with an output power of more than 10 mW. The frequencies of the master and repump lasers are locked to the$|F = 2\rangle \rightarrow |F' = 1 \times 3\rangle$ and the $|F = 1\rangle \rightarrow |F' = 1 \times 2\rangle$ transitions, respectively, of the ^{87}Rb atomic D2 line by their built-in frequency stabilization

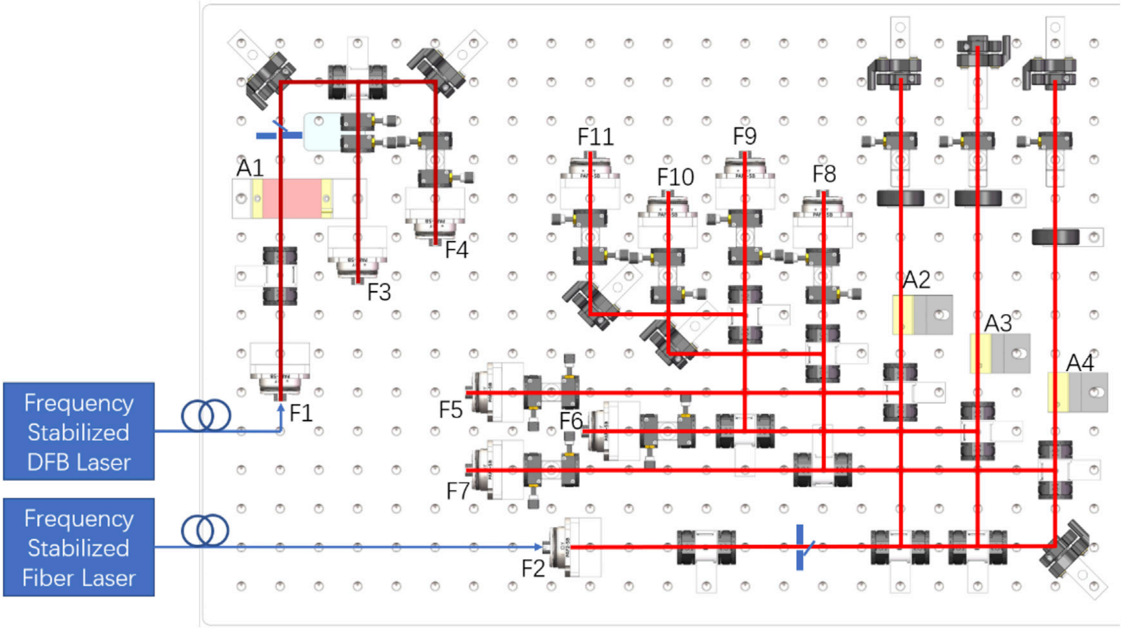

FIGURE 2
Optical schematic of Rb fountain clock (F: Fiber coupler, A: AOM).

modules. Their frequency-stabilized lights are transmitted to a 400 × 600 mm^2 optical bench via two PM fibers and then collimated into free-space light beams (diameter 1 mm, $1/e^2$ level) by fiber collimators, shown as F1 and F2. In this optical bench, the length of the longest path decreases to 1.275 m, which is about half as long as the longest path in the optical system used for the NIM6 Cs fountain clock.

The collimated repump light from F1 is frequency-shifted by A1, a +1-order single-pass AOM working at 78 MHz, and is split into two branches. Each branch is coupled into fibers via F3 and F4, forming the cooling and detection repumping light, respectively. The master laser light collimated by F2 is split into three branches: the detection light, upward and downward cooling lights. Each of them is modulated by a +1-order double-pass AOM, labeled as A2, A3, and A4, driving at 106, 98, and 98 MHz, respectively. The detection light through A2 is directly coupled into a fiber via coupler F5. The upward and downward cooling lights are both divided into three branches with equal powers and coupled into six PM fibers via couplers F6–F11. These fibers transfer the cooling light to the BECMs mounted on the MOT chamber. The cooling light power output from each BECM is greater than 50 mW. According to the diameter of the beams output from the fiber-free space modules, the cooling light density is considerably bigger than the saturation intensity (1.669 mW/cm^2) for cooling and detecting Rb atoms. To minimize the noise induced by fibers, which are easily affected by ambient temperature and air pressure, a half-waveplate (WP) and a quarter-WP placed in front of the fiber are used to align the polarization direction of the input light with the slow axis of the PM fiber.

Furthermore, some special designs are incorporated in the optical bench to ensure its functionality, stability, and compactness. First, the optical path is maximally shortened using small optical elements and by optimizing their layout, and the optical height is minimized to 27 mm above the breadboard surface plane. Next, we aim to decrease the number of adjustable mounts using a spring mechanism. Since the optical path and height are preassigned according the layout of the optical elements, the adjustable range requirements of the mounts for polarization beam splitter (PBS) and AOM are small. In this optical bench, these optical elements are adjusted without any springs. Here, a synthesized module, wherein a half-WP and a PBS are mounted on two rotary adjusting frames fixed on the same pedestal, is proposed to accomplish the functions of light reflection, power splitting, and polarization rotation. The incident light at the 27 mm height level can be power-split via the PBS by rotating the half-WP. While the transmission light of the PBS maintains the same direction and height as the incident light, the deflection light can be modified to be perpendicular to the incident light while maintaining the height by properly rotating the pedestal and mount of PBS. Moreover, the commonly used multi-axis mount for AOM is simplified to an L-shape adapter with a long arm that is used to vertically fix the AOM and a short arm to fix the adapter on the breadboard. To optimize the modulation efficiency, AOM can be adjusted with two freedoms by rotating it vertically and rotating the adapter horizontally. The first-pass +1-order light of AOM will shift from the plane at the fixed optical height of 27 mm, but it will be retro-reflected since the double-pass scheme is applied. As shown in Figure 2, A2, A3, and A4 are mounted on this kind of L-shape adapter. Note that there is an exception for A1, which functions with a single-pass scheme and has to sit on a different horizontal adapter.

2.3 Microwave rack and control rack

To facilitate transportation, all instruments for microwave, vacuum, and laser involved in the fountain clock operation are integrated into two standard racks with the same sizes. The microwave rack comprises a 100 MHz distribution amplifier, two microwave sources for state selection and Ramsey interrogation, a DC power supply for the required DC voltages, three drivers of the vacuum maintenance system, and a precise current source for the C-field. The 100 MHz distribution amplifier is used to split the input signal from the H maser into multiple outputs, with minimal degradation of the input signal. A commercially available microwave source whose frequency can be changed by a computer-controlled program was employed for state selection. The interrogation microwave source is homemade, mainly comprising a 6.8 GHz DRO (dielectric resonator oscillator) and a 34 MHz DDS (direct digital synthesizer), both of which directly reference to the 100 MHz signal output from the H maser. The frequency of the 34 MHz DDS can also be precisely varied using the program. The microwave power can be turned on/off by a TTL (transistor-transistor logic) control microwave switch, which is located between two DC blocks interlinked by the feeding cables. The DC blocks are used to isolate the ground connection while avoiding unexpected perturbation. The control rack includes a display screen, a computer with commercial multifunctional IO cards, an I/O interface chassis, a multichannel signal generator for the AOM driver system, and two laser control systems. Using the control program coded by LabVIEW, the computer with the commercial multifunctional I/O cards can generate digital and analog time sequences, acquire the analog signal from the fluorescent detector at the detection zone, and realize the close-loop control of the frequency of the interrogation microwave source. Since the optical system has been compacted into a small-sized optical breadboard, it can be placed at the bottom of the control rack, but it is currently placed on a single support frame.

2.4 Operation time sequence

In addition to the new hardware designs, some new processes are adopted in the operation time sequence. To improve the short-term instability of the fountain clock, the duration of the operation time sequence is set to 1.2 s, which is similar to that of our cesium fountain clocks. This facilitates the comparison between them. The MOT loading time is 340 ms, and the cold atoms are accelerated upward in steps of 1 ms by modifying the frequency of the cooling beams. Thereafter, the power and frequency of the cooling beams are strictly synchronously changed in steps of 1.2 ms for the polarization gradient cooling. Then the cold atoms exhibit a ballistic trajectory, wherein the atoms experience in series Rabi interactions in the selection cavity, pushing the $|F = 2\rangle$ state ones away by the detecting light, Ramsey interactions in the interrogation cavity and drift tube, and state detection in the detection chamber. To avoid the cross-talk between the selection and interrogation microwave, they are alternatively shuttered with approximately 60 dB attenuation when they are not in use, and the frequency of the selection microwave is set as −30 Hz detuning from the resonance frequency. Since no interference switch is present in the interrogation microwave source, the microwave for interrogation is open while the atoms are in the Ramey interrogation.

3 Instability deterioration related to ramsey cavity and atomic number

The fractional frequency instability of a fountain clock is well known to be [27, 28].

$$\begin{aligned}\sigma_y(\tau) &= \frac{1}{\pi Q_{\text{at}}}\sqrt{\frac{T_{\text{c}}}{\tau}}\left(\frac{1}{N_{\text{at}}}+\frac{1}{N_{\text{at}}n_{\text{ph}}\varepsilon_{\text{c}}}+\frac{2\sigma_{\delta N}^2}{N_{\text{at}}^2}+\gamma\right)^{1/2}\\ &= \frac{1}{\pi Q_{\text{at}}}\sqrt{\frac{T_{\text{c}}}{\tau}}\ \frac{1}{SNR}\end{aligned} \qquad (1)$$

where τ is the averaging time, T_{c} is the duration of one fountain cycle, $Q_{\text{at}} = \nu_0/\Delta\nu$ is the quality factor of the atomic clock transition, $\nu_0$is the central frequency of the clock transition, $\Delta\nu$ isthe line width of the center Ramsey fringe, and *SNR* is the signal-to-noise ratio. In the parentheses, the first term denotes the limitation of the quantum projection noise andN_{at} is the total number of detected atom; the second term denotes the photon scattering noise, n_{ph} is the average scattering photons for each atom, andε_{c} is the coefficient of fluorescent collection; the third term represents the contribution of the detection system and $\sigma_{\delta N}$ is the noise for detection; and the last term represents the phase noise of the local oscillator. Clearly, to achieve lower instability, the interrogation time could be increased, the atom collecting time could be reduced, or the SNR could be improved.

During the operation of fountain clocks, the change of the ambient temperature induces a shift of the cavity resonance frequency from its original design. Thus, the microwave power building inside the cavity will accordingly change, consequently changing the transition probability. In other words, the SNR gets worse, and consequently, the clock instability becomes worse. From Eq. 1, the instability of a

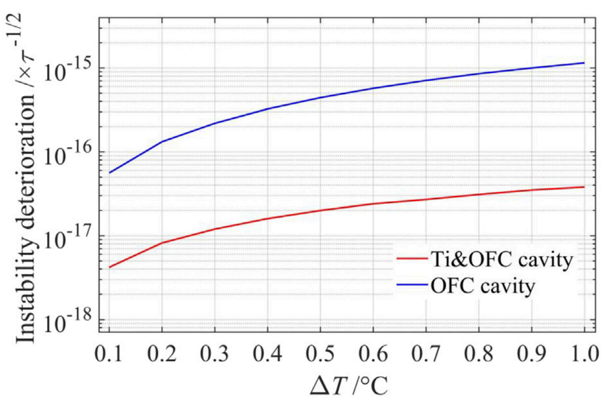

FIGURE 3
Calculated clock instability deterioration due to the temperature variations for two different types of Ramsey cavities. The red line is the instability of an OFC cavity, and the blue dashed line is the instability of a Ti&OFC cavity.

clock can be expressed as the fluctuations of the Ramsey transition probability δP as follows [29]:

$$\sigma_y(\tau) = \frac{\delta P}{2\pi Q_{\mathrm{at}}}\sqrt{\frac{T_c}{\tau}} \tag{2}$$

where δP is the probability fluctuations at the fountain clock operation frequency $\nu_0 \pm \Delta\nu/2$. It can be expressed as

$$\delta P = \frac{1}{2}\sin^2(b\tau_{\mathrm{in}}) - \frac{1}{2}\sin^2[b\tau_{\mathrm{in}}(1-\delta)] \tag{3}$$

where b is proportional to the square root of the microwave power. δ denotes the relative change of $b\tau_{\mathrm{in}}$ with the cavity temperature and it can be expressed as $\delta = 1-(p_{\Delta T}/p_0)^{1/2}$.Here, p_0 is the optimum power of a π/2 Ramsey pulse interrogation, $p_{\Delta T}$ is the applied microwave power with varying cavity temperature ΔT. When the cavity temperature varies, the microwave power building inside it accordingly changes. The deteriorating clock frequency instability can be expressed as

$$\Delta\sigma(\tau) = \frac{1}{4\pi Q_{\mathrm{at}}}\frac{1}{T_{\mathrm{p}}}\sqrt{\frac{T_c}{\tau}}\left|\sin^2(b\tau_{\mathrm{in}}) - \sin^2\left(b\tau_{\mathrm{in}}\sqrt{\frac{p_{\Delta T}}{p_0}}\right)\right| \tag{4}$$

where T_{p} is the time constant when the power changes by $(p_0 - p_{\Delta T})/e$ because it is a slowly time-varying process; we assume its value to be ~10,000 s in the real case.

A new double-metal cavity (Ti&OFC cavity) with a Ti tube and two OFC caps is fabricated to reduce the clock's temperature sensitivity, and the measured temperature sensitivity is −16.3 Hz/°C [26]. Assuming that both the resonance frequencies of the OFC cavity and the Ti&OFC cavity match the Rb clock frequency within 50 kHz, the microwave power inside the cavity will be within 10% from the optimal interrogation power, $T_c = 1.2$ s, and $\Delta\nu = 1.2$ Hz. The instability deterioration due to the interrogating microwave power variations are evaluated from Eq. 4 and are shown in Figure 3.

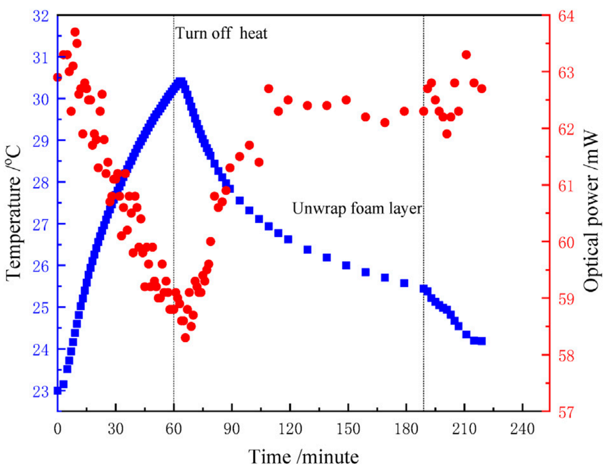

FIGURE 4
Variations of temperatures and output light powers vs time. At 60 min, the heat was turned off. The blue squares indicate the measured bench temperatures, and the red dots indicate the measured light output from the fiber.

Figure 3 shows that when the temperature increases by 1.0°C within 10,000 s, the corresponding instability deterioration is $1.2\times10^{-15}(\tau/\mathrm{s})^{-1/2}$for a traditional OFC cavity. Moreover, the corresponding instability deterioration is only $3.8\times10^{-17}(\tau/\mathrm{s})^{-1/2}$for the Ti&OFC cavity.However, in both cases, the instability is considerably lower than the current best result, which sets an upper limitation for the lab-temperature fluctuations. In other words, owing to the low-temperature sensitivity of the Ramsey cavity, our Rb fountain clock can operate in a relatively wide temperature range. Then, the instability of the clock optical system is a limiting factor that is sensitive to the temperature fluctuations. Thus, we developed a compact and robust optical bench.

4 Experimental results

4.1 Measurement of sensitivity of optical system to the temperature fluctuations

To measure the sensitivity of the optical system to temperature fluctuations, the entire optical bench was heated to different temperatures, and the output power of light from the fiber was monitored at the same time. The longest optical path with a length of 1.275 m was chosen, which should be the most sensitive to temperature variations. The entire optical bench was enclosed in a layer of foam and the air inside was heated using a

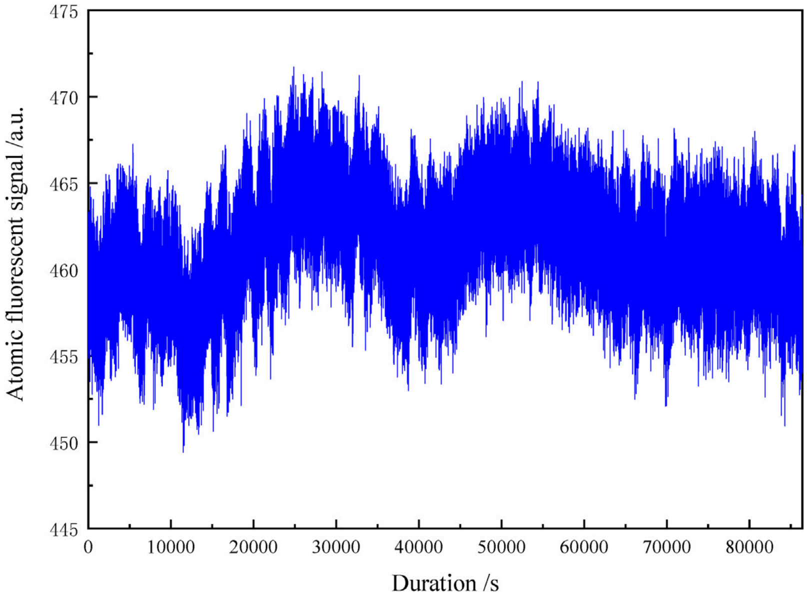

FIGURE 5
Atomic fluorescent signal in 1 day (Vertical axis is the sum of the atomic fluorescent signal of |*F* = *1*⟩ state to |*F* = *2*⟩ state with arbitrary units).

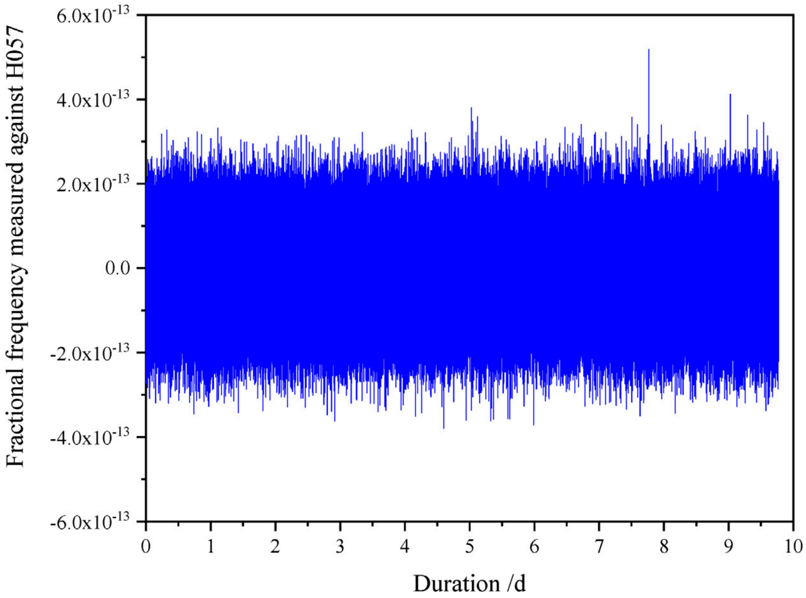

FIGURE 6
The frequency data of measurement.

resistance heater. The duration of the measurement was about 220 min. The results are shown in Figure 4.

In Figure 4, the blue squares represent the measured temperature of the optical bench, and the red dots represent the measure light output from the fiber. The optical bench was heated for 1 h, and the temperature increased from 23 to 30.4°C. Then, the heat was turned off, and the system was cooled. Since the time constant is too long for the system to cool to room temperature, the foam layer was

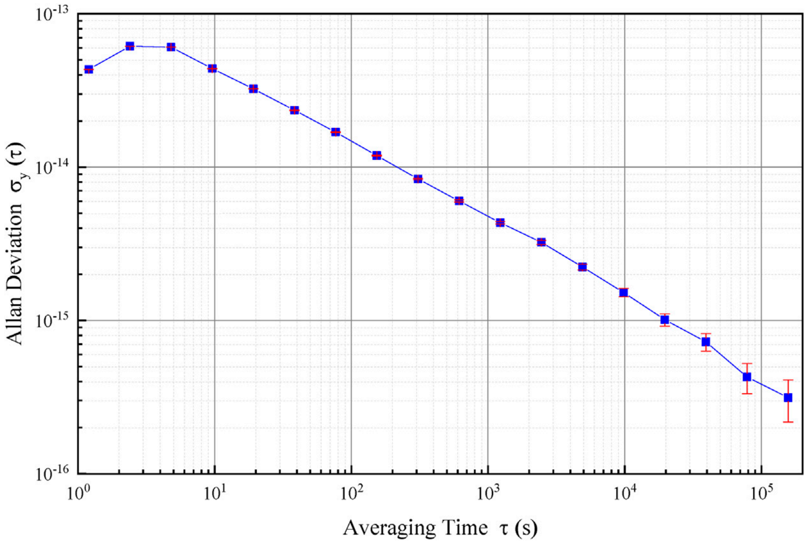

FIGURE 7
The standard Allan deviation of the Rb fountain clock.

unwrapped at 189 min. As shown in Figure 4, the peak-to-peak variation of the light output power during the entire temperature variation was less than 5.8 mW, about 10% of the output power. When the system was cooled down, the power recovered within acceptable level. This suggests that the proposed compact optical system is robust and insensitive to temperature variations within 7°C.

Figure 5 displays the typical atomic fluorescent signals in 1 day for the fountain clock working in the PID locking mode. The standard deviation was 3.07 with a mean value of 461.35 in arbitrary units, and the peak-to-peak atom number fluctuation in 1 day was 4.3%.

Considering that the cavity-pulling frequency shift is proportional to the number of atoms interacting with the microwave in the cavity [30, 31],

$$\left(\frac{\Delta f}{f_0}\right)_{\text{pull}}^{\text{ph}} = CN_{at}\frac{\delta f_{T0}}{(\delta f_{T0})^2 + (f_0/2Q_c)^2} \tag{5}$$

Here, N_{at} is the number of atoms, δf_{T0} is the cavity resonance frequency detuned from the atomic transition frequency f_0 under the temperature $T0$, Q_c is the quality factor of the cavity, and C is an amplitude coefficient whose magnitude depends on the microwave power. According to the cavity parameter adopted in this fountain clock, the resonance frequency of the double-metal Ramsey cavity matches the Rb clock frequency within 49 kHz, and the temperature of the lab was 23±0.2°C, The fluctuation of the cavity-pulling frequency shift corresponding to the atom number fluctuation was evaluated to be less than 2×10^{-17} when N_{at} was 1×10^7.

4.2 Frequency shift evaluations

Although Type B uncertainty evaluations are not necessary for a time-keeping clock, they will help eliminate the unexpected frequency shifts as the residual fluctuations of a large frequency shift deteriorate the frequency instability. The light shift and the microwave-power-related frequency shift could be a problem and were thus examined in the developed Rb fountain clock.

Various methods are used to eliminate stray light and reduce the possible light shift, such as covering up all fiber couplers and optical shutters with black aluminum foils and increasing the frequency detuning of AOMs during the interrogation. To verify that no light shift occurs, the Rb fountain clock was alternatively operated in two sequences with different AOM-driven powers for the cooling/detection beams during the interrogation, and the results show that the fractional frequency difference is less than 1×10^{-15}. The microwave-power-related frequency shifts were also analyzed by operating the fountain at different interrogation microwave powers. The fractional frequency difference between microwave powers of P0 and 9P0 was 2×10^{-15}. All the evaluation results show that regular main frequency shifts, such as the light shift and microwave-power-related shift, are small enough to ensure good instability.

4.3 Long-term instability

The Rb fountain clock with the 100 MHz signal from the H-maser H057 was continuously operated for 10 days from MJD 59693 to MJD 59703. The results are shown in Figure 6. The clock instability was 1.49×10^{-14} and 4.1×10^{-16} for the averaging time of 100 s and 1 day, respectively, as shown in Figure 7.

The cycle time of one fountain sequence is 1.2 s, and the frequency can be locked after two fountain cycles. Thus, the shape of the instability figure in the short time range depends on the parameters of proportional-integral (PI) control. The PI setting used in the Rb fountain clock is small, and the actually servo frequency is small. This makes the stability at the smallest averaging time less than that of the third averaging time, where the frequency is already in steady-state locking.

5 Conclusion

NIM has been devoted to the research of Cs fountain clocks for decades and has developed two fountain clocks NIM5 and NIM6, achieving Type B frequency uncertainties of 9×10^{-16} and 5.8×10^{-16}, respectively. Herein, a novel Rb fountain clock has been built for time keeping by adopting some important features of Cs fountain clocks and some new improvements. One of the most important features of the developed clock is a double-metal Ramsey cavity, which has been used for the first time, to our knowledge, to reduce the clock temperature sensitivity. This cavity functions as both a microwave resonator and a part of the vacuum chamber; consequently, the clock physical package is smaller and lighter, has less microwave leakage to the interrogation regime, and is much easier to assemble. Additionally, the resonance frequency of the cavity can be fine-tuned after vacuum baking. A new compact optical system was also designed and built to ensure stable light power outputs. The temperature dependency of the cavity and optical system were studied. The results show that the Rb fountain clock robustly operates in a large ambient temperature range. During 10 days operation, an instability of $1.49 \times 10^{-13} (\tau/s)^{-1/2}$ was achieved, with 4.1×10^{-16}in 1 day averaging time. The Rb fountain clock has been operating continuously without any invention. NIM has initiated the research of two other Rb fountains with the same configuration and is planning to operate a fountain clock ensemble with three Rb fountain clocks to guide UTC(NIM).

Data availability statement

The original contributions presented in this study are included in the article/Supplementary Material. Further inquiries can be directed to the corresponding author.

Author contributions

CW contributed to the design of the optical system, implementation the experiments, data collection, and interpretation of the results and manuscript preparation. FF was responsible for the physical system and experiment implementation. LK contributed to the magnetic shield, control system, and experiments as well as reviewed the editing. ZF contributed to microwave cavity and physic system design and reviewed the editing. DS contributed to the fluorescent collection system, C-field DC current supply, and reference frequency distribution. ZY helped with the experiment and reviewed the editing. LT supervised the project and contributed to funding acquisition.

Funding

This research was supported by project of the National Natural Science Foundation of China (11873044).

Acknowledgments

We sincerely thank Professor Wang Yuqiu. He is the pioneer in the fountain clock research in China, and as our mentor, he had numerous discussions with us and gave us many valuable suggestions to help us improve our fountain clock. Especially, he has been helped evaluate the cavity pulling and Majorana transition in our NIM5 and NIM6 uncertainty evaluation. We also thank the time keeping lab for their cooperation.

Conflict of interest

The authors declare that the research was conducted in the absence of any commercial or financial relationships that could be construed as a potential conflict of interest.

Publisher's note

References

1. Ramsey NF. The past, present, and future of atomic time and frequency. *Proc IEEE* (1991) 79(7):921–6. doi:10.1109/5.84968

2. Clairon A, Salomon C, Guellati S, Phillips WD. Ramsey resonance in a Zacharias fountain. *Europhys Lett* (1991) 16(2):165–70. doi:10.1209/0295-5075/16/2/008

3. Clairon A, Laurent P, Santarelli G, Ghezali S, Lea S, Bahoura M. A cesium fountain frequency standard: Preliminary results. *IEEE Trans Instrum Meas* (1995) 44(2):128–31. doi:10.1109/19.377790

4. Gerginov V, Nemitz N, Weyers S, Schroder R, Griebsch D, Wynands R. Uncertainty evaluation of the caesium fountain clock PTB-CSF2. *Metrologia* (2010) 47:65–79. doi:10.1088/0026-1394/47/1/008

5. Guéna J, Abgrall M, Rovera D, Laurent P, Chupin B, Lours M, et al. Progress in atomic fountains at LNE-SYRTE. *2012 IEEE Trans Ultrason Ferroelectr Freq Control* (2012) 59:391–409. doi:10.1109/tuffc.2012.2208

6. Domnin S, Baryshev N, Boyko I, Elkin GA, Novoselov AV, Kopylov LN, et al. The MTsR-F2 fountain-type cesium frequency standard. *Meas Tech* (2013) 55: 1155–62. doi:10.1007/s11018-012-0102-0

7. Heavner P, Donley A, Levi F, Costanzo G, Parker TE, Shirley JH, et al. First accuracy evaluation of NIST-F2. *Metrologia* (2014) 51:174–82. doi:10.1088/0026-1394/51/3/174

8. Levi F, Calonico D, Calosso E, Godone A, Micalizio S, Costanzo GA. Accuracy evaluation of ITCsF2: A nitrogen cooled caesium fountain. *Metrologia* (2014) 51: 270–84. doi:10.1088/0026-1394/51/3/270

9. Fang F, Li M, Lin P, Chen W, Liu N, Lin Y, et al. NIM5 Cs fountain clock and its evaluation. *Metrologia* (2015) 52:454–68. doi:10.1088/0026-1394/52/4/454

10. Weyers S, Gerginov V, Kazda M. Advances in the accuracy, stability, and reliability of the PTB primary fountain clocks. *Metrologia* (2018) 55:789–805.

11. Takamizawa A, Yanagimachi S, Hagimoto K. First uncertainty evaluation of the cesium fountain primary frequency standard NMIJ-F2. *Metrologia* (2022) 59: 035004. doi:10.1088/1681-7575/ac5e7b/meta

12. Beattie S, Jian B, Alcock J. First accuracy evaluation of the NRC-FCs2 primary frequency standard. *Metrologia* (2020) 57:035010. doi:10.1088/1681-7575/ab7c54

13. Devengoes L, Domenico G, Stefanov A. Measurement of the magnetic field profile in the atomic fountain clock FOCS-2 using Zeeman spectroscopy. *Metrologia* (2017) 54:239–46. doi:10.1088/1681-7575/aa62d1

14. Acharya A, Yadav S, Arora P. Present status of primary frequency standards at NPL, India. In: 2016 IEEE International Frequency Control Symposium (IFCS); 09-12 May 2016; New Orleans, LA, USA (2016). p. 1–2. doi:10.1109/FCS.2016.7546774

15. Fang F, Chen W. Advances in the NIM Cs fountain clocks. In: 2019 Joint Conference of the IEEE International Frequency Control Symposium and European Frequency and Time Forum; 14-18 April 2019; Orlando, FL, USA, 8856067. EFTF/IFC (2019).

16. Fang F, Chen W, Liu K The preliminary evaluation of the new fountain clock NIM6. 2019 URSI Asia-pacific Radio Science Conference (2019) 8738417:1–2.

17. Guéna J, Abgrall M, Clairon A, Bize S. Contributing to TAI with a secondary representation of the SI second. *Metrologia* (2014) 51(1):108–20. doi:10.1088/0026-1394/51/1/108

18. Lin Y, Wang Q, Fang Z, Cao S, Li Y. A 87 Sr optical lattice clock with 2.9×10^{-17} uncertainty and its absolute frequency measurement. *Metrologia* (2021) 58(3): 035010. doi:10.1088/1681-7575/abf33e

19. Tiesinga E, Verhaar J, Stoof C, van Bragt D. Spin-exchange frequency shift in a cesium atomic fountain. *Phys Rev A (Coll Park)* (1992) 45:2671–3. doi:10.1103/physreva.45.r2671

20. Gibble K, Chu S. Laser-cooled Cs frequency standard and a measurement of the frequency shift due to ultracold collisions. *Phys Rev Lett* (1993) 70:1771–4. doi:10.1103/physrevlett.70.1771

21. Fertig C, Gibble K. Measurement and cancellation of the cold collision frequency shift in an87RbFountain clock. *Phys Rev Lett* (2000) 85(8):1622–5. doi:10.1103/physrevlett.85.1622

22. Fertig C, Bouttier J, Gibble K. Laser-cooled 87Rb clock, conference on precision electromagnetic measurements. *Conf Dig CPEM* (2000) 2000:7. doi:10.1109/CPEM.2000.850848

23. Cheng H, Zhang Z, Deng S, Ji J, Ren W, Xiang J, et al. Design and operation of a transportable ^{87}Rb atomic fountain clock. *Rev Sci Instrum* (2021) 92:054702. doi:10.1063/5.0047715

24. Peil S, Crane S, Swanson T. *The USNO rubidium fountain*. IEEE International Frequency Control Symposium and Exposition (2006). p. 304–6. doi:10.1109/FREQ.2006.275402

25. Blinov I, Boiko A, Kosheliaevskii N, et al. First experiments on application of Rb fountain frequency standards for TA(SU) time scale maintenance. In: 2018 European Frequency and Time Forum; 10-12 April 2018; Turin, Italy. EFTF (2008). p. 257–62. doi:10.1109/EFTF.2018.8409045

26. Zheng F, Fang F, Wang X, Chen W, Liu K, Dai S, et al. A low temperature-sensitive Ramsey cavity for Rb fountain clocks. In: *China satellite navigation conference (CSNC 2022) proceedings*. Singapore: Springer (2022). p. 393–402. doi:10.1007/978-981-19-2576-4_35

27. Wynands R, Weyers S. Atomic fountain clocks. *Metrologia* (2005) 42(3): S64–79. doi:10.1088/0026-1394/42/3/s08

28. Szymaniec K, Park E, Marra G, Chalupczak W. First accuracy evaluation of the NPL-CsF2 primary frequency standard. *Metrologia* (2010) 47(4):363–76. doi:10.1088/0026-1394/47/4/003

29. Santarelli G, Laurent P, Lemonde P, Clairon A, Mann AG, Chang S, et al. Quantum projection noise in an atomic fountain: A high stability cesium frequency standard. *Phys Rev Lett* (1999) 82:4619–22. doi:10.1103/physrevlett.82.4619

30. Bize S, Sortais Y, Mandache C, Clairon A, Salomon C. Cavity frequency pulling in cold atom fountains. *2001 IEEE Trans Instrum Meas* (2001) 50:503–6. doi:10.1109/19.918177

31. Ovchinnikov Y, Marra G. Accurate rubidium atomic fountain frequency standard. *Metrologia* (2011) 48:87–100. doi:10.1088/0026-1394/48/3/003

frontiers | Frontiers in Physics

TYPE Original Research
PUBLISHED 16 September 2022
DOI 10.3389/fphy.2022.985586

Satellite-borne atomic clock based on diffuse laser-cooled atoms

Yan-Ling Meng[1], Xiao-Jun Jiang[1], Jing Wu[1], Mei-Feng Ye[1], Hua-Dong Cheng[2], Lin Li[1]* and Liang Liu[1,2]*

[1]Laboratory of Space Laser Engineering and Technology, Shanghai Institute of Optics and Fine Mechanics, Chinese Academy of Sciences, Shanghai, China, [2]Key Laboratory of Quantum Optics, Shanghai Institute of Optics and Fine Mechanics, Chinese Academy of Sciences, Shanghai, China

EDITED BY
Jingbiao Chen,
Peking University, China

REVIEWED BY
Bin Jian,
National Research Council Canada (NRC-CNRC), Canada
Jiteng Sheng,
East China Normal University, China

*CORRESPONDENCE
Lin Li,
lilin@siom.ac.cn
Liang Liu,
liang.liu@siom.ac.cn

SPECIALTY SECTION
This article was submitted to Atomic and Molecular Physics,
a section of the journal
Frontiers in Physics

RECEIVED 04 July 2022
ACCEPTED 22 July 2022
PUBLISHED 16 September 2022

CITATION
Meng Y-L, Jiang X-J, Wu J, Ye M-F, Cheng H-D, Li L and Liu L (2022), Satellite-borne atomic clock based on diffuse laser-cooled atoms.
Front. Phys. 10:985586.
doi: 10.3389/fphy.2022.985586

The technique of laser cooling of atoms gives an opportunity to improve the performance of atomic clocks by using laser-cooled atoms. The most successful cold atom clock, called the atomic fountain, is now widely used as the primary frequency standard in many labs. The cold atom clock for satellite applications, however, has not been reported so far due to special requirements of space applications. Here, we report the development of an engineering model of a satellite-borne cold atom clock, which satisfied all requirements of in-orbit operation. The core of the clock's principle is the laser cooling of atoms by diffuse laser lights inside the microwave cavity. The structure of the physics package is presented, and its main parameters are also given. The principle and design of the optical bench are described. The initial test results are presented, and the possible improvements are also discussed.

KEYWORDS

diffuse laser cooling, satellite-borne, cold atom clock, microwave frequency standard, satellite navigation

1 Introduction

Atomic clocks with laser-cooled atoms have been developed rapidly since laser cooling of atoms was invented [1]. The atomic fountain is now widely used as a frequency standard in many labs, as summarized in Ref. [2], and even in space [3]. In a fountain clock, laser-cooled atoms, typically from a magneto-optical trap (MOT), are launched upward through a microwave cavity and drop downward through the cavity again due to gravity. The double interrogation between cold atoms and microwave gives Ramsey fringes, whose central fringe has a much narrower linewidth compared to the thermal beam. The fountain clock has excellent performance with accuracy and stability for 1 day around 2.0×10^{-16} but is bulky and difficult to operate.

Several schemes are realized to overcome the bulky volume of the atomic fountain. In these schemes, the MOT, microwave interrogation, and detection of atoms are performed inside the same cavity, and the Ramsey interaction is realized by two microwave pulses [4, 5]. Such an arrangement reduces the size of the fountain clock but keeps its character. Since the MOT requires a strong pulsed magnetic field, which affects the microwave cavity, this kind of setup has problems for long-term performance.

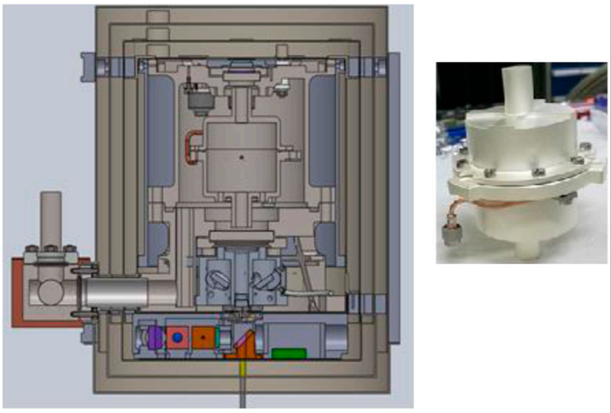

FIGURE 1
Physics package (left) and microwave cavity (right). The package includes a vacuum chamber whose vacuum is maintained using two ion pumps, and the chamber is covered by three layers of the magnetic shield. Inside the chamber is a cylindrical microwave cavity which is made of titanium and coated with silver. Cesium is spread into the microwave cavity from the source. The detection laser passes through the center of the cavity from the bottom to top and reflected.

Diffuse laser cooling (DLC) is insensitive to the magnetic field and is therefore an ideal method to generate cold atoms in the microwave cavity [6–8]. The cold atom clocks based on DLC have been developed in Paris and Shanghai [9, 10]; Paris' setup uses a spherical microwave cavity, while Shanghai's setup is cylindrical. Both obtained excellent performance with a long-term stability around 2.0×10^{-15}.

In this study, we present the development and initial tests of an engineering model of a microwave frequency standard with DLC for satellite systems. Different from the principle model, the engineering model must be designed for non-intervening and long-term continuous operation in space.

2 Design and assembling

The satellite-borne cold atom clock based on DLC has four units, including the physics package, optical bench, microwave electronics, and control system. All units are integrated into one unit, which satisfies the environment inside a satellite.

2.1 Physics package

The physics package includes mainly a vacuum system, a microwave cavity, a cesium source, a magnetic shield, and detection optics, as shown in Figure 1.

The core of the physics package is a cylindrical microwave cavity, placed at the center of the vacuum chamber, shown in Figure 1. This cavity, made of titanium with a silver-coated inner surface, shown in Figure 1 (right), has two functions: one acts as a microwave resonator for the interrogation of microwaves with atoms, and the other is for diffuse laser cooling [10]. The cavity is tuned to be resonant with the atomic transition of two cesium ground states at 9.19 GHz with $Q \approx 4000$. The inner surface of the cavity is specially polished such that it reflects lasers diffusely while keeping the microwave field smooth. The diffuse laser light inside the cavity is generated from the diffuse multi-reflection of injected lasers at the inner surface. In order to make the diffuse lights inside the cavity homogeneously, the four laser beams are injected through four small holes evenly placed at the end surface of the cavity [11, 12]. Such an arrangement makes the diffuse laser-cooled atom cloud concentrated in the middle of the cavity [12].

Vacuum is maintained using two small ion pumps and a getter at around 10^{-7} Pa, and the vacuum chamber is connected to the Cs source, whose temperature can be adjusted in order to control background Cs vapor inside the vacuum chamber. Outside of the vacuum chamber, there are three layers of magnetic shields to keep the magnetic field inside the microwave cavity below 2 nT. The probing laser beam travels along the central axis of the microwave cavity from one end to another and is reflected back to form a standing wave.

2.2 Optical bench

The optical system is designed for laser cooling, pumping, and detection, and the principle is shown in Figure 2. The main laser beam, locked to the cross peak between $F = 4 \rightarrow F' = 3,5$ by saturation absorption spectroscopy, is divided into three beams, including cooling, pumping, and probing. The frequency of the cooling laser is shifted by an acoustic optical modulator (AOM) to the detuning around -16 MHz from the transition between $F = 4 \rightarrow F' = 5$, as shown in the right side of Figure 2. The pumping laser is shifted by an AOM to be resonant with the transition between $F = 4 \rightarrow F' = 4$, and the probing laser is shifted to the resonance between $F = 4 \rightarrow F' = 5$. Another laser is locked to the crossover peak between $F = 3 \rightarrow F' = 2,4$ and shifted by an AOM to the resonance between $F = 3 \rightarrow F' = 4$ as the repumping beam. All AOMs are also used to control the time sequence.

The main optical elements of the optical bench are integrated on an aluminum plate, as shown in the left side of Figure 3. Both sides of the plate are used. Moreover, another layer is added, mainly for backup elements, including a laser. Those elements can be switched on when necessary.

The bench is placed in a sealing box for stable operation in vacuum. The sealing box, as shown in the right side of Figure 3, is filled with dried air at 1 atmosphere at 23°C. The sealing is carefully tested so that the pressure inside the box is kept at about 80% of the original one in vacuum for 10 years. Such a change does not affect the performance of optics.

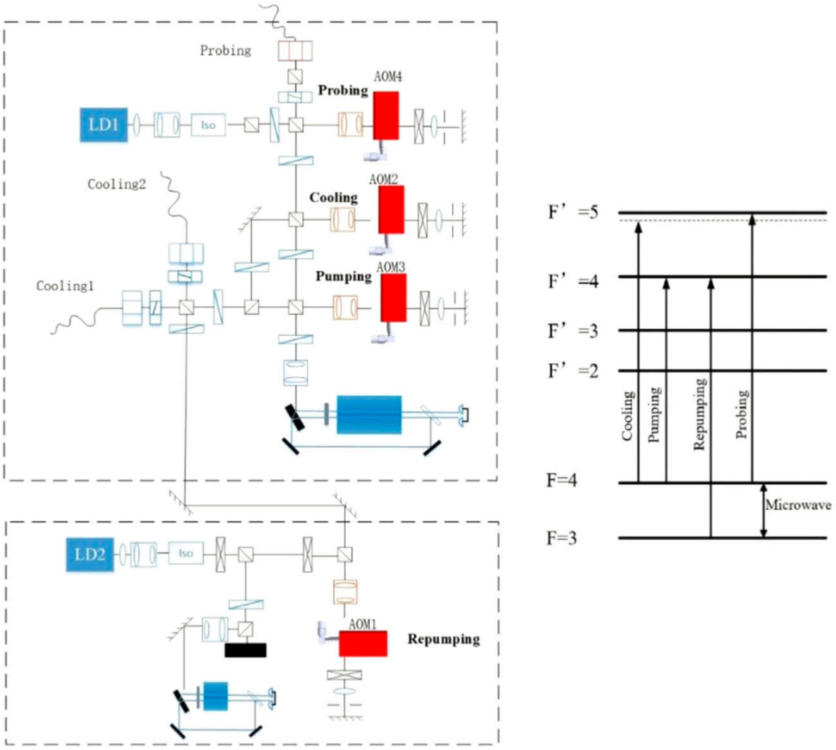

FIGURE 2
Principle of optical systems and energy levels. LD indicates a laser diode, AOM indicates an acoustic optical modulator, and Iso indicates an isolator. LD1 is used for cooling, probing, and pumping. LD2 is used only for repumping. Both lasers are locked by saturation spectroscopy and shifted by AOMs.

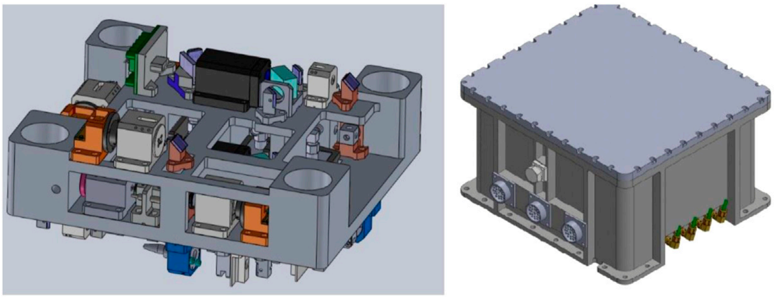

FIGURE 3
Optical bench (left) and its sealing box (right). All optical elements are firmly placed on an aluminum plate. The bench is placed in a sealing box, inside which the pressure is kept at around 1 atmosphere for a long time when the whole clock is placed in vacuum.

2.3 Microwave electronics and control system

All electronics are integrated into one unit, including microwave and control electronics. A 10 MHz signal from a low-noise OCXO crystal oscillator is synthesized into a 9.192 GHz microwave, which is injected into the cavity to interact with diffuse laser-cooled atoms. Two microwave pulses are used to interrogate cold atoms, as the Ramsey scheme requires.

The control system uses an FPGA to control the time sequence, including laser cooling, pumping, microwave interrogation, and probing, and evaluate the feedback error

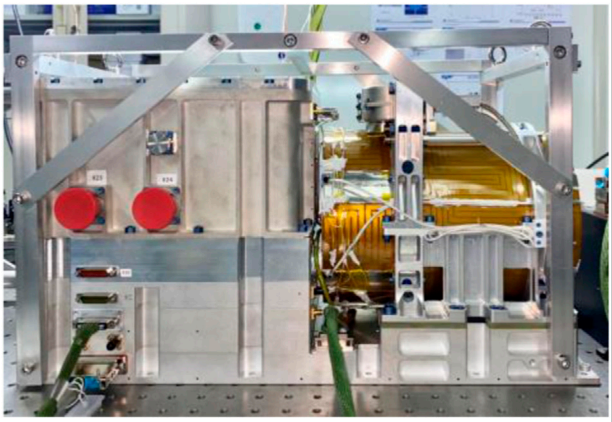

FIGURE 4
Assembled cold atom clock for satellite applications. The bottom shows electronics, top left shows the optical system, and top right shows the physics package.

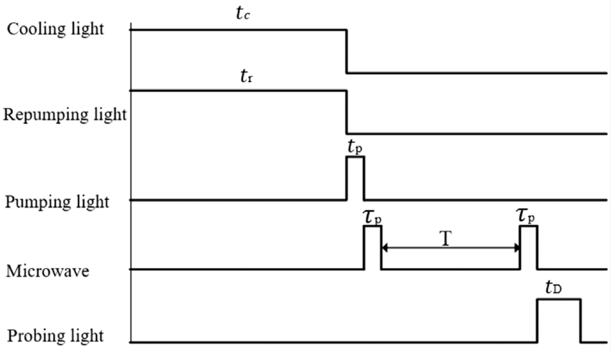

FIGURE 5
Time sequence of the clock operation. Cooling and repumping must be synchronized for effective diffuse laser cooling. A short pumping pulse is used to prepare the system ready for microwave interrogation. Two microwave pulses are used as Ramsey interactions with cold atoms, and the linewidth of the Ramsey fringe is determined by the separation of two pulses. The probing light is used to detect the atomic population after microwave interactions, which is directly related to the microwave frequency.

signal. Moreover, the control system is also used for data processing for laser power monitoring, temperature control, magnetic field control, and necessary communications.

2.4 Assembling

All units are assembled into one unit, as shown in Figure 4. The whole clock is fully functional, and it has a weight of 28 kg with a stable power consumption of around 60 W.

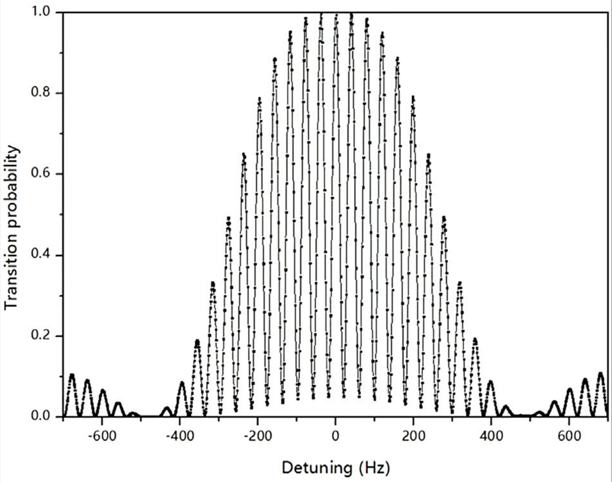

FIGURE 6
Typical Ramsey fringe. The linewidth of the central fringe is 20.0 Hz, and the signal-to-noise ratio is 650.

The clock is designed and tested to satisfy the requirements of the satellite environment. On the ground, the clock is tested in a vacuum chamber which is temperature-controlled, similar to that in a satellite. When the clock is placed in vacuum, the electronics and physics packed are quickly pumped to vacuum, while the optical bench is still at 1 atmosphere due to the protection of the sealing box.

3 Initial tests and discussion

The time sequence for normal operation of the clock is given in Figure 5. The atoms are first cooled by diffuse light in the microwave cavity, typically the cooling and repumping time $t_c, t_r \approx 40$ ms for clock operation. After cooling, all cold atoms are at the ground level of $F = 4$, evenly distributed in magnetic sub-levels $m_F = -4, -3 \cdots 3, 4$. A constant magnetic field at 100 nT along the axis of the microwave cavity is applied to separate the magnetic sub-levels. Pumping light is used to pump all cold atoms from the state $F = 4$ to $F = 3$ at $t_p \approx 1$ ms, and the atoms are distributed evenly in the magnetic sub-levels due to the pumping by diffuse light. Two microwave pulses are then used to interrogate cold atoms in the microwave cavity at the clock transition between $F = 3, m_F = 0 \rightarrow F = 4, m_F = 0$ at 9.192 GHz. The constant magnetic field keeps the interrogation happening only between $F = 3, m_F = 0 \rightarrow F = 4, m_F = 0$ without interference by those atoms in $F = 3, m_F \neq 0$. Here, the interrogation time is fixed in our test, $T = 22$ ms, and the duration of the microwave pulse $\tau_p = 2$ ms. The power of the microwave is carefully adjusted so that $\Omega\tau_p = \pi/2$, where Ω is the Rabi frequency of the microwave.

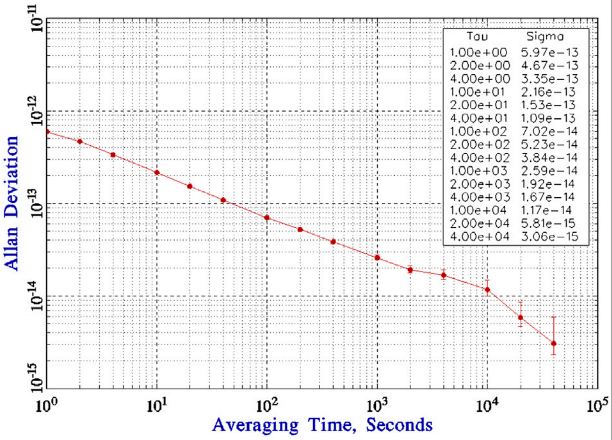

Tau	Sigma
1.00e+00	5.97e−13
2.00e+00	4.67e−13
4.00e+00	3.35e−13
1.00e+01	2.16e−13
2.00e+01	1.53e−13
4.00e+01	1.09e−13
1.00e+02	7.02e−14
2.00e+02	5.23e−14
4.00e+02	3.84e−14
1.00e+03	2.59e−14
2.00e+03	1.92e−14
4.00e+03	1.67e−14
1.00e+04	1.17e−14
2.00e+04	5.81e−15
4.00e+04	3.06e−15

FIGURE 7
Typical Allan deviation, with no drift removed, of the clock compared against an H-maser.

Scanning the microwave frequency gives the Ramsey fringes, as shown in Figure 6.

The full width at half-maximum of the central fringe is measured at around 20.0 Hz, which agrees with the theoretical value of $\Delta\nu \approx 1/2(T + \tau_p) = 20.8$ Hz. The signal-to-noise ratio is around 650, approximately measured by the signal value of the central peak of the Ramsey fringes over the noise level in Figure 6, which gives an estimated short-term stability of around $2.4 \times 10^{-13}/\sqrt{\tau}$.

Figure 7 gives Allan deviation of the cold atom clock with diffuse laser cooling relative to an H-maser. The clock is operated in a temperature-controlled lab at 22 ± 0.5 °C. The clock itself has no active temperature control but is placed on a cold plate whose temperature is controlled at 13 ± 0.5 °C for dissipating heat. Figure 7 gives a short-term stability at $5.97 \times 10^{-13}/\sqrt{\tau}$, which is almost 2.5 times worse than the theoretical estimation. The deterioration may come from the electronic feedback route. It is clearly shown that the deviation is affected by the environment, and it is expected to be improved significantly when active temperature control of the clock is applied. The drift is measured around 8.0×10^{-15} for 1 day.

There is plenty of room for the improvement of the clock. The current time sequence is managed for the specific requirement of the satellite application. A more suitable time sequence can be modified for better performance.

In microgravity, the lifetime of cold atoms in the microwave cavity is much longer than on the ground [13]; thus, the interrogation time can be much longer, and thus, the width of the clock signal can be much narrower. A narrower linewidth leads to better short-term stability, which is expected to be half an order better than on the ground.

In microgravity, the cooling efficiency is several times higher than on the ground due to the lack of gravity [3, 14]. The higher efficiency leads to more cold atoms and a lower temperature, which benefits the signal-to-noise ratio of the clock signal and improves the short-term stability significantly.

DLC based on stimulated forces is also possible [15]. With such a new scheme of DLC, the cooling time can be shortened to even less than 1 ms, which makes the cycle time of clock operation greatly reduced. Such a reduction leads to an increase in short-term stability.

Moreover, the long-term performance of the cold atom clock can benefit from the stable environment inside a satellite in orbit.

4 Conclusion

We have successfully developed a satellite-borne atomic clock with diffuse laser-cooled atoms, tested it in the lab with promising performance, and even compared with the Deep Space Atomic Clock [16]. The clock passes the vibration and thermal tests and has demonstrated long-term operation in vacuum. The results show that a cold atom clock based on DLC can be constructed to satisfy the requirements for satellite application, and its performance can reach even as high as 10^{-16} in 1 day. In addition to the reliability, robustness, and compactness, the cold atom clock with DLC has very small drift and a very high accuracy and thus is an ideal clock for the navigation system and deep space exploration.

The techniques developed in the compact cold atom clock can be used in further cold atom-based space quantum sensors.

Data availability statement

The original contributions presented in the study are included in the article/Supplementary Material; further inquiries can be directed to the corresponding authors.

Author contributions

Y-LM for the physics package, X-JJ for testing, JW for optics, M-FY for mechanical design, H-DC for physics principles, LNL for electronics and microwaves, and LGL for general.

Acknowledgments

The authors would like to thank Wang Yiqiu for his long-term support for this project. Back in the early 2000s, when people believed that an atomic clock with lasers could be used only as a lab device, Prof. Wang always encouraged us to continue this project. We all benefit from his deep insight. Now, we have proved that a cold atom clock is reliable enough for satellite applications. On the occasion of his 90th birthday, the authors would like to thank Prof. Wang Yiqiu again for his help to the development of the atomic clocks in our laboratory.

Conflict of interest

The authors declare that the research was conducted in the absence of any commercial or financial relationships that could be construed as a potential conflict of interest.

Publisher's note

References

1. Metcalf HJ, van der Straten P. *Laser cooling and trapping.* New York: Springer (1999).

2. Wang Q, Rong W, Wang YZ. Atomic fountain frequency standard: Principle and development. *Acta Phys Sin* (2018) 67:163202. doi:10.7498/aps.67.20180540

3. Liu L, Lü DS, Chen WB, Li T, Qu QZ, Wang B, et al. In-orbit operation of an atomic clock based on laser-cooled ^{87}Rb atoms. *Nat Commun* (2018) 9:2760. doi:10.1038/s41467-018-05219-z

4. Müller ST, Magalhaes DV, Alves RF, Bagnato VS. Compact frequency standard based on an intracavity sample of cold cesium atoms. *J Opt Soc Am B* (2011) 28:2592. doi:10.1364/josab.28.002592

5. Lee S, Choi GW, Hong HG, Kwon TY, Lee SB, Heo MS, et al. A compact cold-atom clock based on a loop-gap cavity. *Appl Phys Lett* (2021) 119:064002. doi:10.1063/5.0057150

6. Guillot E, Pottie PE, Dimarcq N. Three-dimensional cooling of cesium atoms in a reflecting copper cylinder. *Opt Lett* (2001) 26:1639. doi:10.1364/ol.26.001639

7. Cheng HD, Zhang WZ, Ma HY, Liu L, Wang YZ. Laser cooling of rubidium atoms from background vapor in diffuse light. *Phys Rev A (Coll Park)* (2009) 79:023407. doi:10.1103/physreva.79.023407

8. Wan JY, Wang X, Zhang X, Meng YL, Wang WL, Sun Y, et al. Quasi-one-dimensional diffuse laser cooling of atoms. *Phys Rev A (Coll Park)* (2022) 105:033110. doi:10.1103/physreva.105.033110

9. Esnault FX, Holleville D, Rossetto N, Guerandel S, Dimarcq N. High-stability compact atomic clock based on isotropic laser cooling. *Phys Rev A (Coll Park)* (2010) 82:033436. doi:10.1103/physreva.82.033436

10. Liu P, Meng YL, Wan JY, Wang XM, Wang YN, Xiao L, et al. Scheme for a compact cold atom clock based on diffuse laser cooling in a cylindrical cavity. *Phys Rev A (Coll Park)* (2015) 92:062101. doi:10.1103/physreva.92.062101

11. Meng YL, Cheng HD, Liu P, Zheng Xiao BCL, Wan JY, Wang XM, et al. Increasing the cold atom density in an integrating spherical cavity. *Phys Lett A* (2014) 378:2034–7. doi:10.1016/j.physleta.2014.05.013

12. Meng YL, Cheng HD, Zheng BC, Wang XC, Xiao L, Liu L. Controlling the shape of a cold atom cloud in a cylindrical cavity. *Chin Phys Lett* (2013) 30:063701. doi:10.1088/0256-307x/30/6/063701

13. Xiao L, Wang XC, Zheng BC, Meng YL, Cheng HD, Liu L, et al. Kinetic behavior of cold ^{87}Rb atoms in integrating sphere. *Optik* (2012) 123:442–6. doi:10.1016/j.ijleo.2011.03.035

14. Becker D, Lachmann MD, Seidel ST, Ahlers H, Dinkelaker AN, Grosse J, et al. Space-borne Bose–Einstein condensation for precision interferometry. *Nature* (2018) 562:391–5. doi:10.1038/s41586-018-0605-1

15. Metcalf H. Colloquium: Strong optical forces on atoms in multifrequency light. *Rev Mod Phys* (2017) 89:041001. doi:10.1103/revmodphys.89.041001

16. Burt EA, Prestage JD, Tjoelker RL, Enzer DG, Kuang D, Murphy DW, et al. Demonstration of a trapped-ion atomic clock in space. *Nature* (2021) 595:43–7. doi:10.1038/s41586-021-03571-7

Advantages of publishing in Frontiers

OPEN ACCESS
Articles are free to read
for greatest visibility
and readership

FAST PUBLICATION
Around 90 days
from submission
to decision

HIGH QUALITY PEER-REVIEW
Rigorous, collaborative,
and constructive
peer-review

TRANSPARENT PEER-REVIEW
Editors and reviewers
acknowledged by name
on published articles

Frontiers
Avenue du Tribunal-Fédéral 34
1005 Lausanne | Switzerland

Visit us: www.frontiersin.org
Contact us: frontiersin.org/about/contact

REPRODUCIBILITY OF RESEARCH
Support open data
and methods to enhance
research reproducibility

DIGITAL PUBLISHING
Articles designed
for optimal readership
across devices

FOLLOW US
@frontiersin

IMPACT METRICS
Advanced article metrics
track visibility across
digital media

EXTENSIVE PROMOTION
Marketing
and promotion
of impactful research

LOOP RESEARCH NETWORK
Our network
increases your
article's readership